University of Nevada, Reno

Simulation of the In-plane and Out-of-plane Seismic Performance of Nonstructural Partition Walls

A dissertation submitted in partial fulfillment of the

requirements for the degree of Doctor of Philosophy in

Civil and Environmental Engineering

by

Esmaeel Rahmanishamsi

Dr. Emmanuel “Manos” Maragakis / Dissertation Advisor

December, 2015

THE GRADUATE SCHOOL

We recommend that the dissertation
prepared under our supervision by

ESMAEEL RAHMANISHAMSI

Entitled

Simulation of the In-plane and Out-of-plane Seismic Performance of Nonstructural Partition Walls

be accepted in partial fulfillment of the
requirements for the degree of

DOCTOR OF PHILOSOPHY

Emmanuel “Manos” Maragakis, Ph.D., Advisor

Ahmad M. Itani, Ph.D., Committee Member

Gokhan Pekcan, Ph.D., Committee Member

Ian G. Buckle, Ph.D., Committee Member

John Anderson, Ph.D., Graduate School Representative

David W. Zeh, Ph.D., Dean, Graduate School

December, 2015

Abstract

Although recent years have witnessed progress in the experimental and analytical simulation of nonstructural partition walls, a robust solution to prevent extensive damage to these walls has not been found. This is due in part to the lack of validated comprehensive analytical tools to better understand and simulate these walls. The current study supports this field of research through proposing a reliable generic method, for the first time, to analytically model the in-plane and out-of-plane seismic performance of partition walls with various configurations.

Initially, a series of full-scale experiments is performed at the UNR-NEES site to investigate the system-level response and damage mechanisms of nonstructural systems, including cold-formed steel-framed (CSF) gypsum partition walls. The experiments reveal that the seismic performance of partition walls depends on the performance of the connections (e.g. gypsum board-to-stud/track connections) as well as the out-of-plane properties of the return walls. Accordingly, a series of component-level experiments (more than 130 experiments) is designed and conducted to characterize the cyclic response of the wall connections, namely gypsum board-to-stud/track, stud-to-track and track-to-concrete connections. The experimental data is used to propose and calibrate analytical nonlinear material models for the connections in OpenSees.

Subsequently, the connection models are employed to propose a novel detailed and yet computationally efficient modeling methodology for nonstructural partition walls. In this methodology, the in-plane and out-of-plane nonlinear behaviors of the connections

are represented by hysteretic load-deformation springs, which have been calibrated using the component-level experimental data. The steel framing members are modeled by nonlinear beam elements and the gypsum boards are simulated using linear four-node shell elements while. The representative models of corner connections are also assembled accounting for stud configurations, stud-to-stud and gypsum-to-stud screw attachments, and gypsum-to-gypsum contacts. The proposed procedure is used to generate analytical models of four configurations of experiments at the University of Buffalo as well as the analytical model of a C-shaped wall system, tested at the University of Nevada, Reno. Comparison of analytical and experimental results shows that the analytical model successfully estimates the force-displacement response, the out-of-plane dynamic characteristics, and the out-of-plane acceleration responses of partition walls. In addition, the model can predict the possible damage mechanisms in partition walls. The procedure proposed here can be adopted in future studies by researchers and also development engineers to assess the seismic performance of partition walls with various dimensions and construction details, especially where test data is not available.

To my parents for their unconditional love and constant support,

and

to my beloved wife for her support, sacrifice, and endurance.

Acknowledgements

The research presented in this study was funded by National Science Foundation (NSF) under grant number CMMI-0721399: Simulation of the Seismic Performance of Nonstructural Systems. However, any opinions, findings, conclusions or recommendations expressed in this document are those of the investigator and do not necessarily reflect the views of the sponsors.

I am deeply indebted to Professor Maragakis, my advisor and the committee chair, for giving me the opportunity to be part of a unique research project. He provided me valuable advice, encouragement, and endless support during my PhD. The members of my graduate advisory committee, Professor Ahmad Itani, Gokhan Pekcan, Ian Buckle, and John Anderson are also greatly thanked for their insightful comments. Additionally, my sincere thanks goes to Dr. Siavash Soroushian, who has guided me on my research work. His useful critiques, supports and inspirations helped me to finish my PhD in the most productive way possible.

The experimental part of the research could not be completed without the efforts of Dr. Sherif Elfass, Dr. Patrick Laplace, Dr. Joseph Weiser, Robert Nelson, Chad Lyttle, and Todd Lyttle, and the staff of the structures lab. The assistance from Mark Lattin during the assembly and testing in department material lab is also appreciated.

I would like to especially thank my best friends, Mahdi and Hanieh for their true friendship and support. They brought truckloads of joy and happiness to my family, and stood by my side when times got hard.

Lastly, I would like to express my deepest gratitude to my family: my parents, my brothers and sisters for supporting me spiritually and providing me unlimited emotional support and confidence in the course of this study. These past several years have not been an easy ride, both academically and personally. I truly thank Reihaneh, my wife, for sticking by my side and telling me "*it's gonna be fine*", even when I was irritable and depressed. Her love, support and constant patience have taught me so much about sacrifice, discipline and compromise.

Table of Contents

Abstract ..... **i**

Acknowledgements ..... **iv**

Table of Contents ..... **vi**

List of Tables ..... **xiv**

List of Figures ..... **xviii**

Chapter 1 : Introduction **1**

1.1. Motivation 1

1.2. Nonstructural Partition Walls 2

1.2.1. Damage in Past Earthquakes 4

1.2.2. Previous Experimental Studies 6

1.2.3. Previous Analytical Studies 13

1.2.4. Discussion 17

1.3. Objectives and Scope of Research 19

1.4. Dissertation Organization 20

1.5. References 23

Chapter 2: **System-Level Experiments on Ceiling/Piping/Partition Systems at UNR-NEES Site** 28

Abstract 28

Introduction 29

Test Specimen 29

Nonstructural Systems 30

Partition Walls 30
Ceiling Systems 31
Fire Sprinkler Piping 32
Excitation Protocol 32
Experimental Observations 33
Partition Walls 33
Ceiling Systems 36
Fire Sprinkler Piping 37
Conclusions 37
Acknowledgments 38
References 38
Chapter 3: Cyclic Shear Behavior of Gypsum Board-to-Steel Stud Screw Connections in Nonstructural Walls 40
Introduction 40
Description of test specimens 44
Test Setup 44
Experimental Program 45
Loading Protocol 46
Experimental Results 47
Individual GSC Force and Displacement 47
Damage Mechanisms 48
Effect of Loading Rate 49

Force-Displacement Responses of Specimens with Gypsum Board Detachment (Failure Mode *D*) 50

Force-Displacement Responses of Specimens with Gypsum Edge Breakout (Failure Model *E*) 52

Capacity fragility analysis 53

Development of a hysteresis model for gypsum-stud connections 58

Calibration of Proposed Numerical Model Using GSC Experiments 59

Development of Generic Models 61

Proposed Generic Models for Untested Edge Distances 63

Summary and conclusions 65

Acknowledgments 66

References 67

Chapter 4: Capacity Evaluation of Typical Stud-Track Screw Connections in Nonstructural Walls 70

1. Introduction 71

2. Description of Test Specimens 73

2.1. Test Setup 73

2.2. Experimental Program 74

2.3. Loading Protocol 75

3. Experimental Results 77

3.1. Individual STC Force and Displacement 77

3.2. Damage Mechanisms 78

3.3. Effect of Loa ding Rate 81

3.4. Force-Displacement Responses of Specimens with 0.48-mm Thick Studs/Tracks 82

3.5. Force-Displacement Responses of Specimens with 0.76-mm-Thick Studs/Tracks 83

4. Capacity Fragility Analysis 85

5. Development of an Analytical Hysteresis Model for Track-Stud Connections 89

5.1. Calibration of Proposed Analytical Model Using STC Experiments 90

5.2. Development of Generic Models 92

5.3. Proposed Generic Models Including Stud-Track Interaction 95

6. Summary and Conclusions 98

7. Acknowledgments 100

8. References 101

Chapter 5: Capacity Evaluation of Typical Track-to-Concrete Power-Actuated Fastener Connections in Nonstructural Walls 105

Abstract 105

Introduction 106

Description of Test Specimens 110

Setup for Tension Tests 110

Setup for Shear Tests 111

Experimental Program 112

Loading Protocol 113

Experimental Results 115

Individual Track-to-Concrete Connection Force and Displacement 115

Damage Mechanisms in Tension 115
Damage Mechanisms in Shear 116
Ultimate Connection Capacity 117
Effect of Loading Rate 119
Force-Displacement Responses of Specimens in Tension 120
Force-Displacement Responses of Specimens in Shear 121
Capacity Fragility Analysis 123
Damage States in Tension 124
Damage States in Shear 125
Fragility Curves 126
Development of a Numerical Hysteresis Model for Track-to-Concrete Connections 128
Calibration of Proposed Numerical Model Using Tension Experiment data 129
Calibration of Proposed Numerical Model Using Shear Experiment Data 131
Development of Generic Models 133
Proposed Generic Models for Untested Track Thicknesses 135
Summary and Conclusions 137
Chapter 6: Analytical model for the in-plane seismic performance of cold-formed steel-framed gypsum partition walls 144
Summary 144
1. Introduction 144
2. The Proposed Analytical Model 146
2.1. Gypsum boards and frame elements 147
2.2. Connections 148

2.3. Contacts 152

3. Validation of the Proposed Analytical Model 154

3.1. Available data from full-scale experiments at UB 154

3.2. Generic Analytical Model for UB Configuration #3 155

3.3. Adjustment of the analytical model for each particular specimen 157

4. Conclusions and future work 161

5. Acknowledgments 161

6. References 162

Chapter 7: Evaluation of the out-of-plane behavior of stud-to-track connections in nonstructural partition walls 165

1. Introduction 166

2. Description of test specimens 169

2.1. Test setup 169

2.2. Experimental program 170

3. Experimental results 172

3.1. Individual stud-to-track connection force and displacement 172

3.2. Damage mechanisms 172

3.3. Ultimate connection capacity 173

3.4. Effect of Loading Rate 176

3.5. Force-displacement response 177

4. Capacity fragility analysis 179

5. Development of a numerical hysteresis model for stud-to-track connections in out-of-plane direction 184

5.1. Calibration of proposed numerical model using experimental data 185

5.2. Development of generic models for tested connections 187

5.3. Proposed generic models for untested stud-to-track connections 189

6. Summary and Conclusions 192

7. Acknowledgments 194

8. References 194

Chapter 8: Analytical Model to Capture the In-Plane and Out-of-Plane Seismic Behavior of Nonstructural Partition Walls with Returns 197

Abstract 197

Introduction 198

The Proposed Modelling Methodology 202

Existing Modeling Technique 202

The Effort to Enhance the Existing Modeling Technique 206

Stud Flexural Hysteretic Response 206

Out-of-Plane Behavior of Connections 207

Modeling the Corner Connections 210

Validation of the Proposed Modelling Methodology 211

Available Data from Full-scale Experiments at UB 212

Force-Displacement Response 214

Damage to the Partition Walls 216

Available Data from Full-Scale Experiments at UNR 217

Dynamic Characteristics of the Partition Walls in the Out-of-Plane Direction 220

The Out-of-Plane Response of the Partition Walls 222

Damage to the Partition Walls 224

Summary and Conclusions 225

Acknowledgments 227

References 227

Chapter 9 : Summary, Conclusion, and Future Research 233

9.1. Summary and Conclusions 233

9.2. Future Research 239

List of Tables

Chapter 2

Table 1. Ceiling description of UNR experiments 31

Table 2. Peak accelerations and story drift ratios 32

Table 3. Partition damage definition 33

Table 4. Drift (%) corresponding to each damage definition for full-height partition walls 34

Table 5. PFA corresponding to each damage definition for transverse walls 34

Table 6. Ceiling damage definition 36

Table 7. PFA (g) corresponding to each damage definition 37

Chapter 3

Table 1. Test Program Matrix 46

Table 2. Engineering Demand Parameters 57

Table 3. Fragility Curve Parameters 57

Table 4. Fixed "Pinching4" Parameters 60

Table 5. Sample Calibrated "Pinching4" Parameters 60

Table 6. "Pinching4" Parameters for Generic GSC Models 62

Table 7. Equations for the Backbone Parameters for Various GSCs 64

Table 8. Backbone Parameters for a GSC with 5/8 in. Edge Distance 65

Chapter 4

Table 1. Test Program Matrix 75

Table 2. Engineering Demand Parameters 88

Table 3. Fragility Curve Parameters 88

Table 4. Fixed "Pinching4" Parameters of STCs 91

Table 5. Sample Calibrated Pinching4 Parameters for Various STCs 92

Table 6. Generic Pinching4 Calculated Parameters for Various STCs 94

Table 7. EPPG Parameters for Various STCs 96

Chapter 5

Table 1. Test Program Matrix 113

Table 2. Shear and Tension Connection Capacity 119

Table 3. Engineering Demand Parameters 128

Table 4. Fragility Curve Parameters 128

Table 5. Fixed "Pinching4" Parameters for Tension Behavior 131

Table 6. Sample Calibrated "Pinching4" Backbone Parameters for Tension Behavior 131

Table 7. Fixed "Pinching4" Parameters for Shear Behavior 132

Table 8. Sample Calibrated "Pinching4" Backbone Parameters for Shear Behavior 133

Table 9. "Pinching4" Backbone Parameters for Generic Models 134

Table 10. "Pinching4" Backbone Parameters for Generic Models for Untested Track Thicknesses 136

Chapter 6

Table 1. Force values for backbone points in various connections 151

Table 2. Displacement values for backbone points in various connections 152

Table 3. Pinching parameters in various connections 152

Table 4. EPPG material parameters 153

Table 5. “ZeroLengthContact3D” element Parameters 154

Table 6. Steel material properties 156

Table 7. Representative contact element parameters 156

Chapter 7

Table 1. Test program matrix 171

Table 2. Connection capacity 176

Table 3. Engineering demand parameters 182

Table 4. Fragility curve parameters 182

Table 5. Fixed "Pinching4" parameters 186

Table 6. Sample calibrated "Pinching4" backbone parameters 187

Table 7. "Pinching4" backbone parameters for generic models 188

Table 8. "Pinching4" backbone parameters for the generic model for untested connections 191

Chapter 8

Table 1. Sample Force and Displacement Values for Backbone Points in Various Connections 205

Table 2. Pinching Parameters in Various Connections 205

Table 3. EPPG Material Parameters* 206

Table 4. “ZeroLengthContact3D” Element Parameters* 206

Table 5. New Calibrated Backbone Curve Parameters for “Pinching4” Materials ... 209

Table 6. Pinching Parameters for New Calibrated “Pinching4” Materials 210

Table 7. Steel Material Properties 214

Table 8. Representative Contact Element Parameters 214

List of Figures

Chapter 1

Figure 1-1- Typical layout and elements of a light-gauge steel-frame gypsum partition walls 4

Figure 1-2- Examples of observed damage in partition walls during past earthquakes (Filiatrault et al. 2001, Dhakal 2010, Eureka Earthquake Clearinghouse 2010, EERI 2010, FEMA-E74 2011, Miranda et al. 2012, Mizutani et al. 2012) 5

Figure 1-3- Lee et al. (2007) experiments, examples of the (a) test setup (unit: mm) and (b) observed damage mechanisms 7

Figure 1-4- Restrepo and Bersofsky (2010) experiments, an examples of the (a) test specimen and (b) the observed damage 8

Figure 1-5- Restrepo and Lang (2011) experiments, (a) the plan view of test specimen and (b) the observed damage mechanisms 9

Figure 1-6- Retamales et al. (2011) experiments, (a) the plan and (b) the isometric view of the specimen 10

Figure 1-7- The UB (Retamales et al. 2013) experiments: (a) the specimen (b) examples of observed damage mechanisms 11

Figure 1-8- The E-Defense (Soroushian et al. 2015b) experiments: (a) the overall partition plan view, and (b) examples of observed damage mechanisms 12

Figure 1-9- The UCSD (Wang et al. 2015) experiments: (a) the partition wall detail, and (b) examples of observed damage mechanisms 13

Figure 1-10- The study by Restrepo and Lang (2011): (a) a sample experimental result, (b) the proposed backbone response 14

Figure 1-11- The study by Davies et al. (2011): (a) the representative analytical model of partition walls, (b) the Wayne Stewart model with degradation (from Carr 2005)..... 15

Figure 1-12- The study by Wood and Hutchinson (2014): (a) the representative analytical model of partition walls, (b) the "Pinching4" material (OpenSees 2015) 16

Figure 1-13- The study by Wood and Hutchinson (2014), comparison of the analytical and experimental result for a sample specimen..... 17

Chapter 2

Figure 1. 2-story steel braced frame test bed (a) Test Setup (b) Elevation view 29

Figure 2. View of partition wall layout of second floor..... 31

Figure 3. Overall plan view of long piping system 32

Figure 4. Full connection walls: (a) partition walls before applying drift, (b) partition walls after applying large drift, (c) popping out of gypsum screws, and (d) forming plastic hinges in field studs..... 35

Figure 5. Slip track partition walls: (a) partition walls after applying large drift, (b) popping out of stud from track, (c) damage GB, (d) damage BS, (e) damage VJ, and (f) damage FT..... 36

Figure 6. Damage in (a) piping hanger clips and (b) ceiling panels 37

Chapter 3

Figure 1. Typical Steel-Framed Gypsum Partition Wall 41

Figure 2. Examples of GSC Failures in Previous Experimental Studies (Bersofsky 2004, Davies et al. 2011, Rahmanishamsi et al. 2014) 42

Figure 3. Schematic Diagram of a Numerical Model of a Steel-Framed Gypsum Partition Wall 44

Figure 4. Specimen and Test Machine 45

Figure 5. Loading Protocol for: (a) Monotonic, (b) Cyclic Tests 47

Figure 6. (a) Applied Force, (b) Free Body Diagram, and (c) Force Distribution 48

Figure 7. Damage Mechanisms of GSCs, Per Fiorino et al. (2006) and Vieira and Schafer (2012): (a) Initial Condition, (b) Screw Tilting, *T*, (c) Screw Pulling Through the Gypsum Board, *P*, (d) Gypsum Board Detaching, *D*, (e) Breaking of Gypsum Board Edge, *E* 49

Figure 8. Typical Experimental responses for: (a) Monotonic, (b) Cyclic Test 49

Figure 9. Effect of Loading Rate (v, in./min.) on: (a) Monotonic Force-Displacement Response, (b) Maximum Force Ratio 50

Figure 10. Monotonic Test Response and Cyclic Test Backbone Curves of an individual GSC for Specimen Series (a) T19E15N6, (b) T19E15N4 51

Figure 11. Effect of (a) Number of Screws, (b) Stud Thickness 52

Figure 12. Edge Distance Effect: Examples of Force-Displacement Hysteresis of GSCs in series (a) T19E05N6, (b) T19E07N6, (c) T19E10N6; and (d) Comparison of Median Backbone Curves of Specimens with Different Edge Distances 53

Figure 13. Examples of Damage State Definitions (a) Specimens with Sufficient Edge Distance (b) Specimens with Insufficient Edge Distance 55

Figure 14. GSC Fragility Curves for (a) *DS1*, (b) *DS2*, and (c) *DS3*..... 57

Figure 15. Pinching4 Material Properties (OpenSees 2014)..... 58

Figure 16. Numerical-Experimental Comparison of Third Specimen from series T19E15N6 59

Figure 17. Sample Numerical-Experimental Hysteresis Comparisons of Two Different GSCs..... 60

Figure 18. Generic Backbone Curve of Specimens with Edge Distances Equal to (a) 1.50 in., (b) 1.00 in., (c) 0.75 in., and (d) 0.50 in. 62

Figure 19. Sample Generic Numerical-Experimental Hysteresis Comparison of Different GSC Groups..... 63

Figure 20. (a) Sample Normalized Force and Displacement Data and Fitted Lines, (b) Proposed Hysteresis Model for a Connection with 5/8 in. Edge Distance . 64

Chapter 4

Figure 1. (a) and (b) Specimen and Test Machine, (c) Screw-Edge Distance and Stud-Track Gap 74

Figure 2. Loading Protocol for: (a) Monotonic, (b) Cyclic Tests 76

Figure 3. (a) Stud-Track Interaction, (b) Modified Loading Protocol for Cyclic Tests77

Figure 4. (a) Applied Force and b) Free Body Diagram 78

Figure 5. Damage Mechanisms of STCs in Tension: (a) Initial Condition, (b) Tilting, (c) Enlarging the Hole, (d) Popping out, (e) Tearing-out of the Track Flange, and (f) Tearing-out of the Stud Flange 79

Figure 6. Damage Observations of STCs in Tension: (a) Initial Condition, (b) Enlarging the Hole, (c) Popping out, (d) Tearing-out of the Track Flange, and (e) Tearing-out of the Stud Flange 79

Figure 7. Damage Mechanisms of STCs in Compression: (a) Tilting, (b) Track Flange Buckling; (c) and (d) Close Views of Local Buckling of the Track Flange in Compression 80

Figure 8. Typical Experimental responses for: (a) Upward and (b) Downward Monotonic Test 80

Figure 9. Typical Experimental responses for Cyclic Tests with: (a) Primary and (b) Modified Loading Protocol 80

Figure 10. Effect of Loading Rate (v, mm/sec) on: (a) Monotonic Force-Displacement Response, (b) Maximum Force Ratio 81

Figure 11. Monotonic Test Response and Cyclic Test Backbone Curves of an individual STC for Specimen Series (a) T48G13E10, (b) T48G06E13 83

Figure 12. Effect of Screw-Edge Distance 83

Figure 13. Effect of (a) Screw-Edge Distance, (b) Stud Thickness 84

Figure 14. Examples of Damage State Definitions; (a) Specimens Tested with Primary Loading Protocol (b) Specimens Tested with Modified Loading Protocol 87

Figure 15. Fragility Curves for (a) Specimens with 0.48-mm-thick Studs/Tracks (Group #1 and #2), (b) Specimens with 0.76-mm-thick Studs/Tracks (Group #3)..... 88

Figure 16. Pinching4 Material Properties (OpenSees, 2014)..... 89

Figure 17. Analytical-Experimental Comparison of the Second Specimen from Series T48G06E06 90

Figure 18. Sample Analytical-Experimental Hysteresis Comparisons of Two Different STCs 92

Figure 19. Generic Backbone Curves of the (a) First and (b) Third Group. 94

Figure 20. Sample Generic Analytical-Experimental Hysteresis Comparison of Different GSC Groups..... 94

Figure 21. Effect of Stud-Track Interaction on the Response of STCs with (a) 0.48-mm- and (b) 0.76-mm-Thick Stud/Track 95

Figure 22. (a) EGGP Material Properties [OpenSees, 2014], (b) Calculating k_g for Specimens with 0.76-mm-Thick Stud/Track 96

Figure 23. (a) Parallel Material [OpenSees, 2014], (b) Schematic Backbone curve of Generic Model of STCs Including Gap Closure Effect 97

Figure 24. Sample Analytical-Experimental Hysteresis Comparisons of Two STCs with (a) 0.48-mm Stud/Track and 13-mm Gap, (b) 0.76-mm Stud/Track and 13-mm Gap..... 98

Chapter 5

Fig. 1. Examples of PAF Connection Failures in Previous Experimental Studies (Restrepo and Bersofsky 2010, Rahmanishamsi et al. 2014, Davies et al. 2011)..... 107

Fig. 2. Schematic Diagram of a Numerical Model of a Steel-Framed Gypsum Partition Wall, After Rahmanishamsi et al. (2015)..... 109

Fig. 3. Tension Test Setup (a) Specimen and Test Machine, (b) Specimen and the Clamping System 111

Fig. 4. Shear Test Setup (a) Specimen and Test Machine, (b) Specimen and the Clamping System 112

Fig. 5. Loading Protocol for: (a) Monotonic and (b) Cyclic Shear Tests 114

Fig. 6. Loading Protocol for Cyclic Tension Tests 114

Fig. 7. Free Body Diagram for (a) Tension and (b) Shear Tests..... 115

Fig. 8. Damage Mechanisms in Tension: (a) Initial Condition, (b) Deformation of the Track Web, (c) and (d) Tearing of the Track Web..... 116

Fig. 9. Damage Mechanisms of Track-to-Concrete PAF Connections Subjected to Shear: (a) Initial Condition, (b) Bending of the Fastener and Tearing of the Track Web, (c) Pulling Through of the Fastener, (d) Shear Failure of the Fastener, (e) Pulling Out of the Fastener..... 117

Fig. 10. Typical Experimental Responses for Tension (a) Monotonic Tests and (b) Cyclic Tests 118

Fig. 11. Typical Experimental Responses for Shear (a) Monotonic Tests and (b) Cyclic Tests 118

Fig. 12. Effect of Loading Rate (v, mm/sec) on: (a) Monotonic Force-Displacement Response, (b) Maximum Force Ratio 120

Fig. 13. Monotonic Response and Cyclic Backbone Curves of Tension Tests on Specimens with: (a) 0.48-mm-thick and (b) 0.76-mm-thick tracks 121

Fig. 14. Effect of Track Thickness on the Response of Cyclic Tension Test 121

Fig. 15. Monotonic Response and Cyclic Backbone Curves of Shear Tests on Specimens with: (a) 0.48-mm-thick and (b) 0.76-mm-thick tracks 122

Fig. 16. Effect of Track Thickness on the Response of Cyclic Shear Test 122

Fig. 17. Examples of Damage State Definitions for: (a) Tension Tests (b) Shear Tests 126

Fig. 18. Fragility Curves of PAF Connections with (a) 0.48-mm-, and (b) 0.76-mm-thick Tracks, Subjected to Tension Force 127

Fig. 19. Fragility Curves of PAF Connections with (a) 0.48-mm-, and (b) 0.76-mm-thick Tracks, Subjected to Shear Force 127

Fig. 20. Pinching 4 Material Properties (OpenSees 2015) 129

Fig. 21. Calibrated Numerical Model for a Sample Specimen (0.48-mm-thick Track, Specimen #3) 130

Fig. 22. Sample Numerical-Experimental Comparisons of Specimens Subjected to (a) Tension and (b) Shear Force 132

Fig. 23. Generic Backbone Curves Group #2 of Specimens, Subjected to (a) Tension and (b) Shear Force 134

Fig. 24. Sample Generic Numerical-Experimental Hysteresis Comparison of Specimens Subjected to (a) Tension and (b) Shear Force 135

Fig. 25. Normalized Generic Backbone Curves for Untested Track Thicknesses, Subjected to (a) Tension and (b) Shear Force 136

Chapter 6

Figure 1. Typical steel-framed gypsum partition walls 147

Figure 2. Schematic diagram of an analytical model of a steel-framed gypsum partition wall, after Rahmanishamsi et al. [28]..... 147

Figure 3. Pinching 4 material parameters [27]..... 148

Figure 4. Analytical-experimental comparison of sample generic models from each partition wall connection..... 150

Figure 5. (a) EPPG material properties [27]; (b) Representative element for gypsum-to-concrete contact 153

Figure 6. Details of specimens 5, 6, and 10, after Retamales et al. [8] (a) plan view; (b) top and bottom connection details..... 154

Figure 7. UB loading protocol [10]..... 155

Figure 8. Experimental hysteresis responses and the comparison of backbone curves of the specimens 5, 6, and 10..... 156

Figure 9. Comparison of the response of the generic analytical model and experimental results..... 157

Figure 10. Comparison of analytical and experimental response of specimen 5..... 158

Figure 11. Analytical deformed shape, comparison of analytical and experimental damage mechanisms, and sample component responses in specimen 5 ... 159

Figure 12. Comparison of analytical and experimental response of specimen 6..... 160

Figure 13. Comparison of analytical and experimental response of specimen 10..... 160

Chapter 7

Fig. 1. (a) and (b) Specimen and Test Machine 170

Fig. 2. Loading protocol for cyclic tests 171

Fig. 3. Free-body diagram for a sample specimen 172

Fig. 4. Damage mechanisms of stud-to-track connections in the out-of-plane direction: (a) initial condition, (b) track-flange deformation, (c) stud popping-out from track, (d) stud-web crippling, (e) screw pull-out..... 173

Fig. 5. Typical experimental responses for (a) monotonic and (b) cyclic tests 175

Fig. 6. Effect of loading rate (v, mm/sec) on: (a) monotonic force-displacement response, (b) maximum force ratio..... 177

Fig. 7. Monotonic response and cyclic backbone curves for specimen series: (a) T48G03DT and (b) T75G13AS 178

Fig. 8. Effect of (a) stud-to-track gap, (b) stud/track thickness and screw-attached configuration on the cyclic response..... 179

Fig. 9. Examples of damage state definitions for: (a) deflection-track configuration (b) screw-attached configuration 181

Fig. 10. Displacement-based fragility curves for (a) first damage state, (b) second damage state, (c) third damage state, and (d) force-based fragility curves for second damage state..... 183

Fig. 11. Pinching 4 material properties (OpenSees 2015) 185

Fig. 12. Calibrated numerical model for a sample specimen (T48G03DT, specimen #2)..... 186

Fig. 13. Sample numerical-experimental hysteresis comparisons of specimen series (a) T48G13AS (b) T75G13DT 187

Fig. 14. (a) Generic backbone curves of specimen series T75G13AS, (b) Sample numerical-experimental hysteresis comparison 189

Fig. 15. (a) Secant stiffness calculation on a sample specimens, (b) force normalized backbone curve of a sample specimen 191

Fig. 16. Fitted lines to secant stiffness values (a) K_{sec1} , (b) K_{sec2}, and (c) K_{sec3} 191

Fig. 17. (a) Normalized generic backbone curve for track-deflection configuration, (b) Schematic modified backbone curve for screw-attached configuration ... 192

Chapter 8

Fig. 1. Typical Steel-Framed Gypsum Partition Wall..... 202

Fig. 2. (a) Pinching 4 Material Properties, (b) EPPG Material Properties (OpenSees 2015)..... 203

Fig. 3. Schematic Diagram of the Analytical Model of a CFS Gypsum Partition Wall with Return..... 207

Fig. 4. Sample Calibrated “Pinching4” Material for (a) the Flexural Behavior of Studs and (b) the Out-of-Plane Behavior of Stud-to-Track Connections 210

Fig. 5. Construction Details (top) and Schematic Diagram of the Analytical Model (bottom) of a (a) Commercial and (b) Institutional Corner Detail..... 211

Fig. 7. Plane View and Corner Details of Configurations 1, 2, and 4, after Retamales et al. (2013) 213

Fig. 8. Comparison of the Analytical Model and Experimental Results for Configuration 2 215

Fig. 9. Comparison of the Analytical Model and Experimental Results for Configuration 1 215

Fig. 10. Comparison of the Analytical Model and Experimental Results for Configuration 4 215

Fig. 11. Examples of Experimental and Analytical Damage Mechanisms: (a) and (b) Tilting and Failure of Screws Connecting Gypsum Boards to Bottom and Top Tracks, (c) Tearing of the Top Track at the PAF location, (d) Plastic Hinges Forming in Studs 217

Fig. 12. UNR Partitions (a) Plan, (b) Elevation of Partitions P3-S and (c) P4-S (Rahmanishamsi et al. 2014) 219

Fig. 13. Experimental Partition/First Floor Transfer Functions in the First White Noise of: (a) Test L1 and (b) Test NL2 222

Fig. 14. Experimental and Analytical Partition Acceleration Response Spectrums for Sample Runs of Test L1 [(a), (b), and (c)] and Test NL2 [(d), (e), and (f)] 223

Fig. 15. Experimental and Analytical Partition Acceleration Response History in Test NL2-Run 1 assuming (a) %16 damping ratio or (b) %5 damping ratio in the model 224

Fig. 16. Experimental and Analytical Partition Acceleration Response Spectrums for Sample Runs of Test L1 assuming %5 damping ratio in the model, (a) First White Noise, (b) Run-1, and (c) Run-4 224

Chapter 1: Introduction

1.1. Motivation

The structural systems of newly designed buildings commonly survive moderate-to-severe earthquakes with low-to-moderate damage (Tasligedik et al. 2014). Nonetheless, recent earthquakes have shown that the nonstructural systems are prone to widespread damage even in low-intensity seismic events (Dhakal 2010, Mizutani 2012, EERI 2012, Miranda et al. 2012, Baird 2014). Damage to nonstructural systems can lower the performance level of the entire building system, even if the structural system of a building achieves a continuous or immediate occupancy performance level (Retamales et al. 2013). Moreover, nonstructural systems almost always represent the major portion (approximately 48% to 70%) of the total construction cost in buildings (Taghavi and Miranda 2003). Consequently, it is not surprising that damage to nonstructural systems has resulted in significant economic loss during recent earthquakes, typically exceeding the economic loss associated with structural damage (Dhakal 2010; Mizutani 2012, EERI 2012, Miranda et al. 2012, Baird 201). Indeed, nonstructural systems account for over 78% of the total estimated national annualized earthquake loss (FEMA E-74 2011).

Among various nonstructural systems, cold-formed steel-framed (CSF) gypsum partition walls represent a substantial contribution to the total investment in a building. In the United States, approximately 60% of steel framing is used in nonstructural partition walls (Restrepo and Bersofsky 2010, Restrepo and Lang 2011). These walls configure the architectural layout of a building, thereby facilitating its functionality for occupants

(Wood and Hutchinson 2014). Partition walls are not designed nor anticipated to contribute to the primary load-carrying system of the building. Nonetheless, they are subjected to differential excitations imposed by the primary structure undergoing seismic loading (e.g. interstory drift), leading to damage to these walls (Wang et al. 2015). This damage has frequently been triggered at story drift levels well below the yield point of structures (Dhakal 2010, Miranda et al. 2012, Tasligedik et al. 2014). Damaged partition walls can leave buildings inoperable, causing huge economic losses and extensive downtime (Jenkins et al. 2015). Note that the downtime is of essential importance to the performance of critical facilities (e.g. hospitals and fire stations), the main function of which is to save lives and reduce the impact of disasters during and immediately after earthquake events (Achour et al. 2011).

Although recent years have witnessed significant progress in the experimental and analytical simulation of nonstructural partition walls, a robust solution to prevent extensive damage to these walls has not been found. This is due in part to the lack of validated comprehensive analytical tools to better understand and simulate partition walls. The current study supports this field of research through proposing, for the first time, a reliable generic method to model the in-plane and out-of-plane seismic performance of partition walls with various geometries, boundary conditions, and construction details.

1.2. Nonstructural Partition Walls

Typical construction of partition walls consists of C-shaped, light-gauge steel studs nested to C-shaped steel tracks at the top and bottom (Figure 1-1). In most cases, the studs are screwed to bottom tracks (fixed stud-to-track connection) while the stud to top-track connections can vary depending on the desired performance. Some examples of stud to top-track connections are the full (fixed) connection detail, the slip track detail, and the newly proposed sliding/frictional connection detail (Rahmanishamsi et al. 2014a). The tracks are usually fastened to the structural slab with powder-actuated fasteners (PAFs) and are used to align the studs (Restrepo and Lang 2011). The most commonly used stud and track profiles are gauge 20 (0.03 in. thick) and gauge 25 (0.018 in. thick) with a web depth of 3.5 inches or 3.62 inches. Gypsum boards, consisting of a rigid gypsum core sandwiched between paper layers, are laid perpendicular to and screwed to the studs with bugle-headed drywall screws (usually #6) placed at regular intervals. The Gypsum boards may also be attached to the tracks. The two most commonly used gypsum thicknesses are 0.5 inch and 0.625 inch (Soroushian et al. 2015a). Various details might be employed for the corner connections, such as commercial and institutional detailing that differ in terms of stud configurations and stud thicknesses used for the corners (Retamales et al. 2013). It should be noted that many other configurations might be used for partition walls depending on the geometry limitations, seismic requirements, desired fire rating and sound isolation preferences. The schematic of a typical light-gauge steel-frame gypsum partition walls is presented in Figure 1-1.

Figure 1-1- Typical layout and elements of a light-gauge steel-frame gypsum partition walls

1.2.1. Damage in Past Earthquakes

Various types of damage to partition walls were identified in past earthquakes including bending of studs, failure of gypsum board-to-stud/track connections, cracking of gypsum boards around openings, damage to stud-to-track connections, failure of track-to-concrete connections, crushing of wall corners, failure of brace connections, damage to corner connections, and complete collapse (Filiatrault et al. 2001, Dhakal 2010, Eureka Earthquake Clearinghouse 2010, EERI 2010, FEMA-E74 2011, Mizutani 2012, EERI

2012, Miranda et al. 2012, Baird 2014). Some examples of partition wall damage mechanisms are provided in Figure 1-2. Partition wall damage was reported even after the moderate earthquake of Eureka (2010) while there was no evidence of damage to the primary structure. The partition damage usually only affects the building performance

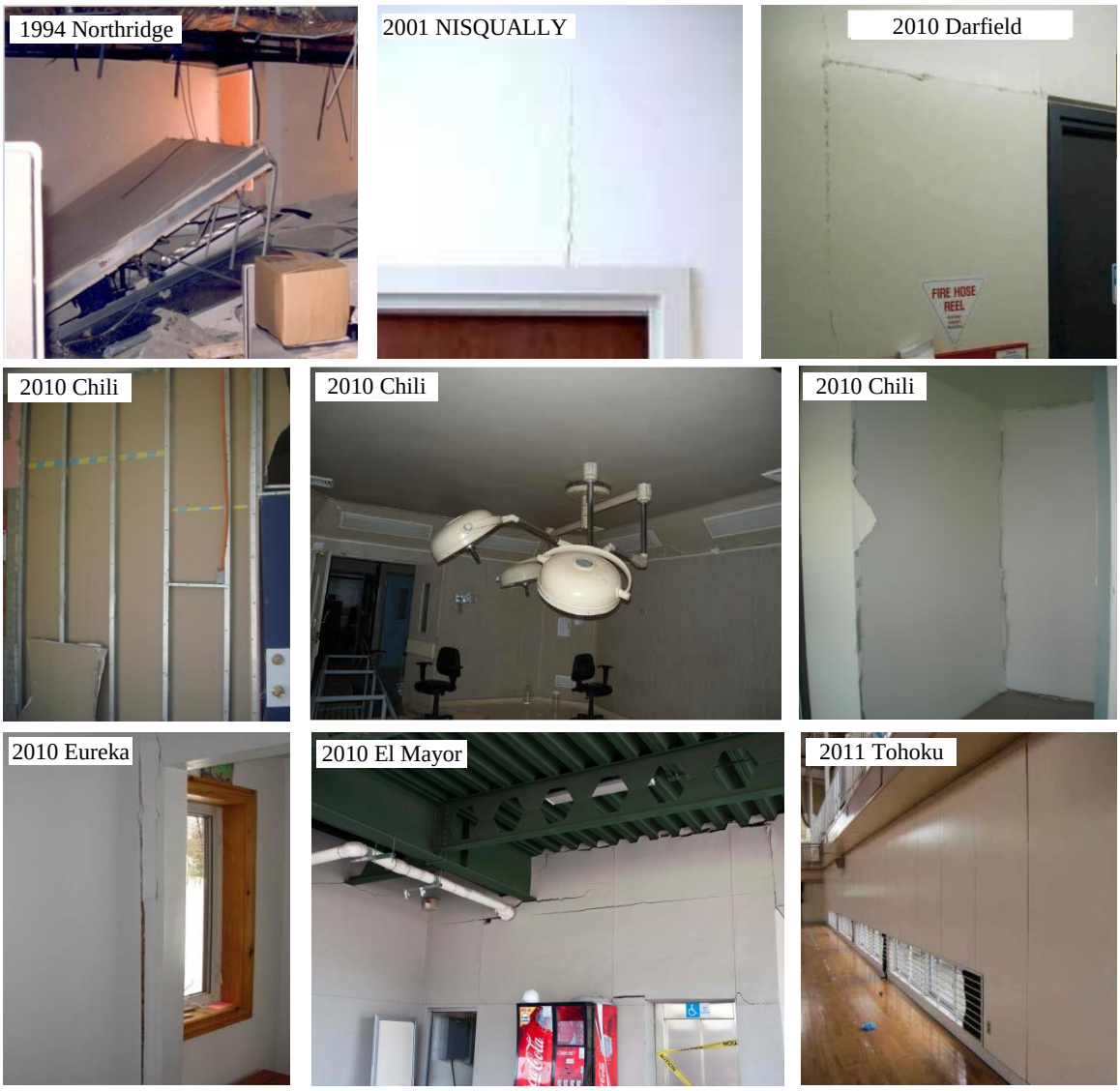

Figure 1-2- Examples of observed damage in partition walls during past earthquakes (Filiatrault et al. 2001, Dhakal 2010, Eureka Earthquake Clearinghouse 2010, EERI 2010, FEMA-E74 2011, Miranda et al. 2012, Mizutani et al. 2012)

after a seismic event. However, the complete or partial collapse of partition walls may also cause serious injuries or death to occupants, as observed following the Northridge earthquake. Moreover, the partition wall damage can be a life-threatening hazard when it compromises the cleanliness standard of a surgical room in a hospital, as was the case after the Chilean earthquake (Wood and Hutchinson 2014).

1.2.2. Previous Experimental Studies

The seismic performance of steel-framed gypsum partition walls has been evaluated in a number of previous experimental studies (Lee et al. 2007, Restrepo and Bersofsky 2010, Restrepo and Lang 2011, Retamales et al. 2011, Retamales et al. 2013, Rahmanishamsi et al. 2014b, Soroushian et al. 2015b, Wang et al. 2015). The current section provides a summary of these studies.

1.2.2.1. Lee et al. 2007

Lee et al. (2007) tested four full-scale partition walls constructed according to the common Japanese building practice to characterize the seismic performance and determine the repair cost. Three different configurations of partition walls, namely plain partition, plain partition with a door, and partition with a return wall, were considered. The plain partitions were 13-feet long by over 9-feet tall while the partition with a return wall was approximately 9-feet tall by 9-3/4-feet long with a return wall of over 5 feet (Figure 1-3a). The experimental program included three quasi-static cyclic loading tests on the three configurations in addition to one dynamic test on the plain partition configuration.

The cyclic response of the wall specimens included pinching as well as stiffness and strength degradation. The damage was concentrated at the perimeters of the partition walls and at the corners of the door (Figure 1-3b). Dynamic loading did not amplify the damage on a partition over the damage observed from the quasi-static test. Damage–repair cost relationships show that the repair cost reaches almost the initial cost under 2% inter-story drift ratio.

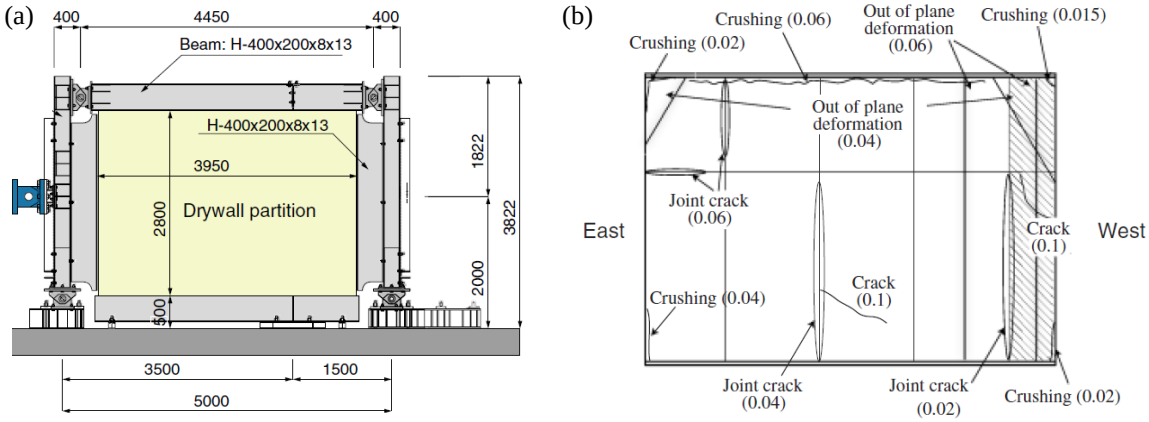

Figure 1-3- Lee et al. (2007) experiments, examples of the (a) test setup (unit: mm) and (b) observed damage mechanisms

1.2.2.2. Restrepo and Bersofsky 2010

Eight pairs of partition walls were subjected to in-plane reverse cyclic lateral displacements. The specimens were 16-feet long and 8-feet tall with a 4-feet long return wall (Figure 1-4a). The main variables were the configuration of the specimen, the spacing of gypsum-to-stud screws, the stud thickness and spacing, the presence of a vertically slotted track at the top of the partition wall, and the gypsum board thickness.

The damage mechanisms observed during the test included: screw pop out, gypsum board cracking, buckling of studs, and shear failure of the bottom track (Figure 1-4b).

These mechanisms were grouped in three damage states: Damage State I (DSI), requiring minor, if any, attention after development, Damage State II (DSII) needing repairs that could cause temporary business interruption, and Damage State III (DSIII) requiring a complete overhaul of the partitions and impacting business operation. Ranges of recorded drifts for damage states were 0.1-2.0% (DSI), 1.5-3.0% (DSII), and 1.5-3.5% (DSIII).

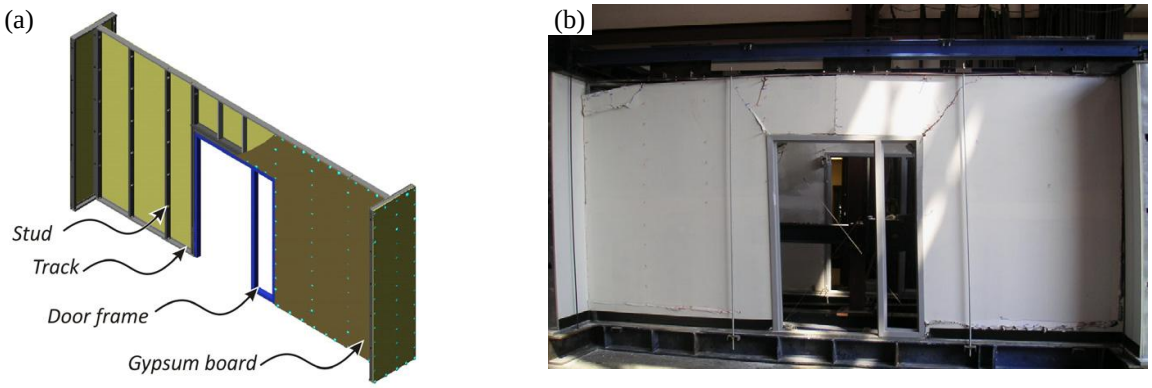

Figure 1-4- Restrepo and Bersofsky (2010) experiments, an examples of the (a) test specimen and (b) the observed damage

1.2.2.3. Restrepo and Lang 2011

Two identical full-scale three-dimensional specimens were constructed to represent a typical room in an office building (Figure 1-5a). The specimens were constructed using 0.030-inch thick (20 gauge), 3-5/8-inch wide studs, spaced 24 inches on center. The gypsum boards were 5/8-inch thick. The specimens were tested quasi-statically using two different loading protocols in order to investigate the sensitivity of loading protocols on damage progression. The first specimen used the recommended loading protocol from ATC-58 and the second specimen utilized a modified version, which reduced the low amplitude cycles while increasing the amplitude rate.

The observed damage mechanisms included failure of track-to-concrete PAF connections, failure of gypsum-to-stud/track connections, the crack and separation of gypsum boards at corners, crushing of gypsum boards, and damage to boundary studs (Figure 1-5b). Moreover, the experiments did not provide clear evidence that the loading protocol has an effect on the shear strength of partition walls.

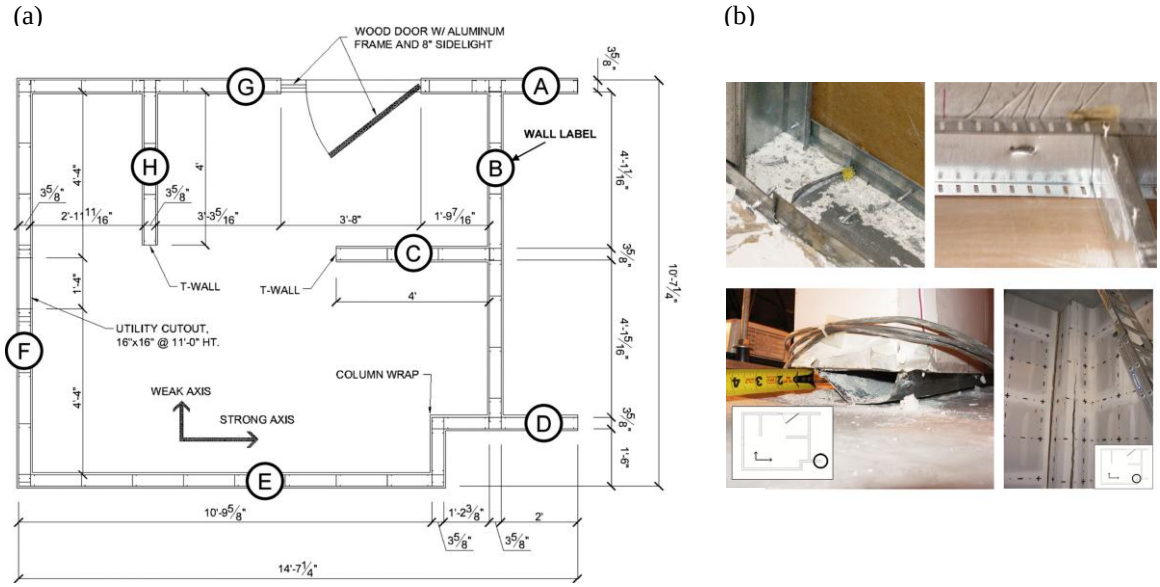

Figure 1-5- Restrepo and Lang (2011) experiments, (a) the plan view of test specimen and (b) the observed damage mechanisms

1.2.2.4. Retamales et al. 2011

Retamales et al. (2011) conducted a series of experiments on a full-scale hospital emergency room replica (Figure 1-6). The room was constructed using 18-gauge studs with typical spacing of 16 inches, 18-gauge slotted tracks, and 5/8-inch thick gypsum boards. The layout of partition walls was based on a similar specimen tested by Restrepo and Lang (2011). The specimen was subjected to a new proposed qualification protocol as well as a series of full-scale simulated building floor motions. During the test, cracks

along corner beads and paper joint tape, damage to gypsum-to-stud/track screw connections, and cracks at opening corners were observed.

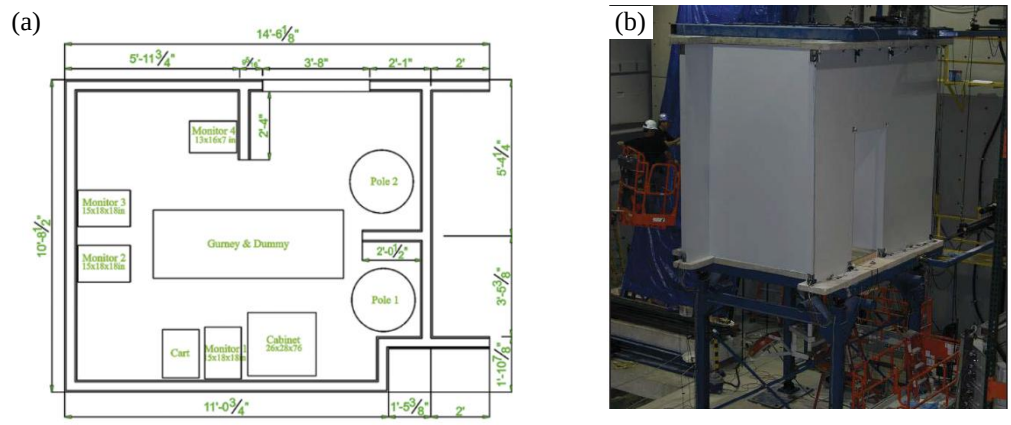

Figure 1-6- Retamales et al. (2011) experiments, (a) the plan and (b) the isometric view of the specimen

1.2.2.5. Retamales et al. 2013

As a part of the "NEESR-GC: Simulation of the Seismic Performance of Nonstructural Systems" project, 50 partition wall specimens corresponding to 22 different configurations of steel-framed gypsum partition walls were tested at the University of Buffalo (UB) (Figure 1-7a). The specimens were approximately 11.5 feet tall by 12 feet long with return walls (perpendicular to the loading direction) of either 2.0 feet or 4.0 feet. The configurations varied in terms of connectivity of the sheathing and studs to the top and bottom tracks (slip track or full connection), spacing of the track-to-concrete fasteners (12 or 24 inches on center), detailing of wall intersection (commercial or institutional), stud and track thicknesses (20 gauge or 25 gauge), and spacing of the steel studs. The specimen was subjected to the loading protocol developed by Retamales et al. (2011).

Various types of damage mechanisms were reported including: damage to gypsum-to-stud/track connections, damage to track-to-concrete PAF connections, the crack and separation of gypsum boards at corners, forming plastic hinges in field studs, crushing of gypsum boards, damage to the return wall top track, out-of-plane bending and cracking of gypsum boards, bending of boundary studs, damage to diagonal braces, and complete collapse of the wall (Figure 1-7b). Damage observations were grouped in three damage states depending on the required level of repair: DS1 referring to light damage, DS2 to moderate damage, and DS3 to complete or severe damage. The drift levels, at which each damage state was triggered for the first time, was then identified. The experimental data were categorized in five groups, and for each group fragility curves were generated.

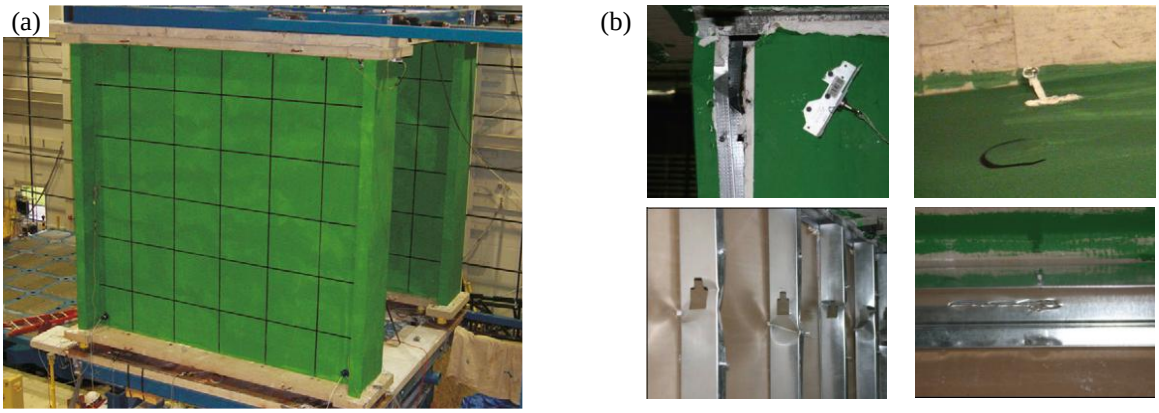

Figure 1-7- The UB (Retamales et al. 2013) experiments: (a) the specimen (b) examples of observed damage mechanisms

1.2.2.6. Soroushian et al. 2015

As part of the NEESR-GC project and in a collaborative effort with NEES TIPS and NIED, partition walls were placed on the 4th and 5th floors of a full-scale 5-story building at the E-Defense facility in Japan. The walls were 9.0 feet tall and the lengths ranged

from 5.0 feet to 32.0 feet (Figure 1-8a). The building was subjected to a total of 41 earthquake motions, including 23 targeted 3D motions. The drift-related damage to partition walls was not noticeable since the inter-story drift ratios of the 4th and 5th floors were limited to 0.78% and 0.62%, respectively. However, atypical damage mechanisms were observed that were caused by the relative vertical acceleration between the floors. The damage mechanisms included diagonal and vertical cracks appeared on the gypsum wallboards and popping out of studs from top tracks (Figure 1-8b). The researchers also evaluated the amplification factors for the out-of-plane acceleration of partition walls and compared the results with recommended values from design provisions (Soroushian et al. 2015b).

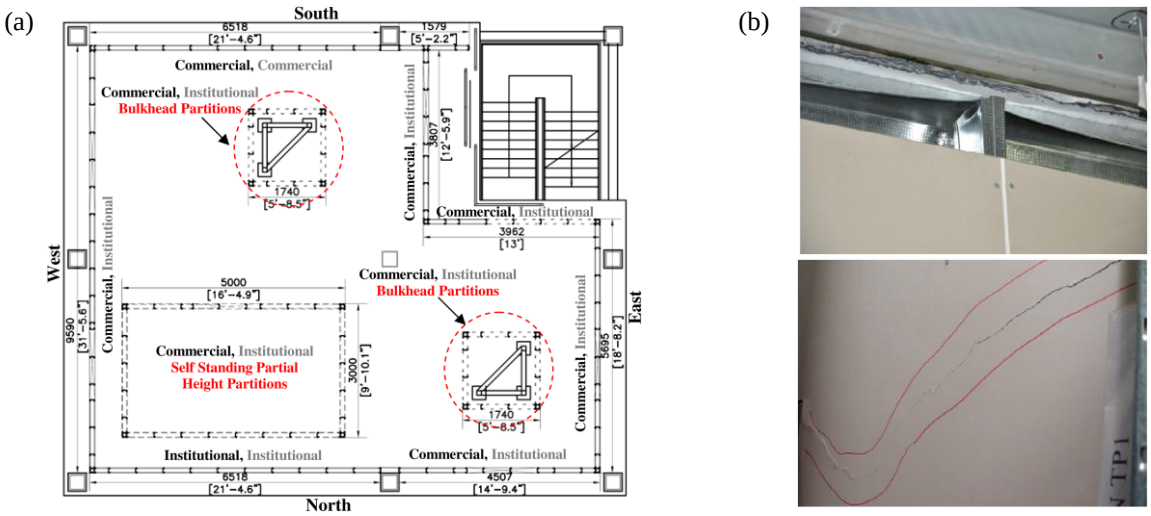

Figure 1-8- The E-Defense (Soroushian et al. 2015b) experiments: (a) the overall partition plan view, and (b) examples of observed damage mechanisms

1.2.2.7. Wang et al. 2015

The partition walls were distributed at all levels of a full-scale 5-story building mounted on the University of California, San Diego (UCSD) shake table. Partition walls

were constructed using either 2.5- or 4.0-inches depth studs (0.8 inch thick) located 24 inches apart. Slotted tracks were utilized as top tracks while conventional tracks were used as bottom tracks. All partition walls were sheathed with 5/8-inch thick gypsum boards (Figure 1-9a). A total of 13 uniaxial earthquake motions was applied to the building. The observed damage mechanisms included damage to gypsum-to-stud/track connections, crushing of gypsum boards, damage to gypsum joint tapes, separation of gypsum boards at corners, detachment of gypsum boards, and bending of studs (Figure 1-9b).

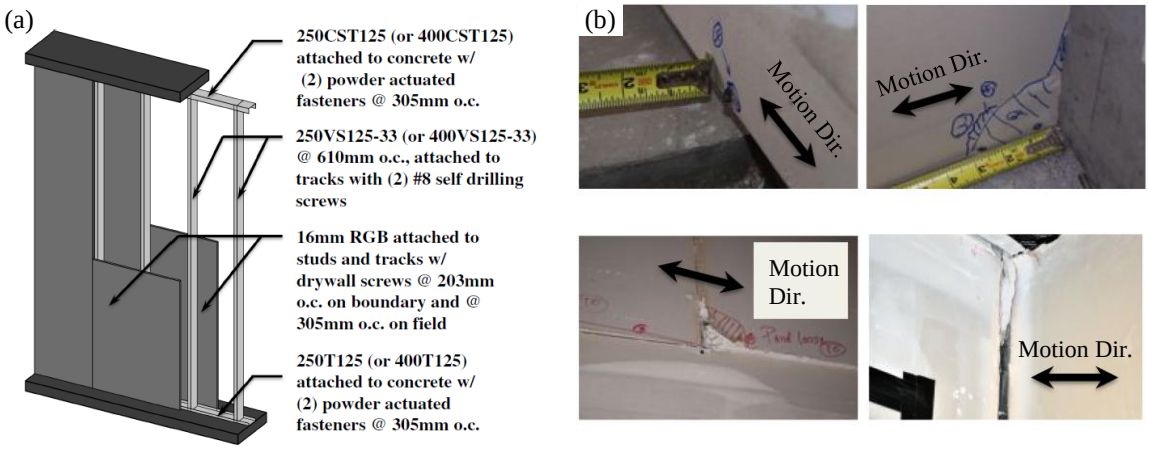

Figure 1-9- The UCSD (Wang et al. 2015) experiments: (a) the partition wall detail, and (b) examples of observed damage mechanisms

1.2.3. Previous Analytical Studies

Although limited, the analytical modeling of nonstructural steel-framed gypsum partition walls were studied in previous research (Restrepo and Lang 2011, Davies et al. 2011, Wood and Hutchinson 2014). The current section provides a summary of these studies.

1.2.3.1. Restrepo and Lang 2011

Adopting the data from a previous experiment performed by Restrepo and Bersofsky (2010) (Figure 1-10a) in addition to data from two new experiments, Restrepo and Lang (2011) postulated a four-line piecewise backbone response envelope for gypsum partition walls (Figure 1-10b). The proposed backbone response envelope was presented in terms of shear force per unit length of wall versus drift ratio. It includes a linear elastic response, followed by a small region where the peak load is maintained, and then by softening up to a residual strength. The researchers mentioned that due to the empirical nature of the proposed envelope, it was only applicable for partitions built with the specific gypsum board thickness and type, self-tapping screws, and screw spacing.

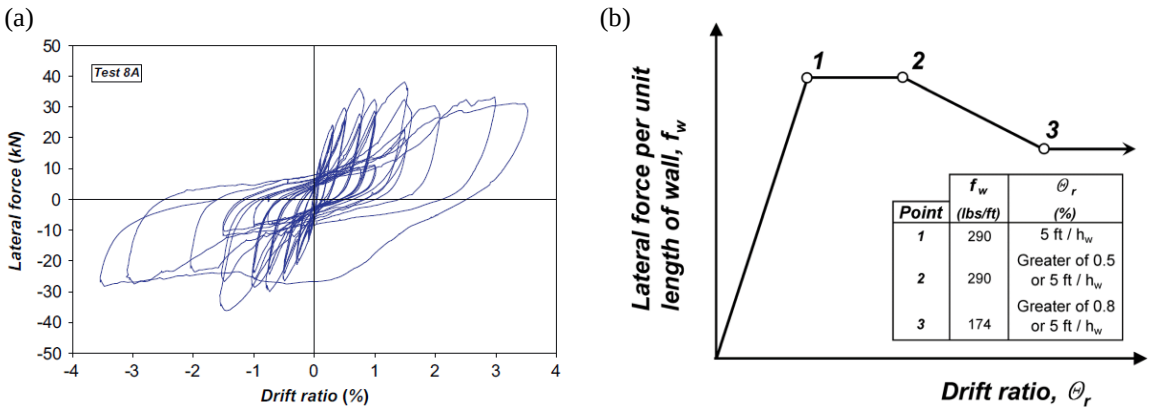

Figure 1-10- The study by Restrepo and Lang (2011): (a) a sample experimental result, (b) the proposed backbone response

1.2.3.2. Davies et al. 2011

Davies et al. modeled the mechanical behavior of partition walls using the RUAUMOKO software (Carr 2005). Three different elements were utilized: two frame type members and one nonlinear shear spring (Figure 1-11a). Frame elements represented

structural columns and beams. The columns performed linearly elastic while the beam was set to be rigid by using the rigid links on each end of the beam extending to the center of the member. The Wayne Stewart Hysteretic model was assigned to the shear spring to simulate the in-plane behavior of the partition walls (Figure 1-11b). Nine parameters were calibrated with experimental results of 35 specimens tested at the University at Buffalo (Retamales et al. 2013): initial stiffness, post yield stiffness factor, post capping stiffness factor considering strength degradation, unloading stiffness factor, yield strength, capping strength, intercept strength, reloading or pinch power factor, and the beta or softening factor. The calibration of parameters was performed for six wall categories: commercial slip track, commercial full connection, institutional slip track, institutional full connection, partial height, and improved detail construction. The calibrated models were then adopted to perform dynamic analyses on an example hospital building with and without partition walls.

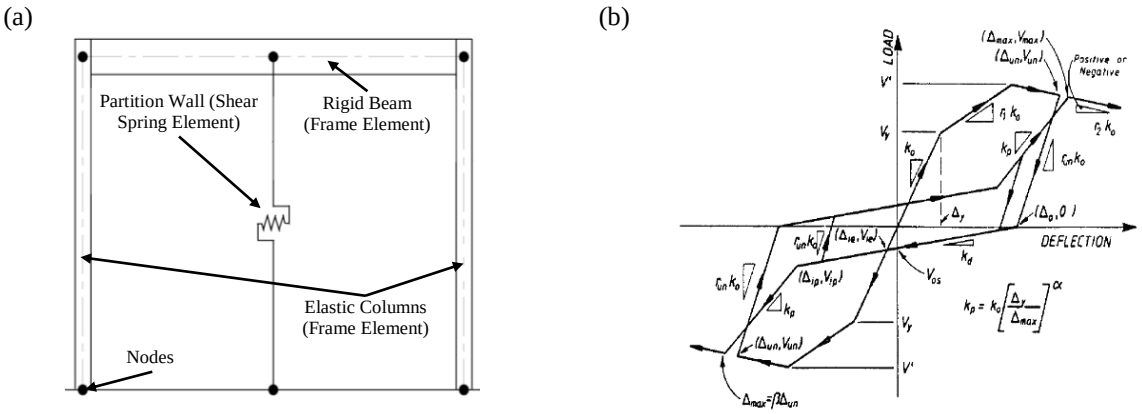

Figure 1-11- The study by Davies et al. (2011): (a) the representative analytical model of partition walls, (b) the Wayne Stewart model with degradation (from Carr 2005)

1.2.3.3. Wood and Hutchinson 2014

In the study by Wood and Hutchinson (2014), a partition wall was modeled by a single nonlinear uniaxial spring placed at mid-height of a floor (Figure 1-12a) with slaved degrees-of-freedom or rigid links extending from floor to floor. The uniaxial spring was implemented only in the in-plane direction whereas the out-of-plane behavior of the partition wall was not characterized. The "Pinching4" material model (Figure 1-12b) along with a zero-length element in OpenSees (2015) was used to represent the uniaxial spring.

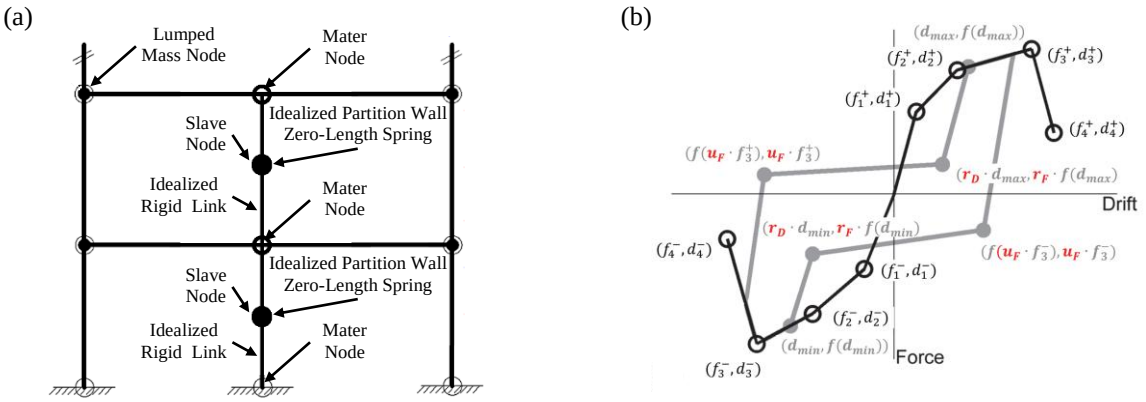

Figure 1-12- The study by Wood and Hutchinson (2014): (a) the representative analytical model of partition walls, (b) the "Pinching4" material (OpenSees 2015)

The "Pinching4" material characteristics, including backbone points, unloading and reloading behavior, and total half-cycle hysteretic energy, were optimized to calibrate the partition models for each subgroup (e.g. commercial slip track, institutional full connection) of specimens tested at University at Buffalo (Retamales et al. 2013) (Figure 1-13). A normalized partition model was also developed in this study, whose definition required wall length and building occupancy (commercial or institutional).

This modelling methodology was then used in conjunction with nine buildings with floor numbers varying from 2 to 20. Several sensitivity analyses were performed, such as studying the structural period or mass participation change due to the installation of partition walls.

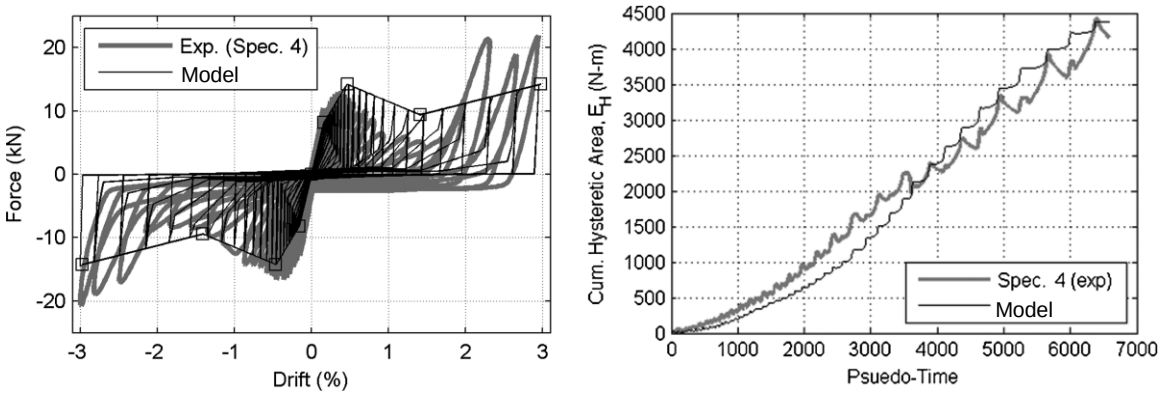

Figure 1-13- The study by Wood and Hutchinson (2014), comparison of the analytical and experimental result for a sample specimen

1.2.4. Discussion

As summarized in the previous section, several damage mechanisms were identified for the CFS gypsum partition walls during past earthquakes and experimental studies including bending of studs, failure of gypsum board-to-stud/track connections, cracking of gypsum boards around openings, damage in stud-to-track connections, failure of track-to-concrete connections, crushing of wall corners, failure of brace connections, and complete collapse. Among them, damage at the connections between various elements of the walls (e.g. gypsum board-to-stud/track connections) was predominant. The experimental studies also revealed that the force and displacement characteristics and behavior of partition walls (i.e. stiffness, strength, degradation, and pinching) depended

on the performance of the wall connections as well as the out-of-plane properties of return walls. Therefore, in order to accurately capture the lateral behavior and damage mechanisms of partition walls through analytical modeling, it is essential to include the behavior of all individual components.

The available analytical models (summarized in section 1.2.3) are limited to lumped level modeling, in which a wall assembly is represented by a single nonlinear spring (the equivalent spring). The methodology is appropriate when the objective is narrowed down to predicting the global behavior of a wall; nonetheless it cannot supply any information on the performance of individual wall elements and connections. Moreover, the equivalent springs only represent the partition walls with details and dimensions for which they were calibrated. Any change in partition dimensions (i.e. length and height) and/or construction details (e.g. stud or connection spacing) means that a new series of full-scale experiments should be performed in order to evaluate the performance and to calibrate the equivalent models. In addition, the equivalent springs do not include the out-of-plane behavior of partition walls or effect of return walls.

In order to capture all local behaviors and damage mechanisms of a wall, a comprehensive model of the wall needs to be assembled, which includes all the components and accounts for the effect of return walls. The comprehensive model can be used for following purposes: 1) to predict force-displacement response and damage mechanisms of partition walls with various dimensions and construction details for which experimental results are not available, 2) to monitor components' local behaviors and identify the sequence of damage mechanisms in walls, and 3) to be utilized as a

preliminary tool to examine and compare the performance of various innovative details for partition walls. The comprehensive model can also be extended to include the out-of-plane behavior of partition walls. The model can then be employed to estimate the out-of-plane acceleration response of partition walls, which is the perimeter input motion in the seismic analysis of ceiling systems.

1.3. Objectives and Scope of Research

The vision of this research is to provide tools that will facilitate the enhancement of seismic resilience of cold-formed steel-framed gypsum partition walls. In particular, the current study focuses on development of an elaborate and yet computationally efficient procedure to analytically model the in-plane and out-of-plane seismic performance of partition walls. The model accounts for the nonlinear behavior of all critical components of partition walls and considers the effect of return walls. For this purpose, the following steps are taken:

1) Conducting a comprehensive experimental study (59 test runs in total) on the in-plane and out-of-plane system-level seismic performance of partition walls;

2) Investigating the experimental results to identify the critical components of partition walls that can affect their seismic response;

3) Conducting thorough component-level experimental studies (more than 130 experiments) to understand the local behavior of the partition wall critical components;

4) Developing and calibrating a series of analytical models for the nonlinear behavior of partition wall components in OpenSees using the component-level experimental data;

5) Implementing the component analytical models to assemble a detailed analytical model of partition walls;

6) Validating the detailed model using the data available from system-level and subsystem-level experiments on partition walls.

1.4. Dissertation Organization

This dissertation consists of six journal papers and one conference paper. Even though each of these papers is free standing, they all contribute to the larger effort to analytically model nonstructural partition walls. The dissertation is categorized into the following chapters:

Chapter 2 presents a self-contained conference paper titled "System-Level Experiments on Ceiling/Piping/Partition Systems at UNR-NEES Site" (Rahmanishamsi et al. 2014a). This paper describes a series of system-level, full-scale experiments that were conducted at the UNR-NEES site from December 2012 to April 2013, as part of the project titled "NEESR-GC: Simulation of the Seismic Performance of Nonstructural Systems". A short summary on the test setup and the installed nonstructural systems are provided followed by a discussion on the damage observations, particularly for partition walls.

Chapter 3 presents a self-contained paper titled "Cyclic Shear Behavior of Gypsum Board-to-Steel Stud Screw Connections in Nonstructural Walls," which has been

accepted for publication by the journal of *Earthquake Spectra* (Rahmanishamsi et al. 2015a). This paper provides the results of a study dedicated to evaluating the cyclic response and damage mechanisms of gypsum-to-stud connections as one of the components in nonstructural partition walls. The test setup and experimental program are described, followed by a summary of observed damage mechanisms. The force-displacement responses of specimens are then presented and compared to evaluate the effect of various parameters, including loading rate, stud thickness, edge distance, and fastener spacing on the connection performance. The test data is also used to generate capacity fragility curves for the connection in terms of displacements. Finally, a series of analytical hinge models are proposed that represent the hysteresis behavior of the gypsum-to-stud connection. These models are validated using the component experimental data.

Chapter 4 presents a self-contained paper titled "Capacity Evaluation of Typical Stud-Track Screw Connections in Nonstructural Walls," which has been accepted for publication by the *Journal of Earthquake Engineering* (Rahmanishamsi et al. 2015b). This paper provides the results of a series of component-level experiments on the cyclic performance of stud-to-track connections. Similar to Chapter 3, the test setup and experimental program, observed damage mechanisms, force-displacement responses, generated capacity fragility curves, and the calibrated analytical models are described.

Chapter 5 presents a self-contained paper titled "Capacity Evaluation of Typical Track-to-Concrete Power-Actuated Fastener Connections in Nonstructural Walls," which has been accepted for publication by the *Journal of Structural Engineering*

(Rahmanishamsi et al. 2015c). The paper deals with the performance of track-to-concrete connections subjected to either tension or shear force. The outline of the paper is similar to Chapters 3 and 4. In addition, the correlation between tested ultimate connection capacities with AISI S100-12 (2012) nominal design strengths was evaluated.

Chapter 6 presents a self-contained paper titled "Analytical Model for the In-plane Seismic Performance of Cold-formed Steel-framed Gypsum Partition Walls," which has been accepted for publication by the *Journal of Earthquake Engineering and Structural Dynamics* (Rahmanishamsi et al. 2015d). This paper employs the results of component-level experiments, described in Chapters 3-5, to provide a detailed analytical model for the in-plane behavior of a single partition wall that accounts for the nonlinear behavior of all critical components. The paper begins with a description of typical partition walls and the proposed analytical model, followed by a summary of required parameters for the modeling. Subsequently, the modeling procedure is adopted to generate the analytical model of three full-scale partition wall assemblies, tested at the University of Buffalo (UB). The analytical and experimental hysteresis force-displacement responses, dissipated energy, and damage mechanisms are compared.

Chapter 7 presents a self-contained paper titled "Evaluation of the Out-of-plane Behavior of Stud-to-Track Connections in Nonstructural Partition Walls," which is under review by the journal of *Thin-Walled Structures* (Rahmanishamsi et al. 2015e). The paper investigates the out-of-plane performance of stud-to-track connections. The outline of the paper is similar to Chapter 5.

Chapter 8 presents a self-contained paper titled "Analytical Model to Capture the In-Plane and Out-of-Plane Seismic Behavior of Nonstructural Partition Walls with Returns," which is under review by the *Journal of Structural Engineering* (Rahmanishamsi et al. 2015f). This paper presents the results of a study to develop an analytical model of partition walls, which includes the effect of return walls and can capture the walls out-of-plane response. The paper begins with a description of typical partition walls and a summary of the authors' previous work (Chapter 6). Afterwards, the new effort to enhance the previous analytical model and include the out-of-plane behavior of partition walls is discussed. The modeling procedure is then adopted to generate analytical models of three configurations of experiments at the University of Buffalo as well as the analytical model of a C-shaped wall system, tested at the University of Nevada, Reno (Chapter 2). The correlation between analytical and experimental hysteresis force-displacement responses, dissipated energy, and damage mechanisms is evaluated. Moreover, the analytical dynamic characteristics and partition acceleration responses in the out-of-plane direction are compared to experimental results.

Finally, in Chapter 9, a summary and conclusions are drawn from the research, and future research needs are outlined.

1.5. References

Achour, N., Miyajima, M., Kitaura, M., and Price, A. (2011). "Earthquake induced structural and nonstructural damage in hospitals." *Earthq. Spectra*, 27(3), 617–634.

Baird A, Tasligedik AS, Palermo S, Pampanin S. (2011). “Seismic performance of vertical non-structural components in the 22nd February 2011 Christchurch earthquake.” *Earthq. Spectra*, 30(1), 401–425.

Davies, D., Retamales, R., Mosqueda, G., Filiatrault, A. (2011) “Experimental Seismic Evaluation, Model Parameterization, and Effects of Cold-Formed Steel-Framed Gypsum Partition Walls on The Seismic Performance of an Essential Facility.” *Technical Report MCEER-11-0005*, MCEER, State University of New York at Buffalo, NY.

Dhakal, R. P. (2010). “Damage to non-structural components and contents in 2010 Darfield earthquake.” *Bulletin of The New Zealand Society for Earthquake Engineering*, 43, 404-411.

EERI (Earthquake Engineering Research Institute). (2012), “The El Mayor Cucapah, Baja California earthquake April 4, 2010.” *An EERI Reconnaissance Rep,* 2010-02, J. Meneses, ed., Oakland, CA.

Eureka Earthquake Clearinghouse . (2010). “Images and Captions Captured from the Web by CSSC Staff”. EERI Earthquake Clearinghouse. Accessed August 12, 2012. <http://www.eqclearinghouse.org/20100110-eureka/uncategorized/images-captionscaptured-from-the-web-by-cssc-staff>.

FEMA 74 (Federal Emergency Management Agency). (2011), “Reducing the Risks of Nonstructural Earthquake Damage: A Practical Guide,” Redwood City, California.

Filiatrault a., Uang C., Folz B., Chrstopoulos C., Gatto K. (2001), “Reconnaissance Report Of The February 28, 2001 Nisqually (seattle-olympia) Earthquake,” Structural Systems Research Report, SSRO-2001/02, Department of Structural Engineering University of California, San Diego La Jolla, California.

Jenkins, C., Soroushian, S., Rahmanishamsi, E., and Maragakis, M. (2015). "Experimental Fragility Analysis of Cold-Formed Steel-Framed Partition Wall Systems." *Structures Congress 2015*: pp. 1760-1773, Portland, OR.

Lee, T., Kato, M., Matsumiya, T., Suita, K., Nakashima, M. (2007) "Seismic Performance Evaluation of Non-structural Components: Drywall Partitions." *Earthquake Eng. Struct. D.,* 36, 367–382.

Miranda, E., Mosqueda. G., Retamales, R., and Pekcan, G. (2012). "Performance of Nonstructural Components during the February 27, 2010 Chile Earthquake." *Earthq. Spectra,* 28, 453-471.

Mizutani, K., Kim, H., Kikuchihara, M., Nakai, T., Nishino, M., Sunouchi, S. (2012). "The damage of the building equipment under the 2011 Tohoku pacific earthquake." *9th International Conference on Urban Earthquake Engineering & 4th Asia Conference on Earthquake Engineering*, Tokyo Institute of Technology, Tokyo, Japan.

Open System for Earthquake Engineering Simulation (OpenSees) website (2015). http://www.opensees.berkeley.edu . PEER, Berkeley, CA.

Rahmanishamsi, E., Soroushian, S., and Maragakis, M. (2014a). "System-Level Experiments on Ceiling/Piping/Partition Systems at UNR-NEES Site." *Proc., Tenth U.S. National Conference on Earthquake Engineering*, Anchorage, AK.

Rahmanishamsi, E., Soroushian, S., and Maragakis, M. (2014b). "Seismic Response of Ceiling/Piping/Partition Systems in NEESR-GC System-level Experiments." *Structures Congress 2014*: pp. 1824-1835. doi: 10.1061/9780784413357.161, Boston, MA.

Rahmanishamsi, E., Soroushian, S., and Maragakis, M. (2015a). "Cyclic shear behavior of gypsum board-to-steel stud screw connections in nonstructural walls." *Earthq. Spectra*. , in press.

Rahmanishamsi, E., Soroushian, S., and Maragakis, M. (2015b). “Capacity evaluation of typical stud-track screw connections in nonstructural walls.” *Earthq. Eng.*, in press.

Rahmanishamsi, E., Soroushian, S., and Maragakis, M. (2015c) “Capacity evaluation of typical track-to-concrete power-actuated fastener connections in nonstructural Partition Walls.” *J. Struct. Eng*., under review.

Rahmanishamsi, E., Soroushian, S., and Maragakis, M. (2015d). “Analytical model for the in-plane seismic performance of cold-formed steel-framed gypsum partition walls.” *Earthquake Eng. Struct. D.*, in press.

Rahmanishamsi, E., Soroushian, S., and Maragakis, M. (2015e). “Evaluation of the out-of-plane behavior of stud-to-track connections in nonstructural partition walls.” *Thin Wall. Struct.*, under review.

Rahmanishamsi, E., Soroushian, S., and Maragakis, M. (2015f) “Analytical model to capture the in-plane and out-of-plane seismic behavior of partition walls with returns.” *J. Struct. Eng*., under review.

Restrepo, J. I., and Bersofsky, A. (2010). “Performance characteristics of light gage steel stud partition walls.” *Thin Wall. Struct.*, 49, 317–324.

Restrepo, J. I., and Lang, A. F. (2011). “Study of loading protocol in light-gauge stud partition wall.” *Earthq. Spectra*, 27, 1169–1185.

Retamales, R., Mosqueda, G., Filiatrault, A., and Reinhorn, A.M. (2011). “Testing protocol for experimental seismic qualification of distributed nonstructural systems.” *Earthq. Spectra*, 27(3):835-856.

Retamales, R., Davies, R., Mosqueda, and G., Filiatrault, A. (2013). “Experimental Seismic Fragility of Cold-Formed Steel Framed Gypsum Partition Walls.” *J. Struct. Eng*., 139, 1285-1293.

Soroushian, S., Maragakis, E. M., Zaghi, A. E., Rahmanishamsi, E., Itani, M., and Pekcan, G. (2015a). "A State of the Art Review on the Analytical Simulation of Ceiling, Piping, and Partitions." *Bulletin of the New Zealand Society for Earthquake Engineering*, in press.

Soroushian, S., Maragakis, E., Ryan, K., Sato, E., Sasaki, T., Okazaki, T., and Mosqueda, G. (2015b). "Seismic Simulation of an Integrated Ceiling-Partition Wall-Piping System at E-Defense. II: Evaluation of Nonstructural Damage and Fragilities." *J. Struct. Eng*.

Taghavi, S. and Miranda, E. (2003) "Response Assessment of Nonstructural Building Elements." *PEER Report 2003/05*, Pacific Earthquake Engineering Research Center (PEER), Berkeley, CA.

Tasligedik, A. S., Pampanin, S., Palermo, A. (2014) "Low Damage Non-structural Drywalls: Details and Their Performance." *Proc. 2014 NZSEE Conference*, Auckland, New Zealand.

Wang, X., Pantoli, E., Hutchinson, T., Restrepo, J., Wood, R., Hoehler, M., Grzesik, P., and Sesma, F. (2015) "Seismic Performance of Cold-Formed Steel Wall Systems in a Full-Scale Building." *J. Struct. Eng*.

Wood, R. L., Hutchinson, T. C. (2014) "Design-Oriented Model for Capturing the In-Plane Seismic Response of Partition Walls." *J. Struct. Eng*., 140.

Chapter 2

System-Level Experiments on Ceiling/Piping/Partition Systems at UNR-NEES Site

E. Rahmanishamsi[1], S. Soroushian[2], E. M. Maragakis[3]

Please note that this chapter is a self-contained paper published in proceedings of the 10th National Conference in Earthquake Engineering where the word 'this paper/study' refers to the chapter itself.

ABSTRACT

Many critical facilities and buildings, like hospitals and fire stations, need to be used immediately after earthquakes. However, seismic damage to ceiling-piping-partition systems (CPP) can result in prolonged loss of function as seen in previous earthquakes. Moreover, the damage can cause injuries and loss of property. As part of the project titled "NEESR-GC: Simulation of the Seismic Performance of Nonstructural System" a series of system-level, large-scale experiments were conducted at the UNR-NEES site from December 2012 to April 2013. These experiments attempted to investigate the system-level response and failure mechanisms of nonstructural systems, including steel-studded gypsum partition walls, suspended ceilings, and fire sprinkler systems. The results also show how these subsystems interact among themselves as well as with the structural system of a building. Initial observations included: failure of perimeter and in-field connections of ceiling system, damage to the boundaries of partition walls, failure of braced detail in partial height partitions, collapse of free standing partitions, tearing of ceiling tiles because of the interaction between piping and ceiling system, damage to the partition studs, and failure of piping hangers.

[1]PhD Student, Department of Civil and Environmental Engineering, University of Nevada, Reno, Reno, NV, 89557, email: erahmanishamsi@unr.edu

[2]Post-Doctoral Fellow, Department of Civil and Environmental Engineering, University of Nevada, Reno, Reno, NV, 89557, email: ssorooshian@unr.edu

[3]Professor, Dean of College of Engineering, University of Nevada, Reno, University of Nevada, Reno, Reno, NV, 89557, email: maragaki@ce.unr.edu

Rahmanishamsi, E., Soroushian, S., Maragakis, M. System-Level Experiments on Ceiling/Piping/Partition Systems at UNR-NEES Site. *Proceedings of the 10th National Conference in Earthquake Engineering*, Earthquake Engineering Research Institute, Anchorage, AK, 2014.

Introduction

Nonstructural components typically represent between 65% and 85% of the construction cost of commercial buildings. Furthermore, damage to most types of nonstructural components in a building is usually triggered at shake intensities much lower than those required to initiate structural damage [1]. Therefore, improving the seismic performance of these components can lead to important reductions in the economic impact of earthquakes [2]. Along with cost benefits, important structures like hospitals can be designed to remain fully functional immediately after a seismic event to handle medical emergencies [3].

Extensive systematic experimental data is required as a supplement to field observation to improve the available nonstructural design provisions such as the NFPA13 [4], ASTM C754 [5], and ASTM E580 [6] (Soroushian et al., [7]). Several studies have been conducted on the seismic response of nonstructural subassemblies and their components, for instance ceiling tiles and piping systems, as early as the 1980s [8]. Recent large-scale experiments by Soroushian et al. [9] showed that ceiling and piping systems can be significantly vulnerable to seismic loads. However, ceiling-piping-partition systems (CPP) consist of several components, have complex three dimensional geometries, and have complicated boundary conditions that require further full-scale experiments to understand their system-level response.

As part of the project titled "NEESR-GC: Simulation of the Seismic Performance of Nonstructural System" a series of system-level, large-scale experiments were conducted at the UNR-NEES site from December 2012 to April 2013. These experiments attempted to investigate the system-level response and failure mechanisms of nonstructural systems, including steel-studded gypsum partition walls, suspended ceilings, and fire sprinkler systems.

Test Specimen

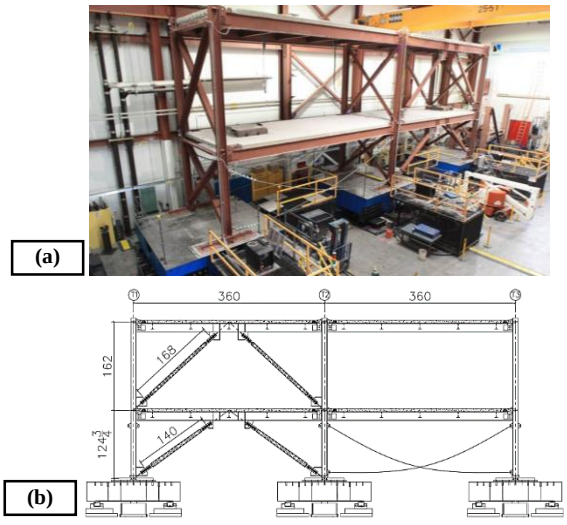

Figure 1. 2-story steel braced frame test bed (a) Test Setup (b) Elevation view

A Test-Bed structure (a two-story, 2-bay by 1-bay steel-braced frame) was designed and constructed to simulate the realistic dynamic environment for the CPP systems. To accommodate large-scale realistic specimens, the Test-Bed was 60 ft. long, 11.5 ft. wide and 24.5 ft. high. This structure was mounted longitudinally over three bi-axial shake tables (Fig. 1).

The proposed experimental program aimed to investigate the performance of acceleration and drift-sensitive non-structural systems. Elastic braces were used in the first phase (linear tests) to obtain high floor acceleration while yielding braces were used in the

second phase (nonlinear tests) to achieve large inter-story drift. The fundamental natural period of the structure was 0.23 sec. and 0.36 sec. for the linear and nonlinear Test-Bed structures respectively. Further information about the Test-Bed is provided in Soroushian et al., [10].

Nonstructural Systems

Looking at technical documents and major manufacturer's catalogs, in addition to commonly used construction details, different variables that could affect the seismic performance of CPP systems were identified. Combining these variables, a total of fifteen different configurations of suspended ceiling systems, two configurations of piping systems, and fourteen configurations of partition walls were designed and installed in the Test-Bed. The following subsections describe each nonstructural system.

Partition Walls

Figure 2 shows the identical layout of partition walls on both floors, with the exception of two additional content rooms installed only on the second floor. To be able to test several configurations (details) of partition walls in each test, the walls were divided in different sections using a 1-ft. gap in between. The considered variables in the wall configurations included the followings: connectivity of the sheathing and studs to the top tracks, presence of return walls, details of wall intersections, height of the partition walls, stud and track thickness (30 mil or 18 mil), direction of walls compared to the excitation direction, and whether an opening was present. All walls were designed per ASTM C754-11[5].

The partition walls were constructed using 5/8-in. gypsum boards and the CEMCO ViperStud drywall framing system (350VS125-18/30 and 350VT125-18/30). Twenty-gauge CH studs (212CH-34) and J runners (212JR-34) with 1/2-in. and 1-in. gypsum boards were utilized to build the shaft walls (P1-F, P7-F, and P8-F in Table 4, experimental observation section). Studs were located 24 in. apart, attached to the gypsum boards by #6 drywall screws spaced 12 in. in the field and 8 in. at boundaries. Partition wall tracks were fastened to concrete slabs using 0.157-in diameter, fully knurled shank Hilti X-U Universal Powder-Actuated Fasteners (PAFs).

Three different details were used to attach the partition walls to the top concrete deck: slip track, full connection, and sliding/frictional. In the full connection detail, studs were screwed to the top tracks, while in the slip track, studs were not. The sliding/frictional detail [2] allows the top tracks to slide in relation to the concrete deck.

All the perimeter walls were full-height while others (such as content room walls) were partial height. Based on ASCE7-10 [10], partitions greater than 6 ft. in height shall be laterally braced to the structure. Therefore, rigid bracing (formed from steel studs) and diagonal wire bracing were utilized to restrain the mid-span and north content room walls, respectively (Fig. 2). For other cases, the walls, which were 6 ft. tall, remained free standing with no lateral restraint. Further information about partition connection details can be found in Davies et al., [3]

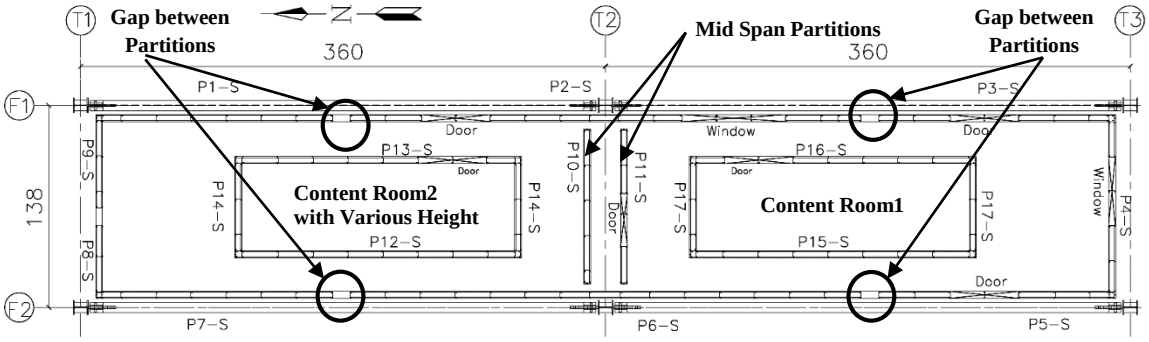

Figure 2. View of partition wall layout of second floor

Ceiling Systems

Twenty-two ceiling assemblies with fifteen different configurations were designed considering the following variables: area of ceiling systems, type of wall angles, detail of perimeter connections, bracing of ceiling systems, material and weight of ceiling tiles, seismic expansion joints, and interaction with other nonstructural systems. All the assemblies were designed and installed in the test frame per ASTM E580/E580M-11b [6]. The descriptions of UNR ceiling configurations are summarized in Table 1. More details on the test configurations are provided in Rahmanishamsi et al., [11]. The ceiling system was constructed from Armstrong Prelude 15/16 in. exposed tee systems with heavy-duty main runners and 24x24x3/4-in. tiles. The main runners, installed in the longitudinal direction (north-south direction), were braced in some configurations with steel stud compression posts and 45-degree, 12-gauge splay wires. Pop rivets or Armstrong BERC2 seismic clips with tight screws were used to attach the ceiling grids to the wall angles on the north and west side. Alternatively, on the south and east side, grid members were attached with 3/4-in. clearance to the wall angles that allowed the grid members to float freely. In all configurations, the ceilings were suspended 3 ft. from the bottom of the structural deck with 12-gauge Hilti X-CW hanger wires, spaced a maximum of 8 in. from perimeter walls and 4 ft. apart elsewhere. Additional hanger wires were used at the location of gypsum board panels that represented the light fixtures.

Table 1. Ceiling description of UNR experiments

Test	Assembly-Floor #	Config. #	Nominal Sizec (ft)	Panel Weight (psf)	Bracing	Perimeter Angle (in.)	Seismic Separation Joint	Comments
L-1	**1-1**	**1**	58×10	1.31	NO	2	NO	No bracing
…*	**…**	**…**	…	…	…	…	…	…
NL-3	**22-2**	**4**	58×10	1.31	Yes	7/8+clip	NO	Nonlinear test

* Due to space limitation, some of the ceiling configurations are not shown. Please see [11] for more information.

Fire Sprinkler Piping

Two fire sprinkler piping systems with different lengths, namely long (Fig. 3) and short systems, were designed per NFPA13 [4] utilizing schedule 40 steel pipes. The long piping system was installed in the first three linear and last two nonlinear tests, while the short piping system was used in the other experiments. The drawing of short piping system is not presented in this paper due to space limitation. Both systems included 4-in. riser pipes, 2.5-4.0-in. main runs, and several branch lines of various lengths and diameters. Considering the geometry limitation, extra mass was added to the end of some branch lines to simulate longer pipe lines. All connections on risers and their connections with main runs were grooved fit, while the rest of the connections were threaded. The piping system was hung from the structure with 3/8-in. all threaded rods that were anchored to the deck with 3/8-in diameter Hilti KH-EZ concrete screw anchors. Lateral resistance was provided by inclined 1-in.-diameter longitudinal and lateral sway braces on the main run near the riser pipe and an additional lateral sway brace at the end of the main run for the long piping system. The ends of the two branch lines were restrained with 45-degree, 12-gauge wires to limit the lateral movement. Two types of drop pipes were installed in the piping system: flexible and conventional (rigid). A minimal gap was provided at the locations of sprinkler heads of all the flexible and some of the conventional drops. A 2-in. oversized ring was used in the rest of conventional drops.

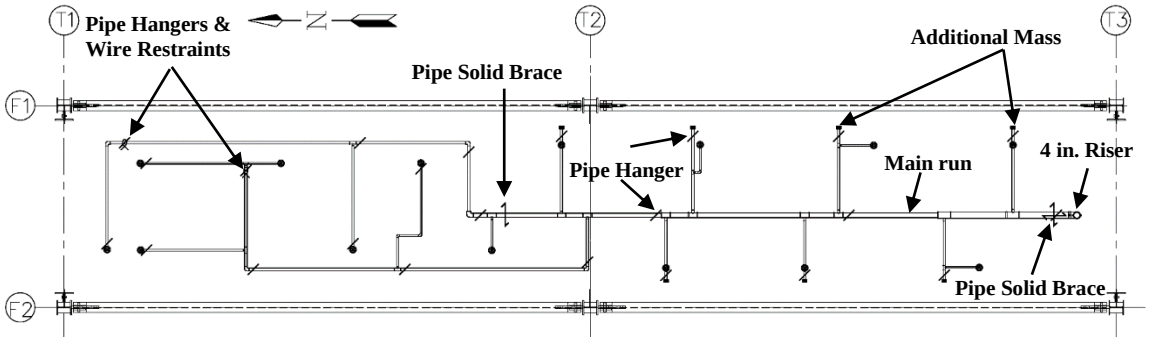

Figure 3. Overall plan view of long piping system

Excitation Protocol

Table 2. Peak accelerations and story drift ratios

Test	Acceleration (g)			Drift Ratio (%)	
	Table	1st floor	2nd floor	1st floor	2nd floor
L-1	0.91	0.99	1.52	0.43	0.16
L-2	1.17	1.39	2.35	0.52	0.25
L-3	1.02	1.31	2.27	0.45	0.24
L-5	1.03	1.39	2.39	0.45	0.23
L-6	0.94	1.59	2.47	0.48	0.25
NL-1	2.04	1.22	1.41	2.97	2.34
NL-2	1.69	1.09	1.21	2.60	2.15
NL-3	1.68	0.89	1.06	2.72	2.25

A set of ramp-up table motions were generated using an analytical procedure in order to achieve the target motions on the desired levels. These levels were the second floor, for the first seven motions of the linear tests, and the shake table for other cases (nonlinear tests and the last two motions of linear tests). The AC156 [12] spectrum with the

maximum parameters of $A_{RIG\text{-}H}$=2.0g, $A_{FLX\text{-}H}$=4.0g, S_{DS}=2.5g, and z/h=0.5 was considered as the target spectrum for the full-scale motion. In total, 59 uniaxial motions were applied in longitudinal direction during eight experiments with PGA (peak average achieved acceleration on the tables) ranging between 0.12g to 2.0g. The peak average achieved floor acceleration (PFA) varied from 0.14g to 1.59g on the columns of first floor and 0.16g to 2.47g on the columns of second floor. Table 2 shows the PGA, PFA, and peak inter-story drift ratio for each experiment.

Experimental Observations

This section describes the observed damage to the nonstructural systems during the UNR experiments with main focus on partition walls, due to space limitation. More information on the performance of ceiling and piping systems is provided in Rahmanishamsi et al., [11].

Partition Walls

The observed damage for the partition walls may be categorized as in Table 3. The last three categories (TB, BC, and CP) are assumed to be related to the out-of-plane acceleration, while the others are mainly due to the in-plane drift or a combination of drift and acceleration. Table 4 and 5 show the minimum average inter-story drift and PFA corresponding to each damage definition for the in-plane and out-of-plane performance of partition walls respectively. Some of the damage mechanisms, such as FS, FT, and TS, could not be detected during the experiments because the studs and tracks were covered by gypsum boards. These mechanisms were observed after removing the boards at the end of the tests. Therefore, the floor drift corresponding to the starting point of this damage could not be accurately reported.

Damage in partition walls with the full connection detail included pulling out gypsum screws from the studs, damage in the boundary studs, and the formation of plastic hinges in the field studs. Figure 4 depicts the damage pattern of the full connection detail. Since the studs are connected to the top tracks, the upper part of the studs (about 1-ft. from the top) moves with the top floor (x_2), while the bottom part moves with the lower floor (x_1) (Fig. 4a&b). In low-amplitude motions, the studs bend slightly at about 1 ft. from the top to handle the relative displacement. However, brittle gypsum boards

Table 3. Partition damage definition

Damage definition	Abbr.
Popping out or rocking of gypsum board screws	**GS**
Damage in connection of studs to top tracks	**ST**
Tape damage and cracks in the wall corners	**VJ**
Cracks at the corners of partition openings (windows or doors)	**CO**
Damage along corner beads and boundary studs	**BS**
Crushing of gypsum boards	**GB**
Damage in flanges of transverse wall top tracks	**FT**
Damage in field studs including forming plastic hinges	**FS**
Failure of top/bottom track connections to the concrete slab	**TS**
Damage in connection of partition braces to top tracks	**TB**
Failure of brace connections to top tracks	**BC**
Collapse of partition walls	**CP**

Table 4. Drift (%) corresponding to each damage definition for full-height partition walls

Partition name	Stud THK (Ga.)	Top Connection Detail	Damage Definition								
			GS	ST	VJ	CO	BS	GB	FT	FS	TS
			Drift (%)								
P1-F*	20	Slip Track	-	-	1.05	-	1.05	-	D**	-	D**
P2-F	25	Full Conn.	0.47	-	-	-	0.75	-	-	D**	-
P3-F	20	Sliding	0.39	-	2.09	2.58	1.05	-	-	D**	-
P4-F	20	Sliding	-	-	-	2.48	-	-	-	-	-
P5-F	20	Sliding	0.39	-	2.09	-	1.05	-	-	D**	-
P6-F	20	Sliding	0.39	-	-	-	1.05	-	-	D**	-
P7-F	20	Slip Track	-	-	2.06	-	1.05	2.97	-	-	-
P8-F	20	Slip Track	-	-	-	-	-	-	-	-	-
P1-S	20	Full Conn.	-	0.52	1.49	-	1.49	-	-	1.62	-
P2-S	20	Slip Track	-	-	--	2.34	1.49	2.34	-	-	-
P3-S	25	Slip Track	-	-	1.40	1.62	1.49	1.40	D**	-	2.15
P4-S	20	Slip Track	-	-	-	-	-	1.40	-	-	-
P5-S	20	Slip Track	-	-	1.40	-	2.34	1.40	D**	-	-
P6-S	20	Slip Track	-	-	-	-	1.40	1.62	-	-	-
P7-S	20	Slip Track	-	-	1.62	-	1.40	-	2.15	-	-
P8-S	20	Slip Track	-	-	1.62	-	-	-	-	-	-
P9-S	20	Full Conn.	-	-	-	-	-	-	-	-	-

*: -F and –S refer to the first and second floor respectively.

D**: This damage was observed after removing the gypsum boards at the end of the test.

cannot deform in the same manner as the studs. As a result, the gypsum screws pull out from the gypsum boards (Fig. 4c), which allows the boards to move independently of the upper part of the studs. Increasing the drift causes damage in the boundary studs (BS) and forms plastic hinges in field studs (FS) (Fig. 4d).

In partition walls with the slip track connections, studs are not screwed to the top tracks. Therefore, the studs and the gypsum boards stay connected together and slide inside the top tracks (Fig 5a). Although this sliding prevents the bending of the studs, it can lead to the crushing of gypsum boards due to the interaction with structural components (Fig. 5c). The boundary studs may also pop out from the top tracks (Fig. 5b). As the boundary studs slide back towards their initial positions, they may get caught in track flanges, causing the studs to pull out from the gypsum boards (Fig 5d). In the case of partitions with return walls, the boards and studs of transverse walls cannot slide in out-of-plane direction,

Table 5. PFA corresponding to each damage definition for transverse walls

Partition name	Height (in.)	Bracing	Damage Definition		
			TB	BC	CP
			PFA(g)		
P10-F	93	braced	0.82	1.03	-
P11-F	93	braced	0.90	-	-
P10-S	93	braced	-	-	-
P11-S	93	braced	1.10	1.10	1.39
P10-F	72	unbraced	n/a	n/a	0.60
P11-F	72	unbraced	n/a	n/a	0.60
P10-S	72	unbraced	n/a	n/a	0.68
P11-S	72	unbraced	n/a	n/a	0.68

and thus the sliding is followed by the separation of gypsum boards at the corners (VJ) (Fig. 5e). In larger drifts, studs of transverse walls may bend the flanges of the top tracks and pop out (FT) to move with the studs of the longitudinal walls (x_1) (Fig 5f). In-plane and out-of-plane sliding of the top tracks in the sliding/frictional detail (P3-F to P6-F in Table 4) improves the performance of partition corners by delaying damage VJ and eliminating damage FT. However, in large drifts, due to the space limitation for sliding, the connection works as a full-connection detail and forms the plastic hinges in the studs. For all details, PAFs used for attachment of the wall tracks to concrete base materials performed well with only two minor damage occurrences noted (TS) in test NL-1 and NL-3.

No lateral restraint was provided for 6-ft., partial-height partitions as it is allowed by ASCE7-10 [10]. However, partitions P10-F, P11-F, P10-S, and P11-S collapsed in low amplitude motions (PFA = 0.60-0.70g) while others (P12-F to P17-F and P12-S to P17-S in Fig. 2) remained damage-free in all experiments. The results suggest that 6-ft., free-standing partitions can be significantly vulnerable to the out-of-plane seismic load if there is no return wall. In addition, even though the bracing improves the performance of partial height partitions, damage in the brace connections may still result in collapse of the wall, as indicated in Table 5.

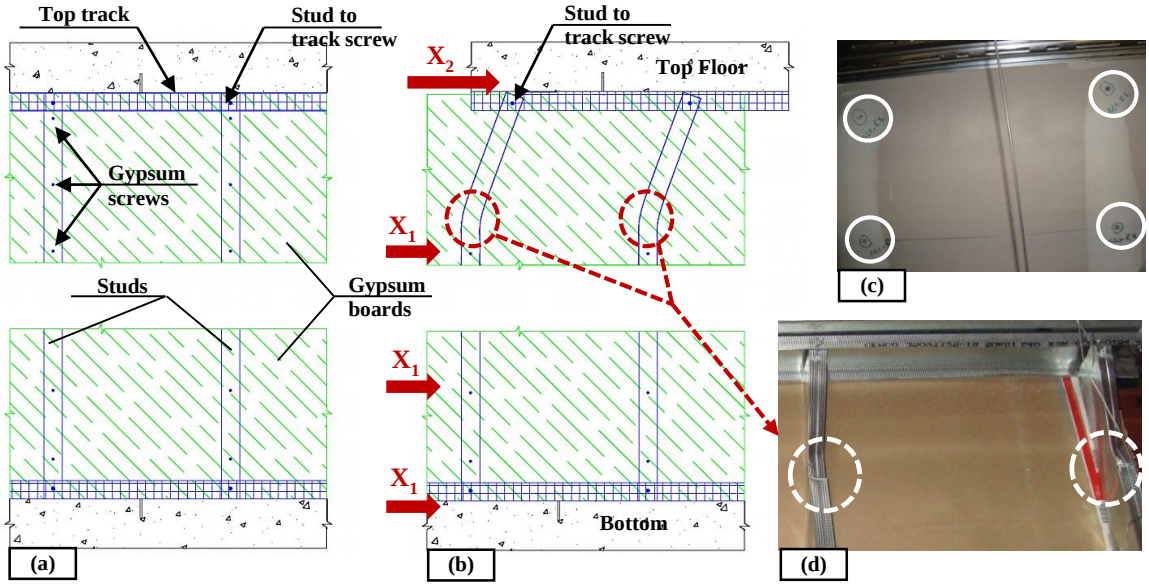

Figure 4. Full connection walls: (a) partition walls before applying drift, (b) partition walls after applying large drift, (c) popping out of gypsum screws, and (d) forming plastic hinges in field studs

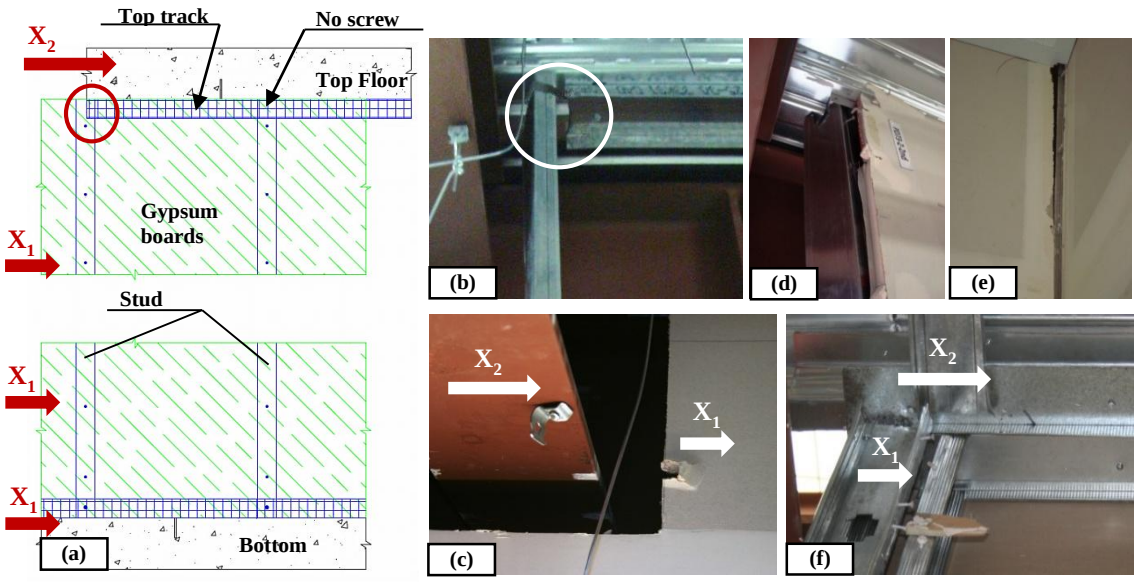

Figure 5. Slip track partition walls: (a) partition walls after applying large drift, (b) popping out of stud from track, (c) damage GB, (d) damage BS, (e) damage VJ, and (f) damage FT

Ceiling Systems

Observed damage in ceiling systems can be categorized as in Table 6. More information on damage definition can be found in Soroushian et al., [13]. Table 7 summarizes the PFA corresponding to each damage definition in the UNR experiments.

In most configurations, the damage was initiated in the perimeter connections followed by deformation of grid latches. Failure of grid latches in larger motions led the ceiling grids and tiles to misalign and fall down. In the ceiling system with 7/8-in. wall angles and seismic clips, perimeter damage included grid unseating, seismic clip damage, and wall angle crushing. This damage was likely due to the insufficient seat length of wall angles [9]. During the linear tests, failure of pop rivets was the only damage in perimeter connections of the ceiling systems with 2-in. wall angles. The damage of ceiling systems with 2-in. wall angles, compared to the ceiling with 7/8-in. wall angles, was observed at a higher PFA followed by less extensive damage in larger motions. Moreover, results showed that increasing the weight of the ceiling system (ceilings with larger area or heavier panels) expedited the failure of perimeter connections in both cases. In all configurations, ceiling hanger wires and compression posts were remained

Table 6. Ceiling damage definition

Damage definition	Abbr.
Misalignment of panels	**M**
Falling of panels	**F**
Damage (tearing) in panels around sprinkler heads	**T**
Failure of pop rivets	**P**
Damage in seismic clips and 7/8 in. wall angles	**S**
Buckling of grids	**B**
Damage in grid latches	**L**
Failure of grid connections	**C**
Unseating of grids and damage in 2 in. wall angles	**U**

intact during the experiments. Further information on observed damage and comparisons of performance of different configurations is provided in Rahmanishamsi et al., (2014).

Table 7. PFA (g) corresponding to each damage definition

Test	Assembly-Floor #	Config. #	Damage Definition								
			M	F	T	P	S	B	L	C	U
			PFA(g)								
L-1	**1-1**	**1**	-	-	-	0.80	n/a	-	0.99	-	-
L-1	**2-2**	**2**	-	-	1.24	1.04	n/a	1.52	1.24	1.52	-
…	**…**	**…**	…	…	…	…	…	…	…	…	…
NL-3	**21-1**	**15**	0.89	0.89	0.81	n/a	0.44	-	0.81	0.84	n/a
NL-3	**22-2**	**4**	1.01	1.01	1.01	n/a	1.01	-	1.01	1.01	n/a

Fire Sprinkler Piping

The piping systems were pressurized to 50 psi to simulate average municipal water pressure and allow observation of any possible leakage. However, no leakage was reported during the UNR experiments. The piping hanger clip next to the longitudinal and lateral sway braces failed at PFA=1.27g (Fig. 8a) in Test NL-1. In the first two experiments (Test L-1 and L-2), the connection of the longitudinal brace on the second floor slipped off from the main run at PFA=1.23g. The connection was replaced with a different detail in later experiments to eliminate the damage. Interaction between the sprinkler heads, with the conventional arm over, and the ceiling panels knocked out up to 8 in. (in the most extreme case) of the panels (Fig. 6b). This damage was prevented in certain locations, using flexible hose drops. Further information on the observed damage can be found in Rahmanishamsi et al., [11].

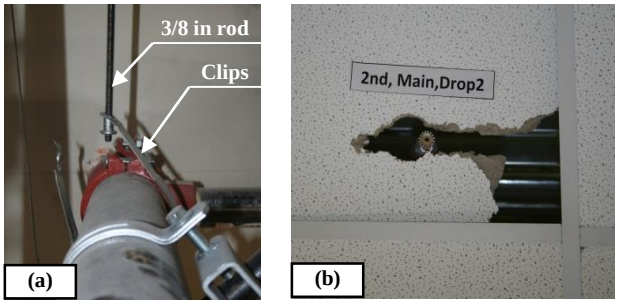

Figure 6. Damage in (a) piping hanger clips and (b) ceiling panels

Conclusions

The following conclusions are based on the observations of the UNR experiments, which may not necessarily be replicated in the field: (1) damage in partitions with the full connection details starts with popping out of gypsum screws followed by significant damage to the field and boundary studs; (2) unbraced 6-ft. tall partitions with no return walls can be highly vulnerable to seismic loads; (3) partition-brace connections need to be carefully designed based on the possible seismic demand; (4) due to unseating of grids in ceiling systems with 7/8-in. wall angles, the first damage initiates at lower PFA, in comparison to the ceiling systems with 2-in. wall angles; (5) larger or heavier ceiling systems are more vulnerable to seismic excitation; and (6) flexible hose drops

substantially reduce the piping-ceiling interaction.

Acknowledgments

This material is based upon work supported by the National Science Foundation under Grant No. 0721399. This Grand Challenge (GC) project to study the seismic response of nonstructural systems is under the direction of E. M. Maragakis from the University of Nevada, Reno and Co-PIs: T. Hutchinson (UCSD), A. Filiatrault (UB), S. French (G. Tech), and B. Reitherman (CUREE). Any opinions, findings, conclusions or recommendations expressed in this document are those of the investigators and do not necessarily reflect the views of the sponsors. The authors recognize and thank the following companies for providing product donations and technical support: Armstrong, Hilti, and CEMCO steel.

References

1. Taghavi, S., Miranda, E. Response Assessment of Nonstructural Building Elements. Berkeley, Pacific Earthquake Engineering Research Center (PEER), 2003.
2. Araya-Letelier, G., Miranda, E. Novel sliding/frictional connections for improved seismic performance of gypsum wallboard partitions, The 15th World Conference on Earthquake Engineering, Lisbon, Portugal, 2012.
3. Davies, R. D., Retamales, R., Mosqueda, G., Filiatrault, A. Experimental Seismic Evaluation, Model Parameterization, and Effects of Cold-Formed Steel-Framed Gypsum Partition Walls on the Seismic Performance of an Essential Facility, Technical Report MCEER -11-0005, Buffalo, NY, 2011.
4. NFPA13. Standard for the Installation of Sprinkler Systems, National Fire Protection Association, 2010 Edition, Quincy, MA, 2011.
5. ASTM C754-11. Standard Specification for Installation of Steel Framing Members to Receive Screw-Attached Gypsum Panel Product, ASTM International, Volume 04.01, 2011.
6. ASTM E580/E580M-11b. Standard Practice for Installation of Ceiling Suspension Systems for Acoustical Tile and Lay-in Panels in Areas Subject to Earthquake Ground Motions, ASTM International, Volume 04.06, 2011.
7. Soroushian, S., Maragakis, E. M., Itani, M., Pekcan, G., Zaghi, A. E. Design of a Test Bed Structure for Shake Table Simulation of the Seismic Performance of Nonstructural Systems, Structures Congress, ASCE, Las Vegas, USA, 2011.
8. ATC. FEMA 461-Interim protocols for determining seismic performance characteristics of structural and nonstructural components through laboratory testing, Redwood City, CA, 2007.
9. Soroushian, S., Rahmanishamsi, E., Ryu, K. P., Maragakis, E. M., Reinhorn, A. M. A Comparative Study of Sub-System and System Level Experiments of Suspension Ceiling Systems, Tenth U.S. National Conference on Earthquake Engineering, Anchorage, USA, 2014.
10. ASCE/SEI 7-10. Minimum Design Loads for Buildings and Other Structures, American Society of Civil Engineers, New York, 2010.
11. Rahmanishamsi, E., Soroushian, S., Maragakis, M., Seismic Response of Ceiling/Piping/Partition Systems in NEESR-GC System-level Experiments, ASCE, Structures Congress, Boston, USA, 2014.
12. ICC Evaluation Services, Inc. ICEE-ES AC 156, Acceptance criteria for seismic qualification by shake-table testing of non-structural components and systems, Whittier, CA, 2007.
13. Soroushian, S., Ryan, K., Maragakis, M., Sato, E., Sasaki, T., Okazaki, T., Tedesco, L., Zaghi,

A., Mosqueda, G., and Alvarez, D., Seismic Response of Ceiling/Sprinkler Piping Nonstructural Systems in NEES TIPS/NEES Nonstructural/NIED Collaborative Tests on a Full Scale 5-Story Building, ASCE, Structures Congress, Chicago, USA, 2012.

Chapter 3

Cyclic Shear Behavior of Gypsum Board-to-Steel Stud Screw Connections in Nonstructural Walls

Esmaeel Rahmanishamsi,[a)] Siavash Soroushian,[a)] and Manos Maragakis[a)]

Please note that this chapter is a self-contained paper accepted for publication in journal of Earthquake Spectra where the word 'this paper/study' refers to the chapter itself.

Gypsum steel-stud partition walls are comprised of light-gauge, cold-formed steel studs and gypsum boards attac hed with self-drilling screws. Previous experimental studies on the seismic performance of these walls have shown widespread failure of gypsum-to-stud connections (GSCs), initiated at very low amplitude excitation. The failure of GSCs resulted in loss of strength and stiffness of the partition walls. A series of component tests has been conducted at University of Nevada, Reno to evaluate the shear force and displacement capacities of GSCs. Fastener spacing (center to center and also center to edge), loading protocol (monotonic or cyclic), and stud thickness were varied between specimens. The test data were then used to develop fragility curves for shear capacities of GSCs in terms of displacements. Additionally, a series of nonlinear GSC hinge models were proposed and validated using component experimental data.

INTRODUCTION

Damage to most types of nonstructural components in a building is usually triggered at shake intensities much lower than those required to initiate structural damage (Taghavi and Miranda 2003). As an example, during the 2011 Tohoku earthquake, there were many types of damage to nonstructural systems, while severe damage to structural elements seemed to be limited (Tsuru and Murakami 2011). Similar observations were

[a)] Dept. of Civil and Environmental Engineering, University of Nevada, Reno, MS 0258, Reno, NV 89557-0258

reported after the 2010 Chile earthquake (Miranda 2012). Damage to nonstructural systems can lower the performance level of the entire building system, even if the structural system of a building achieves a continuous or immediate occupancy performance level after a seismic event (Retamales et al. 2013). Therefore, a better understanding of the seismic behavior of nonstructural systems is required to improve the performance level of buildings.

A widely used nonstructural system that has sustained extensive damage in previous earthquakes is the gypsum board partition wall framed with cold-formed steel (CFS) studs. Typical construction of partition walls in the United States consists of C-shaped, light-gauge steel studs nested in and screwed to C-shaped steel tracks at the top and bottom (Fig. 1). The track is usually fastened to the structural slab with powder-actuated fasteners and is used to align the vertical studs (Restrepo and Lang 2011). Gypsum board, consisting of a rigid gypsum core sandwiched between paper layers, is attached to the studs and track with bugle-headed drywall screws placed at regular intervals. The gypsum board braces the steel studs (Vieira and Schafer 2012) and provides the stiffness and strength of the partition wall (Schafer and Hiriyur 2002).

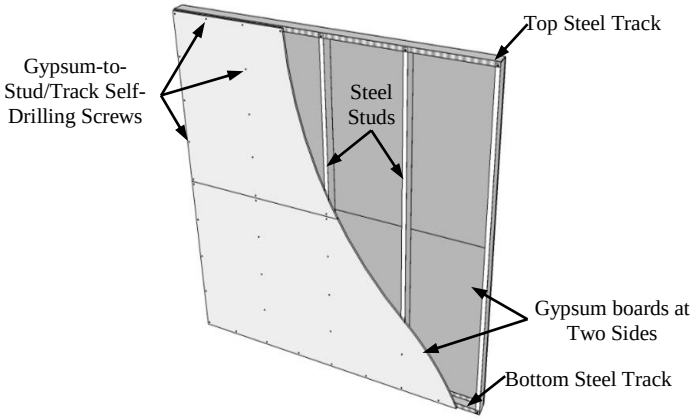

Figure 1. Typical Steel-Framed Gypsum Partition Wall

Past experimental studies on the seismic performance of partition walls (Fülöp and Dubina 2004, Retamales et al. 2008, Restrepo and Bersofsky 2010, Davies et al. 2011, Restrepo and Lang 2011, Wood and Hutchinson 2012, Rahmanishamsi et al. 2014) have shown widespread failure of the gypsum board-to-stud (and track) screw connections

(GSCs) at very low amplitude excitations (0.40% inter-story drift ratio in the study by Retamales et al., 2008). These studies also indicated that failure of GSCs could result in loss of strength and stiffness of the partition walls and lead to subsequent damage, such as the formation of plastic hinges in the studs. Thus, the behavior of the GSCs is of interest for characterizing their role in the performance of steel-stud gypsum partition wall systems. Figure 2 shows some examples of GSC failures during past experimental studies (Bersofsky 2004, Davies et al. 2011, Rahmanishamsi et al. 2014).

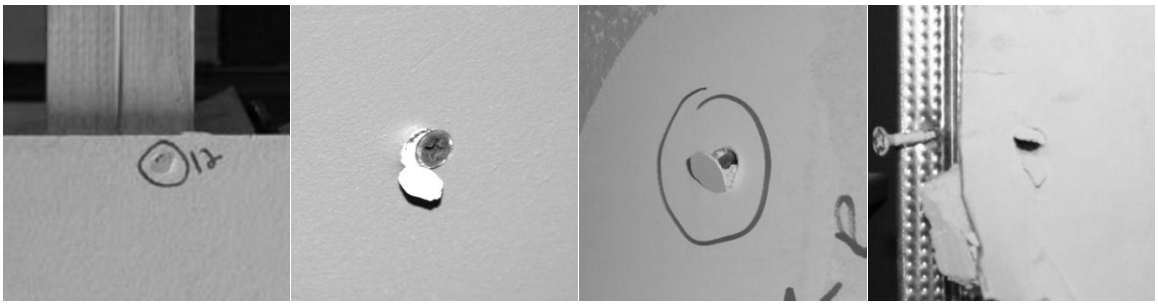

Figure 2. Examples of GSC Failures in Previous Experimental Studies (Bersofsky 2004, Davies et al. 2011, Rahmanishamsi et al. 2014)

The performance of GSCs has been evaluated in the early work of Miller and Pekoz (1994) as well as in more recent works by Fiorino et al. (2006), Vieira and Schafer (2012), and Peterman et al. (2014). Researchers investigated the effects of various parameters on GSC behavior, including loading protocol, loading rate, stud and gypsum thickness, screw spacing (center-to-center distance between screws), and edge distance (the distance from the center of the screws to the gypsum edge). These studies concluded that while loading protocol, loading rate and screw spacing did not have a clear effect on the GSC performance, edge distance could dramatically change the results. Fiorino et al. (2006) and Vieira and Schafer (2012) also reported various damage mechanisms for GSCs, which will be thoroughly discussed in the section about damage mechanisms in this paper.

Although previous studies provided valuable information, they were limited to GSCs in load-bearing walls. The steel stud profiles used in load-bearing walls are different from those used in nonstructural partition walls. Since the nonstructural partition walls are not

part of the structural load-carrying system, thinner studs with smaller web depth are typically used in their construction. Therefore, the performance of GSCs in nonstructural partition walls could be different from that observed in load-bearing walls.

As a part of the project titled "NEESR-GC: Simulation of the Seismic Performance of Nonstructural System," a numerical effort is underway to investigate the seismic performance of nonstructural partition walls. The long-term goal of the effort is to develop a detailed yet computationally efficient numerical model for cold-formed steel-framed gypsum partition walls as shown in Fig 3. In the model, the nonlinear behavior of the members and connections (except gypsum boards) is represented by hysteretic load-deformation springs. In turn, the model supports a mechanically-based method for assessing the lateral response of cold-formed steel-framed gypsum partition wall configurations for which testing is not available (Peterman et al. 2014). The model can be also used for performance-based studies (such as fragility analysis), in which extensive numerical analyses are required. To develop this modeling capability, it is necessary to characterize the cyclic behavior and energy dissipation of individual partition wall components and to represent those behaviors using equivalent hysteretic springs. The characterization can be accomplished with the experimental data from component-level cyclic tests on each of the members and connections (Padilla-Llano et al. 2014). The cyclic tests also help to determine the various possible damage mechanisms in each partition wall component.

This paper presents the findings of a new study dedicated to evaluating the cyclic response and damage mechanisms of GSCs as one the components in nonstructural partition walls. The test setup and experimental program are described, followed by a summary of observed damage mechanisms. The effect of various parameters, including loading rate, stud thickness, edge distance, and fastener spacing on GSC performance is then reviewed and fragility curves are presented for shear capacities of GSCs in terms of displacements. Finally, the development of nonlinear hinges for describing the hysteresis behavior of GSCs is explained, together with the calibration of the hinges using experimental data.

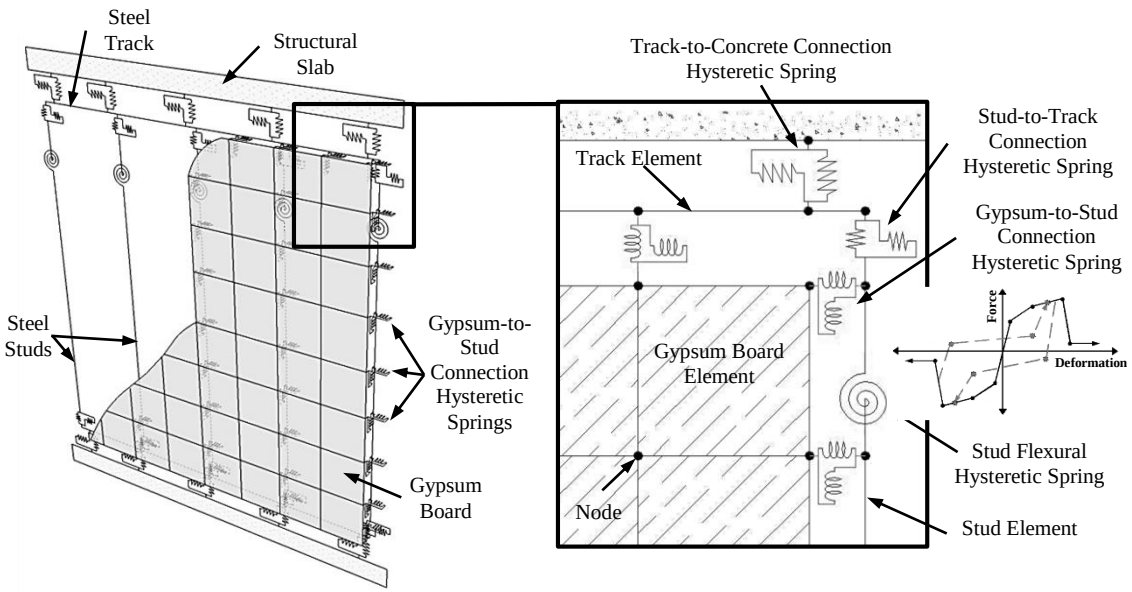

Figure 3. Schematic Diagram of a Numerical Model of a Steel-Framed Gypsum Partition Wall

DESCRIPTION OF TEST SPECIMENS

Test Setup

Specimens were designed to represent the typical GSC details in commercial and hospital construction, using 3-5/8-in.-deep cold-form steel studs and 5/8-in.-thick type X gypsum board. Two stud thicknesses were tested: 0.019 in. (362S125-19), which is common in commercial buildings, and 0.030 in. (362S125-30), which is common in essential facilities such as hospitals (Davies et al. 2011). Figure 4a shows a sample specimen and the testing machine. The design of the test setup was influenced by the early work of Miller and Pekoz (1994) as well as the more recent work of Fiorino et al. (2006), Vieira and Schafer (2012), and Peterman et al. (2014). The specimen consisted of two 12-in.×18-in. gypsum boards, attached to the opposite flanges of 18-in.-long steel studs at top and bottom (Figs. 4b and 4c). Three #6×1-1/4-in. screws (Philips-drive bugle-head fine thread self-drilling drywall screws), spaced 6 in. on center, were used for GSCs at each side (twelve screws in total). The middle screw was omitted in some specimens to increase the spacing to 12 in. (see Table 1 in next section). The screws were driven to provide screwhead penetration just below the gypsum board surface without breaking the surface paper (ASTM C840, 2013). The distance from the center of the

screws to the edge of the gypsum board (edge distance in Fig. 4c) varied from 1/2 in. to 1-1/2 in. in different specimens. Note that based on the ASTM C840 (2013) the screws shall be spaced not less than 3/8 in. from the gypsum board edge. The studs were clamped between one steel plate (18 in.×3 in.×1/4 in.) and two steel angles (1-1/2 in.×1-1/2 in.×1/4 in.) in order to prevent the web from bending, ensuring the deformation was limited to the GSCs on the stud flanges. The steel angles were bolted to T-shape steel plates, which were clamped by the grips of an Instron 5985 machine (Figs. 4a and 4b). The bottom grip was stationary while the top one was movable. The machine measured the axial reaction and displacement of the movable grip.

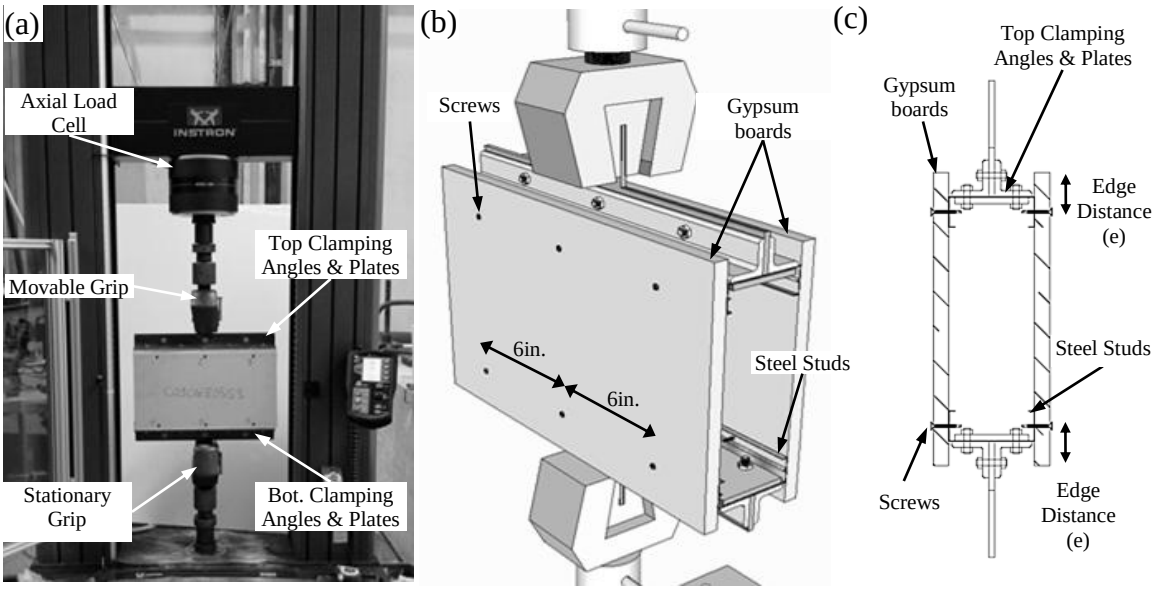

Figure 4. Specimen and Test Machine

Experimental Program

Table 1 lists the 31 specimens included in the testing program. The specimens are categorized in six series, each composed of nominally identical specimens. The series were designed to evaluate the effect of edge distance, loading rate, stud thickness, and number of screws on the performance of GSCs. The series label defines the specimen typology, namely the stud thickness (T19: 0.019 in. thick), edge distance (E15: 1.5 in. edge distance), and number of screws (N6: three screws in each side, spaced 6 in. on center). For each series, at least one monotonic test and three cyclic tests were performed,

which is the minimum number of required tests for the fragility assessment analysis (Davies et al. 2011). The loading rate varied from 0.1 in./min. to 1.0 in./min. for the first series. However, a constant rate (0.5 in./min.) was used for the other series since the GSC response was found to be insensitive to the loading rate. All experiments were conducted at room temperature (68-77 °F) and humidity (40-50%). Responses and failure mechanisms of each series are discussed in detail in subsequent sections.

Table 1. Test Program Matrix

Series Label	Loading Protocol	Loading Direction	Loading Rate, υ (in./min.)	Stud Thickness (in.)	Screw Spacing (in.)	Edge Distance (in.)	Number of Specimens
T19E15N6	Monotonic	Tension	0.1	0.019	6.0	1.5	1
	Monotonic	Compression	0.1	0.019	6.0	1.5	1
	Monotonic	Tension	1.0	0.019	6.0	1.5	1
	Monotonic	Compression	1.0	0.019	6.0	1.5	1
	Monotonic	Tension	0.5	0.019	6.0	1.5	1
	Monotonic	Compression	0.5	0.019	6.0	1.5	1
	Cyclic	-	0.5	0.019	6.0	1.5	3
T19E15N4	Monotonic	Tension	0.5	0.019	12.0	1.5	1
	Monotonic	Compression	0.5	0.019	12.0	1.5	1
	Cyclic	-	0.5	0.019	12.0	1.5	3
T30E15N6	Monotonic	Tension	0.5	0.030	6.0	1.5	1
	Monotonic	Compression	0.5	0.030	6.0	1.5	1
	Cyclic	-	0.5	0.030	6.0	1.5	3
T19E05N6	Monotonic	Tension	0.5	0.019	6.0	0.5	1
	Cyclic	-	0.5	0.019	6.0	0.5	3
T19E07N6	Monotonic	Tension	0.5	0.019	6.0	0.75	1
	Cyclic	-	0.5	0.019	6.0	0.75	3
T19E10N6	Monotonic	Tension	0.5	0.019	6.0	1.0	1
	Cyclic	-	0.5	0.019	6.0	1.0	3

Loading Protocol

Fiorino et al. (2006) investigated the performance of GSCs under three different cyclic loading protocols. They concluded that the loading protocol had no effect on the GSC damage mechanisms and slight effects on the force-displacement response characteristics (such as initial stiffness and maximum force). In the current study, only one loading protocol, proposed by Retamales et al. (2008, 2011), was adopted for the cyclic tests. The loading protocol was specifically developed for evaluating the capacity fragility of primarily drift-sensitive nonstructural components. Figure 5a shows the displacement history that was generated based on the loading protocol defined by Retamales et al. (2008, 2011). For each series, three cyclic tests were conducted using

this displacement history and with a loading rate of 0.5 in./min. Also, in order to study the effect of cumulative cyclic damage on the ultimate capacity of GSCs, at least one additional monotonic tension test was performed for each series (see Table 1). In the monotonic tests, the specimens were subjected to progressive displacements, without unloading phases (Fig. 5b).

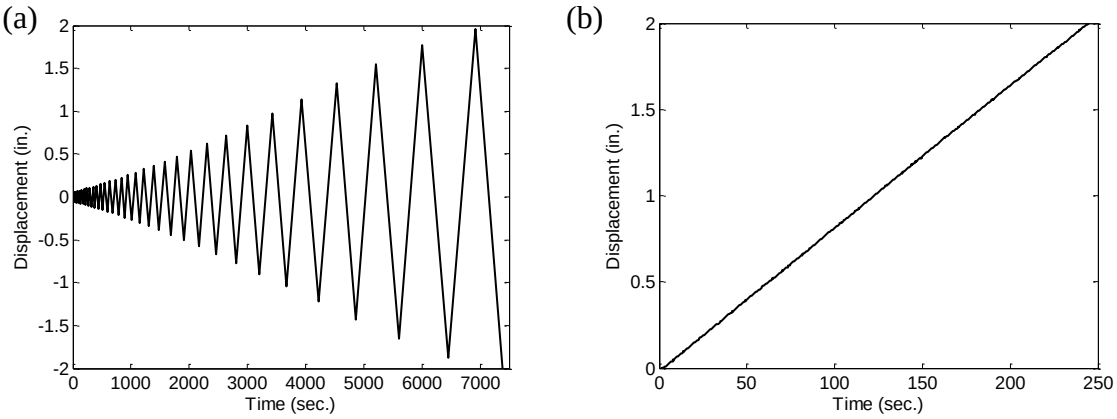

Figure 5. Loading Protocol for: (a) Monotonic, (b) Cyclic Tests

EXPERIMENTAL RESULTS

The experimental results presented in this section are based on the limited number of tests performed on the particular GSCs in this study (see Table 1 and the test setup description). Note that GSCs with other types of gypsum boards (with different thicknesses, densities or paper coverings) or screws may have different behavior and damage mechanisms. The environmental conditions at the time of testing (temperature and humidity) as well as overdriving of the screws are other factors that can influence the experimental results (Vieira and Schafer 2012). Increasing the number of tests along with extending the scope of the experimental program in future studies can enhance our understanding of the complex behavior and damage mechanisms of various GSCs.

Individual GSC Force and Displacement

Figure 6 shows the free body diagram of a specimen during a downward monotonic test. To find the force for each GSC, it was assumed that the total force (F in Fig. 6a and 6b) was uniformly distributed between all screws (Fig. 6c). Therefore, the individual

GSC force was calculated as f = F / N, where N was the number of screws in the top or bottom of the specimen. This assumption was subsequently verified (see discussion of Fig. 11a). Moreover, the displacements of all fasteners were considered to be equal to the displacement of the movable grip. The internal deformations of the grip and fixture were neglected since they were consistently small (less than 0.01 in.).

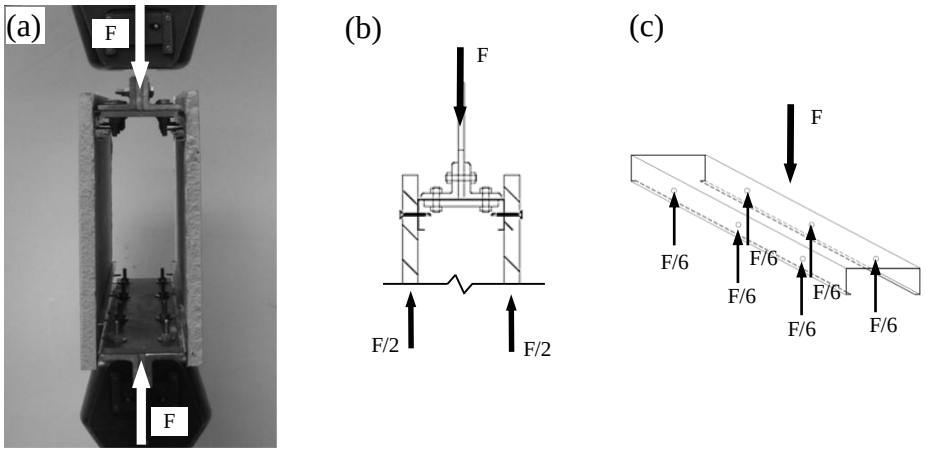

Figure 6. (a) Applied Force, (b) Free Body Diagram, and (c) Force Distribution

Damage Mechanisms

Based on the experimental observations, the GSC damage mechanisms can be categorized as follows: (*T*) tilting of screws, (*P*) pulling of screws through the gypsum boards, (*D*) detaching of gypsum boards from studs, and (*E*) breaking out of gypsum board edges. Similar damage mechanisms have been reported by Fiorino et al. (2006) and Vieira and Schafer (2012). Figure 7 depicts the observed damage and basic behavior of a fastener in a GSC under increasing displacement of the stud flange. The main portion of the shear capacity of the GSC is provided by the bearing resistance of gypsum at the fastener location (Peterman et al. 2014), which depends on parameters such as gypsum thickness, density, and cover paper. Applying the displacement, the fastener tilts and pushes the gypsum in the opposite direction of the stud displacement (Fig. 7b). When the force is larger than the bearing capacity of the gypsum material, the fastener rotates around the attached point and pulls through the board (Fig. 7c). At larger displacements, if sufficient edge distance is provided, the screw head is pulled through the gypsum board, and the gypsum board completely detaches from the stud (Fig. 7d); otherwise, the

gypsum board edge breaks (Fig. 7e). The last two damage descriptions (Fig. 7d and 7e) corresponds to the complete failure of the GSCs. Figure 8 presents typical experimental responses in monotonic and cyclic tests and displacement zones corresponding to each damage descriptions.

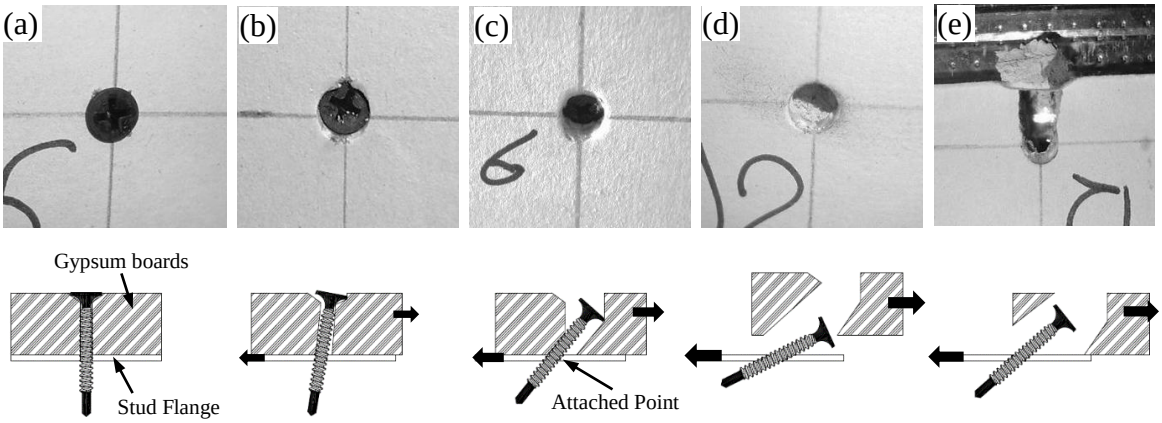

Figure 7. Damage Mechanisms of GSCs, Per Fiorino et al. (2006) and Vieira and Schafer (2012): (a) Initial Condition, (b) Screw Tilting, *T*, (c) Screw Pulling Through the Gypsum Board, *P*, (d) Gypsum Board Detaching, *D*, (e) Breaking of Gypsum Board Edge, *E*

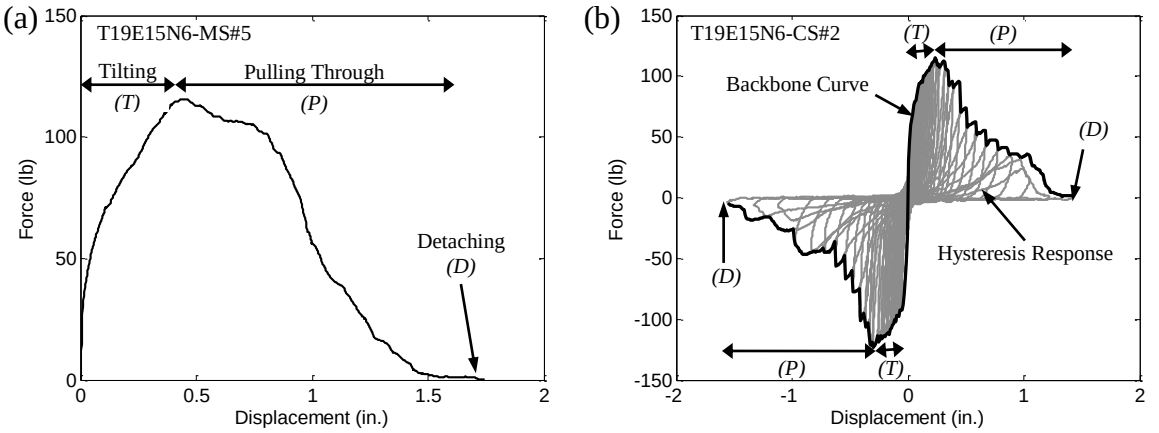

Figure 8. Typical Experimental responses for: (a) Monotonic, (b) Cyclic Test

Effect of Loading Rate

The monotonic tests of the first series of specimens (T19E15N6) were conducted with various loading rates (0.1, 0.5, and 1.0 in./min.) in order to evaluate their effect on the test results. Figure 9a and 9b compare the force-displacement responses and maximum force ratios in monotonic tests with different rates. The maximum force ratio is calculated

by dividing the maximum force of each monotonic test by the maximum force of the upward monotonic test with a loading rate of 0.1 in/min. The results vary slightly, with an unclear trend as the loading rate is changed. This observation is consistent with a previous study by Fiorino et al. (2006). Therefore, the GSC response is considered to be independent of the loading rate within the loading range tested, and a constant value of 0.5 in./min. has been used for the rest of the tests.

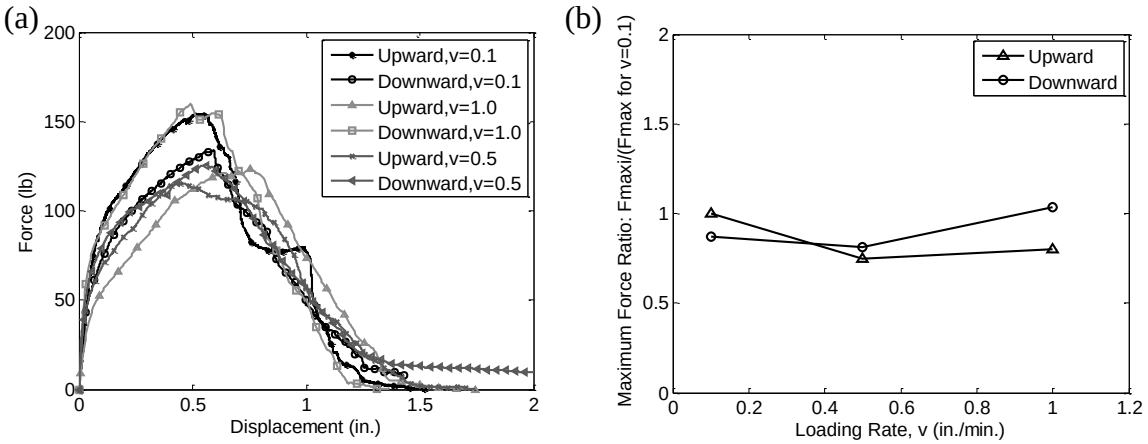

Figure 9. Effect of Loading Rate (v, in./min.) on: (a) Monotonic Force-Displacement Response, (b) Maximum Force Ratio

Force-Displacement Responses of Specimens with Gypsum Board Detachment (Failure Mode *D*)

The force-displacement responses of specimens, in which the failure mode was gypsum detachment (damage description *D*, Fig. 7d) are discussed in the following section. In these specimens, the edge distance was large enough to avoid gypsum edge breakout (damage description E, Fig. 7e). Figure 10 provides the backbone curves of cyclic tests, the median of the backbone curves, and the monotonic response of an individual GSC in specimen series T19E15N6 and T19E15N4. Although the monotonic test results do not perfectly match the backbone curves of cyclic tests, the specimens perform consistently in terms of failure mechanisms for both loading protocols. Moreover, the force-displacement responses of the specimens are similar in three cyclic tests. Therefore, the median of the backbone curves of the cyclic tests are used hereafter to investigate the effect of various parameters (such as the number of screws) on the performance of GSCs. In addition, the results (Fig. 10) show that the specimens

performed symmetrically: measured forces under positive (downward/towards the center of gypsum board) and negative (upward/towards the gypsum edge) displacements are approximately equal.

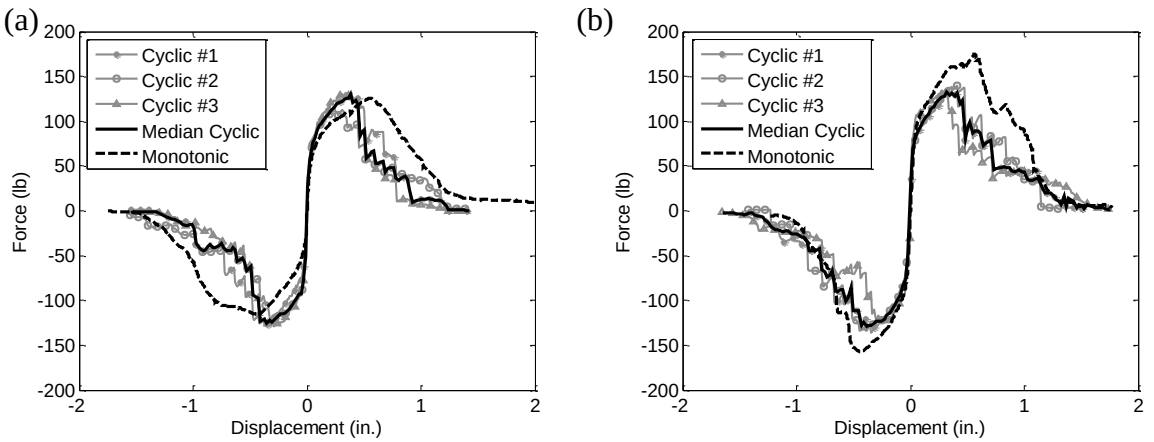

Figure 10. Monotonic Test Response and Cyclic Test Backbone Curves of an individual GSC for Specimen Series (a) T19E15N6, (b) T19E15N4

As mentioned earlier, the individual GSC force was calculated based on the assumption that the total load was uniformly distributed between all screws (f = F/N). To validate the assumption, a different screw pattern was tested in the second specimen series (T19E15N4). Two screws were spaced 12 in. on center (N=4) instead of 3 screws spaced 6 in. on center (N=6). The comparisons of the median backbone curves of specimens with 4 and 6 screws (Fig. 11a) suggest that the individual GSC response is independent from the number of screws. This indicated that the load is distributed practically uniformly through the screws.

Figure 11b compares the performance of GSCs in specimens with different stud thicknesses. The specimens behave similarly in terms of initial stiffness, maximum capacity, and failure mechanisms. Nonetheless, the failure displacements (the displacement corresponding to the complete failure) are different for the specimens. This can be due to the fact that the initial stiffness and maximum capacity of the connection are provided by the bearing resistance of gypsum that is independent of the stud thickness (Fig. 7b and Fig. 8a). In the failure displacement, the fastener rotates around the attached point (Fig. 7c), pulls through and pops out from the gypsum boards (Fig. 7d). A thicker

stud might have limited the fastener rotation and postponed the subsequent failure (damage mechanisms *P* and *D*, Fig. 7c and 7d).

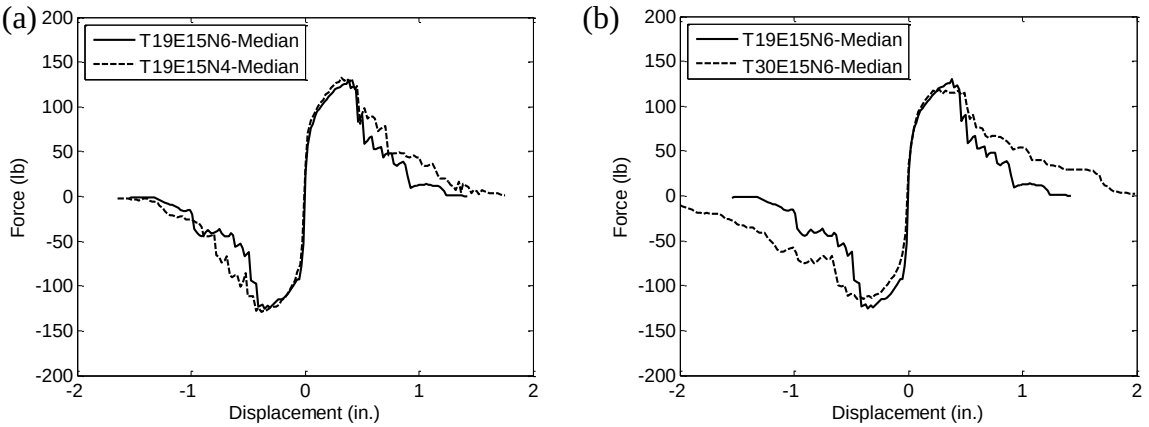

Figure 11. Effect of (a) Number of Screws, (b) Stud Thickness

Force-Displacement Responses of Specimens with Gypsum Edge Breakout (Failure Model *E*)

The last three series of experiments (T19E05N6, T19E07N6, and T19E10N6) were designed to assess the effect of edge distance on the performance of GSCs, adopting the following values: 1/2 in., 3/4 in., and 1 in. For each distance, three cyclic tests and one monotonic test were carried out. Figure 12 depicts an example of the hysteresis curves, the backbone curves, and the monotonic response for each series as well as the median backbone curves of all specimens. In specimens with ½-in. and ¾-in edge distance, the observed failure mode is the breaking-out of the gypsum edge (failure mode *E*, Fig. 7e) in negative displacement (upward/towards the gypsum edge) and detaching of the gypsum board (failure mode *D*) in positive displacement (downward/towards the center of gypsum board). Breakout of the gypsum edges is initiated at very small displacements: 0.07 in. and 0.17 in. for series T19E05N6 and T19E07N6, respectively. As a result, the specimen force-displacement responses are asymmetrical (Fig. 12a and 12b).

In specimen series T19E10N6, a combination of failure modes *E* and *D* in negative displacement and failure mode *D* in positive displacement are reported. In this series, the failure mode *E* is initiated in a larger displacement (0.5 in) in contrast to the series with a smaller edge distance. Figure 12d compares the median backbone curves of specimens

with different edge distances. The figure demonstrates that the gypsum edge breakout can lead to a significant capacity reduction. It is also shown that the force-displacement responses of specimens with edge distances equal to or larger than 1.0 in. are very similar. In fact, an edge distance of 1.0 in. was established as a transition value denoting the onset of gypsum edge breakout. The minimum required edge distance to preclude edge breakout is reasonably taken as 1.5 in., which is in agreement with value suggested by Peterman et al. (2014).

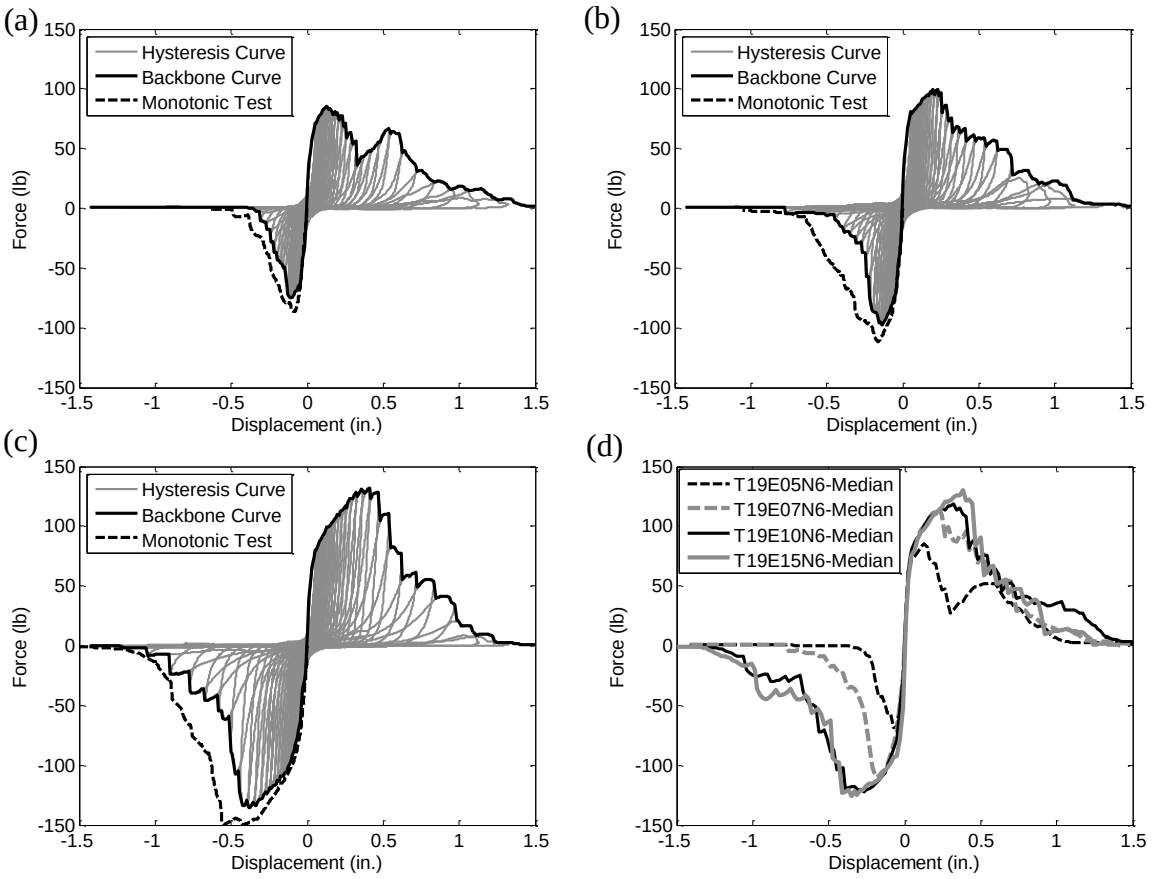

Figure 12. Edge Distance Effect: Examples of Force-Displacement Hysteresis of GSCs in series (a) T19E05N6, (b) T19E07N6, (c) T19E10N6; and (d) Comparison of Median Backbone Curves of Specimens with Different Edge Distances

CAPACITY FRAGILITY ANALYSIS

Capacity fragility curves are conditional probability statements of a component's (or system's) vulnerability as a function of an engineering demand parameter (*EDP*). They

present the probability that the *EDP* in the component exceeds a certain level of capacity or damage states (*DSs*). The steps in generating the fragility curves can be summarized as follows: 1) choose a proper fragility formulation, 2) select appropriate engineering demand parameters, 3) determine capacity (damage state) estimates, and 4) develop fragility curves (Soroushian et al. 2014).

Several methodologies for generating capacity fragility curves have been developed over the years. In the current study, the framework proposed by Porter et al. (method *A* in Porter et al. 2007) is utilized to assess the vulnerability of GSCs. The method is based on experimental studies and can be used where all specimens reach all *DSs* at observed values of *EDP*. According to Porter et al.: $F_{dm}(edp)$ denotes the fragility function for the damage state *dm*, defined as the probability that the component reaches or exceeds damage state *dm*, given a particular *EDP* value (Eq. 1) and idealized by a lognormal distribution (Eq. 2):

$$F_{dm}(edp) \equiv P[DM \geq dm | EDP = edp] \tag{1}$$

$$F_{dm}(edp) = \Phi\left(\frac{ln(edp/x_m)}{\beta}\right) \tag{2}$$

where Φ denotes the standard normal (Gaussian) cumulative distribution function, x_m indicates the median value of the distribution and β represents the logarithmic standard deviation (Porter et al. 2007).

The engineering demand parameter (*EDP*) is the input in the fragility analysis and should be chosen to be most closely related to the failure probability of the specimen. In method A, the *EDP*s are the values at which the damage states occurred (Porter et al. 2007). Since the cyclic performance of a GSC is mainly governed by the displacement of the fastener, displacement is considered as the only *EDP*.

For this investigation, the damage states of GSCs are defined based on the different damage mechanisms (*T*, *P*, and *D* or *E*) observed during the experiments. In specimens with gypsum board detachment, the damage states include initiation of screw tilting (*DS1*), initiation of the screw pulling through the gypsum (*DS2*), and detachment of

gypsum board from the stud (*DS3*). In specimens with insufficient edge distance, the damage states consist of initiation of the screw tilting (*DS1*), initiation of cracks at the gypsum edge (*DS2*), and complete gypsum edge breakout (*DS3*). These *DSs* are shown with their associated points on a representative backbone curve in Fig. 13. *DS1* presents the initiation of nonlinearity in a GSC, while *DS2* is set to the local maximum point on the backbone curve. A strength degradation is triggered after *DS2*, but the gypsum board is still connected to the stud. The third damage state (*DS3*) is defined as the point on the backbone curve that is related to the complete failure of the connection. At this point, a complete separation between the gypsum board and stud was reported during the test. In some specimens the test was continued after *DS3* (Fig. 13b), while for others the test was stopped at this point (Fig. 13a). It is notable that the performance of GSCs with insufficient edge distance is governed by the fastener behavior in the negative displacement (towards the gypsum edge). Therefore, the damage states are defined based on the negative part of the backbone curve.

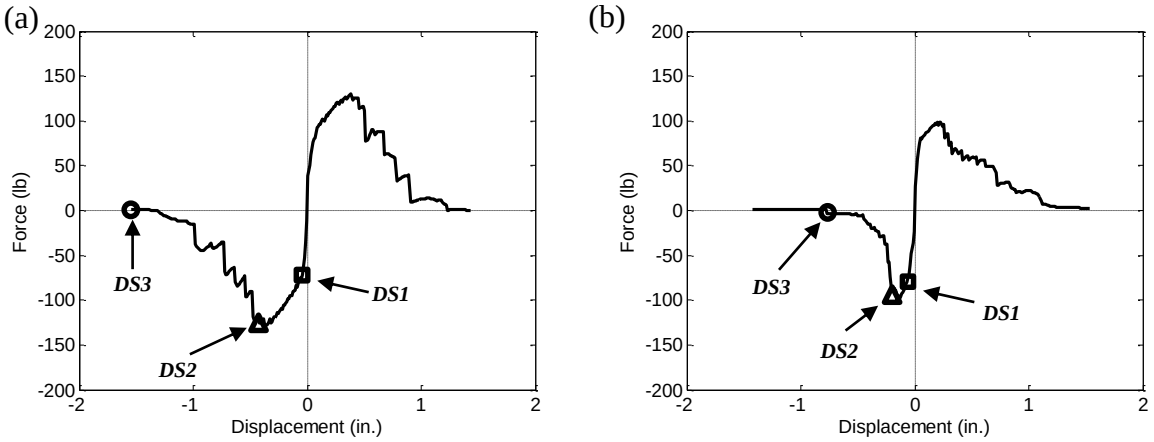

Figure 13. Examples of Damage State Definitions (a) Specimens with Sufficient Edge Distance (b) Specimens with Insufficient Edge Distance

The individual damage states are characterized by representative values for the median, x_m, and dispersion, β, for the component damage state distributions as follows:

$$x_m = e^{\frac{1}{N}\sum_{i=1}^{N} ln(x_i)} \tag{3}$$

$$\beta = \sqrt{\frac{1}{N-1}\sum_{i=1}^{N}\left[\ln\left(\frac{x_i}{x_m}\right)\right]^2} \quad (4)$$

where x_i denotes the i-th measured displacement corresponding to specific damage observation (*EDPs*), and N is the number of cyclic tests conducted for each group of specimens. To generate the fragility curves, specimens are grouped based on the edge distance as follows: 1) specimens with sufficient edge distance (1.5-in. edge distance) including specimen series T19E15N6, T19E15N4, and T30E15N6; 2) specimens with 1.0-in. edge distance (T19E10N6); 3) specimens with 0.75-in. edge distance (T19E07N6); and 4) specimens with 0.5-in. edge distance (T19E05N6). Therefore, N is equal to 9 for the first group and 3 for the other groups. Tables 2 and 3 summarize the EDPs (x_i), x_m, and logarithmic standard deviation obtained for each GSC group and damage level.

Figure 14 presents the GSC fragility curves for different specimen groups using Equation (2). The curves show that the connections with small edge distances are significantly more vulnerable than connections with large edge distances. The difference is especially highlighted in the probability of occurrence of *DS3* (complete failure of the connection). A similar trend can be found by comparing the median values (x_m) in Table 3. Note that these remarks are based on the experimental studies that have been done in this work. One may repeat the experiments with a larger number of specimens to generate more robust fragility curves.

Table 3. Engineering Demand Parameters

Group No.	Specimen Name	Disp. (in.) DS1	DS2	DS3
#1	T19E15N6-S#1	0.048	0.369	1.542
	T19E15N6-S#2	0.037	0.236	1.555
	T19E15N6-S#3	0.050	0.287	1.537
	T19E15N4-S#1	0.040	0.444	2.018
	T19E15N4-S#2	0.048	0.327	2.001
	T19E15N4-S#3	0.045	0.405	2.004
	T30E15N6-S#1	0.042	0.319	1.538
	T30E15N6-S#2	0.049	0.388	1.426
	T30E15N6-S#3	0.040	0.268	1.767
#2	T19E10N6-S#1	0.042	0.408	1.247
	T19E10N6-S#2	0.048	0.319	1.405
	T19E10N6-S#3	0.048	0.319	1.405
#3	T19E07N6-S#1	0.048	0.137	0.781
	T19E07N6-S#2	0.058	0.186	0.781
	T19E07N6-S#3	0.048	0.186	0.920
#4	T19E05N6-S#1	0.048	0.107	0.365
	T19E05N6-S#2	0.040	0.048	0.448
	T19E05N6-S#3	0.049	0.065	0.439

Table 3. Fragility Curve Parameters

Group No.	DS1		DS2		DS3	
	x_m	β	x_m	β	x_m	β
#1	0.044	0.110	0.332	0.208	1.695	0.138
#2	0.046	0.078	0.346	0.142	1.350	0.069
#3	0.051	0.109	0.168	0.178	0.825	0.095
#4	0.045	0.106	0.070	0.400	0.416	0.113

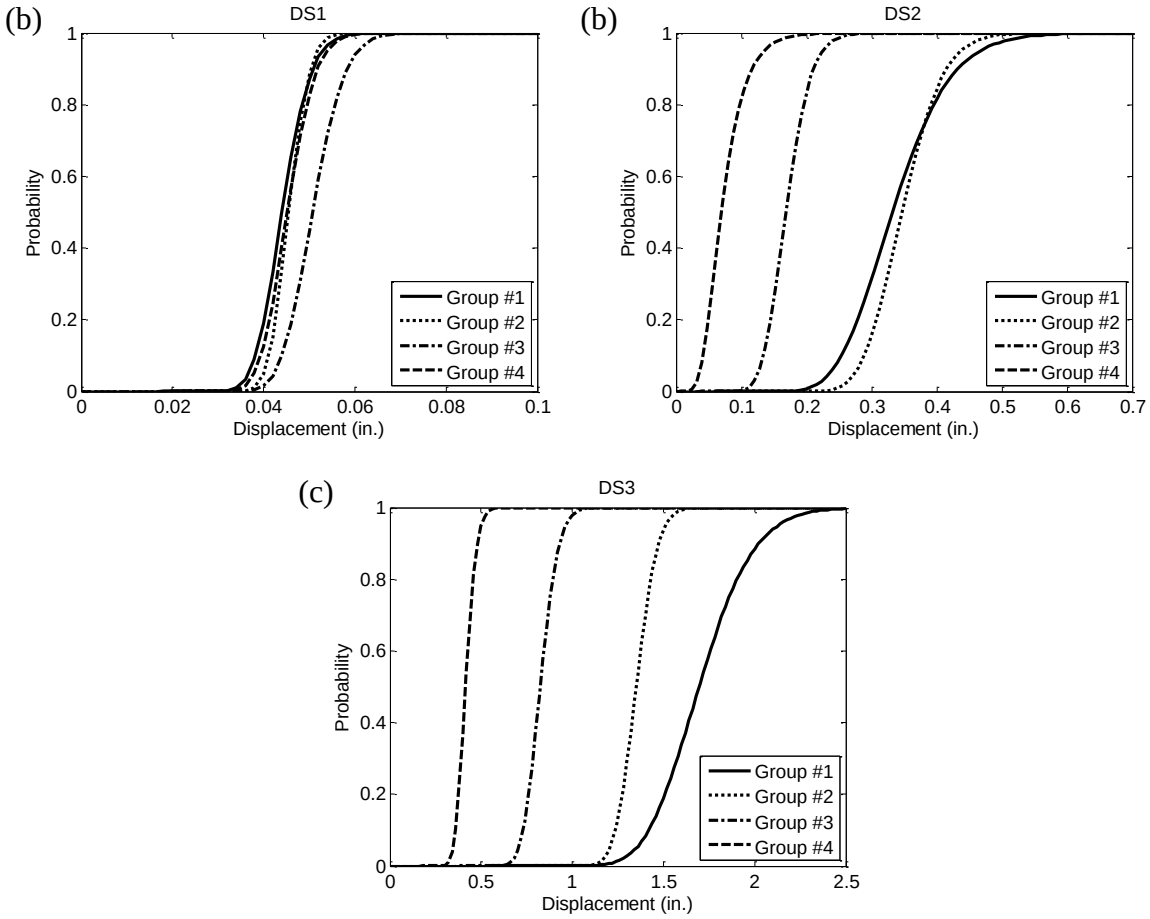

Figure 14. GSC Fragility Curves for (a) *DS1*, (b) *DS2*, and (c) *DS3*

DEVELOPMENT OF A HYSTERESIS MODEL FOR GYPSUM-STUD CONNECTIONS

The experimental data is used to develop a hinge material model for the behavior of GSCs. For this purpose, a one-dimensional hysteresis load-displacement relationship is defined using the "Pinching4" uniaxial material along with a "zeroLength" element in OpenSees (OpenSees 2014). This material enables the simulation of complex, pinched force hysteresis responses accounting for degradations under cyclic loadings (Soroushian 2013) similar to those shown in Fig. 8 and Fig. 10. The "Pinching4" parameters (Fig. 15) include four positive and negative points along the backbone curve (*ePdi*, *ePfi*, *eNdi*, and *eNfi*), in addition to the parameters that define the "pinched" or unloading/re-loading behavior of the model (total 39 parameters). The pinching parameters (*rDispP*, *rForceP*, *uForceN*, etc.), are based upon the ratio of displacement (Disp) or force (Force) to maximum (P) or minimum (N) historic demands at various points in the unloading (u) or reloading (r) curve (Peterman et al. 2014). Unloading and reloading stiffness degradation as well as strength degradation can be considered in the model using *gKi*, *gDi* , and *gFi*. A detailed description of these parameters can be found in the OpenSees website (OpenSees 2014).

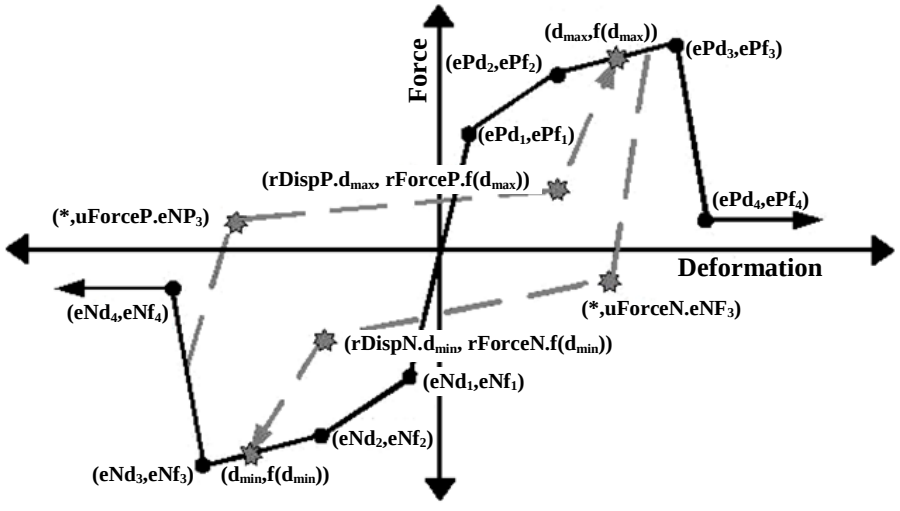

Figure 15. Pinching4 Material Properties (OpenSees 2014)

Calibration of Proposed Numerical Model Using GSC Experiments

Inspired from the previous study by Soroushian et al. (2013), for each test specimen, the hysteresis response, the value of cumulative hysteresis energy, and force histories are used in the calibration process on a visual basis. Moreover, the parameters are calibrated so that the maximum cumulative hysteresis energy remains within the ±10% range of the experimental values. The displacement histories are used as the inputs for the numerical model. Figure 16 shows the aforementioned characteristics of the calibrated hysteresis model for shear response of one sample GSC from the specimen series T19E15N6.

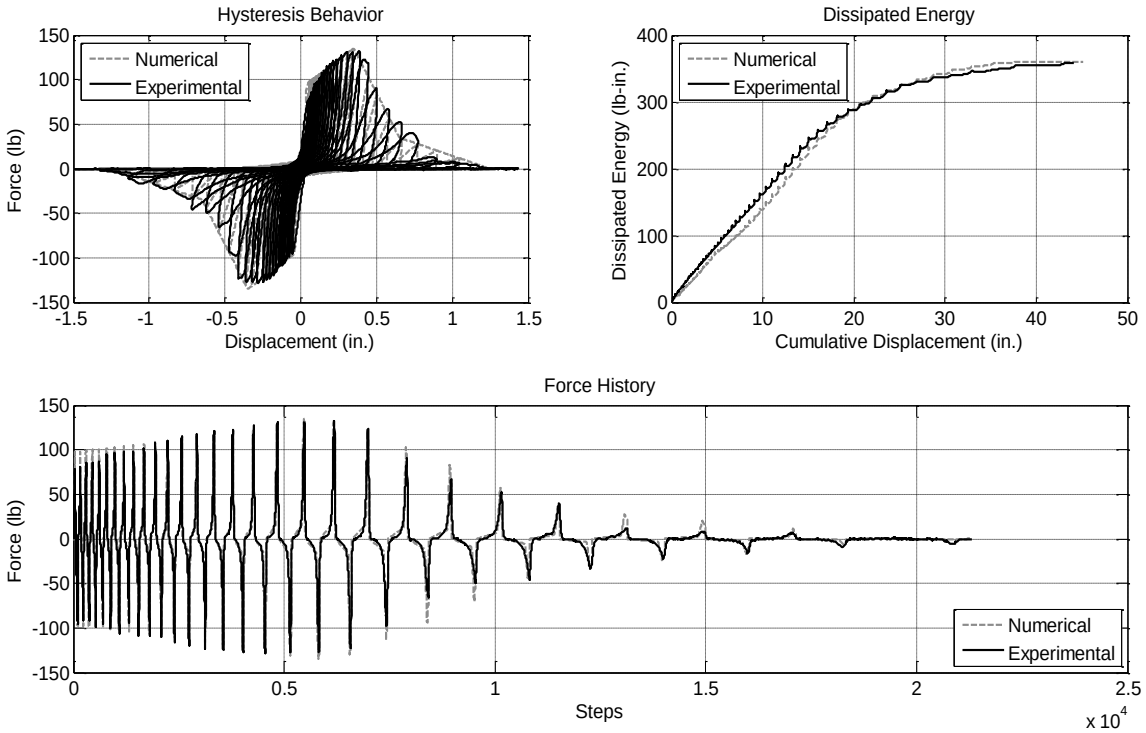

Figure 16. Numerical-Experimental Comparison of Third Specimen from series T19E15N6

Initially, for each specimen, all 39 parameters of "Pinching4" material are changed to find the best match between numerical results and experimental data based on the aforementioned criteria. However, it is noted that the values of pinching and unloading/re-loading parameters (23 out of 39 parameters) are similar for all specimens. In fact, the pinching and unloading/re-loading parameters are found to be independent of the specimen details. Therefore, constant values are assigned to these parameters (Table 4).

Table 4. Fixed "Pinching4" Parameters

Parameters										
rDispP **rDispN**	**rForceP** **rForceN**	**uForceP** **uForceN**	**gK1** **gK2**	**gK3** **gK4**	**gKLimit**	**gD1** **gD2**	**gD3** **gD4**	**gDLimit**	**gF**	**dam**
0.77 0.77	0.12 0.12	-0.01 -0.01	-0.7 -0.2	-0.7 -0.2	-0.2	-0.1 0	0 0.3	0	0	cycle

Subsequently, to generate a numerical model with a backbone curve comparable to the experimental results, backbone points are selected for each specimen individually. In specimens with sufficient edge distance, it is assumed that the backbone curves are symmetric. Thus, similar values (with different signs) are used in positive and negative displacements. For other specimens, the positive and negative points can be different to form an asymmetrical curve. Table 5 presents examples of the values used to define the backbone curves. Figure 17 illustrates the comparisons of sample numerical and experimental results for two GSCs.

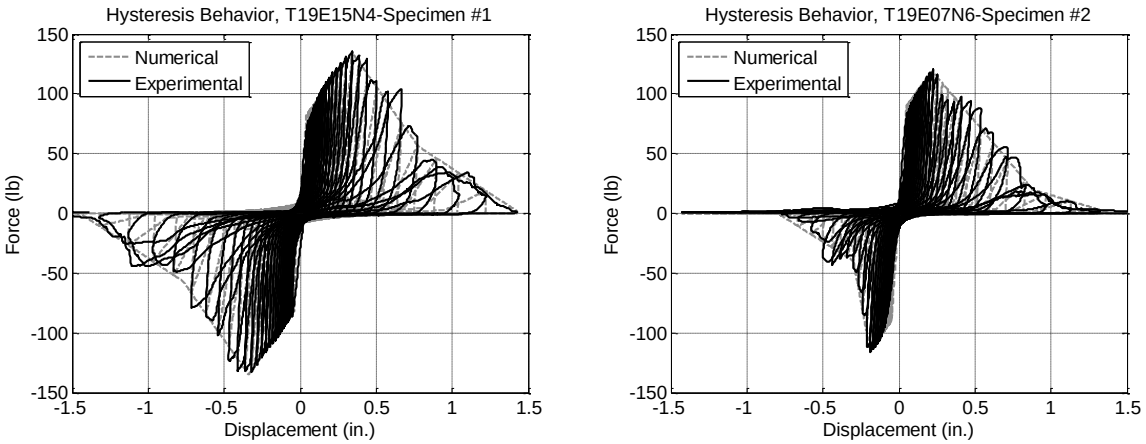

Figure 17. Sample Numerical-Experimental Hysteresis Comparisons of Two Different GSCs

Table 5. Sample Calibrated "Pinching4" Parameters

Component Name	**ePf1** **ePd1**	**ePf2** **ePd2**	**ePf3** **ePd3**	**ePf4** **ePd4**	**eNf1** **eNd1**	**eNf2** **eNd2**	**eNf3** **eNd3**	**eNf4** **eNd4**
Specimens with sufficient edge distances, ePfi (lb), ePdi (in.)								
Specimen #1 **T19E15N4**	82 0.04	135 0.34	57 0.77	0.01 1.45	-82 -0.04	-135 -0.34	-57 -0.77	-0.01 -1.45
Specimens with insufficient edge distances, ePfi (lb), ePdi (in.)								
Specimen #2 **T19E07N6**	90 0.05	115 0.19	40 0.30	0.01 0.80	-90 -0.05	-115 -0.19	-40 -0.30	-0.01 -0.80

Development of Generic Models

In the previous section, a numerical model was generated for each specimen using the "Pinching4" material in OpenSees (OpenSees 2014). The 16 backbone parameters (ePd_i, ePf_i, *etc)* of this model were optimized based on the experimental data of each specimen individually. Comparison of the different numerical models shows that the backbone curve parameters are highly dependent on the edge distance of the GSCs. In addition, there are minor discrepancies between the parameters of specimens with the same edge distances. Therefore, similar to the fragility analysis, the specimens are categorized based on the edge distance (see Table 2). For each group, one suite of material parameters is defined as the representative parameter, called the generic model, implementing the method proposed by Soroushian et al. (2014). The method uses the following assumptions to develop the generic model: 1) For each GSC group, a generic model is defined; 2) the four displacement points of the backbone curve (in each direction), ePd_1, ePd_2, ePd_3, ePd_4 (Fig. 15), are set to the median of the calibrated values corresponding to each of the four points of the backbone curve; 3) a linear interpolation is used to find the force corresponding to the previously mentioned displacements where the force values at the calibrated backbone curves are unavailable. The median of these force values for each set are used for (in each direction) ePf_1 ePf_2, ePf_3, and ePf_4 (Fig. 15) to define the backbone curve; 4) the remainder of the parameters (fixed parameters) are the same as those suggested in Table 4. The generic model parameters, obtained using the previously mentioned assumptions, are presented in Table 6. Figure 18 shows the comparison between the generic backbone curve of each group and all the calibrated backbone curves. Consider that these generic models only represent the GSCs with properties (gypsum type and thickness, stud and screw type, and edge distance) similar to what were tested in each group. For GSCs with other edge distances, the method in the next section can be used to calculate the model parameters. However, for GSCs with different gypsum, stud or screw types, new sets of model parameters need to be calibrated through additional experimental and numerical studies.

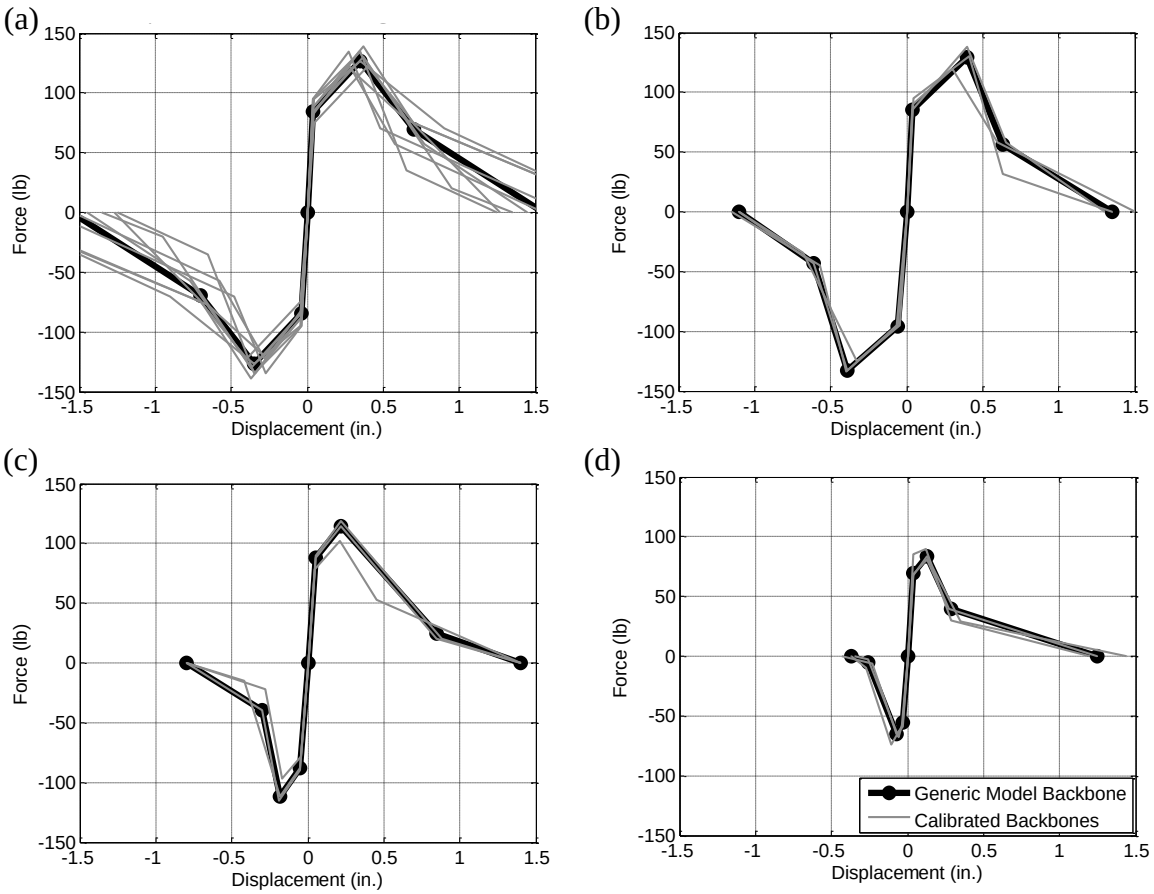

Figure 18. Generic Backbone Curve of Specimens with Edge Distances Equal to (a) 1.50 in., (b) 1.00 in., (c) 0.75 in., and (d) 0.50 in.

Table 6. "Pinching4" Parameters for Generic GSC Models

Group No. Edge Distance	ePf1 ePd1	ePf2 ePd2	ePf3 ePd3	ePf4 ePd4	eNf1 eNd1	eNf2 eNd2	eNf3 eNd3	eNf4 eNd4
Group #1	84.44	127	69.70	0.01	-84.44	-127	-69.70	-0.01
e = 1.5 in.	0.04	0.35	0.7	1.55	-0.04	-0.35	-0.7	-1.55
Group #2	85	129.04	56.07	0.01	-96	-132.84	-43	-0.01
e = 1.0 in.	0.04	0.4	0.63	1.35	-0.06	-0.39	-0.61	-1.1
Group #3	88	114	24.5	0.01	-88	-112	-40	-0.01
e = 0.75 in.	0.05	0.22	0.85	1.4	-0.05	-0.18	-0.3	-0.8
Group #4	69.25	84	39.19	0.01	-55	-65	-5.1	-0.01
e = 0.5 in.	0.037	0.13	0.29	1.25	-0.03	-0.07	-0.26	-0.37

Figure 19 indicates the comparison of the generic model using the aforementioned procedure with sample experimental data from each group. It should be noted that the inconsistency between the experimental results of the nine specimens from the first group is larger compared to the other groups. Therefore, a larger error in the hysteresis behavior is presented between the generic model and each of the experimental specimens.

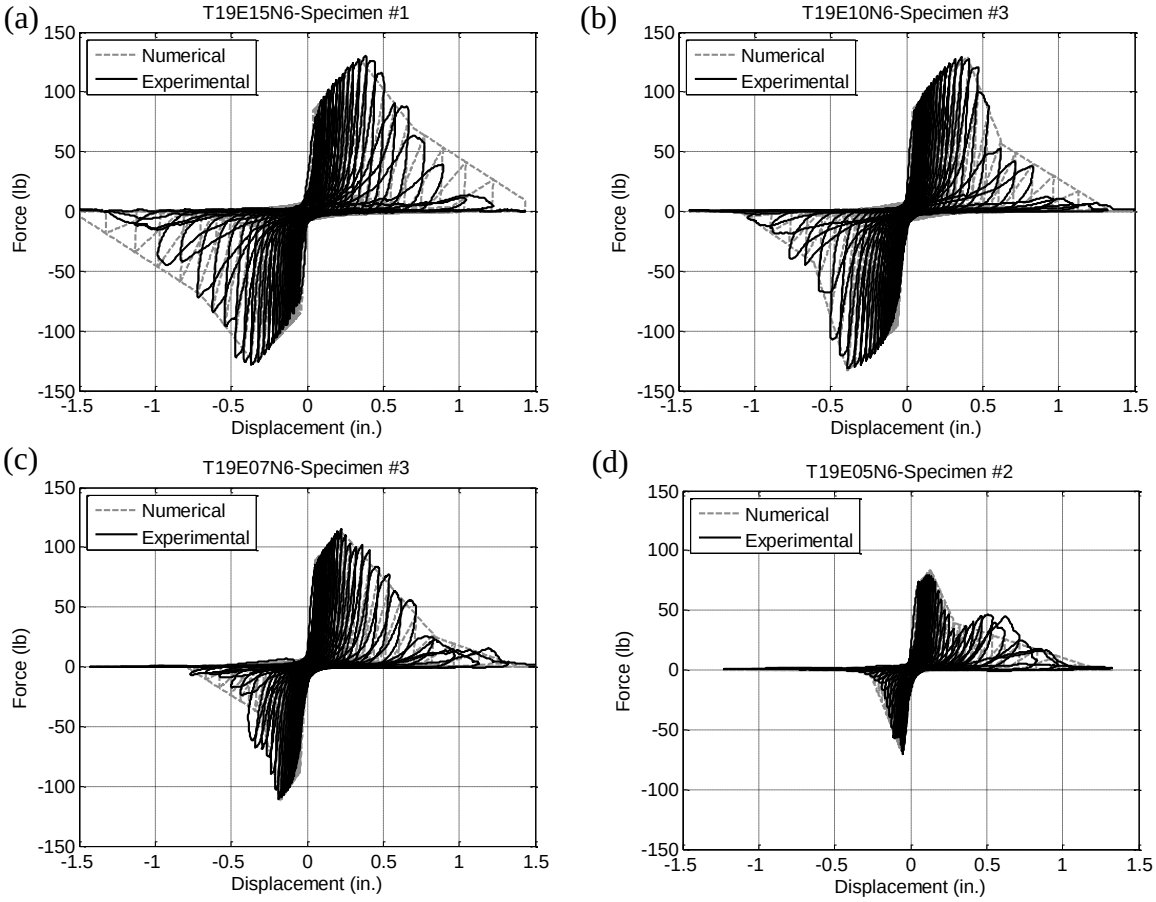

Figure 19. Sample Generic Numerical-Experimental Hysteresis Comparison of Different GSC Groups

Proposed Generic Models for Untested Edge Distances

In the previous section, the backbone curve parameters for GSCs with four specific edge distances were provided based on the experimental data. However, the edge distance in practice might be different from the tested values. Thus, a procedure is proposed to fill this gap in the experimental data and enable estimation of the backbone curve parameters of the generic hysteresis model for the missing edge distances. This methodology is explained in the following steps: 1) all backbone curve displacement and force values (ePd_i, ePf_i, eNf_i and eNf_i) of the four generic models are normalized with respect to the values of these parameters corresponding to the generic model with 1.5-in. edge distance (group #1 in Table 6); 2) all the edge distances are normalized with respect to 1.5 in.; 3)

for each backbone curve point, the normalized displacement and force values (nf_i and nd_i) are plotted against the normalized edge distances (e_n); 4) the least-square regression method is utilized to fit a line to the data (Fig. 20a); 5) the equations of these lines can be used to determine the normalized forces and displacements of GSCs with edge distances other than those that were tested in this study. The nf_i*s* and nd_i*s* are then multiplied by the backbone parameters of group #1 to find the final backbone curve points. Table 7 provides the equations for the backbone parameters obtained from the methodology mentioned above and the coefficient of determination (R^2) of the fitted lines. As an illustration, the calculated values for GSCs with 5/8-in. edge distance (e_n=0.625/1.5=0.42) and corresponding hysteresis model are presented in Table 8 and Figure 20b, respectively. For GSCs with edge distances larger than 1.5 in., parameters suggested for group #1 can be used to generate the numerical models (see the plateau in Fig. 20a).

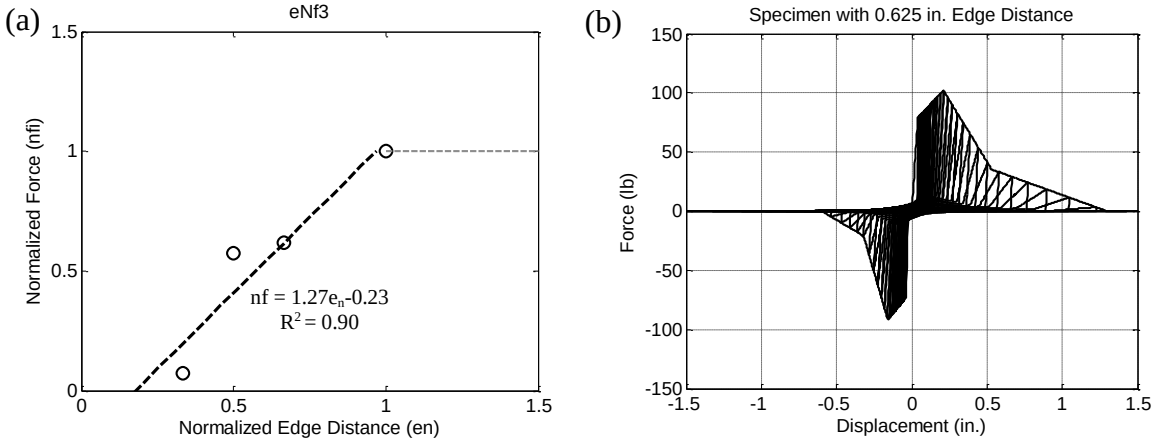

Figure 20. (a) Sample Normalized Force and Displacement Data and Fitted Lines, (b) Proposed Hysteresis Model for a Connection with 5/8 in. Edge Distance

Table 7. Equations for the Backbone Parameters for Various GSCs

Backbone Points	$nd_i = a \times e_n + b$ a	b	R^2	Backbone Points	$nf_i = a \times e_n + b$ a	b	R^2
ePd1	-0.04	1.07	0.01	**ePf1**	0.20	0.85	0.31
ePd2	0.97	0.18	0.62	**ePf2**	0.46	0.61	0.65
ePd3	0.58	0.52	0.23	**ePf3**	0.83	0.16	0.69
ePd4	0.26	0.73	0.84	**ePf4**	0.00	1.00	N/A
eNd1	0.26	0.96	0.05	**eNf1**	0.42	0.69	0.32
eNd2	1.23	-0.06	0.67	**eNf2**	0.65	0.45	0.59
eNd3	1.03	0.03	0.87	**eNf3**	1.27	-0.23	0.90
eNd4	1.11	-0.08	0.98	**eNf4**	0.00	1.00	N/A

Table 8. Backbone Parameters for a GSC with 5/8 in. Edge Distance

Backbone Points	ePf1 ePd1	ePf2 ePd2	ePf3 ePd3	ePf4 ePd4	eNf1 eNd1	eNf2 eNd2	eNf3 eNd3	eNf4 eNd4
nf_i	0.93	0.80	0.51	1.00	0.87	0.72	0.88	1.00
nd_i	1.05	0.59	0.76	0.84	1.07	0.46	0.46	0.39
Backbone Force	78.87	102.01	35.45	0.01	-73.16	-91.82	-21.15	-0.01
And Displacement	0.04	0.21	0.53	1.30	-0.04	-0.16	-0.32	-0.60

SUMMARY AND CONCLUSIONS

Monotonic and reverse cyclic tests were conducted on 18 gypsum-stud connections (GSCs) as part of a larger investigation of nonstructural partition wall behavior. The tests were designed to evaluate the displacement and strength capacities of screw connections between gypsum board and cold-formed steel-studs in nonstructural partition walls. The test data were used to develop capacity fragility curves for shear capacities of GSCs in terms of displacements.

The main observations and conclusions obtained from the experimental study are as follows:

- The shear capacity of the GSC derives primarily from the bearing resistance of gypsum board at the fastener locations.
- The distance of fasteners to the gypsum board edges dramatically affects the behavior of GSCs. Using edge distances smaller than 1.0 in. leads to significant drops in strength and displacement capacities of GSCs due to gypsum edge breakout. For GSCs with edge distances larger than 1 in., this effect is negligible. A 1.0-in. edge distance was determined to be a borderline value to avoid gypsum edge breakout in GSCs tested in this investigation. Specification of an edge distance of 1.5 in. is probably prudent to ensure good GSC performance.
- Damage states of GSCs include fastener tilting and fastener pulling through the gypsum board at small displacements, followed by complete failure of the connection at large displacements. For specimens with edge distances larger than 1.0 in., the failure mechanism is the detachment of the gypsum boards from the studs, while for other GSCs, the failure mechanism is the breakout of the gypsum edges.

- Specimens with different stud thicknesses perform consistently in terms of initial stiffness, maximum capacity and failure mechanisms. Nonetheless, the displacements corresponding to the complete failures are slightly larger for specimens with thicker studs.
- Fragility analysis indicate that GSCs with small edge distances are significantly more vulnerable than GSCs with large edge distances.
- A series of nonlinear GSC hinges are defined and validated for all specimens based on the experimental data. Subsequently, one suite of material parameters is proposed as the representative parameters for each group of specimens. These parameters define the generic models that represent the GSCs with the properties (gypsum type and thickness, stud and screw type, and edge distance) similar to what have been tested in each group. Consider that for GSCs with different gypsum, stud or screw types, new sets of model parameters need to be calibrated through additional experimental and numerical studies.

The experimental fragility curves developed in this study use GSC displacement as the engineering demand parameter. The hinge model of the GSCs could be utilized along with the numerical models of other wall components (such as track-to-stud connections and steel studs) to develop a comprehensive numerical model of a partition wall system. The partition wall model could then be subjected to realistic input motions (e.g. floor accelerations) to estimate the demand parameters on each component. These demand estimations could be used in conjunction with the capacity parameters (e.g. median and deviation) developed in this study (and similar studies for other partition wall components) to generate fragility curves for partition wall systems in terms of more global engineering demand parameters, such as floor accelerations and/or inter-story drifts.

ACKNOWLEDGMENTS

The current material is based upon work supported by the National Science Foundation under Grant No. 0721399. This Grand Challenge (GC) project to study the

seismic response of nonstructural systems is under the direction of M. Maragakis from the University of Nevada, Reno and Co-PIs: T. Hutchinson (UCSD), A. Filiatrault (UB), S. French (G. Tech), and B. Reitherman (CUREE). Any opinions, findings, conclusions, or recommendations expressed in the current document are those of the investigators and do not necessarily reflect the views of the sponsors. The input provided by the Practice Committee of the NEES Nonstructural Project, composed of W. Holmes (Chair), D. Allen, D. Alvarez, and R. Fleming; by the Advisory Board, composed of R. Bachman (Chair), S. Eder, R. Kirchner, E. Miranda, W. Petak, S. Rose and C. Tokas, has been crucial for the completion of this research. Assistance from M. Lattin of the University of Nevada, Reno material lab during the assembly and testing as well as support from Johnnie Stolz of Omboli Interior Inc. is appreciated.

REFERENCES

ASTM C840, 2013. *Standard Specification for Application and Finishing of Gypsum Board, ASTM International*, West Conshohocken, PA.

Bersofsky, A., 2004. *A Seismic Performance Evaluation of Gypsum Wallboard Partitions*, MS Thesis, Department of Structural Engineering, University of California, San Diego, La Jolla, CA.

Davies, D., Retamales, R., Mosqueda, G., and Filiatrault, A., 2011. *Experimental Seismic Evaluation, Model Parameterization, and Effects of Cold-Formed Steel-Framed Gypsum Partition Walls on The Seismic Performance of an Essential Facility, Technical Report MCEER-11-0005, MCEER*, State University of New York at Buffalo, New York.

Fiorino, L., Della Corte, G., Landolfo, R., 2006. *Experimental Tests on Typical Screw Connections for Cold-Formed Steel Housing, Engineering Structures*, 29, 8,1761-1773.

Fülöp, L. A., and Dubina, D., 2004. *Performance of Wall-Stud Cold-Formed Shear Panels under Monotonic and Cyclic Loading, Part I: Experimental research, Journal of Thin-Walled Structures.* 42, 321–338.

Miller, T.H. and Pekoz, T., 1994, *Behavior of Gypsum-Sheathed Cold-Formed Steel Wall Studs*. *ASCE Journal of Structural Engineering*, 120, 1644-1650.

Miranda, E., Mosqueda. G., Retamales, R., and Pekcan, G., 2012. *Performance of Nonstructural Components during the February 27, 2010 Chile Earthquake, Earthquake Spectra* 28, 453-471.

Open System for Earthquake Engineering Simulation (OpenSees) website, 2014: http://www.opensees.berkeley.edu . PEER, Berkeley: University of California

Peterman, K.D., Nakata, N., and Schafer, B.W., 2014. *Hysteretic Characterization of Cold-formed Steel Stud-to-Sheathing Connections, Journal of Construction Steel Research.* 101, 254–264.

Padilla-Llano, D. A., Moen, C. D., and Eatherton, M. R., 2014. *Cyclic Axial Response and Energy Dissipation of Cold-Formed Steel Framing Members, Journal of Thin-Walled Structures.* 78, 95–107.

Porter, K., R. Kennedy and R. Bachman., 2007. *Creating Fragility Functions for Performance-Based Earthquake Engineering, Earthquake Spectra* 23, 471-489.

Rahmanishamsi, E., Soroushian, S., and Maragakis, M., 2014. *System-Level Experiments on Ceiling/Piping/Partition Systems at UNR-NEES Site, Tenth U.S. National Conference on Earthquake Engineering*, Anchorage, AK.

Restrepo, J.I., and Bersofsky, A., 2010. *Performance Characteristics of Light Gage Steel Stud Partition Walls, Thin-Walled Structures,* 49, 317–324.

Restrepo, J.I., and Lang, A.F., 2011. *Study of Loading Protocol in Light-Gauge Stud Partition Wall, Earthquake Spectra,* 27, 1169–1185.

Retamales, R., Mosqueda, G., Filiatrault, A., and Reinhorn, A.M., 2008. *New Experimental Capabilities and Loading Protocols for Seismic Qualification and Fragility Assessment of Nonstructural Components, Technical Report MCEER-08-0026, MCEER*, State University of New York at Buffalo, New York.

Retamales, R., Mosqueda, G., Filiatrault, A., and Reinhorn, A.M., 2011. *Testing protocol for experimental seismic qualification of distributed nonstructural systems, Earthquake Spectra*, 27(3):835-856.

Retamales, R., Davies, R., Mosqueda, and G., Filiatrault, A., 2013. *Experimental Seismic Fragility of Cold-Formed Steel Framed Gypsum Partition Walls, ASCE Journal of Structural Engineering*, 139, 1285-1293.

Schafer, B.W., Hiriyur, B., 2002. *Analysis of Sheathed Cold-Formed Steel Wall Studs, Sixteen International Specialty Conference on Cold-Formed Steel Structures*, Orlando, Florida, USA.

Soroushian, S., Zaghi, E., Maragakis, M., Tian, T., and Filiatrault, A., 2013. *Analytical Seismic Fragility Analyses of Fire Sprinkler Piping Systems with Threaded Joints. Earthquake Spectra,* In-Press.

Soroushian, S., Maragakis, M., and Jenkins, C., 2014. *Axial Capacity Evaluation of Typical Suspended Ceiling Joints. Earthquake Spectra.* (in review)

Taghavi, S. and Miranda, E., 2003. *Response Assessment of Nonstructural Building Elements, PEER Report 2003/05*, Pacific Earthquake Engineering Research Center (PEER), University of California, Berkeley, CA.

Tsuru, J., and Murakami, S., 2011. *Summary of the Field Survey and Research on "The 2011 off the Pacific coast of Tohoku Earthquake" (the Great East Japan Earthquake)*, *Technical Note of NILIM No.647 and BRI Research Paper No.150*, Japan.

Vieira, L.C.M., and Schafer, B.W. 2012. *Lateral Stiffness and Strength of Sheathing Braced Cold-Formed Steel Stud walls, Engineering Structures*, 37, 205-213.

Wood, R.L. and Hutchinson, T.C. 2012. *A Numerical Model for Capturing the In-Plane Seismic Response of Interior Metal Stud Partition Walls. Technical Report MCEER-12-0007, MCEER*, State University of New York at Buffalo, New York.

Chapter 4

Capacity Evaluation of Typical Stud-Track Screw Connections in Nonstructural Walls

ESMAEEL RAHMANISHAMSI[1], SIAVASH SOROUSHIAN[1], and EMMANUEL "MANOS" MARAGAKIS[1]

[1]Department of Civil and Environmental Engineering, University of Nevada, Reno, Reno, NV

Please note that this chapter is a self-contained paper accepted for publication in the Journal of Earthquake Engineering where the word 'this paper/study' refers to the chapter itself.

ABSTRACT

A series of component-level experiments have been conducted aiming to evaluate the force and displacement capacities of typical stud-track screw connections (STCs) in steel-framed partition walls. The variables considered in these experiments included screw-edge distances, loading protocols (monotonic or cyclic), and stud and track thicknesses. The experimental data was then utilized to develop different capacity fragility curves for STCs in terms of displacements. A series of analytical STC hinge models were also proposed and validated using this data. The hinge models can be adopted in future studies to develop a comprehensive analytical model for a typical partition wall assembly.

Keywords: Nonstructural Systems, Partition Walls, Experimental Study, Numerical Model, Capacity Fragility, Cold-Formed Steel.

1. Introduction

Recent earthquakes, including the 2006 Hawaii Earthquake [RMS, 2006], 2010 Chile earthquake [Miranda *et al.*, 2012], 2010 Darfield earthquake [Dhakal, 2010], 2011 Christchurch earthquake [Gould and Marshal, 2012], and 2011 Tohoku Earthquake [Mizutani *et al.*, 2012], have shown widespread damage to the nonstructural systems. The damage resulted in major disruption to the normal functioning of critical facilities and services and also contributed toward large economic losses [Miranda *et al.*, 2012; Retamales *et al.*, 2013]. One of the widely used nonstructural systems, which sustained extensive damage in the recent earthquakes, is cold-formed, steel-framed gypsum partition walls [Restrepo and Bersofsky, 2010; Rahmanishamsi *et al.*, 2014b]. Damage to these walls has usually been triggered at very low seismic demand and has led to the loss of property and interruption to post-earthquake building operations [Wood and Hutchinson, 2014].

In order to evaluate the seismic performance of steel-framed gypsum partition walls, a number of experimental and analytical studies have been conducted in recent years [Bersofsky, 2004; Fülöp and Dubina, 2004; Retamales *et al.*, 2008; Restrepo and Bersofsky, 2010; Davies *et al.*, 2011; Restrepo and Lang, 2011; Soroushian *et al.*, 2012; Retamales *et al.*, 2013; Wood and Hutchinson, 2014; Rahmanishamsi *et al.*, 2014a]. These studies investigated the damage mechanisms and hysteresis behaviors of steel-framed gypsum partition walls with different configurations. One of the observed damage mechanisms during the experimental studies was damage to the screw connections between the steel studs and the tracks. Soroushian *et al.* [2012] and Rahmanishamsi *et al.* [2014a] reported popping out of the screws and buckling of the track flanges at the

locations of the stud-track connections (STCs). In addition, the study by Retamales *et al.* [2013] indicated that the performance of partition walls was affected by the characteristics of the STCs. Therefore, the behavior of the STCs is of interest to understand their role in the performance of steel-stud gypsum partition walls.

The design and behavior of screw connections between cold-formed steel studs and tracks have been investigated in the early work of Pekoz [1990] as well as in more recent works by Zwick and LaBoube [2002] and Babalola and LaBoube [2004]. The researchers evaluated the shear and tensile capacity of the screw connections. Moreover, the out-of-plane performance of the STCs, in walls subjected to the wind load, was studied by Bolte and LaBoube [2004] and Lewis et al. [2008]. All of these studies were limited to the screw connections in the load-bearing walls. The steel stud and track profiles used in load-bearing walls are different from those used in nonstructural partition walls. Since the nonstructural partition walls are not part of the structural load-carrying system, thinner stud and tracks with smaller web depth are usually used in their construction [Rahmanishamsi, 2014b]. As such, the performance of STCs in nonstructural walls could be different than the load-bearing walls. No experimental study has been conducted specifically in order to characterize the behavior of STCs in nonstructural partition walls.

In an effort to address the missing information about the damage mechanisms and force-displacement characteristics of STCs in nonstructural partition walls, a series of monotonic and cyclic experiments have been performed at University of Nevada, Reno. The results of these experiments, along with the supplemental analytical works, are presented in this paper. The paper begins with a brief review of the test setup and

experimental program, followed by a summary of the observed damage mechanisms. The force-displacement responses of specimens are then presented and compared to evaluate the effect of different parameters, including loading rate, stud/track thickness, and fastener-edge distance. The test data is also used to generate capacity fragility curves for stud-track connections (STCs) in terms of displacements. Finally, a series of analytical hinge models are proposed that represent the hysteresis behavior of STCs. These models are validated utilizing the component experimental data.

2. Description of Test Specimens

2.1. Test Setup

All specimens were constructed from either 362S125-19 or 362S125-30 studs along with tracks of similar thickness (362T125-19 or 362T125-30). These products were selected from the common construction details for commercial and institutional buildings [Retamales *et al.*, 2013]. Figures 1a and 1b show a sample specimen and the testing machine. The specimen consisted of an 203-mm-long steel stud, attached to an 457-mm-long steel track using two #8×13-mm (1/2-in.) screws. For specimens with 0.48-mm-(0.019-in.) thick stud/track, sharp-point type screws were used and for other specimens self-drilling type screws were used. The distance from the center of the screws to the edge of the track flanges (track-edge distance in Fig. 1c) varied from 6 mm (1/4 in.) to 19 mm (3/4 in.) in different specimens. The gap between the end of the stud and the web of the track (gap in Fig. 1c) was also changed from 6 mm (1/4 in.) to 13 mm (1/2 in.). These values were selected based on the design guidelines for nonstructural walls [] and also previous studies [Retamales *et al.*, 2013]. A clamping system was designed for the setup

in order to prevent the bending or buckling of the stud/track-web and limit the deformation to the STCs on the stud/track flanges. For the track, the clamping system consisted of two steel plates (190×76×6 mm) and two steel angles (38×38×6 mm). The gap between the two clamping plates (Fig. 1b) allowed the stud to move towards the track web without touching the plates. The steel angles were bolted to a T-shaped steel plate, which was fixed to the stationary grip (bottom grip) of an Instron 5985 machine (Figs. 1a and 1b). The stud was "sandwiched" between two 6-mm-thick steel plates, bolted together at four locations. One of these plates was attached to the movable grip (top grip) of the machine. The machine applied upward and downward displacements to the specimens through the movable grip and measured the reaction using the axial load cell.

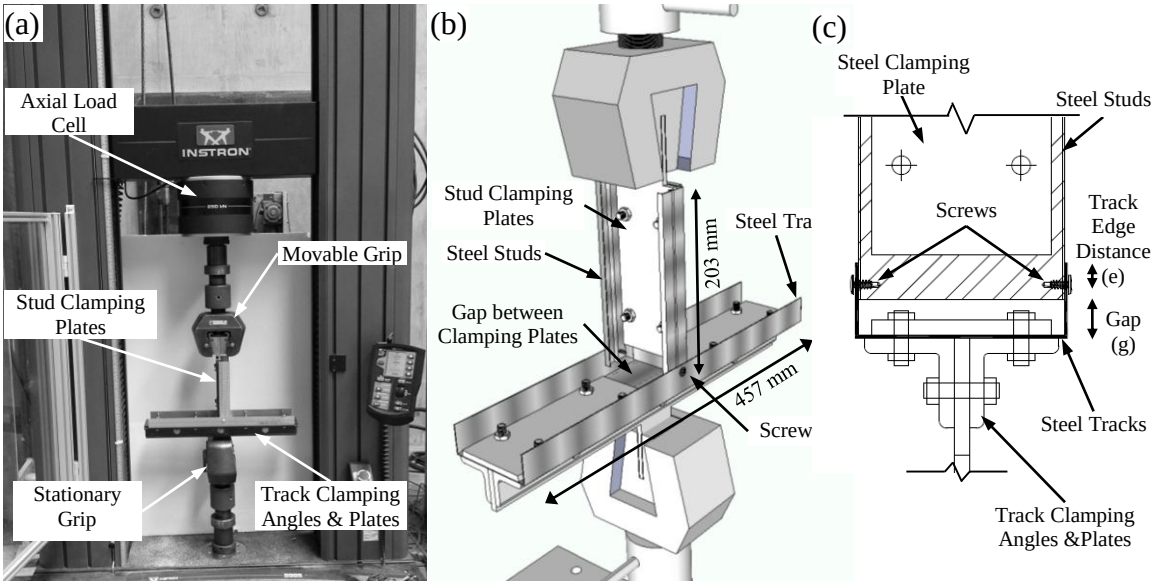

Figure 1. (a) and (b) Specimen and Test Machine, (c) Screw-Edge Distance and Stud-Track Gap

2.2. Experimental Program

The experimental program consisted of 33 specimens, categorized in eight series (Table 1). The series varied in terms of edge distance, gap dimension, loading rate, and

stud/track thickness. The label of each series indicates the specimen thickness (T48: 0.48-mm-thick stud and track), gap dimension (G13: 13-mm gap), and track-edge distance (E10: 10-mm track-edge distance). All series, except the last two series, included at least one monotonic test and three cyclic tests. The first series was tested adopting three different values for loading rates: 0.04, 0.21, and 0.42 mm/sec. However, a constant rate (0.21 mm/sec) was used for the other series since the STC response was found to be independent of the loading rate. The response and failure mechanisms of each series will be discussed in detail in subsequent sections.

Table 1. Test Program Matrix

Series Label	Loading Protocol	Loading Direction	Loading Rate, υ (mm/sec)	Stud/Track Thickness (mm)	Gap (mm)	Edge Distance (mm)		Number of Specimens
						Track	Stud	
T48G13E10	Monotonic	Tension	0.04	0.48	13	10	10	1
	Monotonic	Compressio	0.04	0.48	13	10	10	1
	Monotonic	Tension	0.42	0.48	13	10	10	1
	Monotonic	Compressio	0.42	0.48	13	10	10	1
	Monotonic	Tension	0.21	0.48	13	10	10	1
	Monotonic	Compressio	0.21	0.48	13	10	10	1
	Cyclic	-	0.21	0.48	13	10	10	3
T48G06E06	Monotonic	Tension	0.21	0.48	6	6	19	1
	Cyclic	-	0.21	0.48	6	6	19	3
T48G06E13	Monotonic	Tension	0.21	0.48	6	13	13	1
	Monotonic	Compressio	0.21	0.48	6	13	13	1
	Cyclic	-	0.21	0.48	6	13	13	3
T48G06E19	Monotonic	Tension	0.21	0.48	6	19	6	1
	Cyclic	-	0.21	0.48	6	19	6	3
T76G13E10	Monotonic	Tension	0.21	0.76	13	10	10	1
	Cyclic	-	0.21	0.76	13	10	10	3
T76G06E13	Monotonic	Tension	0.21	0.76	6	13	13	1
	Monotonic	Compressio	0.21	0.76	6	13	13	1
	Cyclic	-	0.21	0.76	6	13	13	3
T76G06E06	Cyclic	-	0.21	0.76	6	6	19	1
T76G06E19	Cyclic	-	0.21	0.76	6	19	6	1

2.3. Loading Protocol

For each series at least one cyclic test was performed using the loading rate of 0.21 mm/sec. Additional monotonic tests were also conducted in all series, except the last two

series, in order to study the effect of cumulative cyclic damage on the ultimate capacity of STCs. In these tests, the specimens were subjected to progressive displacements, without unloading phases as shown in Fig. 2a [Fiorino *et al.*, 2007]. For the cyclic tests, a loading protocol proposed by Retamales *et al.* [2008, 2011] was used. This protocol was developed specifically for evaluating the capacity fragility of primarily drift-sensitive nonstructural components. Figure 2b shows the displacement history that was generated based on the aforementioned loading protocol. In this figure, negative and positive displacements represent the downward and upward movement of the top grip, respectively.

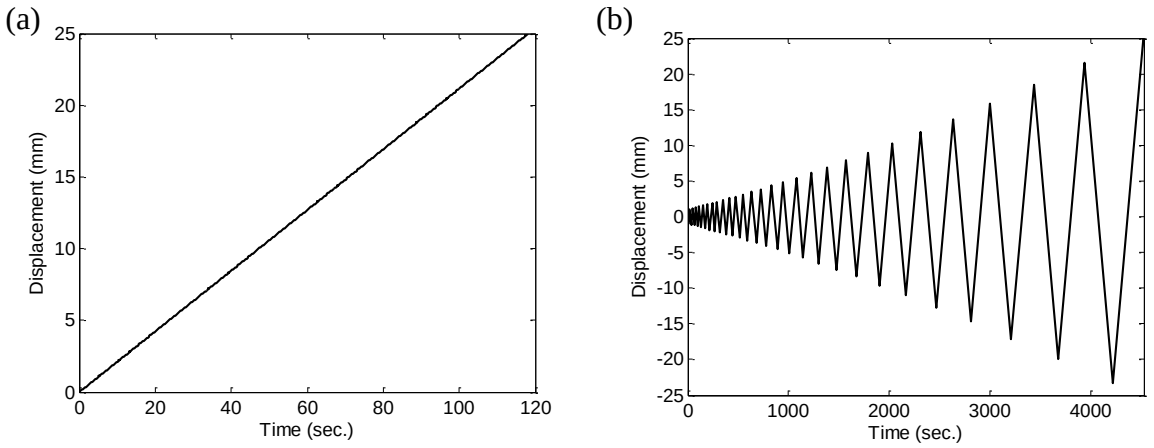

Figure 2. Loading Protocol for: (a) Monotonic, (b) Cyclic Tests

In addition, a modified cyclic displacement history (Fig. 3b) was developed, in which the negative (downward) displacement of movable grip was limited to the available gap (6 mm). The objective was to avoid the interaction between the stud and track web (Fig. 3a) in the very first cycles of the loading. Note that this interaction and the consequent damage was beyond the scope of the current test program. The modified displacement

history was used to test the specimens with a 6-mm gap, while the primary displacement history (Fig. 2b) was utilized to test the rest of the specimens.

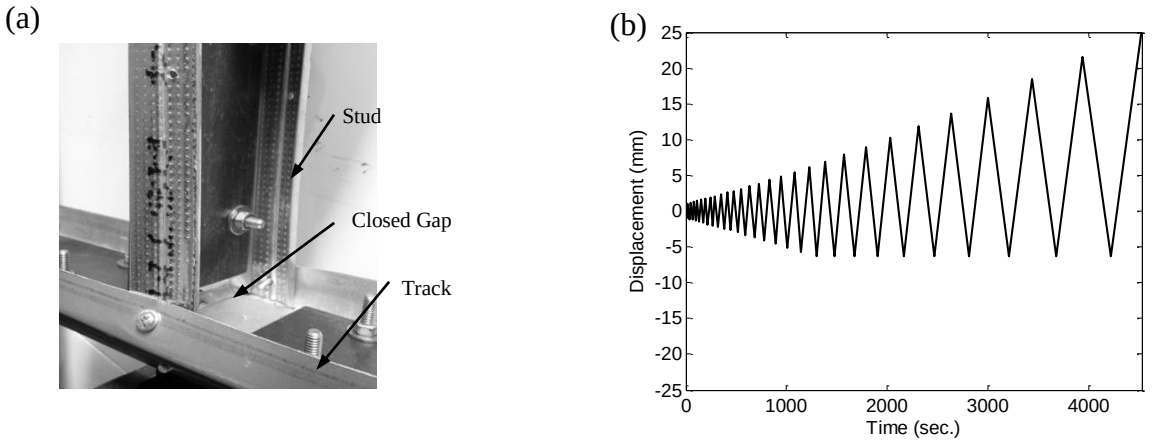

Figure 3. (a) Stud-Track Interaction, (b) Modified Loading Protocol for Cyclic Tests

3. Experimental Results

3.1. Individual STC Force and Displacement

Figure 4 illustrates the free-body diagram of a specimen while performing an upward monotonic test. Assuming that the total force (F in Fig. 4a and 4b) was equally distributed between two screws, the individual STC force was calculated as force = F / 2. Moreover, the displacements of the two screws were considered to be identical and equal to the displacement of the movable grip.

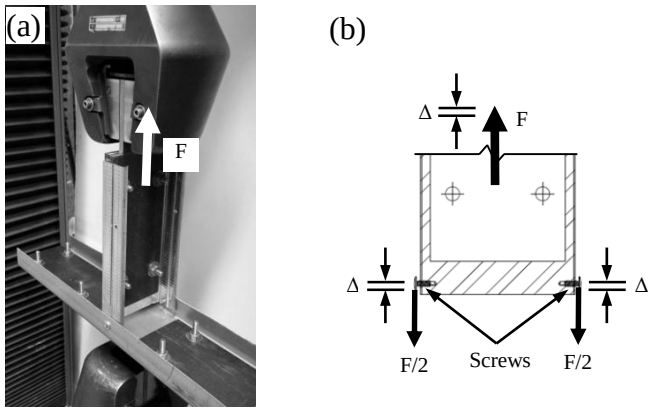

Figure 4. (a) Applied Force and b) Free Body Diagram

3.2. Damage Mechanisms

Based on the experimental observations, the STC damage mechanisms can be categorized as follows: (*T*) tilting of screws, (*E*) enlarging the holes due to excessive bearing stress, (*P*) popping out of screws, (*B*) local buckling of track flanges in compression, (*ST*) shear tearing-out of track flanges, and (*SS*) shear tearing-out of stud flanges in tension. Figures 5 and 6 depict the basic behavior of a fastener in a STC under increasing upward displacement of the stud flange. Applying the displacement, the screw tilted and pushed the stud and track flanges (Fig. 5b), which developed bearing stresses in these components. When the bearing stress was larger than the bearing capacity of the stud and track flanges, the screw hole deformed and enlarged (Fig. 5c and 6b). Subsequently, if the stud- and track-edge distances were large enough, the screw popped out from the connection (Fig. 5d and 6c). Otherwise, the edge of the track or stud flange tore out (Fig. 5e, 5f, 6d, and 6e). The last three damage descriptions (*B*, *ST*, and *SS*) corresponded to the complete failure of STCs.

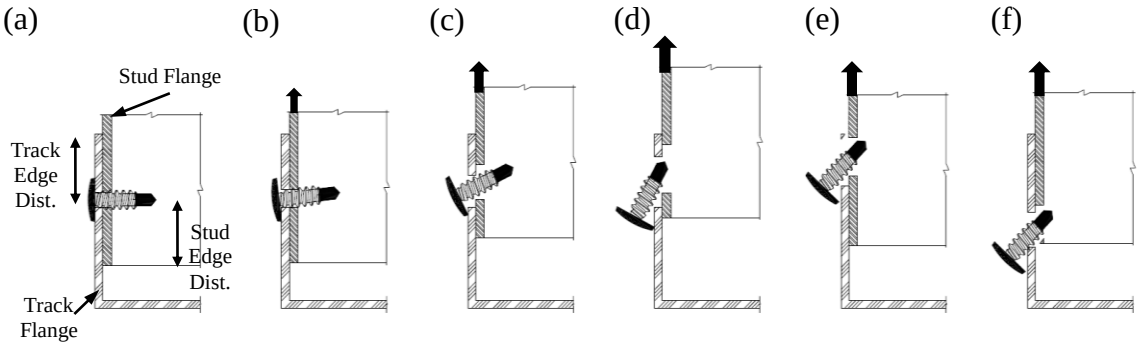

Figure 5. Damage Mechanisms of STCs in Tension: (a) Initial Condition, (b) Tilting, (c) Enlarging the Hole, (d) Popping out, (e) Tearing-out of the Track Flange, and (f) Tearing-out of the Stud Flange

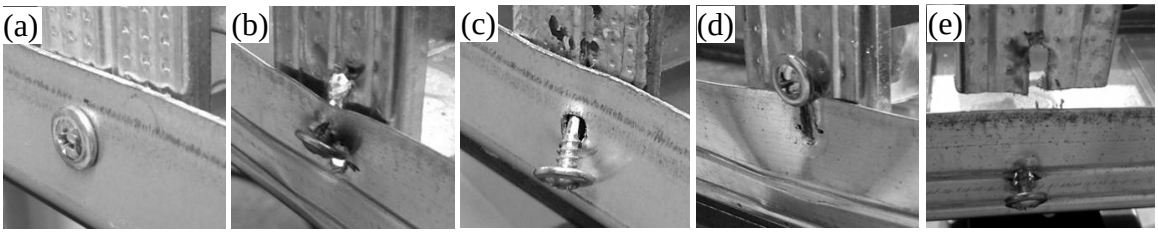

Figure 6. Damage Observations of STCs in Tension: (a) Initial Condition, (b) Enlarging the Hole, (c) Popping out, (d) Tearing-out of the Track Flange, and (e) Tearing-out of the Stud Flange

The basic behavior and the observed damage of a typical STC under increasing downward displacement of the stud are shown in Figure 7. In this case, the track flange was deformed and locally buckled after the screw tilted. In larger displacements, the gap between the end of the stud and track web was closed and the stud pushed against the track web. The stud-track interaction resulted in a significant change in the force-displacement curve (Fig. 8b). Figures 8 and 9 present typical experimental responses in monotonic and cyclic tests and displacement zones corresponding to each damage description.

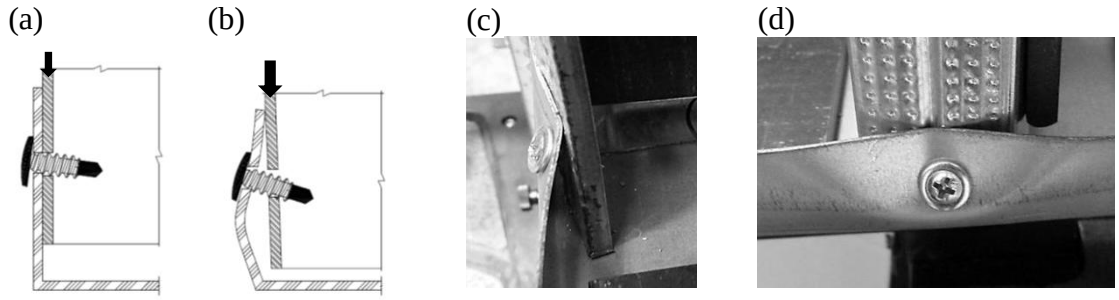

Figure 7. Damage Mechanisms of STCs in Compression: (a) Tilting, (b) Track Flange Buckling; (c) and (d) Close Views of Local Buckling of the Track Flange in Compression

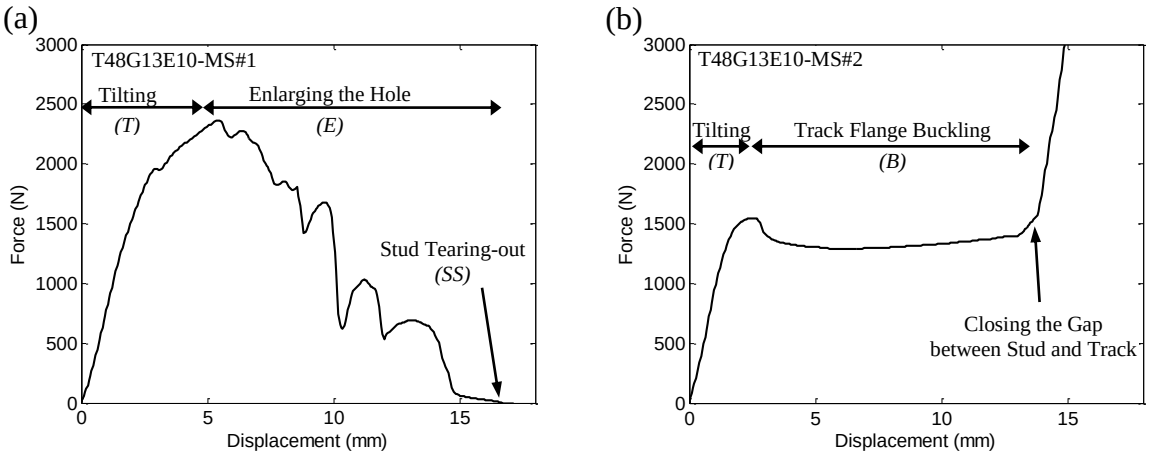

Figure 8. Typical Experimental responses for: (a) Upward and (b) Downward Monotonic Test

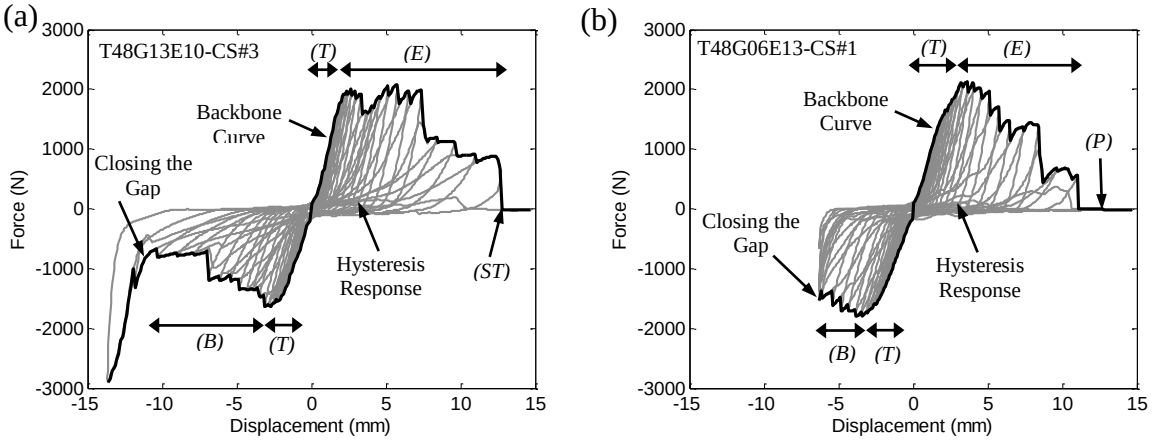

Figure 9. Typical Experimental responses for Cyclic Tests with: (a) Primary and (b) Modified Loading Protocol

3.3. Effect of Loa ding Rate

To assess the impact of the loading rate on the experimental results, monotonic tests of the first series of specimens (T48G13E10) were carried out adopting three different values: 0.04, 0.21, and 0.42 mm/sec. Figures 10a and 10b compare the force-displacement responses and the maximum force ratios in monotonic tests with different rates. The maximum force ratio was calculated by dividing the maximum force of each monotonic test by the maximum force of the monotonic test with a loading rate of 0.04 mm/sec. For downward tests, the maximum forces were determined neglecting the stud-track interaction effect. The results demonstrated a relatively small variation with an unclear trend as the loading rate was increased. Therefore, the STC response was considered to be insensitive to the loading rate and a constant loading rate of 0.21 mm/sec was used for the rest of the experiments.

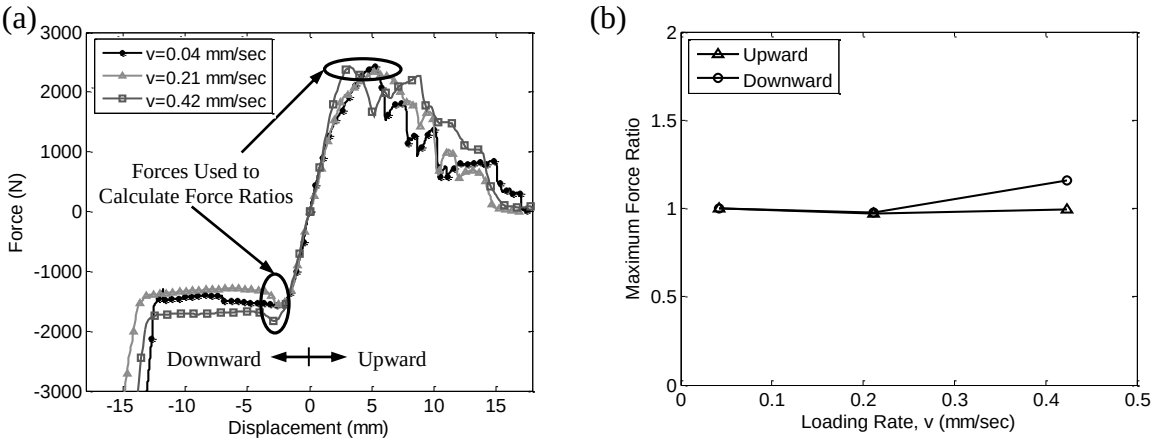

Figure 10. Effect of Loading Rate (v, mm/sec) on: (a) Monotonic Force-Displacement Response, (b) Maximum Force Ratio

3.4. Force-Displacement Responses of Specimens with 0.48-mm Thick Studs/Tracks

The force-displacement responses of specimens with 0.48-mm-thick studs/tracks are discussed in the following section. The backbone curves of cyclic tests, the median of the backbone curves, and the monotonic response of an individual STC in specimen series T48G13E10 and T48G06E13 are provided in Fig. 11. The monotonic and cyclic test results were comparable in terms of initial stiffness and maximum capacity. However, the complete failure of STCs was usually triggered in lower displacements during the cyclic tests in comparison with the monotonic tests. In addition, in the monotonic tests, the force reached a plateau in negative displacements (after the peak force), while in the cyclic tests the force descended. These differences were mainly due to the effect of cumulative damage on the responses of the cyclic tests.

Figure 12 presents the median backbone curves of the specimen series with 0.48-mm-thick studs/tracks: T48G13E10, T48G06E06, T48G06E13, and T48G06E19. As mentioned before, when the sufficient edge distance was provided for the track and stud, the failure mode of STCs was the popping out of the screws (*P*). T48G06E13 was the only series with this type of failure mode for the STCs. In fact, 13 mm was found as the minimum required edge distance to avoid edge tearing-out of the stud and track. In specimen series T48G06E06, tearing-out of the track flange (*TS*) was the dominant failure mode, while in specimen series T48G06E19 it was tearing-out of the stud flange (*SS*). A combination of damage mechanisms *P* and *SS* were observed in the specimen series T48G13E10. Comparisons of the median backbone curves (Fig. 12) show that providing the sufficient edge distance could increase the failure displacement (the

displacement corresponding to the complete failure) of STCs. However, there is no clear effect on the maximum force capacity of the connection.

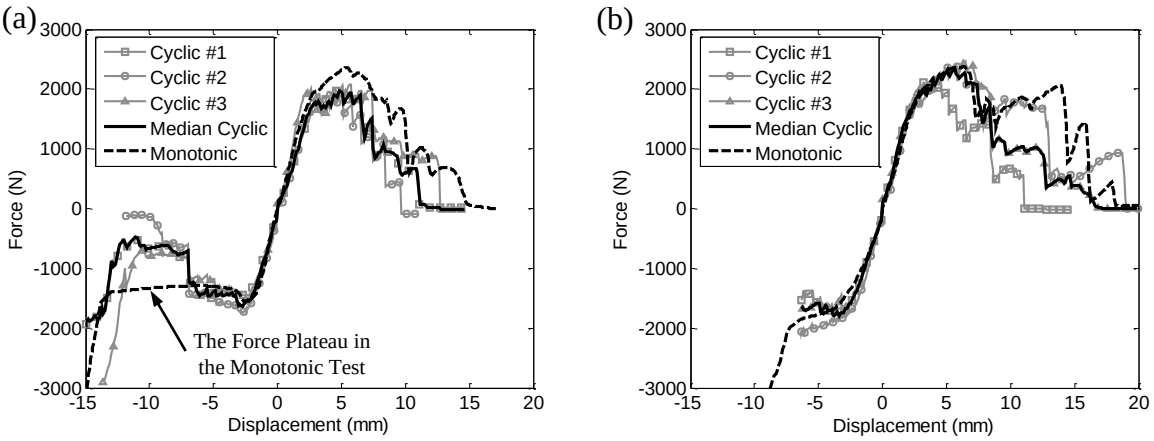

Figure 11. Monotonic Test Response and Cyclic Test Backbone Curves of an individual STC for Specimen Series (a) T48G13E10, (b) T48G06E13

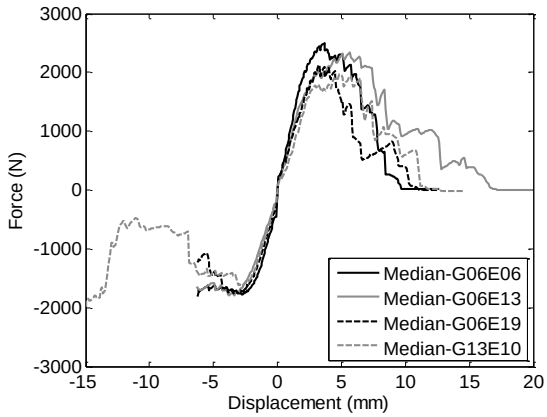

Figure 12. Effect of Screw-Edge Distance

3.5. Force-Displacement Responses of Specimens with 0.76-mm-Thick Studs/Tracks

The last four series of experiments (T76G13E10, T76G06E13, T76G06E06, and T76G06E19) were designed to assess the effect of stud/track thickness on the performance of STCs. The comparisons of the backbone curves of these series (Fig. 13a) suggested that the STC response in 0.76-mm-thick specimens was independent of the

edge distance. This could be due to the fact that in all specimens the failure mechanism was popping out of the screws (*P*), which was not a function of edge distance. No tearing-out of stud or track was observed. Fig. 13a also compares the monotonic and cyclic force-displacement curves. The results were consistent in terms of initial stiffness, but varied in terms of ultimate force and displacement capacities. The cumulative cyclic damage resulted in the capacity reductions during the cyclic tests.

Figure 13b highlights the effect of using 0.76-mm-thick studs/tracks on the response of STCs. Thicker stud/tracks limited the tilting of the screw and led to a higher initial stiffness in the force-displacement curve. The force associated with buckling of the track flange was also larger in these specimens. However, the failure displacement was smaller, which was a result of using self-drilling screws. The threaded length of these screws was shorter than the sharp-point screws, used for 0.48-mm-thick specimens. Therefore, the screws lost their engagement in smaller displacement and popped out from the track.

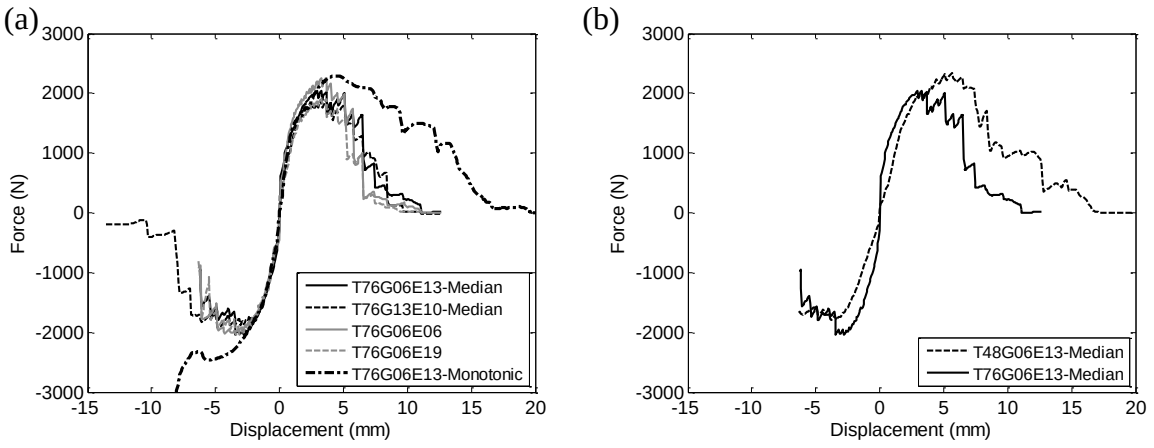

Figure 13. Effect of (a) Screw-Edge Distance, (b) Stud Thickness

4. Capacity Fragility Analysis

Capacity fragility curves are conditional probability statements of a component's (or system's) vulnerability as a function of an engineering demand parameter (*EDP*). They present the probability that the *EDP* in the component exceeds a certain level of capacity or damage states (*DSs*). The steps in generating the fragility curves can be summarized as follows: 1) choose a proper fragility formulation, 2) select appropriate engineering demand parameters, 3) determine capacity (damage state) estimates, and 4) develop fragility curves [Soroushian *et al.*, 2014].

Several methodologies for generating capacity fragility curves have been developed over the years. In the current study, the framework proposed by Porter *et al.* [method *A* in Porter *et al.*, 2007] was utilized to assess the vulnerability of STCs. The method is based on the experimental studies and can be used where all specimens reach all *DSs* at observed values of *EDP*. According to Porter *et al.*: $F_{dm}(edp)$ denotes the fragility function for the damage state *dm*, defined as the probability that the component reaches or exceeds damage state *dm*, given a particular *EDP* value (Eq. 1), and idealized by a lognormal distribution (Eq. 2):

$$F_{dm}(edp) \equiv P[DM \geq dm | EDP = edp] \tag{2}$$

$$F_{dm}(edp) = \Phi\left(\frac{ln(edp/x_m)}{\beta}\right) \tag{3}$$

where Φ denotes the standard normal (Gaussian) cumulative distribution function, x_m indicates the median value of the distribution, and β represents the logarithmic standard deviation [Porter *et al.*, 2007].

The engineering demand parameter (*EDP*) is the input in the fragility analysis and should be chosen to be most closely related to the failure probability of the specimen. In method A, the *EDP*s are the values at which the damage states occurred [Porter *et al.*, 2007]. Since the cyclic performance of a STC was mainly governed by the displacement of the fastener, displacement was considered as the only *EDP*.

The damage states of STCs were defined based on the different damage mechanisms (*T*, *E*, and *P* or *ST*/*TT*) observed during the experiments. The first damage state (*DS1*) represents tilting of the screws or initiation of track flange buckling, and the second damage state (*DS2*) denotes the enlarging of the holes. In specimens with 0.48-mm-thick studs/tracks and insufficient edge distances (edge distances smaller than 13 mm), the third damage state (*DS3*) corresponded to the tearing-out of stud or tracks. Popping out of the screws was considered as the third damage states in the other specimens.

Figure 14 demonstrates the points correlated with the three damage states on two representative backbone curves. *DS1* presented the initiation of nonlinearity in a STC, while *DS2* was set to the local maximum point on the backbone curve. The force capacity of the STC was degraded after *DS2*. The displacement corresponding to the complete failure of the STC was considered as *DS3*. The extensive damage states (*DS2* and *DS3*) were only observed when the stud moved upward (in the positive displacement).

The individual damage states are characterized by representative values for the median, x_m, and dispersion, β, for the component damage state distributions as follows [Porter *et al.*, 2007; Soroushian *et al.*, 2014]:

$$x_m = e^{\frac{1}{N}\sum_{i=1}^{N} ln(x_i)} \quad (4)$$

$$\beta = \sqrt{\frac{1}{N-1}\sum_{i=1}^{N}\left[\ln\left(\frac{x_i}{x_m}\right)\right]^2} \quad (5)$$

where x_i denotes the i-th measured displacement corresponding to specific damage observation (*EDPs*) and N is the number of cyclic tests conducted for each group of specimens. To generate the fragility curves, specimens were grouped based on the stud/track thickness and edge distance as follows: 1) specimens with 0.48-mm-thick stud/track and stud-or track-edge distance smaller than 13 mm, including specimen series T48G13E10, T48G06E06, and T48G06E19; 2) specimens with 0.48-mm-thick stud/track and 13-mm stud- and track-edge distance (T48G13E13); and 3) specimens with 0.76-mm-thick stud/track including T76G13E10, T76G06E06, T76G13E13, and T48G06E19. Therefore, N was equal to 9 for the first group, 3 for the second group and 8 for the last group. Tables 2 and 3 summarize the EDPs (x_i), x_m, and logarithmic standard deviation obtained for each STC group and damage level.

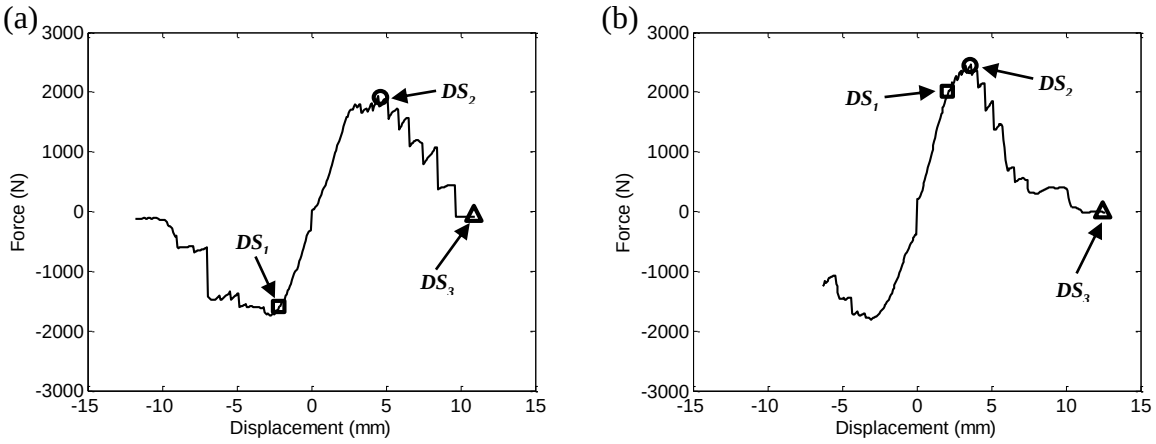

Figure 14. Examples of Damage State Definitions; (a) Specimens Tested with Primary Loading Protocol (b) Specimens Tested with Modified Loading Protocol

Table 3. Engineering Demand Parameters

Group No.	Specimen Name	Disp. (mm)		
		DS1	DS2	DS3
#1	T48G13E10-S#1	2.3	4.5	11.8
	T48G13E10-S#2	2.1	4.5	9.7
	T48G13E10-S#3	1.9	5.8	12.8
	T48G06E06-S#1	2	3.7	11.2
	T48G06E06-S#2	1.7	4	9.7
	T48G06E06-S#3	1.6	3.6	8.5
	T48G06E19-S#1	1.6	3.7	11.1
	T48G06E19-S#2	1.6	4	9.7
	T48G06E19-S#3	1.9	3.3	11.2
#2	T48G06E13-S#1	1.8	3.7	11.1
	T48G06E13-S#2	2.1	5.7	19.1
	T48G06E13-S#3	2.5	6.5	16.8
#3	T76G13E10-S#1	1.4	3.3	11.1
	T76G13E10-S#2	1.1	2.4	9.7
	T76G13E10-S#3	2	6.5	9.7
	T76G06E13-S#1	1.4	3.3	11.1
	T76G06E13-S#2	1.5	2.9	12.5
	T76G06E13-S#3	1.1	3.3	11.1
	T76G06E06-S#1	1.2	3.7	11.1
	T76G06E19-S#1	1.3	3.3	9.7

Table 3. Fragility Curve Parameters

Group No.	DS1		DS2		DS3	
	x_m	β	x_m	β	x_m	β
#1	1.8	0.125	4	0.167	10.5	0.127
#2	2.1	0.168	5.1	0.302	15.3	0.283
#3	1.3	0.198	3.4	0.289	10.7	0.092

Figure 15 presents the STC fragility curves for different specimen groups using Equation (2). The curves show that in specimens with 0.48-mm-thick stud/track, the connections with insufficient edge distances (edge distances smaller than 13 mm) are more vulnerable than connections with sufficient edge distances. The influence of edge distance is particularly highlighted in the probabilities of occurrences of *DS2* and *DS3*. Comparing the median values (x_m) in Table 3 also demonstrates this impact.

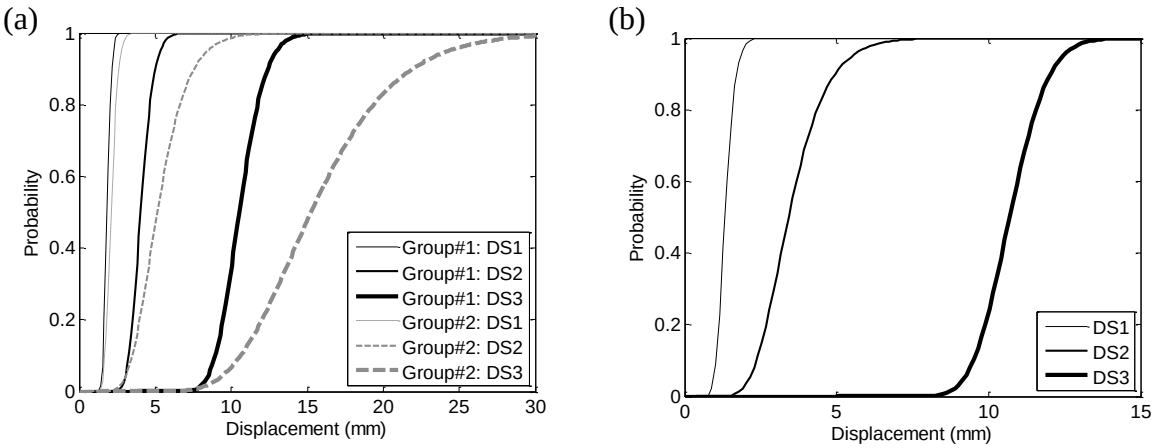

Figure 15. Fragility Curves for (a) Specimens with 0.48-mm-thick Studs/Tracks (Group #1 and #2), (b) Specimens with 0.76-mm-thick Studs/Tracks (Group #3)

5. Development of an Analytical Hysteresis Model for Track-Stud Connections

The experimental data was used to develop a hinge material model for the behavior of STCs. For this purpose, a one-dimensional hysteresis load-displacement relationship was defined using the "Pinching4" uniaxial material along with a "zeroLength" element in OpenSees [OpenSees, 2014]. This material enables the simulation of complex pinched force hysteresis responses accounting for degradations under cyclic loadings [Soroushian *et al.*, 2013] similar to those shown in Fig. 9. The "Pinching4" parameters (Fig. 16) include four positive and negative points along the backbone curve (*ePdi*, *ePfi*, *eNdi*, and *eNfi*), in addition to the parameters that define the "pinched" or unloading/reloading behavior of the model (in total 39 parameters) [Lowes and Altoontash, 2003]. The pinching parameters (*rDispP*, *rForceP*, *uForceN*, etc.), are based upon the ratio of displacement (Disp) or force (Force) to maximum (P) or minimum (N) historic demands at various points in the unloading (u) or reloading (r) curve [Peterman *et al.*, 2014]. Unloading and reloading stiffness degradation as well as strength degradation can be

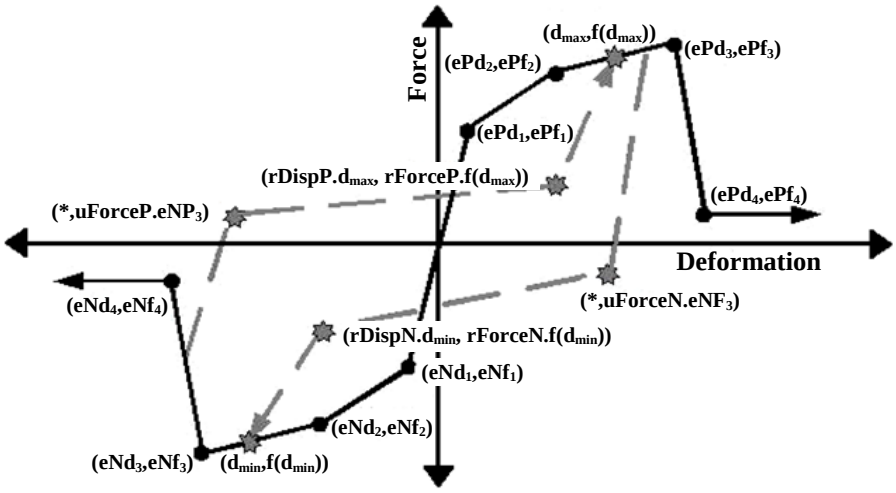

Figure 16. Pinching4 Material Properties (OpenSees, 2014)

considered in the model using *gKi*, *gDi*, and *gFi*. A detailed description of these parameters can be found in the OpenSees website [OpenSees, 2014].

5.1. Calibration of Proposed Analytical Model Using STC Experiments

Inspired by the previous study by Soroushian *et al.* [2013], for each test specimen the hysteresis response, the value of cumulative hysteresis energy, and force histories were used in the calibration process on a visual basis. Moreover, the parameters were calibrated so that the maximum cumulative hysteresis energy stayed within the ±10% range of the experimental values. The displacement histories were used as the inputs for the analytical model. Figure 17 shows the aforementioned characteristics of the calibrated hysteresis model for shear response of one sample STC from the specimen series T48G06E06.

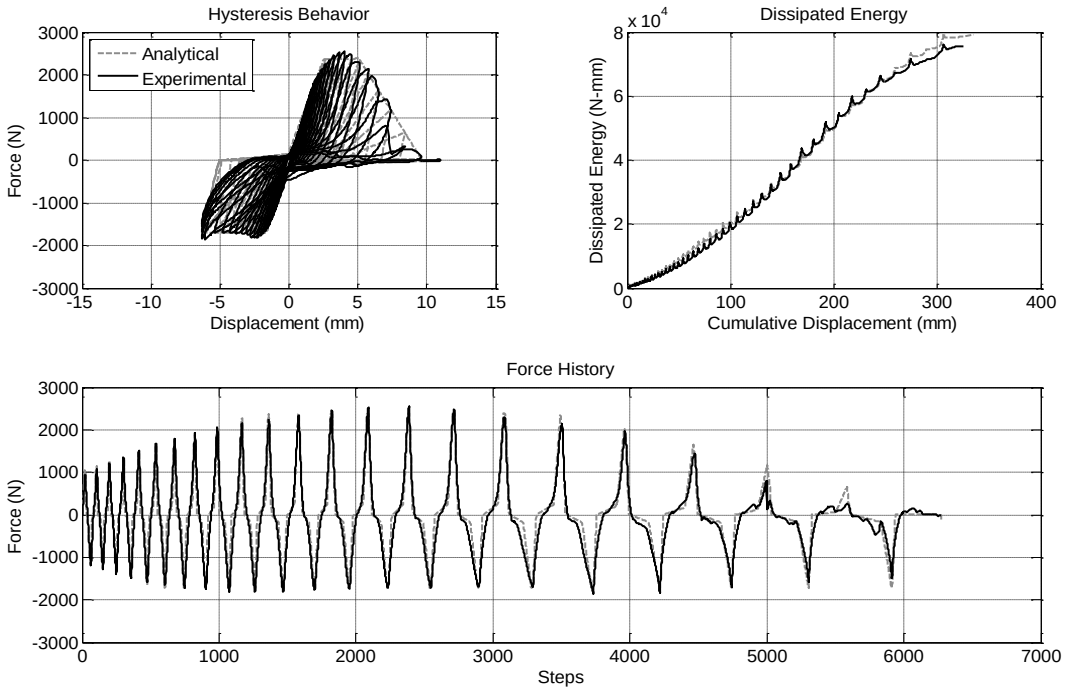

Figure 17. Analytical-Experimental Comparison of the Second Specimen from Series T48G06E06

A sensitivity analysis was performed on the parameters needed to define "Pinching4" material [Rahmanishamsi *et al.*, 2014b]. Initially, all the 39 parameters of "Pinching4" material were calibrated to find the best correlation between analytical and experimental data for each specimen. Nonetheless, the values of pinching and unloading/reloading parameters (23 out of 39 parameters) were found to be similar for all specimens. Indeed, the pinching and unloading/reloading parameters were not sensitive to the specimen details. Accordingly, constant values were assigned to these parameters (Table 4).

Subsequently, to generate an analytical model with a backbone curve comparable to the experimental results, backbone points were selected for each specimen individually. Table 5 presents examples of the values used to define the backbone curves. Figure 18 illustrates the comparisons between analytical and experimental results for two sample STCs. As Fig. 18b shows, the suggested "Pinching4" material does not capture the sudden change in load-displacement relationship, which is caused by stud-track interaction. The effect of this interaction on the analytical model is discussed in detail in the subsequent section.

Table 4. Fixed "Pinching4" Parameters of STCs

Parameters									
rDispP **rDispN**	**rForceP** **rForceN**	**uForceP** **uForceN**	**gK1** **gK2**	**gK3** **gK4**	**gKLimit**	**gD**	**gDLimit**	**gF**	**dam**
0.50 0.35	0.10 0.10	-0.01 -0.01	0 0	0.2 0.4	0.4	0	0	0	cycle

Table 5. Sample Calibrated Pinching4 Parameters for Various STCs

Component Name	ePf1 ePd1	ePf2 ePd2	ePf3 ePd3	ePf4 ePd4	eNf1 eNd1	eNf2 eNd2	eNf3 eNd3	eNf4 eNd4
Specimens with 0.48-mm Thick Stud and Tracks, ePfi (N), ePdi (mm)								
Specimen #1	378.1	2286.4	2290.8	0.01	-289.1	-1757.0	-1245.5	-0.01
T19G25E75	0.1	2.5	3.8	10.2	-0.1	-2.3	-6.4	-6.5
...	...	...	...	...	...	...	...	...
Specimens with 0.76-mm Thick Stud and Tracks, ePfi (N), ePdi (mm)								
Specimen #1	266.9	1734.8	1739.3	0.01	-355.9	-1734.8	-1739.3	-289.1
T30G50E38	0.1	1.5	4.6	11.2	-0.1	-1.4	-6.4	-10.4
...	...	...	...	...	...	...	...	...

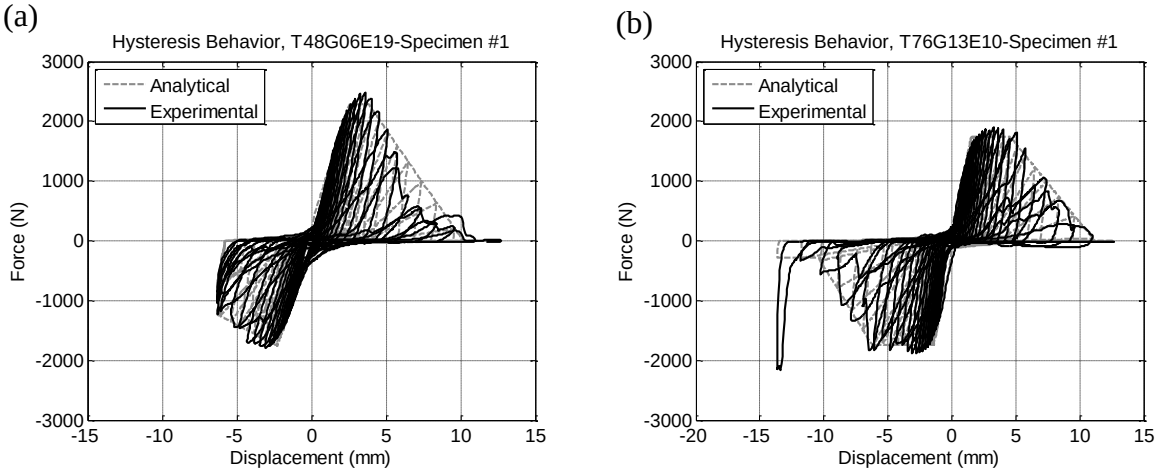

Figure 18. Sample Analytical-Experimental Hysteresis Comparisons of Two Different STCs

5.2. Development of Generic Models

In the previous section, a total of 20 sets of 16 backbone parameters for "Pinching4" material (*ePd*$_i$, *ePf*$_i$, *etc)* were calibrated based on all experimental data. Comparison of these sets showed minor discrepancies between the backbone parameters of specimens with the same edge distances and stud/track thicknesses. In fact, the backbone curve parameters were mainly dependent on the edge distance and stud/track thickness of the STCs. Therefore, similar to the fragility analysis, the specimens were categorized based on these two variables (see Table 2). For each group, one suite of material parameters was defined as the representative parameter, called the generic model, implementing the

method proposed by Soroushian *et al.* [2014]. The method uses the following assumptions to develop the generic model: 1) For each STC group, a generic model is defined; 2) the displacement points of the backbone curve (in each direction), ePd_1, ePd_2, ePd_3, ePd_4 (Fig. 16), are set to the median of the calibrated values corresponding to each of these points of the backbone curve; 3) a linear interpolation is used to find the force corresponding to the previously mentioned displacements where the force values at the calibrated backbone curves are unavailable. The median of these force values for each set defines the backbone points in each direction (ePf_1 ePf_2, ePf_3, and ePf_4 in Fig. 16); 4) the remainder of the parameters (fixed parameters) are the same as those suggested in Table 4.

For all the positive and the first three negative backbone points (ePd_1, ePf_1 ... eNd_3, eNf_3), the calibrated values of specimens with both 6-mm and 13-mm gaps were utilized to determine the generic backbone curve. However, the calibrated backbones of specimens with a 6-mm gap did not represent the behavior of the STCs beyond the eNd_3. This was due to the fact that these specimens were tested using the modified protocol in which the negative displacement was limited to 6 mm. Therefore, to find the last negative point (eNd_4, eNf_4) of the generic model, only the calibrated values from the specimens with a 13-mm. gap were used. It was assumed that the trend of backbone curves of the specimens with a 6-mm. gap after eNd_3 would be similar to the trend of backbone curves of specimens with a 13-mm. gap. The generic model parameters, obtained using the previously mentioned assumptions, are presented in Table 6. Figure 19 shows the comparison between the generic backbone curve of the first and third groups and all the

calibrated backbone curves. Figure 20 compares the generic model with a sample of the experimental data from each group.

Table 6. Generic Pinching4 Calculated Parameters for Various STCs

	ePfi (N) and ePdi (mm) for Each Group							
Group No.	**ePf1** **ePd1**	**ePf2** **ePd2**	**ePf3** **ePd3**	**ePf4** **ePd4**	**eNf1** **eNd1**	**eNf2** **eNd2**	**eNf3** **eNd3**	**eNf4** **eNd4**
Group #1	253.5 0.1	1908.7 2.5	1866.8 5.1	0.01 10.2	-200.2 -0.1	-1554.3 -2.0	-1516.8 -6.4	-622.8 -8.4
Group #2	222.4 0.1	1998.1 2.8	2134.7 7.1	0.01 16.8	-177.9 -0.1	-1663.6 -2.5	-1668.1 -6.1	-622.8 -8.4
Group #3	289.1 0.1	1801.5 1.5	1831.4 4.6	20.4 10.0	-333.6 -0.1	-1728.3 -1.5	-1672.4 -6.2	-111.2 -10.2

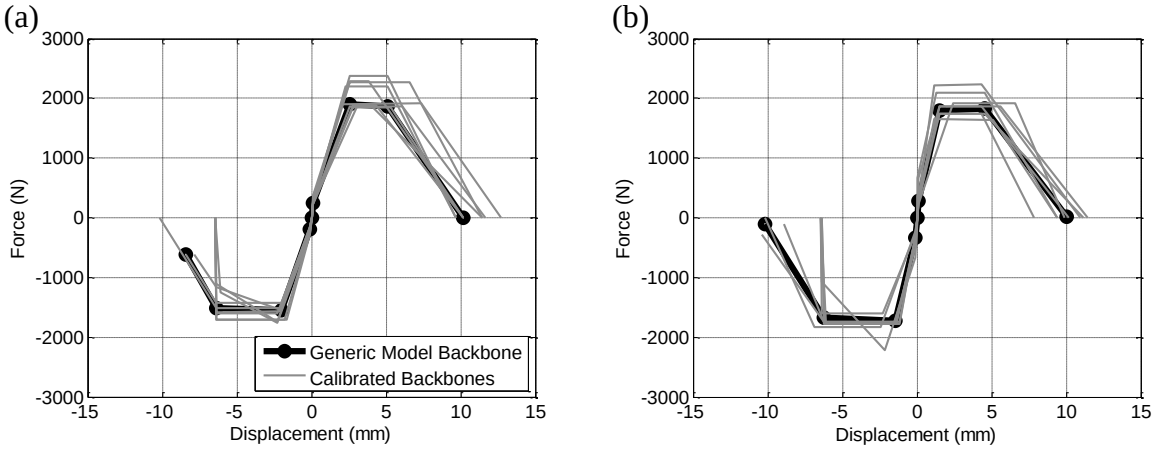

Figure 19. Generic Backbone Curves of the (a) First and (b) Third Group.

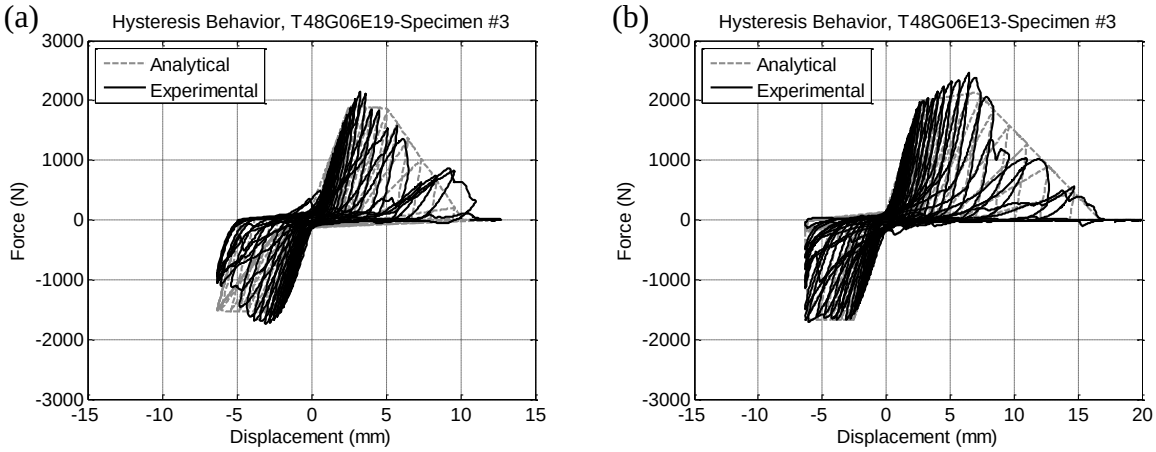

Figure 20. Sample Generic Analytical-Experimental Hysteresis Comparison of Different GSC Groups

5.3. Proposed Generic Models Including Stud-Track Interaction

The stud-track interaction and the consequent damage is not a point of interest in the current study. Nonetheless, an approximate method is proposed in this section to include the effect of this interaction on the force-displacement relationship of the STCs. Note that supplemental experimental studies are needed in order to determine the accurate hysteresis behavior of the stud-track interaction.

Figure 21 presents the force-displacement responses of downward monotonic tests as well as the backbone curves of cyclic tests in which the closure of the gap was observed. The gap closure resulted in a substantial increase in force with similar rates in all tests with the same stud/track thicknesses. In order to address this change, the "Elastic Perfectly Plastic Gap (EPPG)" material in OpenSees [OpenSees, 2014] was utilized. The material parameters (Fig. 22a) include: 1) initial stiffness, k_g; 2) yield force, F_y; 3) initial gap deformation, (gap); 4) post-yield stiffness ratio, $b=k_h/k_g$; 5) damage type (not used in this model), which is an optional parameter to specify whether damage is accumulated or not in the material model.

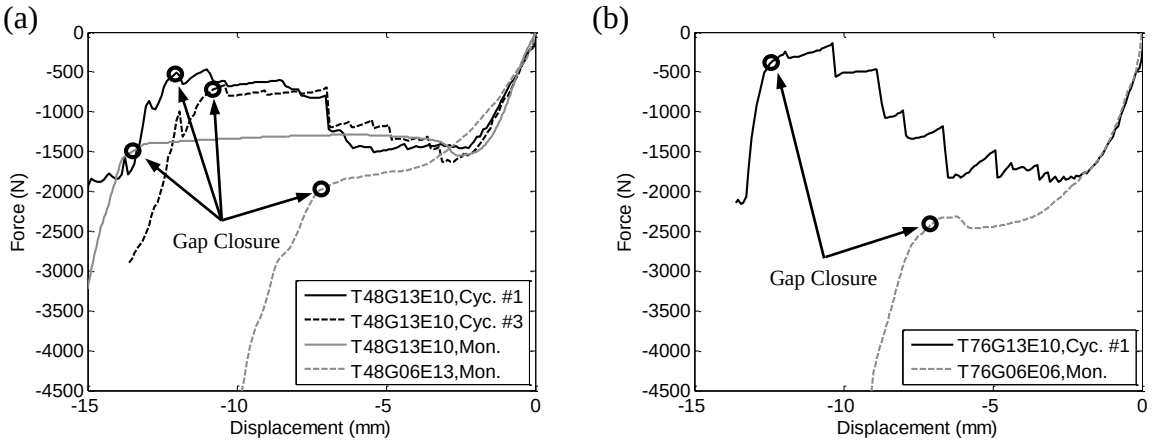

Figure 21. Effect of Stud-Track Interaction on the Response of STCs with (a) 0.48-mm- and (b) 0.76-mm-Thick Stud/Track

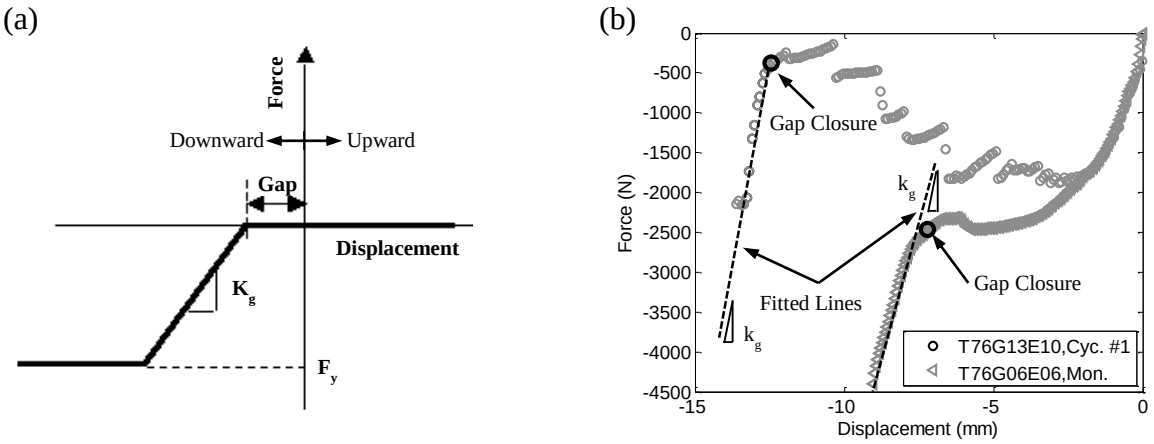

Figure 22. (a) EGGP Material Properties [OpenSees, 2014], (b) Calculating k_g for Specimens with 0.76-mm-Thick Stud/Track

To find the k_g the following procedure was adopted: 1) for each specimen the displacement associated with the gap closure was recognized; 2) the least-square regression method was utilized to fit a line to the data points after the gap closure; 3) the slope of this line would be the k_g value for each specimen (Fig. 22b); 4) the median of k_g values of specimens with similar stud/track thickness was considered as the k_g values for the generic models. Table 7 presents the "EPPG" material parameter for each stud/track thickness. Since the accurate nonlinear behavior of stud-track interaction was not available, a large value was assumed for the yield force to avoid any nonlinearity in the material. The gap size varied between 6 mm and 13 mm in this study. However, it can be modified so as to represent any gap size (between the stud and track web) in the actual construction.

Table 7. EPPG Parameters for Various STCs

Group No.	Stud/Track Thickness (mm)	k_g (N/mm)	F_y (N)	Gap (mm)	b	damage
Group #1 and #2	0.48	958.3	Used 50800 Can Vary	Can Vary	0.0	"noDamage"
Group #3	0.76	2216.2	Used 50800 Can Vary	Can Vary	0.0	"noDamage"

The “EPPG” material was located in parallel with the “Pinching4" material, generated in the previous section. In order to combine the effect of these two materials, the parallel uniaxial material in Opensees [OpenSees, 2014] (Fig. 23a) was used along with a zero-length element. Before the gap is closed, the “Pinching4” material controls the behavior of the zero-length element since the stiffness of gap material is zero. Afterwards, the element behavior is dominated by the gap material. The reason is that k_g is much larger than the stiffness of the “Pinching4" material, which might be as low as zero. Figure 23b illustrates the proposed backbone curve for the generic model, including the gap closure effect. Figure 24 compares the hysteresis behavior of the generic analytical models with experimental results in two sample specimens.

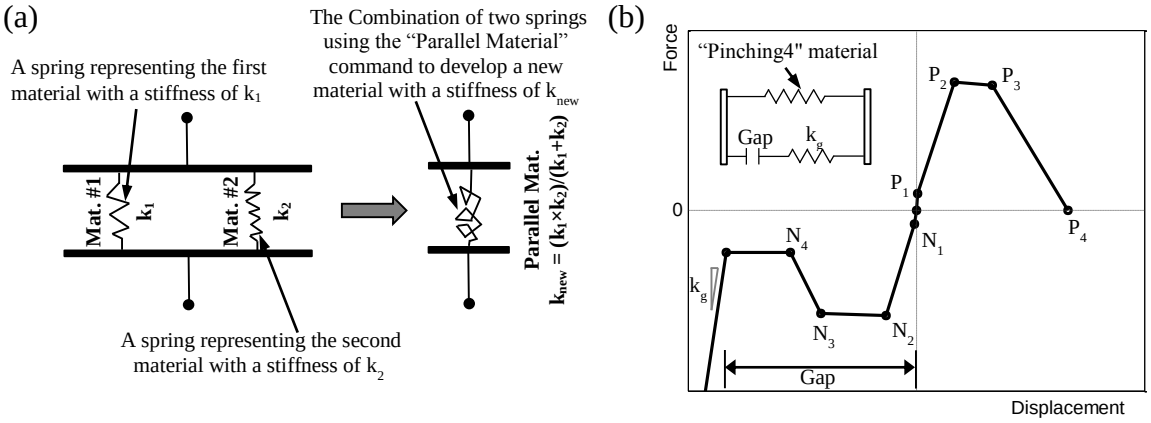

Figure 23. (a) Parallel Material [OpenSees, 2014], (b) Schematic Backbone curve of Generic Model of STCs Including Gap Closure Effect

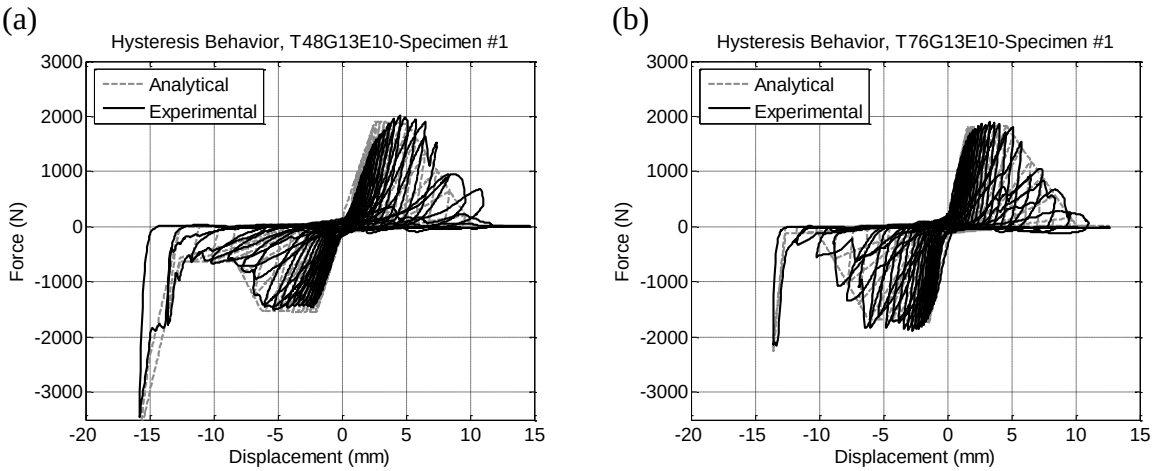

Figure 24. Sample Analytical-Experimental Hysteresis Comparisons of Two STCs with (a) 0.48-mm Stud/Track and 13-mm Gap, (b) 0.76-mm Stud/Track and 13-mm Gap

6. Summary and Conclusions

A total of 33 experiments were performed on the typical stud-track screw connections (STCs). The test program was designed to evaluate the displacement and force capacities of the STCs with different thicknesses and screw-edge distances. The specimens were constructed from 92-mm- (3-5/8-in.) deep studs and tracks as well as #8×13-mm (1/2-in.) screws. The test data was also used to develop capacity fragility curves for STCs in terms of displacements.

The main observations and conclusions obtained from the experimental study are as follows:

- The main portion of the capacity of the STCs was provided by the bearing resistance of stud and track flanges at the screw locations.
- In 0.48-mm-thick specimens, the distance of screws to the stud and track flange edges affected the behavior of STCs. The insufficient edge distances led to drops in

displacement capacities of STCs due to the edge tearing-out. A 13 mm (0.5 in.) was found to be the minimum required edge distance for both stud and track to avoid edge tearing-out.

- In specimens with 0.76-mm-thick studs/tracks, the force and displacement capacities of the STCs were independent of edge distance. In addition, using thicker studs and tracks led to higher initial stiffness and buckling force (the force associated with buckling of the track flange) in the force-displacement curve.
- The damage sequences of STCs included tilting of screws, enlarging of holes, and buckling of the track flanges in small displacements, followed by the complete failure of the connection in the large displacements. For 0.48-mm-thick specimens with insufficient edge distances (edge distances smaller than 13 mm), the failure mechanism was the tearing-out of stud or track flanges, while for other specimens, the failure mechanism was the popping out of the screws.
- The experimental fragility curves were developed for the STCs considering the displacement as the engineering demand parameter. The fragility analysis showed that the connections with insufficient distances were more vulnerable than connections with sufficient edge distances.
- A series of analytical hinge models were defined that represent the hysteresis behavior of all STC specimens. These models were validated using the experimental data. In addition, for each group one suite of material parameters was proposed as the representative parameter, called the generic model. The generic (representative) models could be used in the future analytical studies of the partition walls.

The hinge model of the STCs could be utilized along with the analytical models of other wall components (such as track-to-concrete floor connections and steel studs) to develop a comprehensive analytical model of a partition wall system. The partition wall model could then be subjected to realistic input motions (e.g. floor accelerations) to estimate the demand parameters on each component. These demand estimations could be used in conjunction with the capacity parameters (e.g. median and deviation) developed in this study (and similar studies for other partition wall components) to generate fragility curves for partition wall systems in terms of more global engineering demand parameters, such as floor accelerations and/or inter-story drifts.

7. Acknowledgments

The current material is based upon work supported by the National Science Foundation under Grant No. 0721399. This Grand Challenge (GC) project to study the seismic response of nonstructural systems is under the direction of M. Maragakis from the University of Nevada, Reno and Co-PIs: T. Hutchinson (UCSD), A. Filiatrault (UB), S. French (G. Tech), and B. Reitherman (CUREE). Any opinions, findings, conclusions, or recommendations expressed in the current document are those of the investigators and do not necessarily reflect the views of the sponsors. The input provided by the Practice Committee of the NEES Nonstructural Project, composed of W. Holmes (Chair), D. Allen, D. Alvarez, and R. Fleming and by the Advisory Board, composed of R. Bachman (Chair), S. Eder, R. Kirchner, E. Miranda, W. Petak, S. Rose and C. Tokas, has been crucial for the completion of this research. Assistance from M. Lattin of the University of

Nevada, Reno material lab during the assembly and testing as well as support from Johnnie Stolz of Omboli Interior Inc. is appreciated.

8. References

ASTM C754 [2011], Standard Specification for Installation of Steel Framing Members to Receive Screw-Attached Gypsum Panel Products, ASTM International, West Conshohocken, PA.

Babalola, M. R., LaBoube, R. A. [2004] "Strength of Screw Connections Subject to Shear Force," Research Report *RP04-2*, American Iron and Steel Institute.

Bersofsky, A. [2004] "A Seismic Performance Evaluation of Gypsum Wallboard Partitions*,"* MS Thesis, Department of Structural Engineering, University of California, San Diego, La Jolla, CA.

Bolte, W.G., LaBoube, R.A. [2004] "Behavior of Curtain Wall Stud to Srack Connections," *Thin-Walled Structures* **42**, 1431–1443.

Davies, D., Retamales, R., Mosqueda, G., and Filiatrault, A. [2011] "Experimental Seismic Evaluation, Model Parameterization, and Effects of Cold-Formed Steel-Framed Gypsum Partition Walls on The Seismic Performance of an Essential Facility," Technical Report *MCEER-11-0005*, MCEER, State University of New York at Buffalo, New York.

Dhakal, R. P. [2010] "Damage to non-structural components and contents in 2010 Darfield earthquake," *Bulletin of The New Zealand Society for Earthquake Engineering* **43**, 404-411.

Fiorino, L., Della Corte, G., Landolfo, R. [2007] "Experimental Tests on Typical Screw Connections for Cold-Formed Steel Housing," *Engineering Structures* **29**, 1761-1773.

Fülöp, L. A., and Dubina, D. [2004] "Performance of Wall-Stud Cold-Formed Shear Panels under Monotonic and Cyclic Loading, Part I: Experimental research," *Journal of Thin-Walled Structures* **42**, 321–338.

Gould, N. C., and Marshall, J. D. [2012] "Structural and Non-Structural Damage to Industrial Facilities during the February 2011 Christchurch, New Zealand, Earthquake," *Proceeding of 43rd Structures Congress, ASCE/SEI,* Chicago, IL.

Lewis, A.V., Fox, S.R., Schuster, R.M., [2008] "Strength of Cold-Formed Steel Jamb Stud-to-Track Connections," *Nineteenth International Specialty Conference on Cold-Formed Steel Structures*, St. Louis, Missouri, U.S.A.

Lowes, L.N., Altoontash, A. [2003] "Modeling Reinforced-Concrete Beam-Column Joints Subjected to Cyclic Loading," *ASCE Journal of Structural Engineering* **139**, 1285-1293.

Mizutani K., Kim H., Kikuchihara M., Nakai T., Nishino M., Sunouchi S. [2012] "The damage of the building equipment under the 2011 Tohoku pacific earthquake," *9th International Conference on Urban Earthquake Engineering & 4th Asia Conference on Earthquake Engineering*, Tokyo Institute of Technology, Tokyo, Japan.

Miranda, E., Mosqueda. G., Retamales, R., and Pekcan, G. [2012] "Performance of Nonstructural Components during the February 27, 2010 Chile Earthquake," *Earthquake Spectra* **28**, 453-471.

Open System for Earthquake Engineering Simulation (OpenSees) website [2014]: http://www.opensees.berkeley.edu . PEER, Berkeley: University of California

Pekoz, T., [1990] "Design of Cold-Formed Steel Screw Connections," *Tenth International Specialty Conference on Cold-formed Steel Structures*, St. Louis, Missouri, U.S.A.

Peterman, K.D., Nakata, N., and Schafer, B.W. [2014] "Hysteretic Characterization of Cold-formed Steel Stud-to-Sheathing Connections," *Journal of Construction Steel Research* **101**, 254–264.

Porter, K., R. Kennedy and R. Bachman. [2007] "Creating Fragility Functions for Performance-Based Earthquake Engineering," *Earthquake Spectra* **23**, 471-489.

Rahmanishamsi, E., Soroushian, S., and Maragakis, M. [2014a] "System-Level Experiments on Ceiling/Piping/Partition Systems at UNR-NEES Site," *Tenth U.S. National Conference on Earthquake Engineering*, Anchorage, AK.

Rahmanishamsi, E., Soroushian, S., and Maragakis, M. [2014b] "Shear Capacity Evaluation of Typical Gypsum-Stud Screw Connections," *Earthquake Spectra*. (in review)

Restrepo, J.I., and Bersofsky, A. [2010] "Performance Characteristics of Light Gage Steel Stud Partition Walls," *Thin-Walled Structures* **49**, 317–324.

Restrepo, J.I., and Lang, A.F. [2011] "Study of Loading Protocol in Light-Gauge Stud Partition Wall," *Earthquake Spectra* **27**, 1169–1185.

Retamales, R., Davies, R., Mosqueda, and G., Filiatrault, A. [2013] "Experimental Seismic Fragility of Cold-Formed Steel Framed Gypsum Partition Walls," *ASCE Journal of Structural Engineering* **139**, 1285-1293.

Retamales, R., Mosqueda, G., Filiatrault, A., and Reinhorn, A.M. [2008] "New Experimental Capabilities and Loading Protocols for Seismic Qualification and Fragility Assessment of Nonstructural Components," *Technical Report MCEER-08-0026*, MCEER, State University of New York at Buffalo, New York.

Retamales, R., Mosqueda, G., Filiatrault, A., and Reinhorn, A.M. [2011] "Testing protocol for experimental seismic qualification of distributed nonstructural systems," *Earthquake Spectra* **27**(3):835-856.

Risk Management Solutions (RMS) Inc. [2006] *"*Kiholo Bay, Hawaii Earthquake", RMS Event Report, Newark, CA.

Soroushian, S., Ryan, K. L., Maragakis, M., Wieser, J., Sasaki, T., Sato, E., Okazaki, T., Tedesco, L., Zaghi, A. E., Mosqueda, G., Alarez, D., [2012] "NEES/E-Defense tests: Seismic performance of ceiling/sprinkler piping nonstructural systems in base isolated and fixed base building," *15th World Conference on Earthquake Engineering (15WCEE)*, Lisbon, Portugal.

Soroushian, S., Zaghi, A. E., Maragakis, M., Tian, T., and Filiatrault, A. [2013] "Analytical Seismic Fragility Analyses of Fire Sprinkler Piping Systems with Threaded Joints," *Earthquake Spectra* In-Press.

Soroushian, S., Maragakis, M., and Jenkins, C. [2014] "Axial Capacity Evaluation of Typical Suspended Ceiling Joints," *Earthquake Spectra*. (in review)

Wood, R. L. and Hutchinson, T. C. [2014] "Design-Oriented Model for Capturing the In-Plane Seismic Response of Partition Walls," *ASCE Journal of Structural Engineering*, **140**.

Zwick, K., LaBoube, R. [2002] "Self-Drilling Screw Connections Subject to Combined Shear and Tension," Research Report *RP02-4*, American Iron and Steel Institute.

Chapter 5

Capacity Evaluation of Typical Track-to-Concrete Power-Actuated Fastener Connections in Nonstructural Walls

Esmaeel Rahmanishamsi[1]; Siavash Soroushian, M. ASCE[2]; and Emmanuel "Manos" Maragakis[3]

Please note that this chapter is a self-contained paper accepted for publication in the ASCE Journal of Structural Engineering where the word 'this paper/study' refers to the chapter itself.

Abstract

Damage to track-to-concrete connections was widely reported in previous experimental studies on the seismic performance of nonstructural partition walls. These connections are commonly comprised of light-gauge cold-formed steel tracks attached to the concrete base material with power-actuated fasteners (PAFs). Failure of PAF connections resulted in loss of strength and stiffness of the partition walls and led to subsequent damage mechanisms. A series of component-level experiments has been conducted at University of Nevada, Reno to characterize the cyclic response and damage mechanisms of track-to-concrete PAF connections subjected to either tension or shear force. The observed damage mechanisms and force-displacement responses are presented and compared for two track thicknesses. Also, the accuracy of available design provisions for predicting the ultimate connection capacity was investigated. The data was then

1 PhD Candidate, Department of Civil and Environmental Engineering, University of Nevada, Reno, NV, 89557-0258, E-mail: erahmanishamsi@unr.edu

2 Structural Analyst, Advanced Technology & Research, Arup, 560 Mission Street, 7th Floor, San Francisco, CA, 94105.

3 Professor, Dean of College of Engineering, University of Nevada, Reno, 1664 N. Virginia Street, Reno, NV, 89557-0258.

employed to develop the capacity fragility curves in terms of connection displacement. Additionally, a series of nonlinear numerical hinge models were proposed and calibrated using component experimental data to represent the hysteresis behavior of track-to-concrete connections.

Introduction

Cold-formed light-gauged steel framing is regularly employed in the construction of walls for both commercial and industrial buildings in many parts of the world. In United States, approximately 60% of steel framing is used in nonstructural partition walls (Restrepo and Bersofsky 2010, Restrepo and Lang 2011). These walls support the architectural layout of a building and facilitate its functionality for occupants (Wood and Hutchinson, 2014). Partition walls are not designed nor anticipated to contribute to the primary load-carrying system of the building. Nonetheless, they are subjected to differential excitations imposed by the primary structure undergoing seismic loading (e.g. interstory drift), leading to damage to these walls (Xang et al., 2015). Unfortunately, this damage has frequently been triggered at story drift levels well below the yield point of structures (Dhakal 2010, Miranda et al. 2012, Tasligedik et al. 2014). Damaged partition walls can leave buildings inoperable, causing huge economic losses and extensive downtime, even in low-intensity earthquake events (Jenkins et al. 2015). Note that the downtime is of essential importance to performance of critical facilities, such as hospitals and fire stations, that need to be operational immediately after earthquake events.

The seismic performance of steel-framed partition walls has been the subject of a number of experimental studies in recent years (Bersofsky 2004, Fülöp and Dubina 2004,

Lee et al. 2007, Retamales et al. 2008, Restrepo and Bersofsky 2010, Davies et al. 2011, Restrepo and Lang 2011, Soroushian et al. 2012, Retamales et al. 2013, Rahmanishamsi et al. 2014). These studies investigated the damage mechanisms and hysteresis behaviors of partition walls with different configurations. Based on the experimental observations, one of the vulnerable elements of partition walls was the power-actuated fastener (PAF) connection between steel tracks and the concrete base material. Various damage mechanisms were reported for this connection, including tearing of steel tracks at the location of the fastener, fastener pulling- through the steel tracks, fastener pulling-out from the concrete, and failure of the fastener. The failure of PAF connections resulted in loss of strength and stiffness of the partition walls and led to interactions with return walls and other nonstructural components such as ceiling systems. These interactions caused subsequent damage mechanisms, including crushing and breaking of sheathing boards at partition corners. Therefore, the behavior of the track-to-concrete connections is of interest for characterizing their role in the performance of steel-framed partition wall systems. Fig. 1 shows some examples of PAF connection failures during past experimental studies (Restrepo and Bersofsky 2010, Davies et al. 2011, Rahmanishamsi et al. 2014).

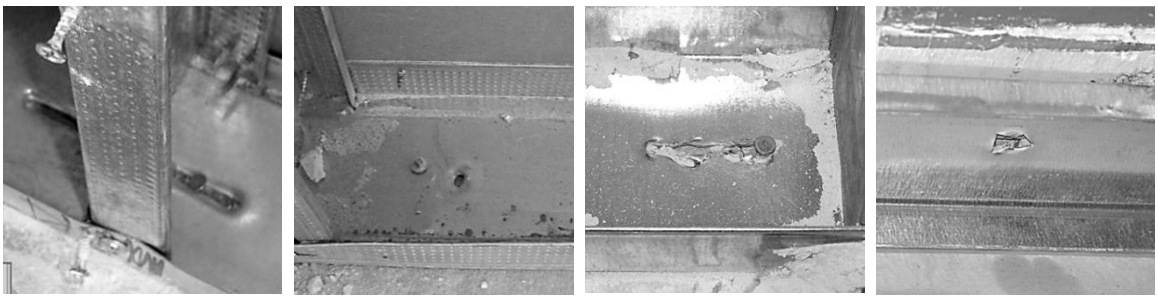

Fig. 1. Examples of PAF Connection Failures in Previous Experimental Studies (Restrepo and Bersofsky 2010, Rahmanishamsi et al. 2014, Davies et al. 2011)

A limited number of studies are available on the performance of PAF connections. Mujagic et al. (2010) suggested a strength prediction model for fasteners embedded in steel substrate and subjected to either shear or tension force. Recently, an experimental study was performed by Ramirez and LaBoube (2013) on the shear performance of PAF connections between cold-formed steel tracks and concrete base material. The researchers tested two types of PAFs and various types of steel tracks. The observed damage mechanisms included tearing of the track, deformation of the fastener, and pulling out of the fastener. The tested connection capacities were compared with the predicted values based on the AISI S100-12 (2012) and some modifications to current design provisions were proposed. Although this study provided valuable information on PAF behaviors, it was limited to track-to-concrete connections in load-bearing walls. The steel track profiles used in load-bearing walls are different from those used in nonstructural partition walls. Since the nonstructural partition walls are not part of the structural load-carrying system, thinner tracks with smaller web depth are usually used in their construction (Rahmanishamsi et al. 2015). As such, the performance of track-to-concrete connections in nonstructural walls could be different than the load-bearing walls. In addition, no study has evaluated the hysteresis force-displacement behavior of these connections.

As a part of the project titled “NEESR-GC: Simulation of the Seismic Performance of Nonstructural System,” a numerical effort is underway to assess the seismic performance of nonstructural partition walls. The long-term goal of the effort is to develop a detailed yet computationally efficient numerical model for cold-formed steel-framed gypsum partition walls as shown in Fig. 2. In the model, the nonlinear behavior of the members and connections (except gypsum boards) is represented by hysteretic load-deformation

springs. In turn, the model supports a mechanically based method for assessing the lateral response of cold-formed steel-framed gypsum partition wall configurations for which testing is not available. The model can also be used for performance-based studies (such as fragility analysis), in which extensive numerical analyses are required. To develop this modeling capability, it is necessary to characterize the cyclic behavior and energy dissipation of individual partition wall components and to represent those behaviors using equivalent hysteretic springs. The characterization can be accomplished with the experimental data from component-level cyclic tests on each of the members and connections. The cyclic tests also help to determine the various possible damage mechanisms in each partition wall component (Rahmanishamsi et al. 2015).

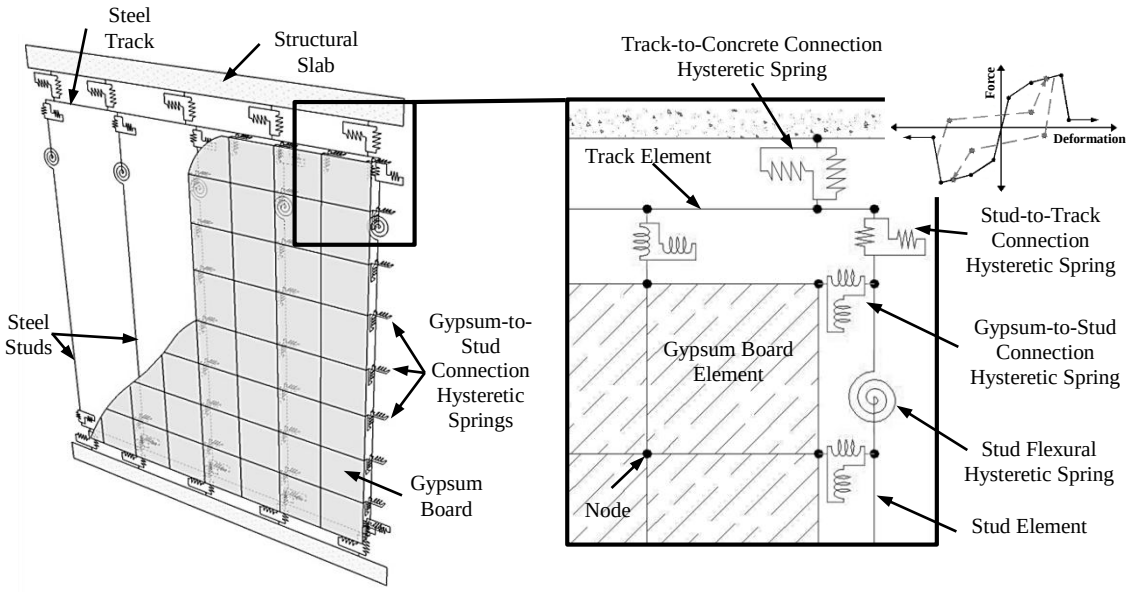

Fig. 2. Schematic Diagram of a Numerical Model of a Steel-Framed Gypsum Partition Wall, After Rahmanishamsi et al. (2015)

The purpose of this paper is to characterize the cyclic response and damage mechanisms of track-to-concrete PAF connections as one the components in

nonstructural partition walls. The paper starts with a description of the test setups and experimental program. Afterwards, the observed damage mechanisms and force-displacement responses are presented and compared for two track thicknesses. In addition, the correlation between tested ultimate connection capacities with AISI S100-12 (2012) nominal design strengths were evaluated. The data was then employed to generate the capacity fragility curves in terms of connection displacement. Finally, a series of nonlinear numerical hinge models were proposed and calibrated using component experimental data to represent the hysteresis behavior of track-to-concrete connections subjected to either tension or shear force.

Description of Test Specimens

A total of 22 tests were conducted to estimate the strength and stiffness of track-to-concrete PAF connections, subjected to either shear or tension forces. The specimens were constructed form 362T125-19 or 362T125-30 cold-formed steel tracks, attached to the concrete with 4-mm- (0.157-in.) diameter, 25-mm- (1-in.) long knurled shank PAFs. The actual diameter of PAF head was 7.9 mm (0.313 in.). Based on the cylinder tests, the compressive strength of the concrete was between 20 MPa (3.0 ksi) to 27 MPa (4.0 ksi). The specimens represented the common construction details for commercial and institutional buildings (Retamales et al. 2013).

Setup for Tension Tests

Fig. 3(a) and Fig. 3(b) show a sample specimen and the testing machine during a tension test. The specimen included a 178-mm- (17-in.) long steel track, connected to a 229x229x533-mm (9x9x21-in.) concrete block with a single PAF at center. The concrete

block was tightened to the stationary base of an Instron 5985 machine using four threaded rods [Fig. 3(a)]. Each flange of the track was clamped between two steel plates in order to prevent any bending or buckling of the flange and limit the deformation to the web. Four steel angles attached the clamping plates to a T-shaped plate [Fig. 3(b)], which was held by the movable grip (top grip) of the machine [Fig. 3(a)]. All the steel plates and angles were 6-mm- (0.25-in.) thick. The machine applied upward displacement to the specimens through the movable grip and measured the reaction by the axial load cell.

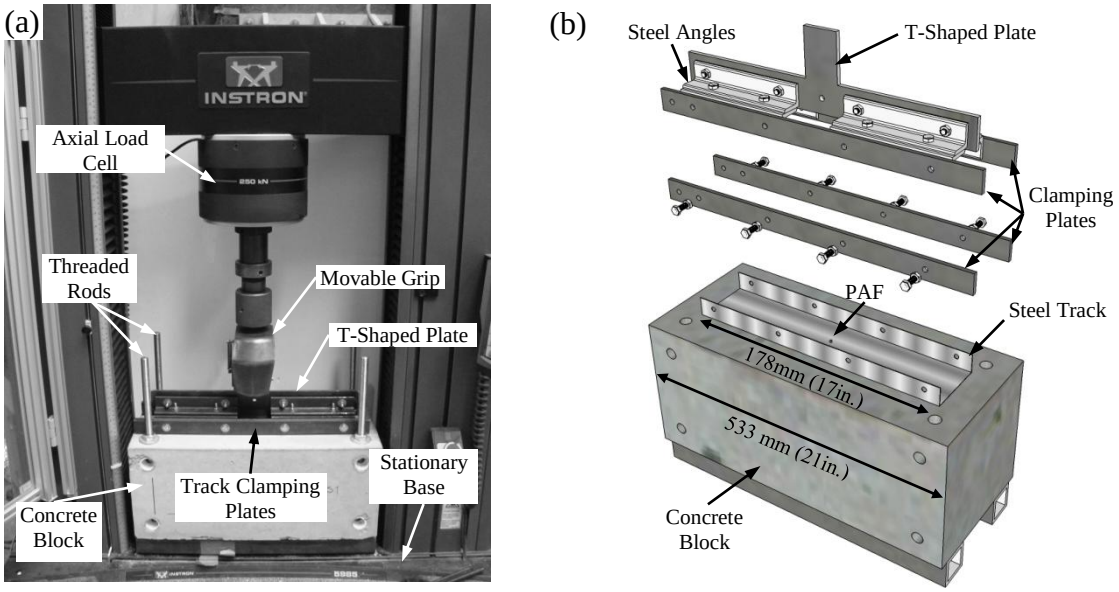

Fig. 3. Tension Test Setup (a) Specimen and Test Machine, (b) Specimen and the Clamping System

Setup for Shear Tests

The same Instron machine was used for the shear test as illustrated in Fig. 4. A 508-mm- (20-in.) long steel track was attached to a 203x203x610-mm (8x8x24-in.) concrete block with two PAFs. The PAFs were spaced 203 mm (8 in.) on center. Similar to the tension test, the concrete block was fixed to the machine with threaded rods. The

clamping system consisted of a steel angle at the internal side of each track flange and a steel plate outside. They were bolted together at four locations to restrict the flange deformation. A combination of a T-shaped steel plate and two steel angles [loading angles in Fig. 4 (b)] transferred the upward and downward displacements from the movable grip to the specimen. All the steel plates and angles were 6-mm- (0.25-in.) thick.

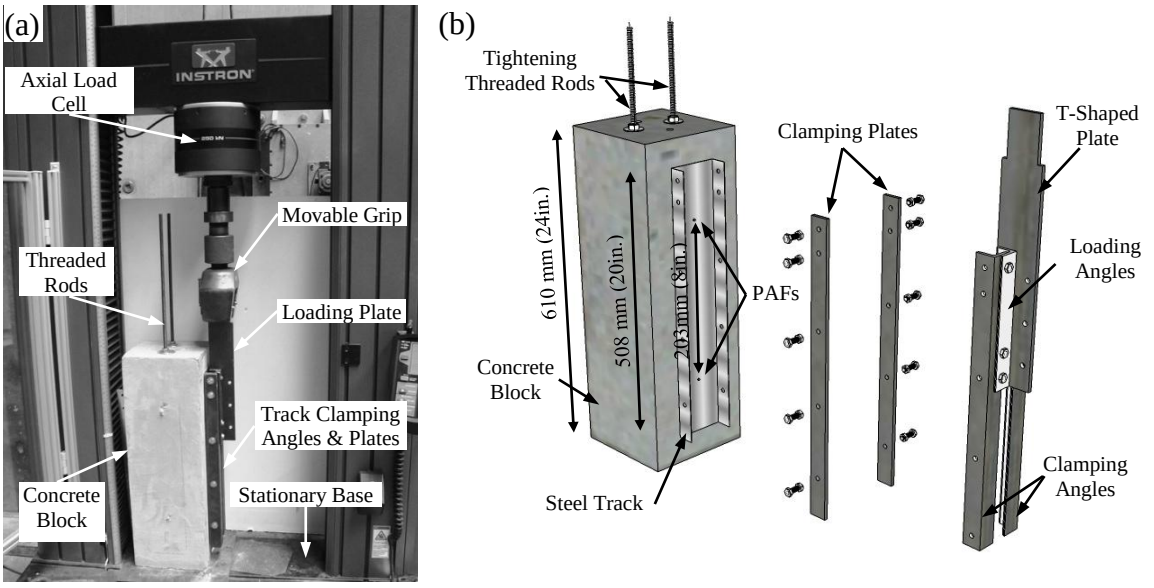

Fig. 4. Shear Test Setup (a) Specimen and Test Machine, (b) Specimen and the Clamping System

Experimental Program

Table 1 lists the 22 specimens considered in the experimental program. The experimental program consisted of two phases. In the first phase the tension capacity was evaluated, while in the second phase the shear capacity of the track-to-concrete PAF connections were evaluated. Each phase involved two different track types: (1) 362T125-19 [0.48-mm- (0.019-in) thick track], and (2) 362T125-30 [0.76-mm- (0.030-in) thick track]. For fragility assessment purposes, at least three nominally identical specimens were tested under cyclic loading for each track type (Retamales et al. 2013). Additional

monotonic tests were also conducted in order to assess the effect of cumulative cyclic damage on the capacity of the track-to-concrete connections. The loading rate varied from 0.04 mm/sec (0.1 in./min.) to 0.42 mm/sec (1.0 in./min.) for the first three monotonic tests. However, a constant rate [0.21 mm/sec (0.5 in./min.)] was considered for the remaining tests since the response of the connection was found to be independent of the loading rate. The response and failure mechanisms of track-to-concrete PAF connections will be discussed in detail in subsequent sections.

Table 1. Test Program Matrix

Test Type	Track Thickness, mm (in.)	Loading Protocol	Loading Direction	Loading Rate, mm/s (in./min.)	Number of Specimens
Tension	0.48 (0.019)	Monotonic	Tension	0.04 (0.1)	1
		Monotonic	Tension	0.42 (1.0)	1
		Monotonic	Tension	0.21 (0.5)	1
		Cyclic	-	0.21 (0.5)	3
	0.76 (0.030)	Monotonic	Upward	0.21 (0.5)	1
		Cyclic	-	0.21 (0.5)	3
Shear	0.48 (0.019)	Monotonic	Upward	0.21 (0.5)	1
		Monotonic	Downward	0.21 (0.5)	1
		Cyclic	-	0.21 (0.5)	4
	0.76 (0.030)	Monotonic	Upward	0.21 (0.5)	1
		Monotonic	Downward	0.21 (0.5)	1
		Cyclic	-	0.21 (0.5)	4

Loading Protocol

In the monotonic tests, the specimens were subjected to unidirectional increasing displacements as shown in Fig. 5(a). For the cyclic tests, a loading protocol proposed by Retamales et al. (2008, 2011) was used. This protocol was developed specifically for evaluating the performance of primarily drift-sensitive nonstructural components (Retamales et al. 2013). Fig. 5(b) shows the displacement history that was generated based on the aforementioned loading protocol and used in the shear tests. In this figure,

negative and positive displacements represent the downward and upward movement, respectively, of the top grip.

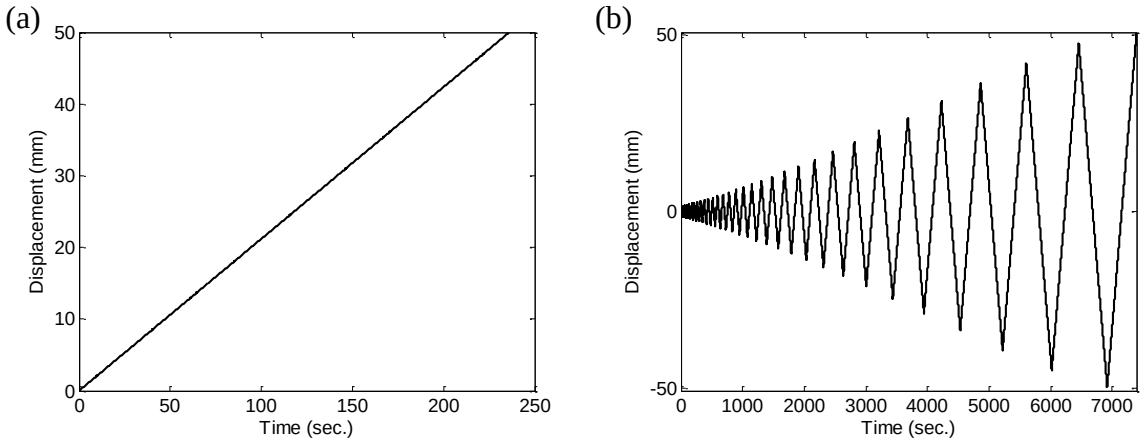

Fig. 5. Loading Protocol for: (a) Monotonic and (b) Cyclic Shear Tests

In addition, a modified cyclic displacement history (Fig. 6) was developed for the tension tests. In this displacement history, the negative (downward) displacement of the movable grip was limited to zero in order to avoid compression in the connections. The compressive behavior of track-to-concrete connections is bound to be mainly dominated by concrete properties, which are beyond the scope of the current test program.

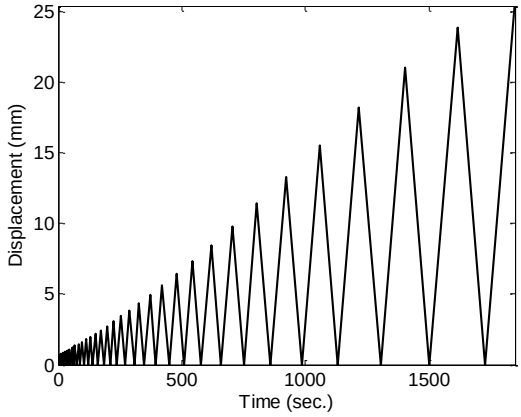

Fig. 6. Loading Protocol for Cyclic Tension Tests

Experimental Results

Individual Track-to-Concrete Connection Force and Displacement

In tension tests, the measured values by the testing machine were directly used as the track-to-concrete connection force and displacement [Fig. 7(a)]. For the shear tests, assuming that the total force was equally distributed between two PAF connections, the individual connection force was calculated as force = P / 2 [Fig. 7(b)]. Moreover, the displacements of two connections were considered to be identical and equal to the displacement of the movable grip.

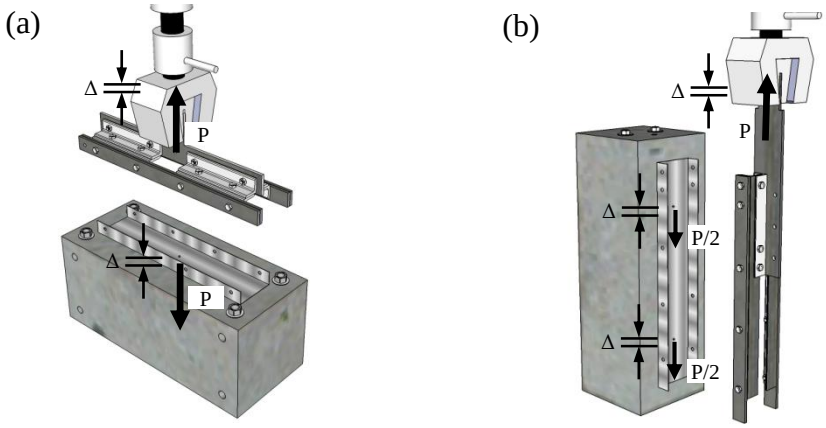

Fig. 7. Free Body Diagram for (a) Tension and (b) Shear Tests

Damage Mechanisms in Tension

Fig. 8 depicts the basic behavior of track-to-concrete PAF connections under increasing upward displacement of the track flanges. Applying the displacement, the track web deformed and then tore out at the location of the fastener (*T*). In fact, web tearing [Fig. 8(d)] was recognized as the tension failure mode of the track-to-concrete connections in all specimens. This failure mode corresponds to the limit state of pull-over in section E5 of AISI S100-12 (2012).

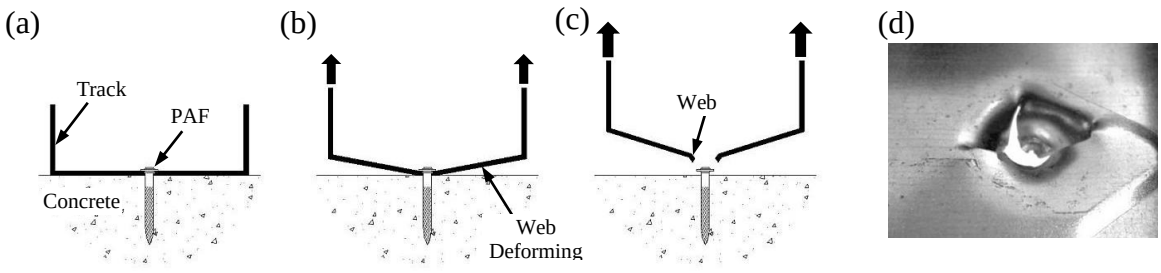

Fig. 8. Damage Mechanisms in Tension: (a) Initial Condition, (b) Deformation of the Track Web, (c) and (d) Tearing of the Track Web

Damage Mechanisms in Shear

The basic behavior and damage mechanisms of track-to-concrete PAF connections under lateral displacement of the track flanges are illustrated in Fig. 9. As the track moved, the fastener slightly bent and tore the track web (*B*). This damage mechanism correlates with the limit state of bearing and tilting, as defined by AISI S100-12 (2012). The tearing could extend until the end of the tests. However, for some specimens the track web passed over the fastener head after a number of displacement cycles [Fig. 9 (c)]. This damage, called pulling through of the fastener (*PT*) hereafter, detached the track from the concrete. Shear failure of the fastener (*S*) [Fig. 9 (d)] and pulling out of the fastener from the concrete (*PO*) [Fig. 9 (e)] were other damage mechanisms observed in the experiments. Damage mechanisms *S* and *PO* were only reported in specimens with 0.76-mm- (0.030-in.) thick tracks, while the damage mechanisms *B* and *PT* were observed in both track types (see Table 2).

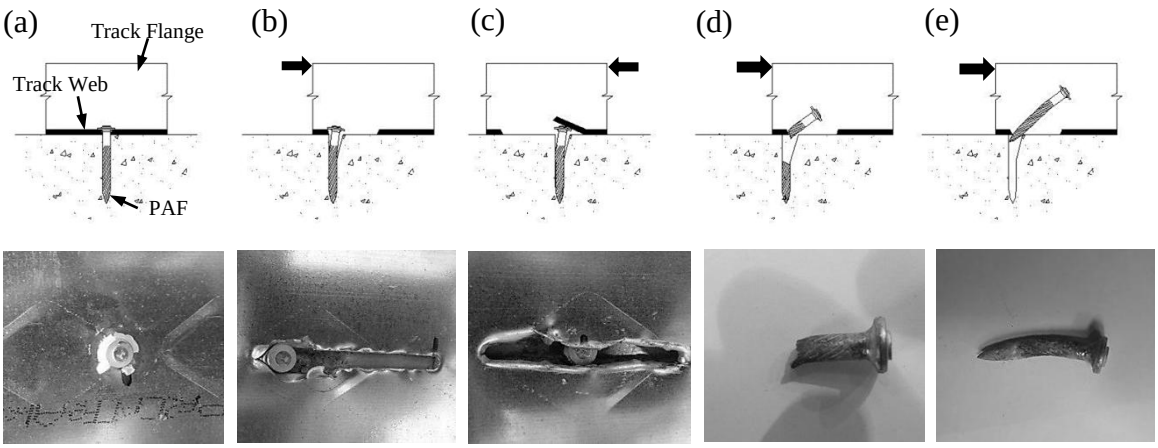

Fig. 9. Damage Mechanisms of Track-to-Concrete PAF Connections Subjected to Shear: (a) Initial Condition, (b) Bending of the Fastener and Tearing of the Track Web, (c) Pulling Through of the Fastener, (d) Shear Failure of the Fastener, (e) Pulling Out of the Fastener

Ultimate Connection Capacity

Fig. 10 and Fig. 11 show typical experimental force-displacement responses in tension and shear tests. In all specimens, the maximum load (considered as the ultimate tested capacity) was governed by the tearing of the track web (*T* in tension and *B* in shear*)*. As mentioned before, this damage mechanism corresponds to the AISI limit state of pull-over in tension and bearing and tilting in shear. Sections E5.2.3 and E5.3.2 of AISI S100 (AISI 2012) provide the following equations to calculate the tension and shear capacities of PAF connections based on these failure modes:

$$Pull - Over\ Strength\ in\ Tension: P_{nov} = \alpha_W t_1 \acute{d}_W F_{u1} \quad (1)$$

$$Beating\ and\ Tilting\ Strength\ in\ Shear: P_{nbp} = \alpha_b t_1 d_s F_{u1} \quad (2)$$

where $\alpha_W = 1.5$ and $\alpha_b = 3.2$ for simple PAFs, t_1 = track thickness, $\acute{d}_W$ = actual diameter of PAF head in contact with the track, d_s = nominal shank diameter, and F_{u1} = tensile strength of track.

Eqs. (1) and (2) were used to estimate the tension and shear connection capacity for each specimen. A tensile strength of 448 MPa (65 ksi) was considered for tracks, based on the manufacturer catalog. Table 2 presents the comparison of ultimate tested (P_{max}) and estimated capacity as well as the ratio of these values. The AISI S100-12 (2012) provision predicted the tested capacity very well. Note that for design purposes, the AISI S100-12 (2012) reduces the calculated capacity by factors of 3.0 and 2.05 (Ω factors) for tension and shear, respectively.

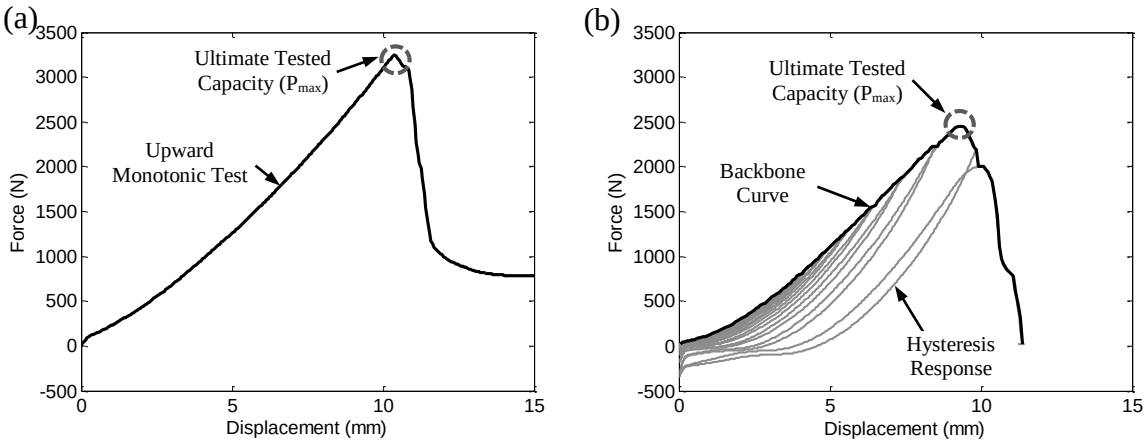

Fig. 10. Typical Experimental Responses for Tension (a) Monotonic Tests and (b) Cyclic Tests

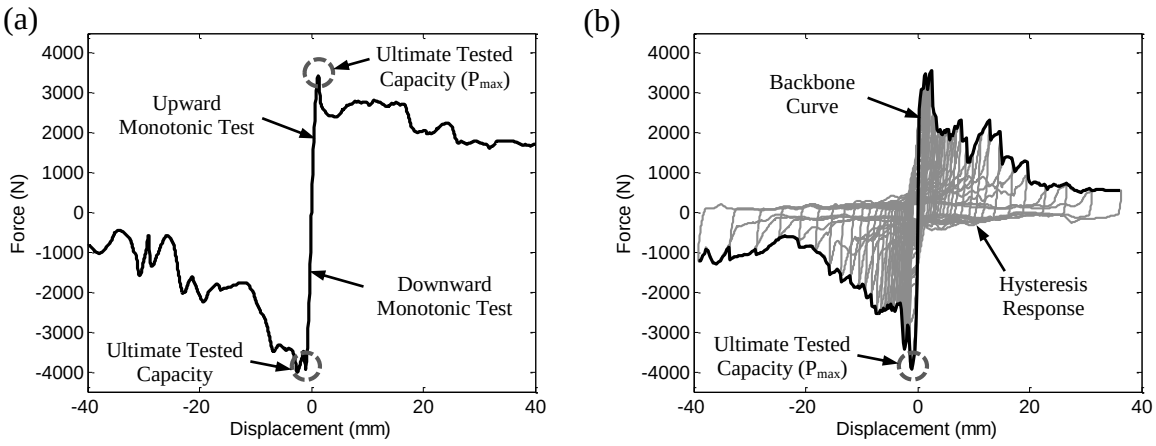

Fig. 11. Typical Experimental Responses for Shear (a) Monotonic Tests and (b) Cyclic Tests

Table 2. Shear and Tension Connection Capacity

Test Type	Track Thickness, mm (in.)	Loading Protocol	Specimen #	Ultimate Tested Capacity (P_{max}), N (lb)	Estimated Capacity, N (lb)	Tested/Estimated Ratio	Observed Damage Mechanisms
Tension	0.48 (0.019)	Monotonic	1	2726 (613)	2575 (579)	1.1	T
		Monotonic	1	3248 (730)	2575 (579)	1.3	T
		Monotonic	1	2337 (525)	2575 (579)	0.9	T
		Cyclic	1	1975 (444)	2575 (579)	0.8	T
		Cyclic	2	2452 (551)	2575 (579)	1.0	T
		Cyclic	3	2374 (534)	2575 (579)	0.9	T
	0.76 (0.030)	Monotonic	1	4413 (992)	4066 (914)	1.1	T
		Cyclic	1	4330 (973)	4066 (914)	1.1	T
		Cyclic	2	3696 (831)	4066 (914)	0.9	T
		Cyclic	3	3617 (813)	4066 (914)	0.9	T
Shear	0.48 (0.019)	Monotonic	1	3441 (774)	2760 (620)	1.2	B, PT
		Monotonic	1	4023 (904)	2760 (620)	1.5	B, PT
		Cyclic	1	2663 (599)	2760 (620)	1.0	B, PT
		Cyclic	2	3945 (887)	2760 (620)	1.4	B, PT
		Cyclic	3	3222 (724)	2760 (620)	1.2	B, PT
		Cyclic	4	3111 (699)	2760 (620)	1.1	B, PT
	0.76 (0.030)	Monotonic	1	4353 (979)	4358 (980)	1.0	B, PT
		Monotonic	1	6738 (1515)	4358 (980)	1.5	B, PT
		Cyclic	1	4513 (1014)	4358 (980)	1.0	B, PT
		Cyclic	2	4685 (1053)	4358 (980)	1.1	B, PT, S
		Cyclic	3	4649 (1045)	4358 (980)	1.1	B, PT, PO
		Cyclic	4	4450 (1000)	4358 (980)	1.0	B, S, PT

Effect of Loading Rate

The first monotonic tension test was repeated using three different loading rates [0.04 mm/sec (0.1 in./min.), 0.21 mm/sec (0.5 in./min.), and 0.42 mm/sec (1.0 in./min.)] in order to assess the effect of loading rate on the experimental results. Fig. 12(a) and Fig. 12(b) compare the force-displacement responses and the maximum force ratios in monotonic tests with different rates. The maximum force ratio was calculated by dividing the maximum force of each monotonic test by the maximum force of the monotonic test with a loading rate of 0.04 mm/sec (0.1 in./min.). Within the loading rates tested, the results varied slightly with an unclear trend. Therefore, the connection response was assumed to be not sensitive to the loading rate, and a constant loading rate of 0.21 mm/sec (0.5 in./min.) was used for the rest of the experiments. However, one may want to repeat the tests with a wider range of loading rates, test setups (including shear tests),

and specimen configurations to derive a more comprehensive conclusion on the effect of loading rates.

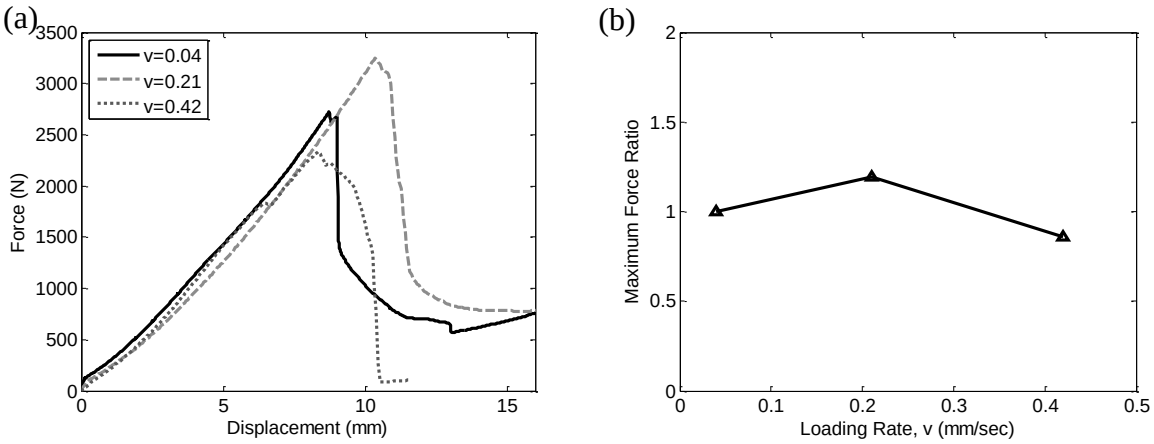

Fig. 12. Effect of Loading Rate (v, mm/sec) on: (a) Monotonic Force-Displacement Response, (b) Maximum Force Ratio

Force-Displacement Responses of Specimens in Tension

The backbone curves of cyclic tests, the median of the backbone curves, and the monotonic response of track-to-concrete PAF connections, subjected to tension force, are provided in Fig. 13. The monotonic and cyclic test results were comparable in terms of initial stiffness and failure displacement (the displacement corresponding to the complete failure of the connection). However, the cumulative damage in cyclic tests led to a reduction in the ultimate force capacity. Fig. 14 compares the median backbone curves of the specimens with 0.48-mm- and 0.76-mm- thick tracks. Using thicker tracks resulted in higher stiffness, larger capacity, and larger failure displacement. This could be due to the fact that in all specimens the failure mechanism was tearing of the track web (*T*), which was directly a function of track thickness.

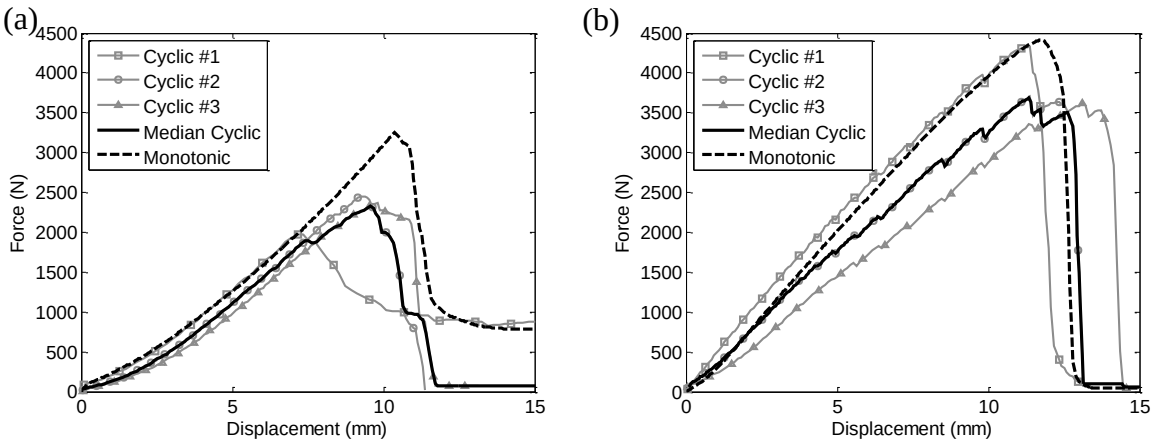

Fig. 13. Monotonic Response and Cyclic Backbone Curves of Tension Tests on Specimens with: (a) 0.48-mm-thick and (b) 0.76-mm-thick tracks

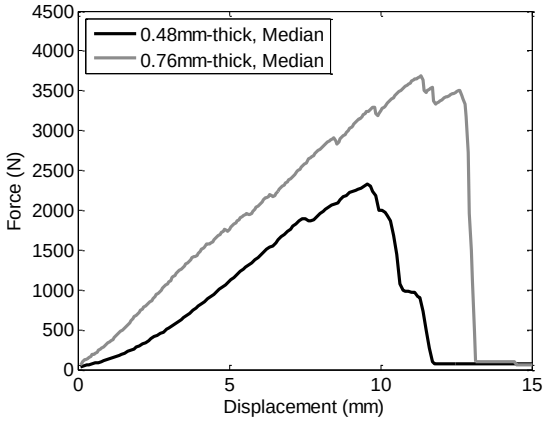

Fig. 14. Effect of Track Thickness on the Response of Cyclic Tension Test

Force-Displacement Responses of Specimens in Shear

Fig. 15 presents the force-displacement response of specimens in monotonic and cyclic tests. Similar to tension tests, the cyclic and monotonic results were consistent in terms of initial stiffness and failure displacement, but different in terms of ultimate force capacity. The ultimate force capacity in monotonic tests was larger than cyclic tests. Fig. 16 demonstrates that using thicker tracks enhanced the bearing capacity of the connection

and postponed the associated damage mechanism (*B*). However, the complete failure of the connection was usually triggered in smaller displacement in specimens with thicker tracks. In fact, the thicker specimens were less ductile than thinner specimens. Note that the failure mechanisms in specimens with 0.76-mm tracks were different from those in specimens with 0.48-mm tracks.

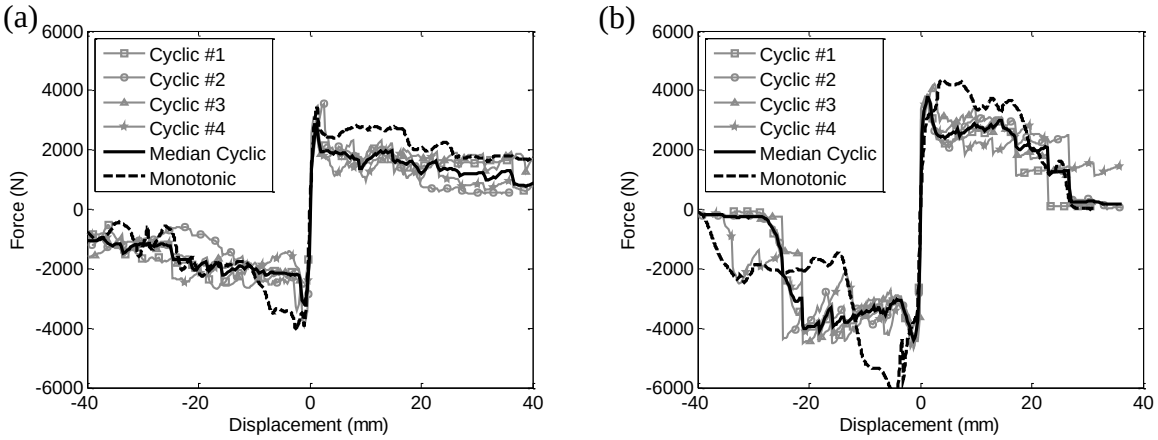

Fig. 15. Monotonic Response and Cyclic Backbone Curves of Shear Tests on Specimens with: (a) 0.48-mm-thick and (b) 0.76-mm-thick tracks

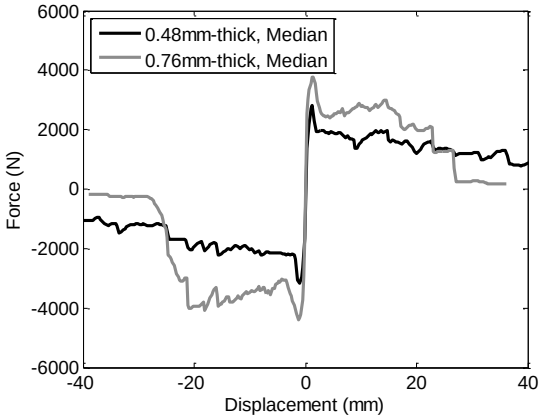

Fig. 16. Effect of Track Thickness on the Response of Cyclic Shear Test

Capacity Fragility Analysis

Capacity fragility curves are conditional probability statements of a component's (or system's) vulnerability as a function of an engineering demand parameter (*EDP*). They present the probability that the *EDP* in the component exceeds a certain level of capacity or damage states (*DSs*). The steps in generating the fragility curves can be summarized as follows: 1) choose a proper fragility formulation, 2) select appropriate engineering demand parameters, 3) determine capacity (damage state) estimates, and 4) develop fragility curves (Soroushian et al. 2014).

Several methodologies for generating capacity fragility curves have been developed over the years. In the current study, the framework proposed by Porter et al. (method *A* in Porter et al. 2007) was utilized to assess the vulnerability of track-to-concrete PAF connections. The method is based on the experimental studies and can be used where all specimens reach all *DSs* at observed values of *EDP*. According to Porter et al.: $F_{dm}(edp)$ denotes the fragility function for the damage state *dm*, defined as the probability that the component reaches or exceeds damage state *dm*, given a particular *EDP* value [Eq. (3)], and idealized by a lognormal distribution [Eq. (4)]:

$$F_{dm}(edp) \equiv P[DM \geq dm | EDP = edp] \tag{3}$$

$$F_{dm}(edp) = \Phi\left(\frac{ln(edp/x_m)}{\beta}\right) \tag{4}$$

where Φ denotes the standard normal (Gaussian) cumulative distribution function, x_m indicates the median value of the distribution, and β represents the logarithmic standard

deviation (Porter et al., 2007). The engineering demand parameter (*EDP*) should be chosen to be most closely related to the failure probability of the specimen. The tension and also shear cyclic performances of the track-to-concrete PAF connections were mainly governed by the relative displacement of the track to concrete. Therefore, such displacement was considered as the *EDP*.

In method *A*, the individual damage states are characterized by representative values for the median, x_m, and dispersion, β, for the component damage state distributions as follows (Porter et al. 2007, Soroushian et al. 2014):

$$x_m = e^{\frac{1}{N}\sum_{i=1}^{N} ln(x_i)} \tag{5}$$

$$\beta = \sqrt{\frac{1}{N-1}\sum_{i=1}^{N}\left[\ln\left(\frac{x_i}{x_m}\right)\right]^2} \tag{6}$$

Where x_i denotes the i-th measured displacement corresponding to specific damage observation (*EDPs*) and *N* is the number of cyclic tests conducted for each group of specimens. To generate the fragility curves, specimens were grouped based on the test type (tension or shear) as well as the track thickness. Therefore, *N* was equal to 3 for the tension tests and 4 for the shear tests.

Damage States in Tension

Three damage states were defined for PAF connections in tension. The first damage state (*DS1*), which denoted the onset of nonlinearity in the connection, was defined as the displacement corresponding to $0.40P_{max}$ (Peterman et al. 2014). The second damage state

(*DS2*) was set to the local maximum point on the backbone curve. This point denoted the observation of the tearing of the track web (*T*). The force capacity of the connection was significantly degraded after *DS2*, leading to the complete failure of the connection. The third damage state (*DS3*) was considered as the displacement corresponding to the complete failure of the PAF connection or 15 mm, whichever is smaller. The l5 mm limit was arbitrary defined to restrict the uplift of the track-to-concrete connection, in order to preclude the wall from interacting with other nonstructural components (such as ceiling systems) and avoid subsequent damage. Note that this limitation governed the *DS3* only in one specimen. The *DSs* are shown with their associated points on a representative backbone curve in Fig. 17(a).

Damage States in Shear

The damage states of PAF connections in shear were defined based on the extent of the nonlinearity in connections and observed damage mechanisms. *DS1*, standing for the initiation of nonlinearity in the connection, was set to the first local maximum point on the backbone curve. The bending/tilting of the fastener and tearing of the track web (*B*) was triggered at this point. The extensive damage in the connection was represented by *DS3*. The connection was assumed to be extensively damaged when it lost 60% of its force capacity ($P<0.4P_{max}$). In the experiments, this point was associated with the failure of at least one of two PAFs (damage mechanisms *PT*, *PO* or *S*). *DS2*, which indicated moderate nonlinearity in the connection, was selected as the average value between *DS1* and *DS3*. Fig. 17(b) depicts the damage states on a sample backbone curve.

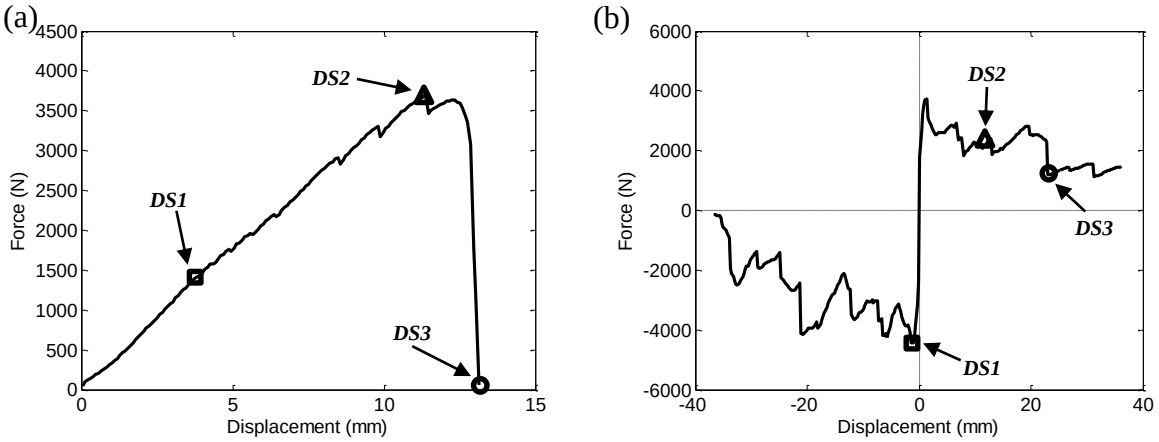

Fig. 17. Examples of Damage State Definitions for: (a) Tension Tests (b) Shear Tests

Fragility Curves

Tables 3 and 4 summarize the EDPs (x_i), x_m, and logarithmic standard deviation obtained for each group and damage level, utilizing Eqs. (5) and (6). Fig. 18 presents the fragility curves for two specimen thicknesses subjected to tension force. The curves show that the connections with thinner tracks are slightly more vulnerable than connections with thicker tracks. In contrast, increasing the track thickness intensifies the vulnerability of the connections in shear (Fig. 19). The difference is highlighted in the probability of occurrence of *DS2* and *DS3*. A similar trend can be found by comparing the median values (x_m) in Table 4. It should be mentioned that the Lilliefors goodness-of-fit test at 5% significance level (Lilliefors 1967) was performed for each group of specimens in order to check the validity of lognormal distribution. The considered fragility groups satisfied the Lilliefors goodness-of-fit test. Therefore, the lognormal distribution appropriately fitted the data.

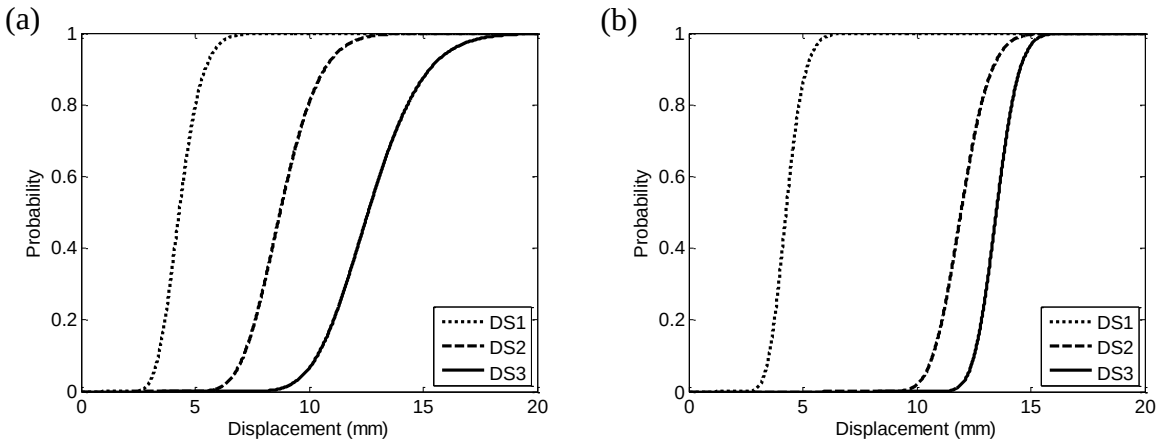

Fig. 18. Fragility Curves of PAF Connections with (a) 0.48-mm-, and (b) 0.76-mm-thick Tracks, Subjected to Tension Force

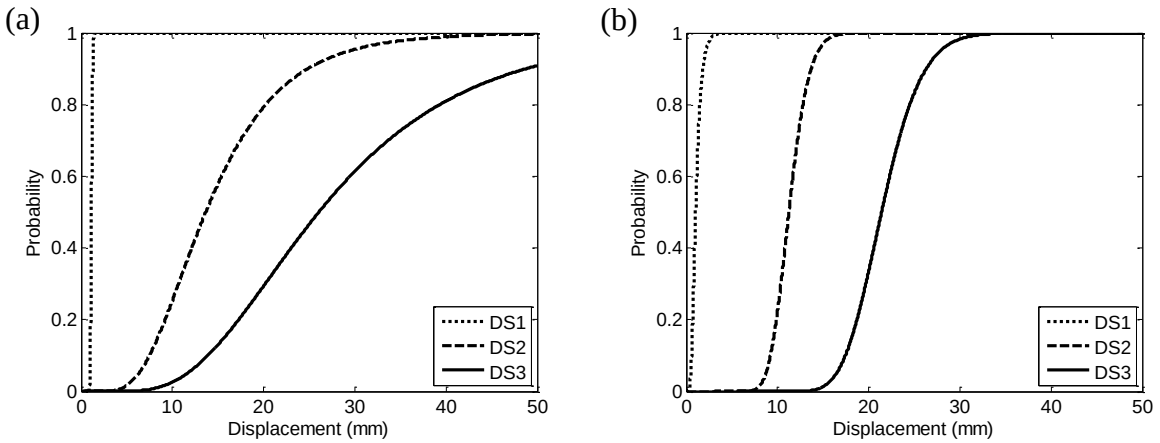

Fig. 19. Fragility Curves of PAF Connections with (a) 0.48-mm-, and (b) 0.76-mm-thick Tracks, Subjected to Shear Force

Table 3. Engineering Demand Parameters

Test Type	Group No.	Track THK, mm	Spec. No.	Disp., mm		
				DS1	*DS2*	*DS3*
Tension	#1	0.48	1	3.5	7.3	15.0
			2	4.6	9.3	11.4
			3	4.9	9.8	11.7
	#2	0.76	1	3.8	11.4	12.9
			2	4.0	11.4	13.1
			3	5.1	13.2	14.4
Shear	#1	0.48	1	1.11	17.5	33.9
			2	1.06	7.5	13.9
			3	1.29	21.9	42.5
			4	1.05	12.1	23.1
	#2	0.76	1	1.23	9.2	17.2
			2	1.30	13.1	25.0
			3	0.52	10.9	21.3
			4	1.31	12.2	23.0

Table 4. Fragility Curve Parameters

Test Type	Track THK, mm	*DS1*		*DS2*		*DS3*	
		x_m, mm	β	x_m, mm	β	x_m, mm	β
Tension	0.48	4.3	0.1	8.7	0.1	12.	0.1
	0.76	4.3	0.1	11.	0.0	13.	0.0
Shear	0.48	1.1	0.1	13.	0.4	26.	0.4
	0.76	1.0	0.4	11.	0.1	21.	0.1

Development of a Numerical Hysteresis Model for Track-to-Concrete Connections

The experimental data was used to develop two numerical hinge material models for the tension and shear behavior of track-to-concrete PFA connections. For this purpose, a one-dimensional hysteresis load-displacement relationship is defined using the "Pinching4" uniaxial material along with a "zeroLength" element in OpenSees (OpenSees 2015). This material enables the simulation of complex, pinched force hysteresis responses accounting for degradations under cyclic loadings (Soroushian et al. 2013) similar to those shown in Fig. 10(b) and Fig. 11(b). The "Pinching4" material model requires the definition of 39 parameters as presented in Fig. 20. Sixteen parameters describe the backbone curve in positive (*ePdi* and *ePfi*) and negative direction (*eNdi* and *eNfi*), while an additional eight parameters characterize the "pinched" or unloading/reloading behavior of the model. The pinching parameters include the ratio of reloading/maximum historic deformation *rDisp(P-N),* the ratio of reloading/maximum historic force *rForce(P-N),* and the ratio of negative (positive) unloading/maximum

(minimum) monotonic strength *uForceP(N)* (Soroushian et al. 2013). Unloading and reloading stiffness degradation as well as strength degradation can be considered in the model using *gKi*, *gDi* , and *gFi*. A detailed description of these parameters can be found in the OpenSees website (OpenSees 2015).

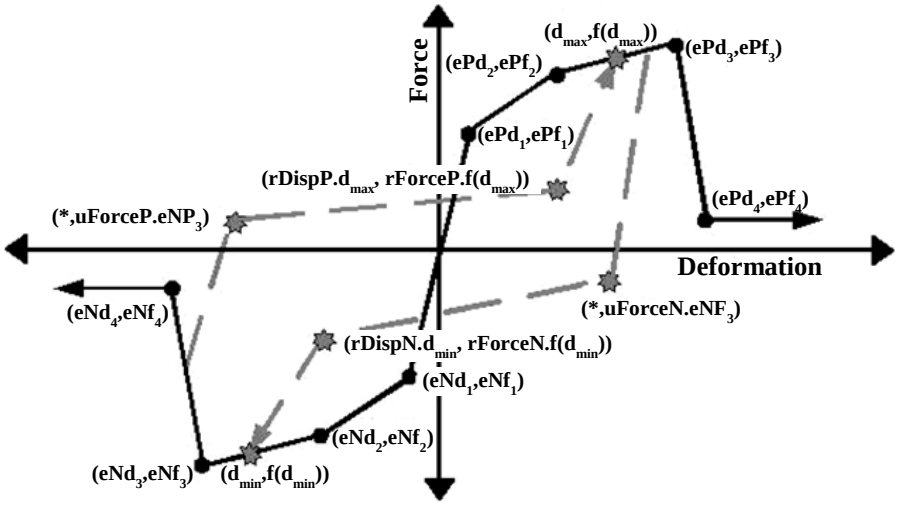

Fig. 20. Pinching 4 Material Properties (OpenSees 2015)

Calibration of Proposed Numerical Model Using Tension Experiment data

Inspired from the previous study by Soroushian et al. (2013), for each test specimen, the hysteresis response, the value of cumulative hysteresis energy, and the force histories were used in the calibration process on a visual basis. Moreover, the parameters were calibrated so that the maximum cumulative hysteresis energy remains within the ±10% range of the experimental values. The displacement histories were employed as the inputs for the numerical model. An additional 0.07-mm initial strain was applied to the model to preclude possible convergence errors. Fig. 21 shows the aforementioned characteristics of the calibrated hysteresis model for the tension response of one sample track-to-concrete PAF connection with 0.48-mm-thick track.

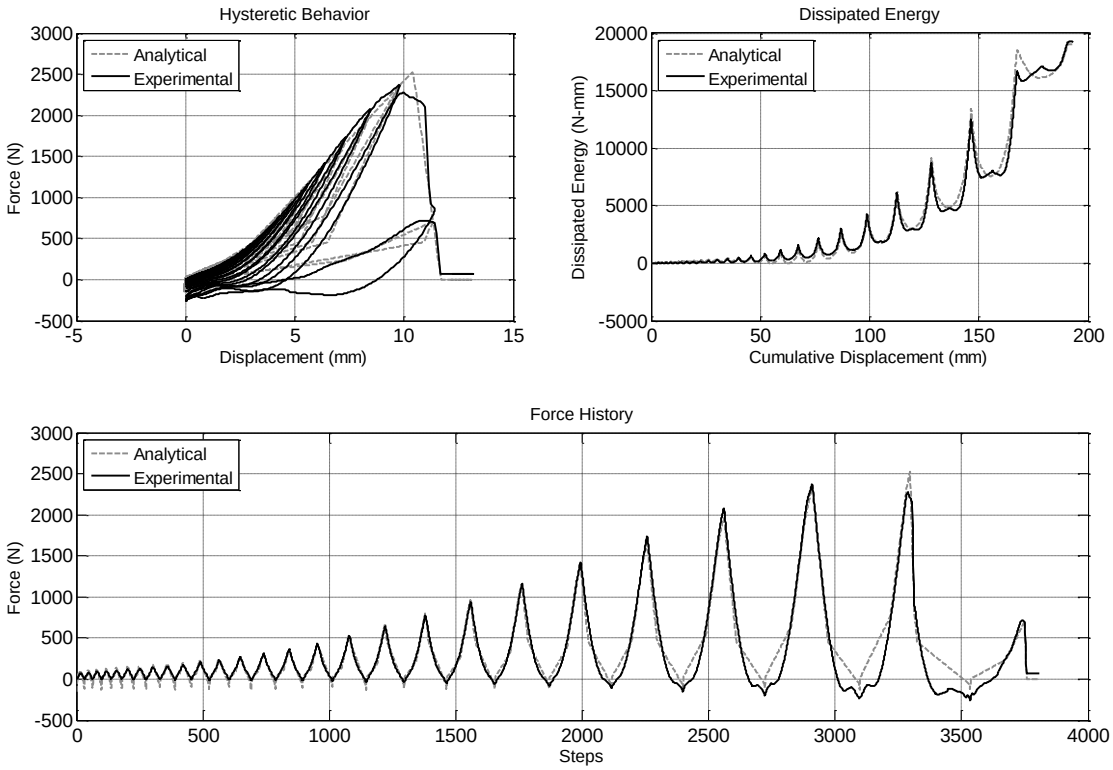

Fig. 21. Calibrated Numerical Model for a Sample Specimen (0.48-mm-thick Track, Specimen #3)

Initially, for each specimens, all 39 parameters of "Pinching4" material were calibrated to find the best correlation between numerical results and experimental data. However, the values of force and stiffness degradation parameters (*gKi*, *gDi* , and *gFi*) were found to be independent of the specimen details. Thus, constant values were assigned to these parameters. In addition, the pinching and unloading/reloading parameters were similar for specimens with the same track thickness. Table 5 shows the fixed value parameters of the hinge model.

Subsequently, to generate a numerical model with a backbone curve comparable to the experimental results, backbone points were selected for each specimen individually. As mentioned before, the specimens were tested using a tension-only loading protocol.

The negative (downward) displacement was limited to zero. However, in order to simulate the pinching and unloading/reloading behavior of the connection, the negative portion of the backbone curve of the "Pinching4" model need to be defined. The first point of the negative backbone curve (eNf_1) was selected based on the observed negative force for zero displacement. For other negative points, the values of the positive portion of the backbone curve, but with different signs, were used. Table 6 presents examples of the values used to define the backbone curves. Fig. 22(a) illustrates the comparisons of numerical and experimental results for a sample specimen.

Table 5. Fixed "Pinching4" Parameters for Tension Behavior

Track THK, mm	Parameters									
	rDispP *rDispN*	*rForceP* *rForceN*	*uForceP* *uForceN*	*gK*	*gKLimit*	*gD*	*gDLimit*	*gF*	*gE*	*dam*
0.48	0.65	0.33	0.01	0	0	0	0	0	1	cycle
	0.65	0.33	-0.18	0	0	0	0	0	1	cycle
0.76	0.60	0.20	-0.05	0	0	0	0	0	1	cycle
	0.60	0.50	-0.07	0	0	0	0	0	1	cycle

Table 6. Sample Calibrated "Pinching4" Backbone Parameters for Tension Behavior

Track THK in mm, Component Name	*ePfi* and *eNfi* in N, *ePdi* and *eNdi* in mm							
	ePf1 *ePd1*	*ePf2* *ePd2*	*ePf3* *ePd3*	*ePf4* *ePd4*	*eNf1* *eNd1*	*eNf2* *eNd2*	*eNf3* *eNd3*	*eNf4* *eNd4*
0.48 mm, Specimen #2	53	356	2491	0.01	-200	-356	-2491	-0.01
	0.1	2.5	9.5	11.7	-0.1	-2.5	-9.5	-11.7
0.76 mm, Specimen #2	89	979	3914	0.01	-756	-979	-3914	-0.01
	0.1	2.5	12.4	13.3	-0.1	-2.5	-12.4	-13.3

Calibration of Proposed Numerical Model Using Shear Experiment Data

The same procedure, explained in the previous section, was employed to calibrate the shear numerical model based on the hysteresis response, the value of cumulative hysteresis energy, and force histories. After performing a sensitivity analysis on 39 parameters of "Pinching4" material, all pinching and unloading/reloading parameters,

except *rForce(P-N)*, were found to be independent of specimen details. Besides that, the values of *rForce(P-N)* were similar for specimens with the same track thickness. Therefore fixed values were adopted for these parameters. Table 7 shows the fixed value parameters of the hinge models for track-to-concrete PAF connections, subjected to shear force.

Table 7. Fixed "Pinching4" Parameters for Shear Behavior

Track THK, mm	Parameters									
	rForceP-N	*rDispP-N*	*uForceP-N*	*gK*	*gKLimit*	*gD*	*gDLimit*	*gF*	*gE*	*dam*
0.48	0.12	0.75	0.01	0	0	0	0	0	1	cycle
0.76	0.17	0.75	0.01	0	0	0	0	0	1	cycle

The shear response of the connection was assumed be symmetric. Accordingly, similar values (with different signs) were assigned to the positive and negative portions of the backbone curves. Examples of the values used to define the backbone curves are provided in Table 8. Fig. 22(b) depicts the comparisons of sample numerical and experimental results.

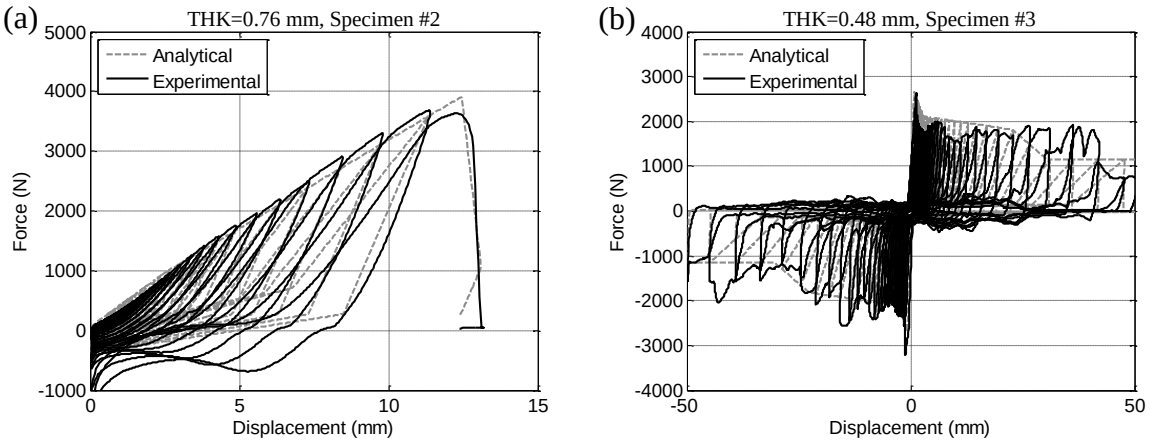

Fig. 22. Sample Numerical-Experimental Comparisons of Specimens Subjected to (a) Tension and (b) Shear Force

Table 8. Sample Calibrated "Pinching4" Backbone Parameters for Shear Behavior

Track THK in mm, Component Name	*ePfi* and *eNfi* in N, *ePdi* and *eNdi* in mm							
	ePf1	*ePf2*	*ePf3*	*ePf4*	*eNf1*	*eNf2*	*eNf3*	*eNf4*
	ePd1	*ePd2*	*ePd3*	*ePd4*	*eNd1*	*eNd2*	*eNd3*	*eNd4*
0.48 mm, Specimen #4	3069	1779	1775	890	-3069	-1779	-1775	-890
	1.0	2.5	22.9	24.1	-1.0	-2.5	-22.9	-24.1
0.76 mm, Specimen #1	4048	3203	3198	0.01	-4048	-3203	-3198	-0.01
	0.8	2.5	19.1	27.9	-0.8	-2.5	-19.1	-27.9

Development of Generic Models

In the previous section, the 16 backbone parameters (ePd_i, ePf_i, *etc)* of "Pinching4" material were optimized based on the experimental data of each specimen individually. Although the pinching and unloading/re-loading parameters for each group of specimens (as defined in Table 4) were quite similar, there were minor discrepancies between the backbone parameters. Therefore, for the simplicity of future numerical studies, one suite of material parameters was defined as the representative parameter for each group of specimens, called the generic model. For this purpose, the method proposed by Soroushian et al. (2014) was implemented. The method uses the following assumptions to develop the generic model for tension/shear behavior: 1) For each specimen group, a generic model is defined; 2) the displacement points of the backbone curve (in each direction), ePd_1, ePd_2, ePd_3, ePd_4 (Fig. 20), are set to the median of the calibrated values corresponding to each of these points of the backbone curve; 3) a linear interpolation is used to find the force corresponding to the previously mentioned displacements where the force values at the calibrated backbone curves are unavailable. The median of these force values for each set defines the backbone points in each direction (ePf_1 ePf_2, ePf_3, and ePf_4 in Fig. 20); 4) the remainder of the parameters (fixed parameters) are the same as those suggested in Table 5 for tension and Table 7 for shear behavior.

The generic model parameters, obtained based on the previously mentioned assumptions, are presented in Table 9. Fig. 23 demonstrates the comparison between the generic backbone curves and all the calibrated backbone curves in two sample groups. Consider that these generic models only represent the track-to-concrete PAF connections with properties (track material and thickness, and PAF type) similar to what were tested in each group. Fig. 24 compares the generic models with the sample experimental data from tension and shear tests.

Table 9. "Pinching4" Backbone Parameters for Generic Models

Test Type	Group No.	Track THK, mm	*ePfi* and *eNfi* in N, *ePdi* and *eNdi* in mm							
			ePf1	*ePf2*	*ePf3*	*ePf4*	*eNf1*	*eNf2*	*eNf3*	*eNf4*
			ePd1	*ePd2*	*ePd3*	*ePd4*	*eNd1*	*eNd2*	*eNd3*	*eNd4*
Tension	#1	0.48	47	356	2284	0.01	-47	-356	-2284	-0.01
			0.1	2.5	9.5	11.7	-0.1	-2.5	-9.5	-11.7
	#2	0.76	102	979	3506	0.01	-102	-979	-3506	-0.01
			0.1	2.5	12.4	13.3	-0.1	-2.5	-12.4	-13.3
Shear	#1	0.48	2577	2111	1816	1151	-2577	-2111	-1816	-1151
			0.8	2.8	22.9	30.5	-0.8	-2.8	-22.9	-30.5
	#2	0.76	4115	3180	3051	204	-4115	-3180	-3051	-204
			0.8	2.8	19.7	30.1	-0.8	-2.8	-19.7	-30.1

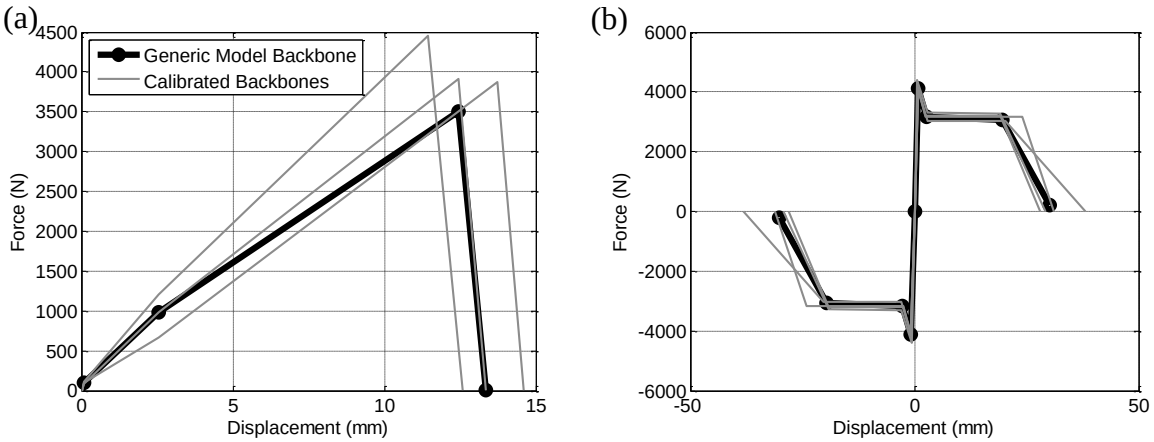

Fig. 23. Generic Backbone Curves Group #2 of Specimens, Subjected to (a) Tension and (b) Shear Force

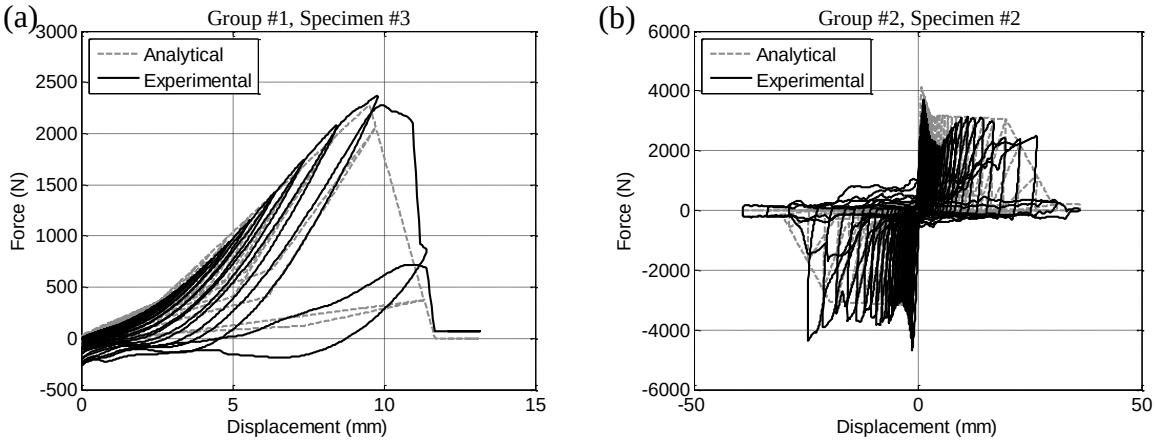

Fig. 24. Sample Generic Numerical-Experimental Hysteresis Comparison of Specimens Subjected to (a) Tension and (b) Shear Force

Proposed Generic Models for Untested Track Thicknesses

The main goal of the current study was to provide the numerical model for track-to-concrete connections with two common track thicknesses (0.48 mm and 0.76 mm). Nonetheless, an approximate method is proposed in this section to generate numerical models of connections with different track thicknesses. The proposed method is based on the assumption that the maximum connection capacity is always governed by the tearing of the track web. Note that supplemental experimental and numerical studies are needed in order to determine the accurate hysteresis behavior of the track-to-concrete connections with various track profiles, concrete materials, and PAF types.

The generic numerical model for untested track thicknesses can be developed using the following procedure: : 1) two generic models, one for tension behavior and one for shear behavior, are suggested, 2) the backbone curve displacement values (ePd_i and eNd_i) are considered to be constant (independent of the track thickness) and equal to the median of the calibrated values of all (eight) tested specimens, 3) all backbone curve force values

(ePf_i and eNf_i) of each specimen model are normalized with respect to the maximum force value (ePf_3 in tension and ePf_1 in shear), 4) the median of eight normalized force values corresponding to each backbone point are used to define the normalized generic backbone curve (Fig. 25 and Table 10), 5) the normalized generic backbone curve are then multiplied by the ultimate tension/shear capacity, calculated based on Eqs. (1) and (2), to develop the numerical backbone curve for any track thicknesses, 6) the "pinching" and unloading/reloading parameters of the model can be set to the average values presented in Tables 5 and 7.

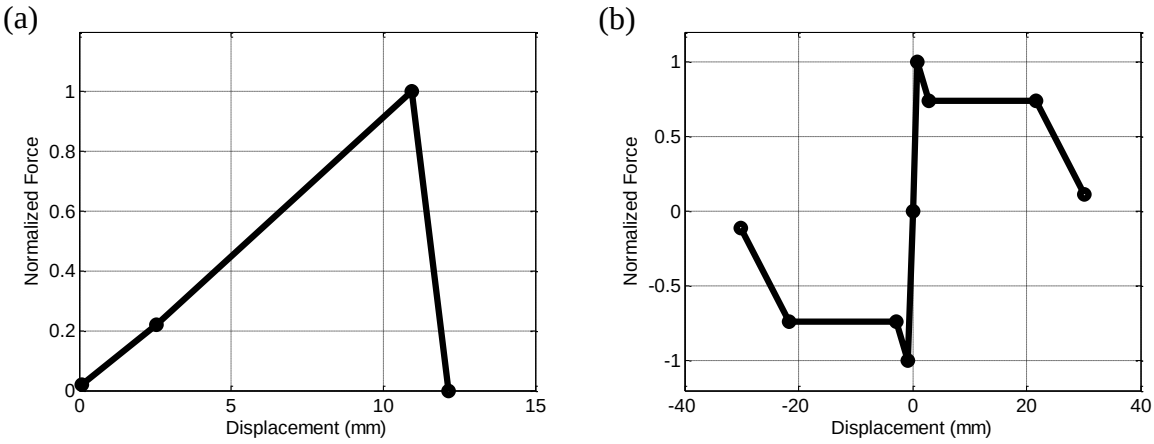

Fig. 25. Normalized Generic Backbone Curves for Untested Track Thicknesses, Subjected to (a) Tension and (b) Shear Force

Table 10. "Pinching4" Backbone Parameters for Generic Models for Untested Track

Test Type	Normalized *ePfi* and *eNfi* (unitless), *ePdi* and *eNdi* (mm)							
	ePf1 *ePd1*	*ePf2* *ePd2*	*ePf3* *ePd3*	*ePf4* *ePd4*	*eNf1* *eNd1*	*eNf2* *eNd2*	*eNf3* *eNd3*	*eNf4* *eNd4*
Tension	0.02	0.21	1.00	0.00	-0.13	-0.21	-1.00	-0.00
	0.1	2.5	10.9	12.1	-0.1	-2.5	-10.9	-12.1
Shear	1.00	0.74	0.74	0.11	-1.00	-0.74	-0.74	-0.11
	0.8	2.8	21.6	30.1	-0.8	-2.8	-21.6	-30.1

Summary and Conclusions

A total of 22 monotonic and reverse cyclic tests were conducted on track-to-concrete PAF connections as part of a larger investigation of nonstructural partition wall behavior. The test program was designed to evaluate the displacement and strength capacities and stiffness of PAF connections between concrete base material and cold-formed steel-tracks in nonstructural partition walls, subjected to either tension or shear force. The test data were adopted to develop capacity fragility curves for the connection in terms of displacement.

The main observations and conclusions obtained from the experimental study are as follows:

- The damage mechanisms of the track-to-concrete connection in tension included plastic deformation and tearing-out of the track web at the fastener location. In shear, the damage mechanisms consisted of bending of the fastener and tearing of the track web, as well as pulling through of the fastener, shear failure of the fastener, and pulling out of the fastener.
- The suggested equations by AISI S100-12 (AISI 2012) could appropriately predict the ultimate force capacity of the connection in both tension and shear. The ultimate force capacity was mainly dominated by tearing of the web of the track.
- Specimens with thicker tracks showed higher stiffness and larger force capacity in both tension and shear tests. However, using thicker tracks led to different failure mechanisms in shear tests, which resulted in failure of the connection in smaller displacements.

- The fragility analysis showed that, for the shear force, the connections with thicker tracks were more vulnerable in terms of achieving the last damage state.
- A series of nonlinear hinges were defined and calibrated for all specimens based on the experimental data. Subsequently, one suite of material parameters is proposed as the representative parameters for each group of specimens. These parameters define the generic models that represent the track-to-concrete PAF connections with properties (track material and thickness, and PAF type) similar to what have been tested in each group. Consider that for connections with different material or PAF types, new sets of model parameters need to be calibrated through additional experimental and numerical studies.

The hinge model of track-to-concrete connections could be utilized along with the numerical models of other wall components (such as gypsum-to-stud connections and steel studs) to develop a comprehensive numerical model of a partition wall assembly. The partition wall model could then be subjected to realistic input motions (e.g. floor accelerations) to estimate the demand parameters on each component. These demand estimations could be used in conjunction with the capacity parameters (e.g. median and deviation) developed in this study (and similar studies for other partition wall components) to generate fragility curves for partition wall systems in terms of more global engineering demand parameters, such as floor accelerations and/or inter-story drifts.

Acknowledgments

The current material is based upon work supported by the National Science Foundation under Grant No. 0721399. This Grand Challenge (GC) project to study the seismic response of nonstructural systems is under the direction of M. Maragakis from the University of Nevada, Reno and Co-PIs: T. Hutchinson (UCSD), A. Filiatrault (UB), S. French (G. Tech), and B. Reitherman (CUREE). Any opinions, findings, conclusions, or recommendations expressed in the current document are those of the investigators and do not necessarily reflect the views of the sponsors. The input provided by the Practice Committee of the NEES Nonstructural Project, composed of W. Holmes (Chair), D. Allen, D. Alvarez, and R. Fleming, and by the Advisory Board, composed of R. Bachman (Chair), S. Eder, R. Kirchner, E. Miranda, W. Petak, S. Rose and C. Tokas, has been crucial for the completion of this research. Assistance from M. Lattin of the University of Nevada, Reno material lab during the assembly and testing as well as support from Johnnie Stolz of Omboli Interior Inc. is appreciated.

References

AISI S100-12 (2012). "North American Specification for the Design of Cold- Formed Steel Structural Members." American Iron and Steel Institute, Washington, DC.

Bersofsky, A. M. (2004). "A Seismic Performance Evaluation of Gypsum Wallboard Partitions." M.S. Thesis, Dept. of Structural Engineering, Univ. of California, San Diego, La Jolla, CA.

Dhakal, R. P. (2010). "Damage to non-structural components and contents in 2010 Darfield earthquake." *Bulletin of The New Zealand Society for Earthquake Engineering*, 43, 404-411.

Davies, D., Retamales, R., Mosqueda, G., and Filiatrault, A., (2011). "Experimental Seismic Evaluation, Model Parameterization, and Effects of Cold-Formed Steel-Framed Gypsum Partition Walls on The Seismic Performance of an Essential Facility." *Technical Report MCEER-11-0005,* State Univ. of New York, Buffalo, NY.

Fülöp, L. A., and Dubina, D. (2004). "Performance of Wall-Stud Cold-Formed Shear Panels under Monotonic and Cyclic Loading, Part I: Experimental research." *Thin-Walled Structures,* 42, 321–338.

Jenkins, C., Soroushian, S., Rahmanishamsi, E., and Maragakis, M. (2015). "Experimental Fragility Analysis of Cold-Formed Steel-Framed Partition Wall Systems." *Structural Congress, ASCE*, Portland, OR.

Lee, T., Kato, M., Matsumiya, T., Suita, K., Nakashima, M. (2007) "Seismic Performance Evaluation of Non-structural Components: Drywall Partitions." *Earthquake Engineering and Structural Dynamics,* 36, 367–382.

Lilliefors, H. (1967). "On the Kolmogorov-Smirnov test for normality with mean and variance unknown." *Journal of the American Statistical Association,* 62, 399-402.

Miller, T.H. and Pekoz, T. (1994). "Behavior of Gypsum-Sheathed Cold-Formed Steel Wall Studs." *Journal of Structural Engineering*, 120, 1644-1650.

Miranda, E., Mosqueda. G., Retamales, R., and Pekcan, G. (2012). "Performance of Nonstructural Components during the February 27, 2010 Chile Earthquake." *Earthquake Spectra*, 28, 453-471.

Open System for Earthquake Engineering Simulation (OpenSees) website (2015). <http://www.opensees.berkeley.edu . PEER, Berkeley: University of California>.

Peterman, K.D., Nakata, N., and Schafer, B.W. (2014). "Hysteretic Characterization of Cold-formed Steel Stud-to-Sheathing Connections." *Journal of Construction Steel Research*. 101, 254–264.

Porter, K., R. Kennedy and R. Bachman. (2007). "Creating Fragility Functions for Performance-Based Earthquake Engineering." *Earthquake Spectra*, 23, 471-489.

Rahmanishamsi, E., Soroushian, S., and Maragakis, M. (2014). "System-Level Experiments on Ceiling/Piping/Partition Systems at UNR-NEES Site." *Proc., Tenth U.S. National Conference on Earthquake Engineering*, Anchorage, AK.

Rahmanishamsi, E., Soroushian, S., and Maragakis, M. (2015). "Cyclic Shear Behavior of Gypsum Board-to-Steel Stud Screw Connections in Nonstructural Walls." *Earthquake Spectra*, in press.

Ramirez, R., LaBoube, R. A. (2013). "Report on Laboratory Testing of Fastening CFS Tracks to Concrete Base Materials with PAFs." *Research Report RP04-2*, American Iron and Steel Institute, Washington, DC.

Restrepo, J.I., and Bersofsky, A. (2010). "Performance Characteristics of Light Gage Steel Stud Partition Walls." *Thin-Walled Structures*, 49, 317–324.

Restrepo, J.I., and Lang, A.F. (2011). "Study of Loading Protocol in Light-Gauge Stud Partition Wall." *Earthquake Spectra,* 27, 1169–1185.

Retamales, R., Mosqueda, G., Filiatrault, A., and Reinhorn, A.M. (2008). "New Experimental Capabilities and Loading Protocols for Seismic Qualification and Fragility Assessment of Nonstructural Components". *Technical Report MCEER-08-0026,* State Univ. of New York, Buffalo, NY.

Retamales, R., Mosqueda, G., Filiatrault, A., and Reinhorn, A.M. (2011). "Testing protocol for experimental seismic qualification of distributed nonstructural systems." *Earthquake Spectra,* 27(3):835-856.

Retamales, R., Davies, R., Mosqueda, and G., Filiatrault, A. (2013). "Experimental Seismic Fragility of Cold-Formed Steel Framed Gypsum Partition Walls." *Journal of Structural Engineering*, 139, 1285-1293.

Soroushian, S., Ryan, K. L., Maragakis, M., Wieser, J., Sasaki, T., Sato, E., Okazaki, T., Tedesco, L., Zaghi, A. E., Mosqueda, G., Alarez, D. (2012) "NEES/E-Defense tests: Seismic performance of ceiling/sprinkler piping nonstructural systems in base isolated and fixed base building," *15th World Conference on Earthquake Engineering (15WCEE)*, Lisbon, Portugal.

Soroushian, S., Maragakis, M., and Jenkins, C., 2014. *Axial Capacity Evaluation of Typical Suspended Ceiling Joints. Earthquake Spectra*, in-press.

Soroushian, S., Zaghi, E., Maragakis, M., Tian, T., and Filiatrault, A. (2013). "Analytical Seismic Fragility Analyses of Fire Sprinkler Piping Systems with Threaded Joints." *Earthquake Spectra,* in-Press.

Tasligedik, A. S., Pampanin, S., Palermo, A. (2014) “Low Damage Non-structural Drywalls: Details and Their Performance.” *Proc. 2014 NZSEE Conference*, Auckland, New Zealand.

Ubejd Mujagic, J. R., Green, P. S., and Gould, W. G. (2010). “Strength Prediction Model for Power Actuated Fasteners Connecting Steel Members in Tension and Shear–North American Applications.” *Proc. Twentieth International Specialty Conference on Cold-Formed Steel Structures*, St. Louis, MO.

Wang X, Pantoli E, Hutchinson T, Restrepo J, Wood R, Hoehler M, Grzesik P, and Sesma F. (2015) “Seismic Performance of Cold-Formed Steel Wall Systems in a Full-Scale Building.” *ASCE Journal of Structural Engineering.*

Wood, R.L. and Hutchinson, T.C. (2012). “A Numerical Model for Capturing the In-Plane Seismic Response of Interior Metal Stud Partition Walls.” *Technical Report MCEER-12-0007*, State Univ. of New York, Buffalo, NY.

Chapter 6

Analytical model for the in-plane seismic performance of cold-formed steel-framed gypsum partition walls

E. Rahmanishamsi, S. Soroushian, E. M. Maragakis

Please note that this chapter is a self-contained paper accepted for publication in the Journal of Earthquake Engineering and Structural Dynamics where the word 'this paper/study' refers to the chapter itself.

SUMMARY

This paper proposes an experimentally verified procedure to analytically model cold-formed steel-framed gypsum nonstructural partition walls considering all the critical components. In this model, the nonlinear behaviors of the connections are represented by hysteretic load-deformation springs, which have been calibrated using the component-level experimental data. The studs and tracks are modeled adopting beam elements with their section properties accounting for nonlinear behavior. The gypsum boards are simulated by linear four-node shell elements. The proposed procedure is implemented to generate the analytical models of three full-scale partition wall specimens in the OpenSees platform. The specimens were tested as a part of the NEESR-GC Project on Simulation of the Seismic Performance of Nonstructural Systems. Force-displacement responses, cumulative dissipated energy, and damage mechanisms from the analytical simulation are compared to the experimental results. The comparison shows that the analytical model accurately predicts the trend of the response as well as the possible damage mechanisms. The procedure proposed here can be adopted in future studies by researchers and also engineers to assess the seismic performance of partition walls with various dimensions and construction details, especially where test data is not available.

KEYWORDS: nonstructural systems; partition walls; analytical model; seismic response

1. INTRODUCTION

After many years of the development of performance-based earthquake engineering (PBEE) methodologies, it is now well-known that nonstructural systems play a critical role in PBEE methodology [1]. These systems account for approximately 48% to 70% of the total investment in buildings [2]. Unfortunately, damage to most types of nonstructural systems has been often triggered at shake intensities much lower than those required to initiate structural damage [2-7]. Damage to these systems can lead to huge economic loss and lower the performance level of the entire building, even if the structural system remains intact [8**]**. Among various nonstructural systems, partition walls

represent a large portion of the total investment. These walls configure the architectural layout of a building and facilitate its functionality for occupants [9]. Previous earthquakes have shown pervasive damage to partition walls, frequently initiated at story drift levels well below the yield point of structures [9]. Such damage can result not only in property loss but also in loss of function of essential facilities, such as hospitals, even in low- or mid- intensity earthquake events.

This study focuses on light-gauge steel-framed gypsum partition walls, as one of the most widely used nonstructural systems. Several damage mechanisms were identified for these walls during past earthquakes, including bending of studs, failure of gypsum board-to-stud/track connections, cracking of gypsum boards around openings, damage in stud-to-track connections, failure of track-to-concrete connections, crushing of wall corners, failure of brace connections, and complete collapse [2-7]. Among them, damage at the connections between various elements of the walls (e.g. gypsum board-to-stud/track connections) was predominant. Similar observations were reported in recent experimental studies on the seismic performance of partition walls [1,8-15]. The experimental studies also revealed that the force and displacement characteristics and behavior of partition walls (i.e. stiffness, strength, degradation, and pinching) depended on the performance of the wall connections as well as the properties of framing elements. Therefore, in order to accurately capture the lateral behavior and damage mechanisms of partition walls through analytical modeling, it is essential to include the behavior of all individual components.

While a significant body of literature is available on the analytical modeling of structural shear walls constructed from either wood or steel studs [16-24], limited studies have been conducted on the analytical modeling of nonstructural partition walls. Kanvinde and Deierlein [25] proposed analytical models to determine the lateral shear strength and initial elastic stiffness of wood-framed gypsum partition walls, taking into account the effect of wall geometry, door and window openings, connector type and spacing, and wall boundary conditions. The authors also presented coefficients required to calibrate a peak-oriented hysteretic model. Adopting the data from previous experiments performed by Restrepo and Bersofsky [12] in addition to data from two new experiments, Restrepo and Lang [13] postulated a four-line piecewise backbone response envelop for gypsum partition walls. Recently, Davies et al. [26] and Wood and Hutchinson [9] used the experimental data from the NEESR-GC project (NEESR-GC: Simulation of the Seismic Performance of Nonstructural Systems) to calibrate equivalent analytical models that represented the in-plane hysteresis behavior of cold-formed steel-framed partition walls.

Although the aforementioned studies provided valuable information on characteristics of partition wall behavior, they were limited to lumped level modeling. In this modeling methodology, a wall assembly is represented by a single nonlinear element. The methodology is appropriate when the objective is narrowed down to predicting the global behavior of a wall; nonetheless it cannot supply the information on the performance of individual wall components. In fact, a comprehensive model of the wall, which includes all the components, needs to be assembled in order to capture all local behaviors and damage mechanisms. The comprehensive model can be used to predict force-displacement response and damage mechanisms of partition walls with various dimensions (i.e., length and height) and construction details (e.g., stud spacing and

connection spacing) for which experimental results are not available. The model can also help to identify the sequence of damage mechanisms in the walls. This is particularly important for damage mechanisms that cannot be detected during experiments, such as forming plastic hinges in field studs and tearing of track webs. These mechanisms occur at locations that are enclosed within the sheathing boards. In addition, there are some efforts underway by researchers to introduce new details, such as details for stud to top-track connections, to mitigate the damage in partition walls [26]. The comprehensive model can be used as a preliminary tool to investigate and compare various details and select the most persuasive ones to be tested in a subsequent experimental study. This reduces the required time and cost to design and evaluate the new details.

This study employs the results of a series of component-level experiments, performed at the University of Nevada, Reno (UNR), to provide a detailed yet computationally efficient analytical model for cold-formed steel-framed gypsum partition walls that accounts for the nonlinear behavior of all critical components. The paper begins with a description of typical partition walls and the proposed analytical model, followed by a summary of required parameters for the modeling. Subsequently, the modeling procedure is adopted to generate the analytical model of three full-scale partition wall assemblies, tested at the University of Buffalo (UB). The analytical and experimental hysteresis force-displacement responses, dissipated energy, and damage mechanisms are compared. This research provides a mechanically based method to estimate the lateral response of various steel-framed gypsum partition wall configurations. The model can also be adopted for seismic assessment studies (such as fragility analysis), in which extensive analytical analyses are necessary.

2. THE PROPOSED ANALYTICAL MODEL

Typical construction of partition walls consists of C-shaped, cold-formed light-gauge steel studs nested in and screwed to C-shaped steel tracks at the top and bottom. The track is usually fastened to the structural slab with power-actuated fasteners (PAFs) and is used to align the vertical studs [12]. The gypsum board, consisting of a rigid gypsum core sandwiched between paper layers, is attached to the studs and track with bugle-headed drywall screws placed at regular intervals (Figure 1). The goal of this study is to develop an elaborated and yet computationally efficient procedure to analytically model the steel-framed gypsum partition walls considering all these components (Figure 2). For this purpose, various combinations of the material and element models, available in the OpenSees library [27], have been deeply investigated. The following sections summarize the findings of this investigation and present general recommendations required to construct the analytical model of a partition wall in future studies, without repeating the trial-and-error process. The proposed model, Figure 2, is considered appropriate to accurately capture the in-plane force-displacement responses and damage mechanisms of partition walls.

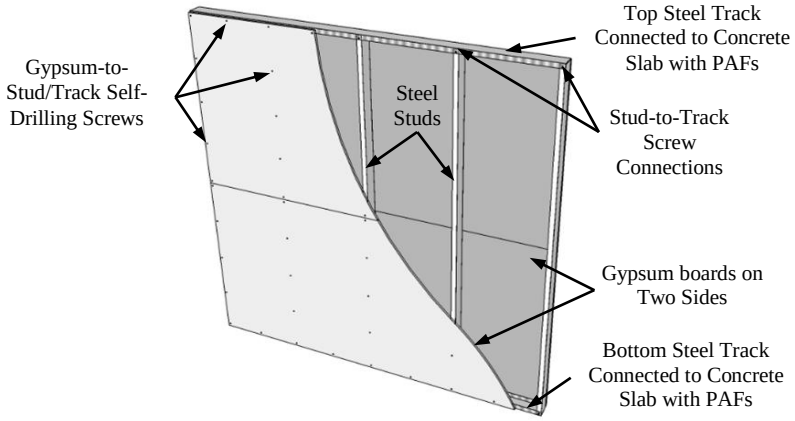

Figure 1. Typical steel-framed gypsum partition walls

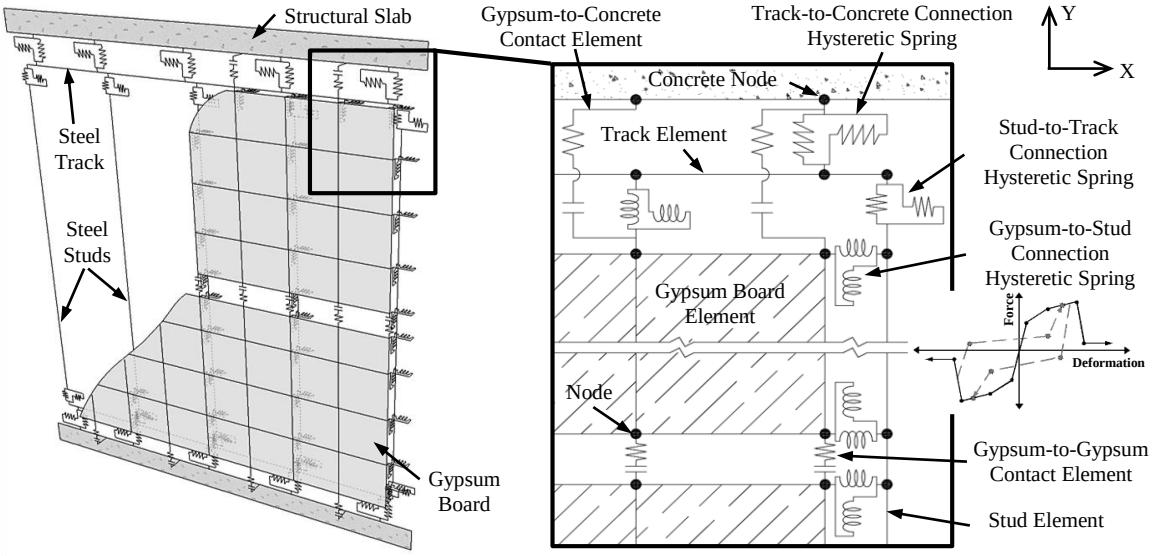

Figure 2. Schematic diagram of an analytical model of a steel-framed gypsum partition wall, after Rahmanishamsi et al. [28]

2.1. Gypsum boards and frame elements

The studs and tracks are modeled using nonlinear "Force-Based Beam-Column" elements with a fiber-section consisting of the Giuffre-Menegotto-Pinto steel material [29]. The gypsum boards are simulated by "ShellMITC4" four-node elements with the "ElasticMembranePlate-Section." The shell and frame elements are meshed into a number of subelements in order to provide nodes at locations of gypsum-to-stud/track connections and increase the accuracy of modeling. The maximum size of the subelements are specified based on the distance between gypsum-to-stud/track connections. The section properties, such as dimensions and weight, are selected from the manufacturer catalog [30,31]. When the factory punch-outs are provided on studs, a modified section is defined for the location of punch-outs. The material properties,

including modulus of elasticity, yield strength, Poisson ratio, and hardening slope ratio, can be determined based on the manufacturer catalog (especially for gypsum boards) or more accurately based on coupon test results. The mass of stud and track elements are concentrated at the nodal points, while the mass of gypsum boards are considered by assigning a unit mass to "ElasticMembranePlate-Section." The weights of the elements are defined as the nodal loads.

2.2. Connections

The nonlinear behaviors of partition wall connections, namely the gypsum board-to-stud/track, stud-to-track, and track-to-concrete connections, are represented employing the "Pinching4" material along with "twoNodeLink" elements [27]. The "Pinching4" material enables the simulation of complex pinched force hysteresis responses accounting for degradations under cyclic loadings [32]. This material model requires the definition of 39 parameters as presented in Figure 3. Sixteen parameters describe the backbone curve in positive (*ePdi* and *ePfi*) and negative direction (*eNdi* and *eNfi*), while an additional eight parameters characterize the "pinched" or unloading/reloading behavior of the model. The pinching parameters include the ratio of reloading/maximum historic deformation *rDisp(P-N)*, the ratio of reloading/maximum historic force *rForce(P-N)*, and the ratio of negative (positive) unloading/maximum (minimum) monotonic strength *uForceP(N)* [32]. Unloading and reloading stiffness degradation as well as strength degradation can be considered in the model using *gKi*, *gDi*, and *gFi*.

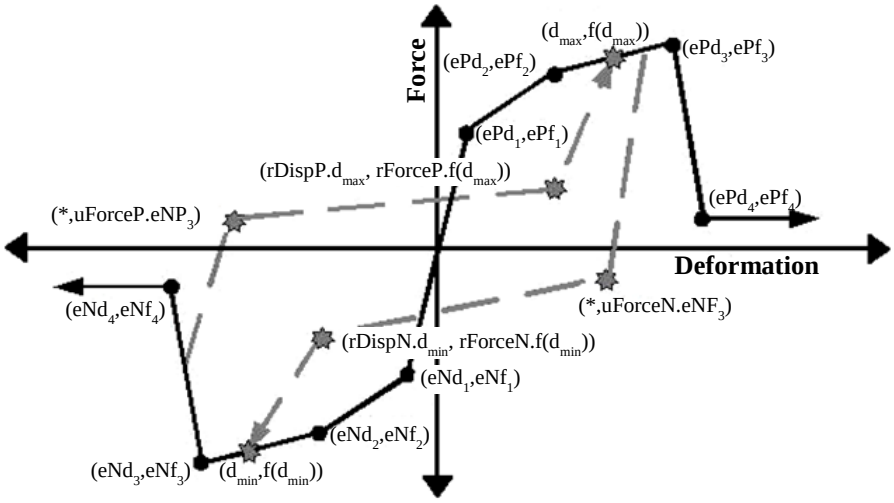

Figure 3. Pinching 4 material parameters [27]

The parameters of the "Pinching4" material have been calibrated using the component-level experimental data, conducted as a part of the current project [28,33,34]. Tables 1-3 summarize the material parameters for various connections. The connections are categorized based on the connection type (gypsum board-to-stud/track, stud-to-track, and track-to-concrete connections) and connection properties (e.g. stud thickness). In

Table 1, for each category three subgroups are introduced as follows: generic, lower bound, and upper bound backbones. The generic subgroups indicate the median force values for backbone points. The authors suggest adopting the generic backbone models for estimating the average response of a partition wall assembly in future analytical studies. However, one may also consider the upper or lower bound force values, instead of median values, in order to account for the effect of uncertainty of connection capacities on the performance of a partition wall. Other material parameters, including pinching parameters, stiffness degradation parameters, and force degradation parameters, are identical for all three subgroups. Figure 4 shows the comparison of the sample generic models with experimental data, as well as the lower and upper bound backbones for each connection. More information on the component-level studies of partition wall connections can be found in [28,33,34]. The following subsections demonstrate how the "Pinching4" material is used along with the "twoNodeLink" elements to represent the connections. Note that the proposed material models are limited to the connections, which are constructed from either 0.48-mm-thick or 0.76-mm-thick studs/tracks, and 15.9 mm gypsum boards. For connections with different gypsum, stud or track types, new sets of model parameters need to be calibrated through additional experimental and analytical studies. In addition, the model does not perform the geometric transformation of stiffness and resisting force from the basic system to the global coordinate system, which can introduce approximation in the response when the displacement is large.

2.2.1. Gypsum board-to-stud/track connections

The gypsum board elements are connected to the stud and track elements at every fastener location using "twoNodeLink" elements. The nonlinear "Pinching 4" material (Tables 1-3), is assigned in two perpendicular, in-plane directions (X and Y directions in Figure 2). To define the material parameters for the perimeter connections, the screw-to-gypsum edge distance is determined based on the construction. For field connections, the material model with an edge distance larger than 38 mm is adopted. The elements are assumed to be rigid in the out-of-plane direction.

2.2.2. Stud-to-track connections

The stud elements are attached to the track elements at the top and bottom with "twoNodeLink" elements. When studs are screwed to tracks in the construction, the "Pinching 4" material, proposed for stud-to-track connections (Tables 1-3), is assigned to these elements in the in-plane directions (X and Y directions in Figure 2). However, when the screw connection is not provided between studs and tracks, an "Elastic" material with minimal stiffness is used. In the vertical direction, an additional compression only "Elastic-Perfectly Plastic Gap" (EPPG) material was located in parallel with the primary material ("Pinching 4" or "Elastic" material). The EPPG material can simulate the stud-track interactions due to the gap closure in compression. The material parameters (Figure 5a) include: 1) initial stiffness, k_g; 2) yield force, F_y; 3) initial gap, *gap*; 4) post-yield stiffness ratio, $b=k_h/k_g$; and 5) damage type, which is an optional parameter to specify whether damage is accumulated or not in the material model. Table 4 presents the EPPG material parameter for each stud/track thickness. The initial gap

should be determined based on the available gap between the end of the stud and the web of the track. The "twoNodeLink" elements are rigid in the out-of-plane direction. The rotational stiffness of stud-to-track connections is neglected.

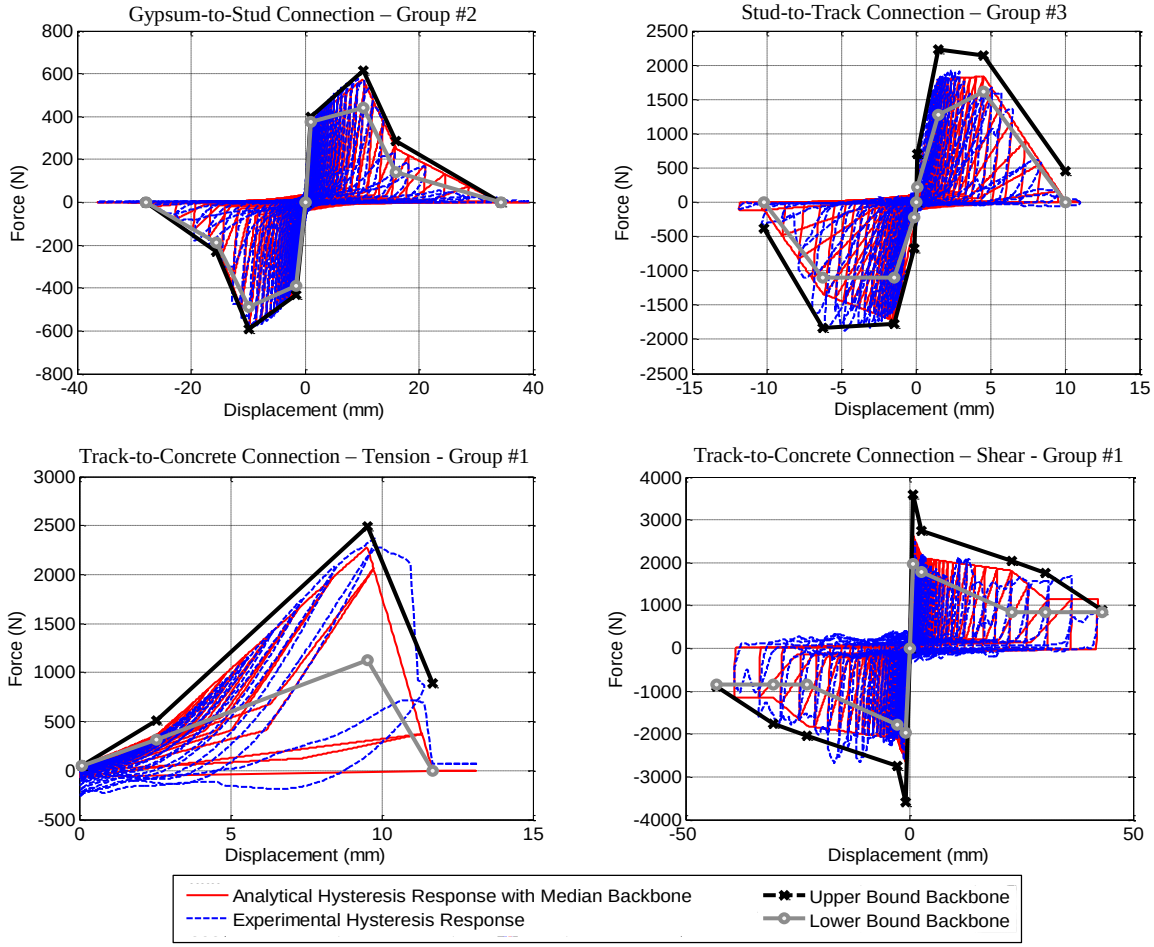

Figure 4. Analytical-experimental comparison of sample generic models from each partition wall connection

2.2.3. Track-to-concrete connections

Two coincident nodes, one on the track element and one as the concrete representative node, are defined at the location of each PAF. The concrete nodes are fixed in all directions. The track nodes are connected to the concrete nodes by the "twoNodeLink" elements. For the vertical direction (Y direction), the material model developed for the tension behavior is used, while for the horizontal directions (X direction and out-of-plane direction) the material model developed for the shear behavior of the track-to-concrete connections is utilized (Tables 1-3). In addition, the "Elastic-No Tension (ENT)" material [27] is assigned to the elements in the vertical direction in order to represent the compressive behavior of the concrete material. An initial stiffness of 16,000 kN/mm is chosen for the ENT material based on the properties of typical concrete material.

Table 1. Force values for backbone points in various connections

Description	Backbone values	*ePfi* and *eNfi* (N)							
		ePf1	*ePf2*	*ePf3*	*ePf4*	*eNf1*	*eNf2*	*eNf3*	*eNf4*
Gypsum-to-stud connection									
THK=0.48/0.76 mm, e1 ≥ 38 mm	Generic	376	565	310	0.01	-376	-565	-310	-0.01
	Lower bound	297	475	143	0.01	-297	-475	-143	-0.01
	Upper bound	423	605	404	0.01	-423	-605	-404	-0.01
THK=0.48/0.76 mm, e1 ≥ 25 mm	Generic	427	591	191	0.01	-378	-574	-249	-0.01
	Lower bound	390	487	186	0.01	-376	-442	-142	-0.01
	Upper bound	430	592	232	0.01	-400	-614	-286	-0.01
THK=0.48/0.76 mm, e1 ≥ 19 mm	Generic	391	498	178	0.01	-391	-507	-109	-0.01
	Lower bound	350	401	94	0.01	-350	-445	-89	-0.01
	Upper bound	400	504	282	0.01	-400	-529	-137	-0.01
THK=0.48/0.76 mm, e1 ≥ 13 mm	Generic	245	289	23	0.01	-308	-374	-174	-0.01
	Lower bound	225	288	13	0.01	-280	-360	-133	-0.01
	Upper bound	262	294	62	0.01	-378	-385	-196	-0.01
Stud-to-track connections									
THK=0.48 mm, e2 < 13 mm	Generic	254	1909	1867	0.01	-200	-1554	-1517	-623
	Lower bound	222	1581	1611	0.01	-156	-1419	-415	-0.01
	Upper bound	302	2375	2380	911	-289	-1708	-1713	-708
THK=0.48 mm, e2 ≥ 13 mm	Generic	222	1998	2135	0.01	-178	-1664	-1668	-623
	Lower bound	222	1966	1386	0.01	-178	-1619	-1624	-0.01
	Upper bound	222	2131	2135	598	-222	-1953	-1956	-1956
THK=0.76 mm, e2 can vary	Generic	289	1802	1831	20	-334	-1728	-1672	-111
	Lower bound	222	1270	1615	0.01	-222	-1105	-1103	-0.01
	Upper bound	697	2225	2143	448	-667	-1780	-1828	-377
Track-to-concrete connections subjected to tension force									
THK=0.48 mm	Generic	47	356	2284	0.01	-200	-356	-2284	-0.01
	Lower bound	44	311	1128	0.01	-179	-311	-1128	-0.01
	Upper bound	53	507	2491	890	-222	-507	-2491	-890
THK=0.76 mm	Generic	102	979	3506	0.01	-756	-979	-3506	-0.01
	Lower bound	89	667	494	0.01	-578	-667	-494	-0.01
	Upper bound	107	1201	3914	3761	-890	-1201	-3914	-3761
Track-to-concrete connections subjected to shear force									
THK=0.48 mm	Generic	2577	2111	1816	1151	-2577	-2111	-1816	-1151
	Lower bound	1968	1779	845	845	-1968	-1779	-845	-845
	Upper bound	3587	2748	2042	1766	-3587	-2748	-2042	-1766
THK=0.76 mm	Generic	4115	3180	3051	204	-4115	-3180	-3051	-204
	Lower bound	4048	3143	2970	0.01	-4048	-3143	-2970	-0.01
	Upper bound	4293	3403	3155	1359	-4293	-3403	-3155	-1359

THK: stud/track thickness
e1: edge distance, here the distance from the center of the screws to the edge of the gypsum board
e2: edge distance, here the distance from the center of the screws to the edge of the stud/track flanges

Table 2. Displacement values for backbone points in various connections

Description	*ePdi* and *eNdi* (mm) for generic, lower and upper bound backbone curves							
	ePd1	*ePd2*	*ePd3*	*ePd4*	*eNd1*	*eNd2*	*eNd3*	*eNd4*
Gypsum-to-stud connection								
THK=0.48/0.76 mm, e1 ≥ 38 mm	1.0	8.9	17.8	39.4	-1.0	-8.9	-17.8	-39.4
THK=0.48/0.76 mm, e1 ≥ 25 mm	1.5	9.9	15.5	27.9	-1.0	-10.2	-16.0	-34.3
THK=0.48/0.76 mm, e1 ≥ 19 mm	1.3	4.6	7.6	20.3	-1.3	-5.6	-21.6	-35.6
THK=0.48/0.76 mm, e1 ≥ 13 mm	0.8	1.8	6.6	9.4	-0.9	-3.3	-7.4	-31.8
Stud-to-track connections								
THK=0.48 mm, e2 < 13 mm	0.1	2.5	5.1	10.2	-0.1	-2.0	-6.4	-8.4
THK=0.48 mm, e2 ≥ 13 mm	0.1	2.8	7.1	16.8	-0.1	-2.5	-6.1	-6.4
THK=0.76 mm, e2 can vary	0.1	1.5	4.6	10.0	-0.1	-1.5	-6.2	-10.2
Track-to-concrete connections subjected to tension force								
THK=0.48 mm	0.1	2.5	9.5	11.7	-0.1	-2.5	-9.5	-11.7
THK=0.76 mm	0.1	2.5	12.4	13.3	-0.1	-2.5	-12.4	-13.3
Track-to-concrete connections subjected to shear force								
THK=0.48 mm	0.8	2.8	22.9	30.5	-0.8	-2.8	-22.9	-30.5
THK=0.76 mm	0.8	2.8	19.7	30.1	-0.8	-2.8	-19.7	-30.1

Table 3. Pinching parameters in various connections

Description	For generic, lower and upper bound backbone curves									
	rForceP *rForceN*	*rDispP* *rDispN*	*uForceP* *uForceN*	*gK1* *gK2*	*gK3* *gK4*	*gD1* *gD2*	*gD3* *gD4*	*gKLimit* *gDLimit*	*gF* *gE*	*dam*
Gypsum-to-stud connections										
THK=0.48/0.76 mm, e1 can vary	0.12	0.77	-0.01	0	0	0	0	0	0	cycle
	0.12	0.77	-0.01	0	0	0	0	0	1	
Stud-to-track connections										
THK=0.48/0.76 mm, e2 can vary	0.10	0.50	-0.01	0	0.2	0	0	0.4	0	cycle
	0.10	0.50	-0.01	0	0.2	0	0	0	1	
Track-to-concrete connections subjected to tension force										
THK=0.48 mm	0.33	0.65	0.01	0	0	0	0	0	0	cycle
	0.33	0.65	-0.18	0	0	0	0	0	1	
THK=0.76 mm	0. 20	0.60	-0.05	0	0	0	0	0	0	cycle
	0.50	0.60	-0.07	0	0	0	0	0	1	
Track-to-concrete connections subjected to shear force										
THK=0.48 mm	0.12	0.75	0.01	0	0	0	0	0	0	cycle
	0.12	0.75	0.01	0	0	0	0	0	1	
THK=0.76 mm	0.17	0.75	0.01	0	0	0	0	0	0	cycle
	0.17	0.75	0.01	0	0	0	0	0	1	

2.3. Contacts

The contacts between the gypsum boards and the top and bottom concrete slabs are modeled utilizing two parallel "zeroLengthContact3D" elements, each in series with an additional "twoNodeLink" element with EPPG material (Figure 5b). The elements are defined between two virtual nodes in 3DOF (degrees of freedom) domain, at the location of each gypsum board node. The virtual nodes are constrained to corresponding gypsum board and concrete nodes by the "EqualDOF" command. The "zeroLengthContact3D" element simulates the friction between two surfaces (here gypsum and concrete surfaces) when the nodes move towards each other. The parameters of this element include: 1) penalty in the normal direction, *Kn*; 2) penalty in the tangential direction, *Kt*; 3) friction coefficient, μ; and 4) cohesion, *c*. The EPPG material accounts for the cumulative

damage (crushing) in gypsum boards due to interaction with concrete. Using two sets of elements in a parallel configuration provides a better control of contact properties and helps to preclude the possible convergence errors in the model. Tables 4 and 5 show the recommended values for parameters of the EPPG material and "zeroLengthContact3D" element. The EPPG material initial gap is chosen based on the available gap between the gypsum board edge and the concrete slab in the construction. The initial stiffness of EPPG material is assumed to be consistently equal to the penalty value in the normal direction (*Kn*) for the "zeroLengthContact3D" element. A horizontal friction coefficient (μ) of 0.5-0.8 is suggested for the contact elements [35, 36]. The other parameters have been established through the validation process of the analytical model with the experimental data, after investigating a wide range of material and element model properties.

The contacts between the adjacent gypsum boards are represented by a single "zeroLengthContact3D" element between every two gypsum board nodes. To switch from 6DOF to 3DOF, virtual nodes are added. The elements are always oriented perpendicular to the gypsum board edges. The initial gap between gypsum boards is assumed to be negligible. The parameters of "zeroLengthContact3D" elements are reported in Table 5. Note that the contact element parameters for both gypsum-to-concrete and gypsum-to-gypsum contact surfaces are established assuming an average spacing of 250-300 mm between contact elements. In fact, it is assumed that each contact element represents a contact surface with a length of approximately 250-300 mm. Whenever a different spacing is used, the element parameters need to be scaled.

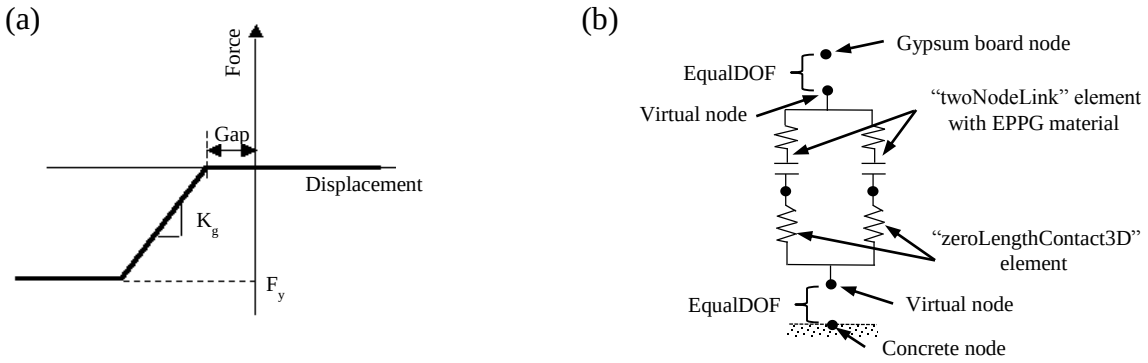

Figure 5. (a) EPPG material properties [27]; (b) Representative element for gypsum-to-concrete contact

Table 4. EPPG material parameters

Location	Stud/Track THK (mm)	k_g (N/mm)	F_y (N)	b	Gap	damage
Stud-to-Track Connection	0.48	650-1450	6000-9000	0.0	Can vary	"noDamage"
	0.76	1950-2500	6000-9000	0.0	Can vary	"noDamage"
Gypsum-to-Concrete Contact	n/a	3.0e3-3.0e4	900-1400	0.0	Can vary	"Damage"

Table 5. "ZeroLengthContact3D" element Parameters

Location	*Kn* (N/mm)	*Kt* (N/mm)	*μ*	*c*
Gypsum-to-Concrete Contact	3.0e3-3.0e4	3.0e2-3.0e3	0.5-0.8	0.0
Gypsum-to- Gypsum Contact	3.0e3-3.0e4	3.0e3-3.0e4	0.5-0.8	0.0

3. VALIDATION OF THE PROPOSED ANALYTICAL MODEL

3.1. Available data from full-scale experiments at UB

As a part of the "NEESR-GC" project, 50 partition wall specimens corresponding to 22 different configurations of cold-formed steel-framed gypsum partition walls were tested at the University of Buffalo (UB). The configurations varied in terms of 1) connectivity of the sheathing and studs to the top and bottom tracks, 2) spacing of the track-to-concrete fasteners, 3) wall intersection detailing, 4) stud and track thicknesses, and 5) spacing of the steel studs [8]. To validate the proposed analytical model of the partition walls, three nominally identical specimens of configuration #3 from the UB experiments, namely specimens 5, 6, and 10, were used in the current study. The specimens were approximately 3480 mm long by 3500 mm tall (Figure 6a). The partition wall frame was constructed using 350S125-18 steel studs with a typical spacing of 610 mm and 350T125-18 tracks. Gypsum board panels (1219x2438 mm) with a thickness of 15.9 mm were laid perpendicular to the studs and screwed to the steel frame using standard Phillips self-drilling screws #6, spaced 305 mm on center at both the perimeter and field. The panel joints were offset on opposite faces of the partition walls. The gypsum boards and boundary studs were screwed to the top and bottom tracks (Figure 6b). The specimen was subjected to the loading protocol developed by Retamales et al. [11] (Figure 7).

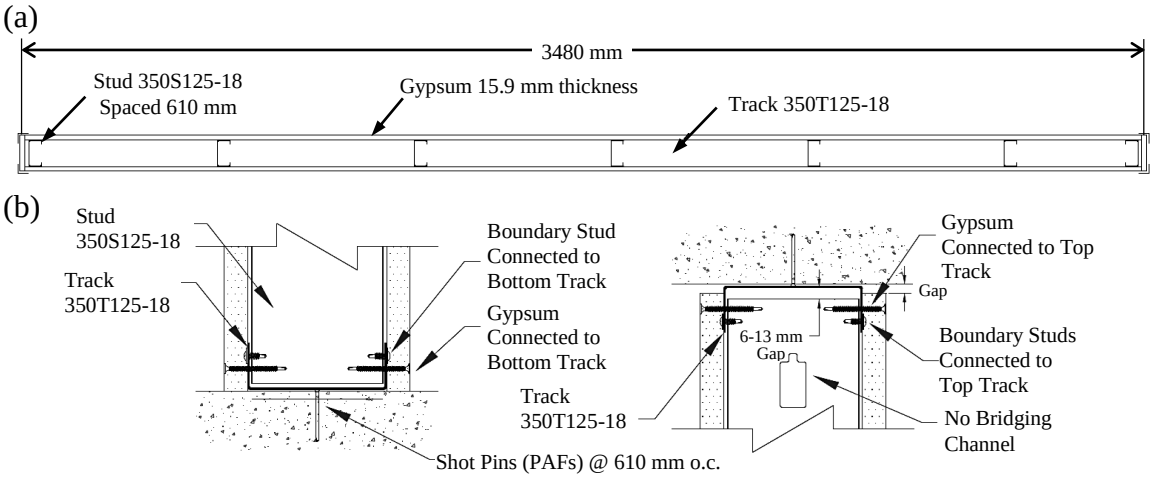

Figure 6. Details of specimens 5, 6, and 10, after Retamales et al. [8] (a) plan view; (b) top and bottom connection details

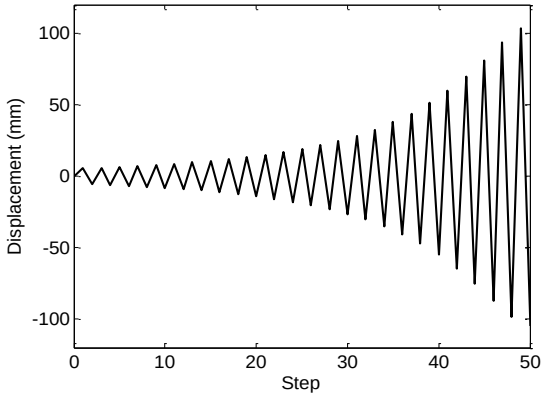

Figure 7. UB loading protocol [11]

Figure 8 presents the recorded hysteresis responses and the comparison of backbone curves of the three specimens. Although these specimens were intended to be identically designed and constructed, their force-displacement responses were different in terms of initial stiffness, maximum force, and hysteresis energy. In addition, the reported damage mechanisms in specimen 10 were different from those observed in specimens 5 and 6. These differences might be consequences of slight variations in construction (such as variations in gypsum screw edge distances or variations in available gaps between gypsum boards and concrete slabs) and/or differences in material properties.

3.2. Generic Analytical Model for UB Configuration #3

The generic analytical model of UB configuration #3 was created in OpenSees [27], following the methodology proposed in section 2 of this paper and using the average (or median) values for the properties of all components, including wall connections and contact elements. The schematic diagram of the analytical model, elements, and equivalent springs are shown in Figure 2. The properties of stud and track materials (Table 6), were determined according to coupon test results [26]. The weight of the stud and track elements were considered to be 5.7 N/m and 5.6 N/m respectively [30]. An "ElasticMembranePlate-Section" section with a modulus of elasticity of 993 MPa, Poisson ratio of 0.3, and a weight density of 6931 N/m^3 was assigned to the gypsum board elements [31].

To represent the wall connections, the material models with the generic backbone curves (Tables 1-3) were employed. For the perimeter gypsum-to-stud/track connections, the edge distance was assumed to be 19 mm on studs and 13 mm on tracks. An initial gap of 13 mm and screw-to-stud/track edge distance of 10 mm were considered for stud-to-track connections. The initial stiffness and yield force of the EPPG material was assumed to be 1000 N/mm and 7000 N, respectively. Parameters of representative contact elements are provided in Table 7. Note that these values were selected from typical construction details since the actual values were not reported in the experiment.

The generic analytical model was subjected to the displacement history recorded during the experiment at UB [8]. Figure 9 compares the analytical and experimental force-displacement backbone curves and cumulative hysteresis energies. Although there

are some differences between the analytical and experimental results, the analytical model has successfully estimated the average response of the UB specimens. In addition, the predicted damage mechanisms in the analytical model consisted of damage to gypsum-to-top tracks/studs screw connections, bending of boundary studs, crushing of gypsum boards, and damage to track-to-concrete PAF connections, which were comparable to the experimental damage mechanisms. These results confirmed that the proposed modeling methodology accomplished its objective of predicting the general force-displacement response and the possible damage mechanisms of a partition wall.

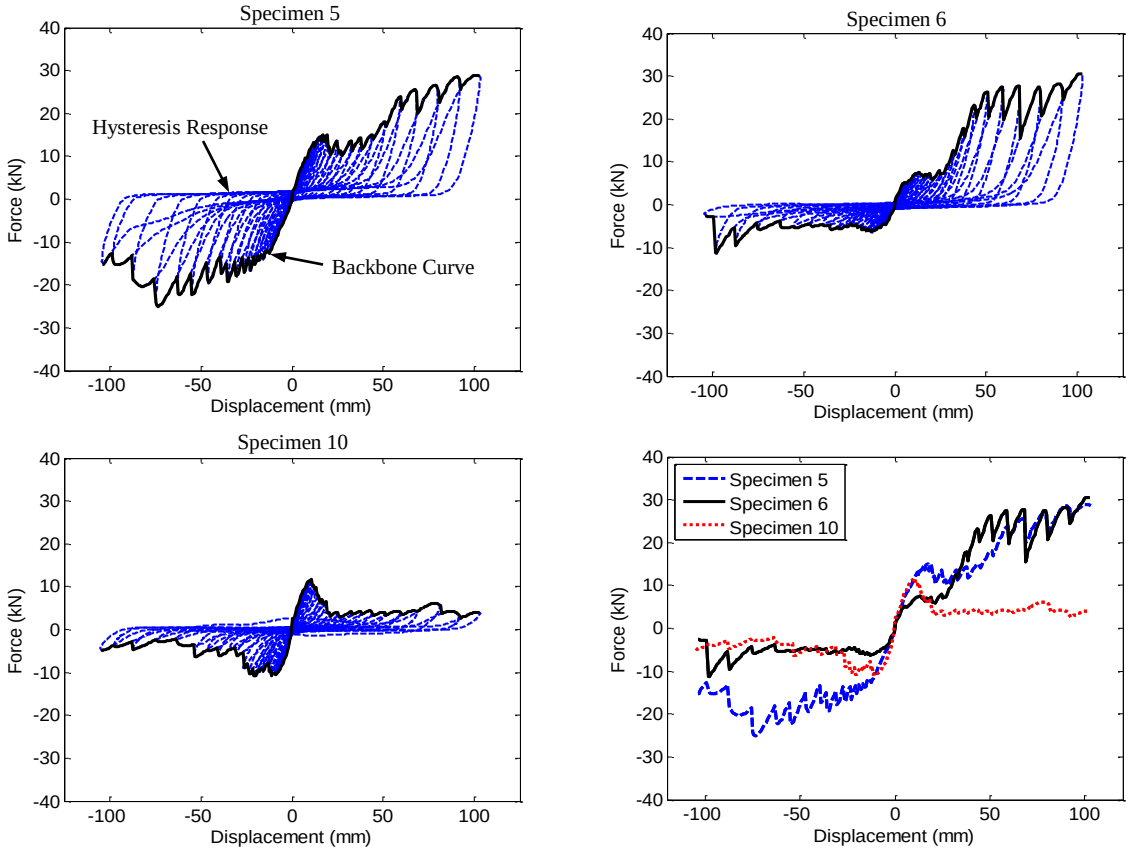

Figure 8. Experimental hysteresis responses and the comparison of backbone curves of the specimens 5, 6, and 10

Table 6. Steel material properties

Element	modulus of elasticity (GPa)	yield strength (MPa)	Hardening slope ratio (%)
Stud	219	330	0.1
Track	153	359	2.0

Table 7. Representative contact element parameters

Location	*Kn* (N/mm)	*Kt* (N/mm)	*μ*	*c*	F_y (N)	*Gap (mm)*
Gypsum-to-Concrete Contact	7.0e3	3.5e2	0.6	0.0	1100	13
Gypsum-to- Gypsum Contact	3.0e4	3.0e4	0.6	0.0	-	0.0

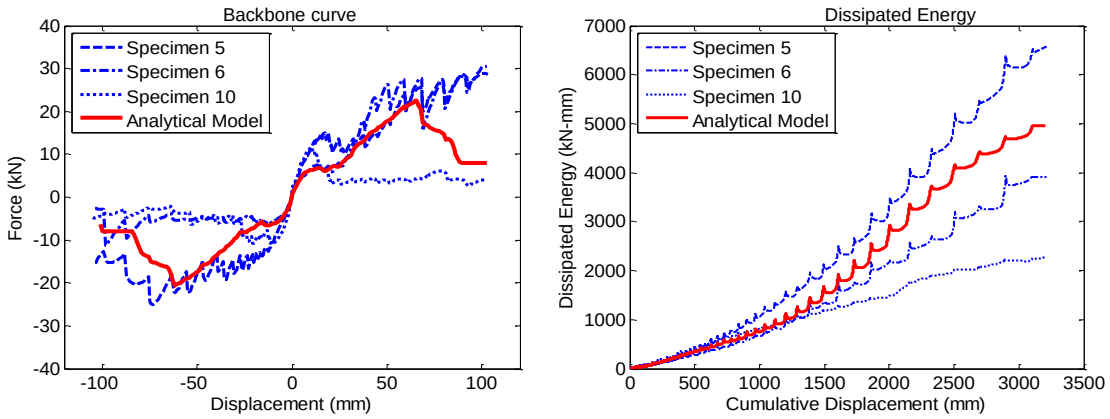

Figure 9. Comparison of the response of the generic analytical model and experimental results

3.3. Adjustment of the analytical model for each particular specimen

In the previous section, the generic analytical model of UB configuration #3 was developed and validated. As supplementary verification, this section shows that with slight adjustments to the generic modeling assumptions, even better correlation between the analytical and experimental results could be achieved for each particular specimen. These adjustments were justified considering the possible source of discrepancies in the experimental results. Note that, even with no adjustment, the proposed generic model works well within usable engineering and construction tolerance.

3.3.1. The analytical model for specimen 5

The following updates were applied to the generic model to optimized the model specifically for specimen 5: 1) for track-to-concrete connections and field gypsum-to-track connections, the material model with the upper bound backbone values was adopted; 2) an initial gap of 19 mm and screw-to-stud/track edge distance of 7 mm was considered for stud-to-track connections; and 3) the initial gap for contact elements varied from zero (between two gypsum boards) to 17 mm (between gypsum boards and concrete). Figure 10 compares the analytical and experimental force-displacement hysteresis responses and cumulative hysteresis energies for specimen 5. The hysteretic loops from the analytical model are generally consistent with the experimental results. The initial stiffness, maximum force, pinching, and unloading stiffness are accurately predicted, which led to a good estimation of cumulative dissipated energy. However, there is a discrepancy between the analytical and experimental results in the last cycle. This could be due to the effect of large displacement on the specimen response, which was not included in the analytical model. Figure 11 depicts the analytical deformed shape of the partition wall and compares the predicted damage mechanisms in the analytical model with the experimental observations. To determine whether a component suffered damage in the analytical model, the force-displacement response of the components, in conjunction with available data from component-level tests, was utilized. According to the analytical model, the possible damage mechanisms in specimen 5 included failure of gypsum-to-top track and gypsum-to-boundary studs screw connections, extensive

bending of boundary studs, crushing of gypsum board corners due to interaction with concrete, nonlinearity in gypsum-to-bottom track screw connections, and tensile failure of track-to-concrete PAF connections at boundaries, which were consistent with the observed damage mechanims in the experiment.

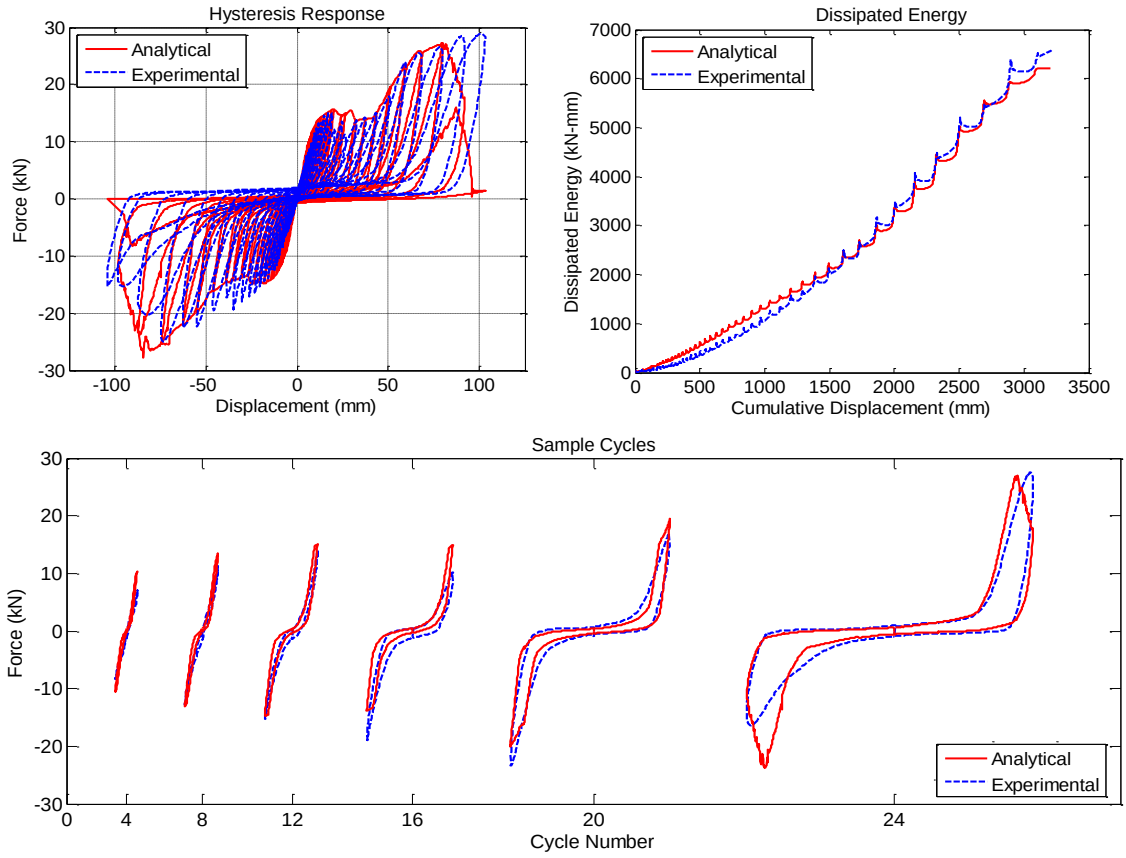

Figure 10. Comparison of analytical and experimental response of specimen 5

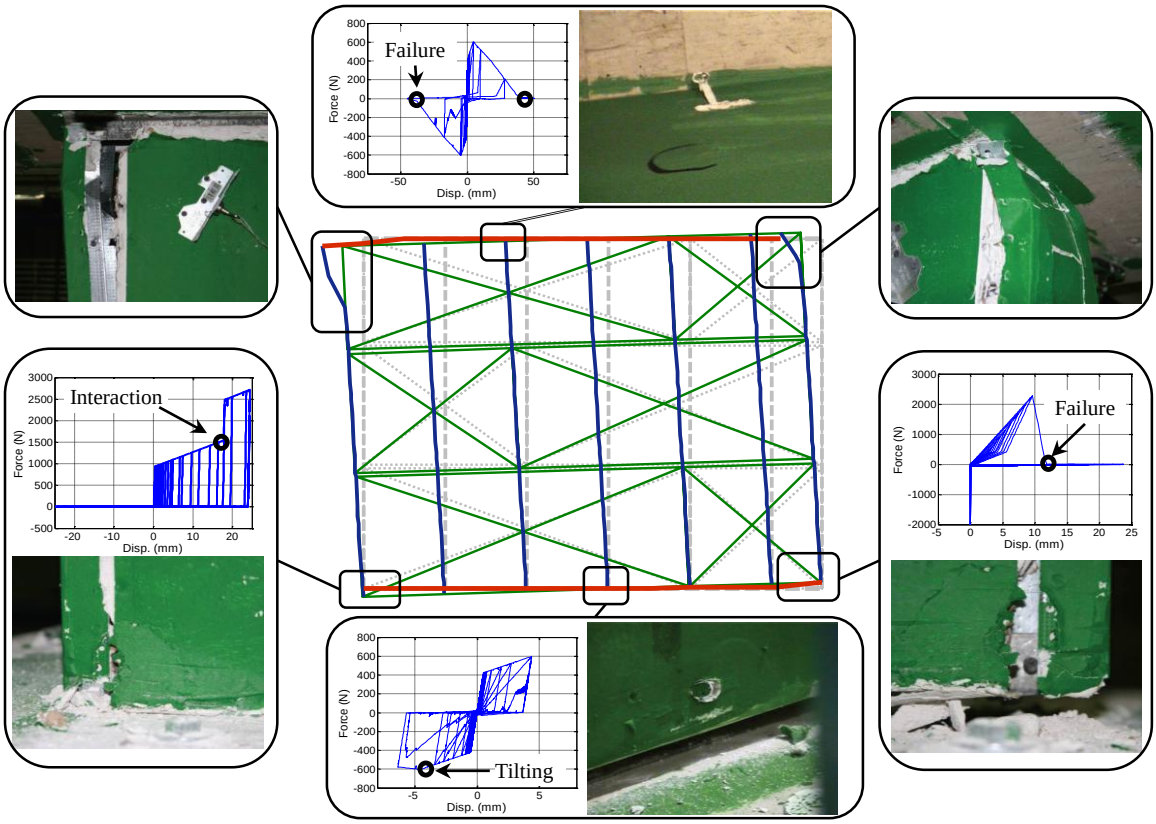

Figure 11. Analytical deformed shape, comparison of analytical and experimental damage mechanisms, and sample component responses in specimen 5

3.3.2. The analytical model for specimen 6

In order to capture the asymmetrical behavior of specimen 6, the generic model was modified as follow: 1) a material model with upper bound backbone values in positive displacement and lower bound backbone values in negative displacement was adopted for field gypsum board-to-track connections; 2) two different edge distances (19 mm and 13 mm) were used for gypsum board-to-boundary stud/track connections at two sides of the wall; 3) the initial gaps between the gypsum boards and concrete slab were assumed to be different (11 mm and 18 mm) at two sides of the wall; and 4) for stud-to-track connections, the initial gaps were considered to vary from 13 mm to 18 mm.

The analytical and experimental force-displacement hysteresis responses and cumulative dissipated energies of specimen 6 are compared in Figure 12. The analytical model successfully captures the asymmetrical experimental response. Similar to specimen 5, there is a discrepancy between analytical and experimental results in the last cycle, which could be due to the effect of large displacement. The experimental damage mechanisms in specimen 6, which were analogous to those of specimen 5, were well predicted by the anytical model.

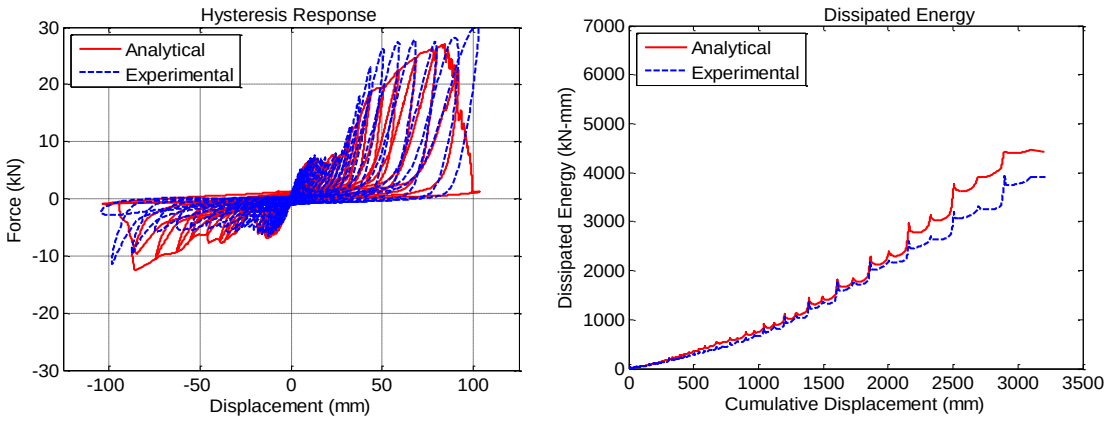

Figure 12. Comparison of analytical and experimental response of specimen 6

3.3.3. The analytical model for specimen 10

For specimen 10, the modifications included the following: 1) the initial gaps between the end of the studs and the web of the tracks were assumed to be minimal, 2) the edge distance for connections of gypsum boards to boundary studs was assumed to be 25 mm; 3) for the shear behavior of the track-to-concrete connections, the material model with lower bound backbone values was employed.

Figure 13 depicts the comparison of the analytical and experimental force-displacement hysteresis responses and cumulative dissipated energies of specimen 10. Although the analytical model slightly overestimates the maximum force and the dissipated energy, it can predict the trend of the response very well. The predicted damage mechanisms in specimen 10, based on the analytical models, included shear failure of top track-to-concrete PAF connections, nonlinearity in gypsum-to-tracks screw connections, and crushing of gypsum borad corners. These damage mechanisms were consistent with observed damage mechanims in the experiment.

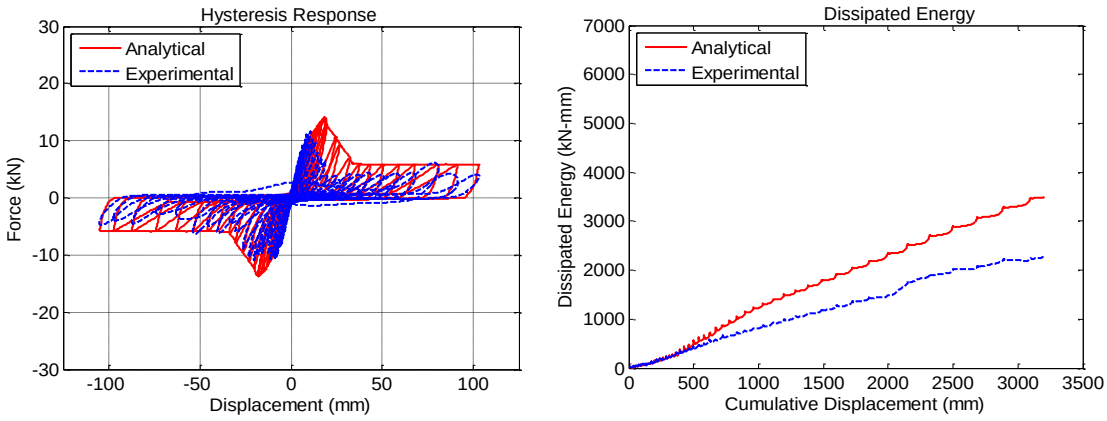

Figure 13. Comparison of analytical and experimental response of specimen 10

4. CONCLUSIONS AND FUTURE WORK

A detailed and yet computationally efficient analytical model of cold-formed steel-framed gypsum partition walls was proposed. In this model, studs and tracks were modeled using beam elements with their section properties accounting for nonlinear behavior. The gypsum boards were simulated by linear four-node shell elements. The nonlinear behaviors of the connections (including gypsum-to-stud, stud-to-track, and track-to-slab connections) were represented by hysteretic load-deformation springs. The behavior of springs was characterized based on the results of a series of component-level experiments performed at the University of Nevada, Reno (UNR). The contacts between gypsum boards and concrete slabs as well as the contacts between the adjacent gypsum boards were incorporated in the model.

To validate the proposed modeling procedure, three nominally identical specimens of configuration #3 from the UB experiments were used. Initially, a generic analytical model of these specimens was assembled adopting the average (or median) values for the properties of all components, including wall connections and contact elements. The model was subjected to the displacement history recorded during the experiment. Force-displacement responses, cumulative dissipated energy, and damage mechanisms from the analytical simulation were compared to the experimental results. The comparison showed that the generic analytical model accurately predicted the trend of the response as well as the observed damage mechanisms. Subsequently, the authors indicated that the generic model could be slightly adjusted for each particular specimen in order to achieve even better correlation between the analytical and experimental results.

The procedure proposed here can be utilized in future studies to investigate the in-plane force-displacement response and damage mechanisms of partition walls with various dimensions (i.e. length and height) and construction details (e.g. stud spacing, screw spacing, and initial gap). This is especially important where the experimental results are not available. In this case, various parameter ranges should be considered in order to account for all possible failure modes and behaviors. The investigation results can be then used to improve/modify the current design provisions of nonstructural walls. However, the analytical presented here model does have limitations, which are under investigation by the authors. For instance, the model has only been generated for single partition walls with no returns. In addition, the out-of-plane behavior of partition walls has not been included in the model. Further studies on connections of perpendicular walls at corners, in addition to studies on the out-of-plane behavior of wall connections, are required in order to develop a more comprehensive model of partition walls. The new model can be then employed to perform fragility analysis on the seismic performance of partition walls with various traditional/innovative design details.

5. ACKNOWLEDGMENTS

The current material is based upon work supported by the National Science Foundation under Grant No. 0721399. This Grand Challenge (GC) project to study the seismic response of nonstructural systems is under the direction of M. Maragakis from the University of Nevada, Reno and Co-PIs: T. Hutchinson (UCSD), A. Filiatrault (UB),

S. French (G. Tech), and B. Reitherman (CUREE). Any opinions, findings, conclusions, or recommendations expressed in the current document are those of the investigators and do not necessarily reflect the views of the sponsors. The input provided by the Practice Committee of the NEES Nonstructural Project, composed of W. Holmes (Chair), D. Allen, D. Alvarez, and R. Fleming, and by the Advisory Board, composed of R. Bachman (Chair), S. Eder, R. Kirchner, E. Miranda, W. Petak, S. Rose and C. Tokas, has been crucial for the completion of this research.

6. REFERENCES

1. Lee T, Kato M, Matsumiya T, Suita K, Nakashima M. Seismic Performance Evaluation of Non-structural Components: Drywall Partitions. *Earthquake Engineering and Structural Dynamics* 2007; **36**: 367–382. DOI: 10.1002/eqe.638.
2. Taghavi S, and Miranda E. Response Assessment of Nonstructural Building Elements, *PEER Report 2003/05*, Pacific Earthquake Engineering Research Center (PEER), Berkeley, CA, 2003.
3. Dhakal RP. Damage to non-structural components and contents in 2010 Darfield earthquake. *Bulletin of The New Zealand Society for Earthquake Engineering* 2010; **43**:404-411.
4. Baird A, Tasligedik AS, Palermo S, Pampanin S. Seismic performance of vertical non-structural components in the 22nd February 2011 Christchurch earthquake. *Earthquake Spectra* 2014; **30**(1), 401–425. DOI: 10.1193/031013EQS067M.
5. Mizutani K, Kim H, Kikuchihara M, Nakai T, Nishino M, Sunouchi S. The damage of the building equipment under the 2011 Tohoku pacific earthquake. *9th International Conference on Urban Earthquake Engineering & 4th Asia Conference on Earthquake Engineering*, Tokyo Institute of Technology, Tokyo, Japan, 2012.
6. EERI (Earthquake Engineering Research Institute). The El Mayor Cucapah, Baja California earthquake April 4, 2010. *An EERI Reconnaissance Rep* 2012; 2010-02, J. Meneses, ed., Oakland, CA.
7. Miranda E, Mosqueda G, Retamales R, Pekcan G. Performance of Nonstructural Components during the 27 February 2010 Chile Earthquake. *Earthquake Spectra* 2012; **28**:S1:S453–S471. DOI: 10.1193/1.4000032.
8. Retamales R, Davies R, Mosqueda G, Filiatrault A. Experimental Seismic Fragility of Cold-Formed Steel Framed Gypsum Partition Walls. ASCE *Journal of Structural Engineering* 2013; **139**:1285-1293. DOI: 10.1061/(ASCE)ST.1943-541X.0000657.
9. Wood RL, Hutchinson TC. Design-Oriented Model for Capturing the In-Plane Seismic Response of Partition Walls. ASCE *Journal of Structural Engineering* 2014, 140. DOI: 10.1061/(ASCE)ST.1943-541X .0000899.
10. Xang X, Pantoli E, Hutchinson T, Restrepo J, Wood R, Hoehler M, Grzesik P, Sesma F. Seismic Performance of Cold-Formed Steel Wall Systems in a Full-Scale Building. ASCE *Journal of Structural Engineering* 2015. DOI: 10.1061/(ASCE)ST.1943-

541X.0001245.

11. Retamales R, Mosqueda G, Filiatrault A, Reinhorn AM. New Experimental Capabilities and Loading Protocols for Seismic Qualification and Fragility Assessment of Nonstructural Components. *Technical Report MCEER-08-0026*, State University of New York at Buffalo, NY, 2008.
12. Restrepo JI, Bersofsky A. Performance Characteristics of Light Gage Steel Stud Partition Walls. *Thin-Walled Struct*ures 2010; 49:317–324. DOI: 10.1016/j.tws.2010.10.001.
13. Restrepo JI, Lang AF. Study of Loading Protocol in Light-Gauge Stud Partition Wall. *Earthquake Spectra* 2011; **27**:1169–1185. DOI: 10.1193/1.3651608.
14. Soroushian S, Ryan KL, Maragakis M, Wieser J, Sasaki T, Sato E, Okazaki T, Tedesco L, Zaghi AE, Mosqueda G, Alarez D. NEES/E-Defense tests: Seismic performance of ceiling/sprinkler piping nonstructural systems in base isolated and fixed base building. *15th World Conference on Earthquake Engineering (15WCEE)*, Lisbon, Portugal, 2012.
15. Rahmanishamsi E, Soroushian S, Maragakis M. System-Level Experiments on Ceiling/Piping/Partition Systems at UNR-NEES Site. *Tenth U.S. National Conference on Earthquake Engineering*, Anchorage, AK, 2014. DOI: 10.4231/D3BR8MG8F.
16. Folz B, Filiatrault A. Cyclic analysis of wood shear walls. *Journal of Structural Engineering* 2001; 127: 433-441. DOI: 10.1061/(ASCE)0733-9445(2001)127:4(433).
17. Van de Lindt JW, Walz MA. Development and application of wood shear wall reliability model. ASCE *Journal of Structural Engineering* 2003; **129**:405-413. DOI: 10.1061/(ASCE)0733-9445(2003)129:3(405).
18. Fülöp LA, Dubina D. Performance of wall-stud cold-formed shear panels under monotonic and cyclic loading.Part II: Numerical modelling and performance analysis. *Thin-Walled Structures* 2004; **42**:339-349. DOI: 10.1016/S0263-8231(03)00064-8
19. Ibarra LF, Medina RA, Krawinkler H. Hysteretic models that incorporate strength and stiffness deterioration. *Earthquake Engineering and Structural Dynamics* 2005; **34**:1489–1511. DOI: 10.1002/eqe.495.
20. Della Corte G, Fiorino L, Landolfo R. Seismic behavior of sheathed cold-formed structures: numerical study. *Journal of Structural Engineering* 2006; **132**:558-569. DOI: 10.1061/(ASCE)0733-9445(2006)132:4(558).
21. Pang WC, Rosowsky DV, Pei S, Van de Lindt JW. Evolutionary parameter hysteretic model for shear walls. ASCE *Journal of Structural Engineering* 2007; **133**:1118–1129. DOI: 10.1061/(ASCE)0733-9445(2007)133:8(1118).
22. Martínez-Martínez J, Xu L. Simplified nonlinear finite element analysis of buildings with CFS shear wall panels. *Journal of Constructional Steel Research* 2011; **67**:565-575. DOI: 10.1016/j.jcsr.2010.12.005.
23. Nithyadharan M, Kalyanaraman V. Modelling hysteretic behaviour of cold-formed steel wall panels. *Engineering Structures* 2013; **46**: 643–652. DOI:

10.1016/j.engstruct.2012.08.022.

24. Buonopane SG, Tun TH, Schafer BW. Fastener-based computational models for prediction of seismic behavior of CFS shear walls. *Tenth U.S. National Conference on Earthquake Engineering*, Anchorage, AK, 2014.
25. Kanvinde AM, Deierlein GG. Analytical models for the seismic performance of gypsum drywall partitions. *Earthquake Spectra* 2006; **22**:391–411. DOI: 10.1193/1.2191927.
26. Davies D, Retamales R, Mosqueda G, Filiatrault A. Experimental Seismic Evaluation, Model Parameterization, and Effects of Cold-Formed Steel-Framed Gypsum Partition Walls on The Seismic Performance of an Essential Facility. *Technical Report MCEER-11-0005*, *MCEER*, State University of New York at Buffalo, NY, 2011.
27. Open System for Earthquake Engineering Simulation (OpenSees) website. http://www.opensees.berkeley.edu . PEER, Berkeley, CA, 2015.
28. Rahmanishamsi E, Soroushian S, Maragakis EM. Cyclic Shear Behavior of Gypsum Board-to-Steel Stud Screw Connections in Nonstructural Walls. *Earthquake Spectra* 2015. In-Press. DOI: 10.1193/062714EQS091M
29. Comite Euro-interational du Beton (CEB). RC elements under cyclic loading, state of the art report. Thomas Telford Publications, London, England, 1996.
30. Steel Stud Manufacturers Associations (SSMA). Product Technical Information, S.S.M. Association, Chicago, IL, 2011.
31. GA-235-10. Gypsum Board Typical Mechanical and Physical Properties. Gypsum Association: Hyattsville, MD, USA, 2010.
32. Soroushian S, Zaghi AE, Maragakis M, Tian T, Filiatrault A. Analytical Seismic Fragility Analyses of Fire Sprinkler Piping Systems with Threaded Joints. *Earthquake Spectra* 2013, In-Press. DOI: 10.1193/083112EQS277M.
33. Rahmanishamsi E, Soroushian S, Maragakis EM. Capacity Evaluation of Typical Stud-Track Screw Connections. *Journal of Earthquake Engineering* 2015. Under Review.
34. Rahmanishamsi E, Soroushian S, Maragakis EM. Capacity Evaluation of Typical Track-to-Concrete Power-Actuated Fastener Connections in Nonstructural Partition Walls. ASCE *Journal of Structural Engineering* 2015. Under Review.
35. http://www.atlasconcorde.it/
36. Desjarlais AO, Zarr RR. Insulation Materials, Testing and Applications. ASTM International, 4th Volume, Issue 1426, Jan 1, 2002.

Chapter 7

Evaluation of the out-of-plane behavior of stud-to-track connections in nonstructural partition walls

Esmaeel Rahmanishamsi[1] [a], Siavash Soroushian [b], Emmanuel "Manos" Maragakis [c]

[a] *Ph.D. Candidate, Department of Civil and Environmental Engineering, University of Nevada, Reno, Reno, NV, 89557, email: erahmanishamsi@unr.edu*
[b] *Structural Analyst, Advanced Technology and Research, Arup, San Francisco, CA, 94105, email: siavash.soroushian@arup.com*
[c] *Professor, Dean of College of Engineering, University of Nevada, Reno, Reno, NV, 89557, email: maragaki@unr.edu*

Please note that this chapter is a self-contained paper submitted to the journal of Thin-Walled Structure where the word 'this paper/study' refers to the chapter itself

Abstract

A series of component-level experiments have been performed aiming to characterize the out-of-plane force-displacement response and damage mechanisms of stud-to-track connections in nonstructural steel-framed partition walls. The performance of connections with various stud-to-track gap dimensions, stud/track thicknesses, and screw-attachment configurations were evaluated and compared. In addition, the accuracy of available design provisions for estimating the ultimate connection capacity was assessed. The experimental data was then used to generate capacity fragility curves in terms of displacement and force. Finally, a series of nonlinear numerical hinge models were developed and calibrated that represent the out-of-plane hysteresis behavior of stud-to-track connections.

[1] Corresponding author

Keywords: Nonstructural systems, Partition walls, Cold-formed steel, Stud-to-track connections, Fragility analysis, Numerical modeling

1. Introduction

Nonstructural systems almost always represent the major portion (approximately 48% to 70%) of the total construction cost in buildings [11]. During an earthquake event, these systems are subjected to the dynamic environment of the building. However, they are rarely considered in current earthquake design methodology of new buildings [2]. Consequently, it is not surprising that recent earthquakes have demonstrated poor performance of nonstructural systems, resulting in significant economic loss, typically exceeding the economic loss associated with structural damage [3, 4, 5, 6, and 7]. Indeed, nonstructural systems account for over 78% of the total estimated national annualized earthquake loss [11].

Among various nonstructural systems, steel-framed gypsum partition walls represent a substantial contribution to the total investment in a building. These walls configure the architectural layout of a building, thereby facilitating its functionality for occupants [8]. Pervasive damage to partition walls has been observed in previous earthquakes. The damage was often initiated at shake intensities much lower than those causing structural damage [9]. Partition damage can lead not only to property loss, but also to loss of functionality of critical facilities, such as operating rooms in hospitals, which might be followed by fatalities, even in low or mid-intensity earthquakes.

A number of experimental studies were carried out in recent years in order to assess the in-plane and out-of-plane seismic performance of steel-framed partition walls

[10, 11121321415, 16, 17, and 9]. These studies investigated the damage mechanisms and hysteresis behaviors of partition walls with different configurations. Where the return walls were included in the test, one of the observed damage mechanisms was damage to the stud-to-track connections in the out-of-plane direction. Retamales et al. [15] and Rahmanishamsi et al. [16] reported extensive deformation of track flanges of return walls. The deformation allowed return-wall studs to pop out from tracks. Moreover, the stud webs were crippled at the locations of some of the stud-to-track connections, when walls were subjected to extreme out-of-plane excitations. The research also showed that the out-of-plane stiffness and strength of partition walls depend on the characteristics of stud-to-track connections. Therefore, the behavior of the stud-to-track connections in the out-of-plane direction is of interest to determine its role in the performance of steel-framed gypsum partition walls.

Limited research has been conducted on the performance of stud-to-track connections in the out-of-plane direction. Compiling and analyzing the experimental data from a variety of sources, Fox and Schuster [18] recognized crippling of stud webs and punching-through of track flanges as dominant failure modes of stud-to-track connections. They also proposed design expressions to predict the connection capacities based on these failure modes. Bolte and LaBoube [19] expanded the available data with 24 additional tests. The specimens were different in terms of stud-to-track gaps, stud/track thicknesses, and whether studs were screwed to tracks (screw-attached configuration) or not (deflection-track configuration). The researchers compared the experimental results with the available design provisions, including AISI specification [20] and US Army Corps of Engineers technical instruction [2122], and recommended some modifications. Moreover, the failure

of the connection due to track-flange deformation was discussed. Recently, a comprehensive study was also conducted on the performance of jamb stud-to-track connections [22]. The previous studies provided valuable information on stud-to-track connections; nonetheless, they were limited to connections in load-bearing walls. The steel track and stud profiles in load-bearing walls are different from those used in nonstructural partition walls. Thinner track/stud profiles with smaller web depth are usually employed in nonstructural partition walls since they are not part of the structural load-carrying system [23]. In addition, according to best of the authors' knowledge, no study has evaluated the hysteresis force-displacement behavior of stud-to-track connections.

This study is aimed at addressing the missing information about the out-of-plane damage mechanisms and force-displacement characteristics of stud-to-track connections in nonstructural partition walls. For this purpose, a series of monotonic and cyclic experiments have been performed at the University of Nevada, Reno, as part of a grand challenge project titled "NEESR-GC: Simulation of the Seismic Performance of Nonstructural Systems." The test setup and experimental program are described in this paper, followed by an outline of the observed damage mechanisms. The force-displacement responses of connections with various stud/track thicknesses, stud-to-track gaps, and connection configurations (either screw-attached or deflection-track) are then compared. In addition, the correlation between the tested ultimate connection capacities with currently available design provisions was evaluated. Afterwards, the experimental data was utilized to generate capacity fragility curves in terms of displacement and force. Finally, a series of nonlinear numerical hinge models were proposed and calibrated using component experimental data to represent the hysteresis behavior of stud-to-track connections in the

out-of-plane direction. Note that the long-term objectives of these models are to be used in conjunction with the numerical models of other wall components (such as gypsum-to-stud connections and steel studs) in order to develop a detailed numerical model of steel-framed gypsum partition walls [23].

2. Description of test specimens

2.1. Test setup

A sample specimen and the testing machine is presented in Fig. 1. The specimens consisted of two 457-mm-long steel tracks and one 486±10 –mm-long steel stud. The stud and tracks were either 0.48 mm thick (362S/T125-19) or 0.75 mm thick (362T125-30). These products were selected from the common construction details of nonstructural partition walls in commercial and institutional buildings [15]. The stud was nested into the tracks, which were bolted to vertical supports spaced 511 mm apart. The gap between the end of the stud and the web of the tracks (gap in Fig. 1b) was changed from 3 mm to 22 mm. For some specimens two #8×13-mm screws were used to attach the stud to the tracks, while for others the screws were omitted to represent a deflection track configuration [21]. The vertical supports were fixed to the stationary base of an Instron 5985 machine. In order to prevent the bending of the stud and limit the deformation to stud-to-track connections, the middle of the stud was clamped between two 140×89×6-mm steel plates. One of these plates was held by the movable grip of the machine. The machine applied upward and downward displacement to the specimens through the movable grip and measured the reaction force by the axial load cell (Fig. 1a).

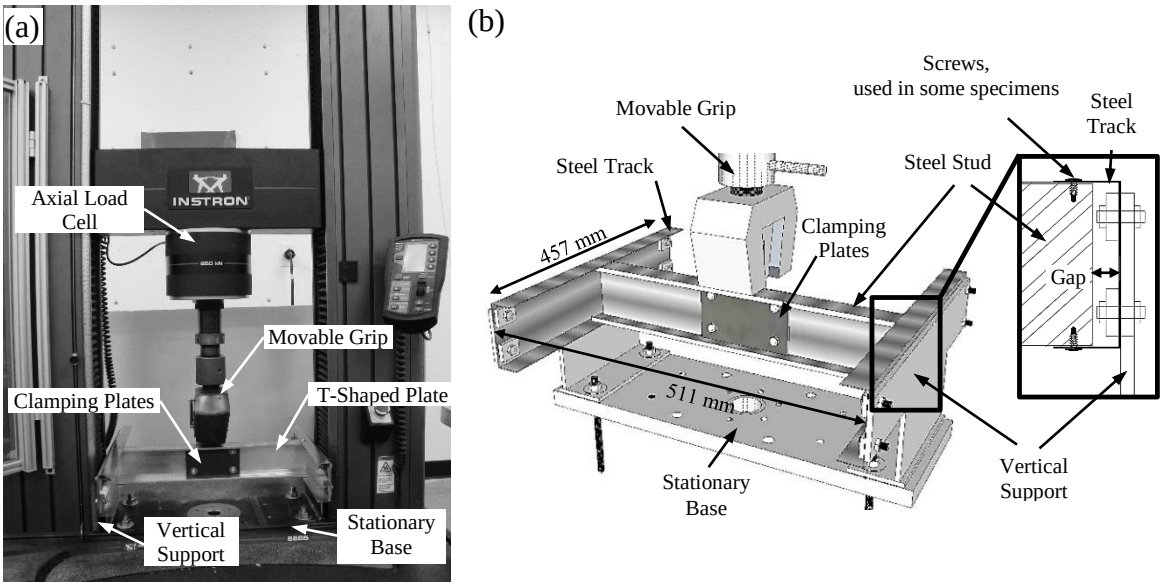

Fig. 1. (a) and (b) Specimen and Test Machine

2.2. Experimental program

A total of 26 specimens, categorized in six series, were tested to evaluate the strength and stiffness of stud-to-track connections in the out-of-plane direction (Table 1). The series were different in terms of the stud/track thicknesses, the stud-to-track gaps, and the stud-to-track connection configurations (screw-attached or deflection-track). An abbreviated nomenclature was adopted to label the series that described all these characteristics. Namely, the first group of characters denotes the stud/track thickness (T48: 0.48 mm thick), the second group of characters indicates the gap (G13: 13 mm gap), and the third group of characters stands for the connection configuration (SA: screw-attached and DT: deflection-track). For fragility assessment purposes, at least three nominally identical specimens were tested under cyclic loading for each series [15]. For cyclic tests, a loading protocol proposed by Retamales et al. [24] was adopted. The loading protocol was established for evaluating the performance of drift-sensitive nonstructural components. Fig. 2 shows the

displacement history that was generated based on this loading protocol and applied to the specimens. Additional monotonic tests were also performed in order to determine the effect of cumulative cyclic damage on the capacity of stud-to-track connections. The loading rate varied from 0.04 mm/sec to 0.42 mm/sec for the first series. However, a constant rate (0.21 mm/sec) was used for the remaining tests since the response of the connection was found to be insensitive to the loading rate.

Table 1
Test program matrix

Series label	Loading protocol	Loading rate, υ (mm/min.)	Stud/Track thickness (mm)	Gap (mm)	Connection configuration	Number of specimens
T48G13DT	Monotonic	0.04	0.48	13	Deflection track	1
	Monotonic	0.42	0.48	13	Deflection track	1
	Monotonic	0.21	0.48	13	Deflection track	1
	Cyclic	0.21	0.48	13	Deflection track	3
T48G03DT	Monotonic	0.21	0.48	3	Deflection track	1
	Cyclic	0.21	0.48	3	Deflection track	3
T48G22DT	Monotonic	0.21	0.48	22	Deflection track	1
	Cyclic	0.21	0.48	22	Deflection track	3
T48G13SA	Monotonic	0.21	0.48	13	Screw attached	1
	Cyclic	0.21	0.48	13	Screw attached	3
T75G13DT	Monotonic	0.21	0.75	13	Deflection track	1
	Cyclic	0.21	0.75	13	Deflection track	3
T75G13SA	Monotonic	0.21	0.75	13	Screw attached	1
	Cyclic	0.21	0.75	13	Screw attached	3

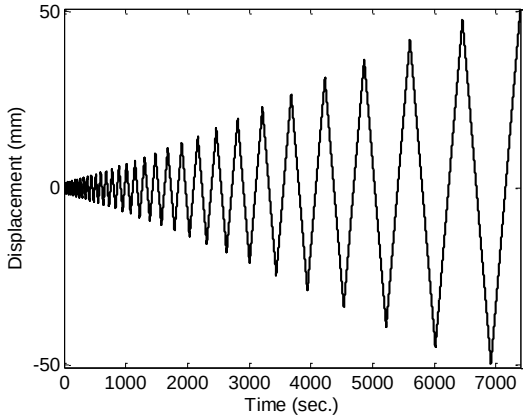

Fig. 2. Loading protocol for cyclic tests

3. Experimental results

3.1. Individual stud-to-track connection force and displacement

The free-body diagram of force and displacement of the test setup in a downward monotonic test is provided in Fig. 3. It is assumed that the displacement of two stud-to-track connections are identical and equal to the displacement of the movable grip. Moreover, the total force (P in Fig. 3) is considered to be equally distributed between two connections. Thus, the force for an individual connection was calculated as P / 2.

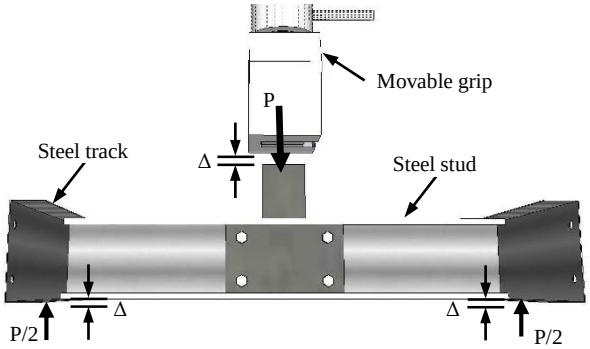

Fig. 3. Free-body diagram for a sample specimen

3.2. Damage mechanisms

Fig. 4 depicts the basic behavior and damage mechanisms of a stud-to-track connection subjected to an increasing downward displacement. A slight track-flange deformation (*SD*) was initially observed as the stud moved downward. For deflection-track configurations with large stud-to-track gaps (equal to or larger than 13 mm), this damage was followed by an excessive track-flange deformation (*ED*) and led to the popping out of the stud from the track (*PO*) (Fig. 4c). For other specimens, increasing the downward displacement caused the crippling of the stud web (*WC*) (Fig. 4d). Where screws were used to attach the stud to tracks, the screws were subsequently pulled from the studs (*SP*) (Fig. 4e). All tests were

continued until the studs popped out from the tracks, which was considered a complete failure of the connection. The last column of Table 2 (in section 3.3) summarizes the damage mechanisms observed in every test.

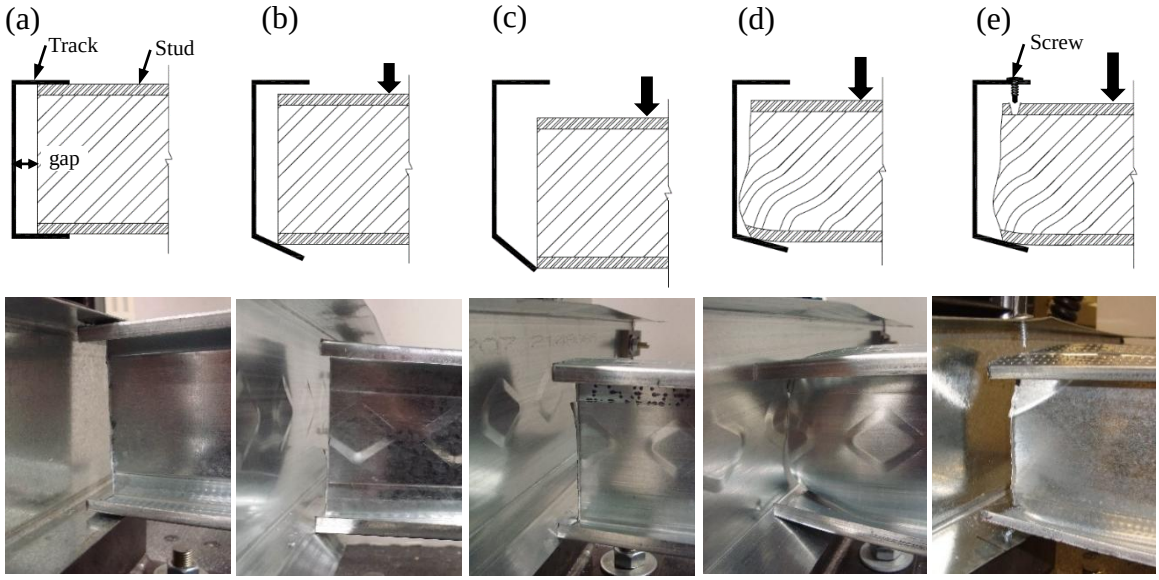

Fig. 4. Damage mechanisms of stud-to-track connections in the out-of-plane direction: (a) initial condition, (b) track-flange deformation, (c) stud popping-out from track, (d) stud-web crippling, (e) screw pull-out

3.3. Ultimate connection capacity

The typical experimental force-displacement responses in monotonic and cyclic tests and displacement zones corresponding to each damage description are provided in Fig. 5. The maximum recorded force, called the ultimate tested capacity, was dominated by track deflection (ED), web crippling (WC), or a combination of web crippling and screw pull-out (SP). According to AISI S100 [25] the web crippling strength of studs can be computed as below:

$$Web\ crippling: P_n = Ct^2F_y\left(1 - C_R\sqrt{R/t}\right)\left(1 - C_N\sqrt{N/t}\right)\left(1 - C_h\sqrt{h/t}\right) \quad (1)$$

where $C: 4$, $C_R: 0.14$, $C_N: 0.35$, $C_h: 0.02$, t: stud thickness, F_y: yield strength of the stud material, R: stud inside bend radius, N: stud bearing length, and h: flat dimension of stud web.

The AISI provision [25] also includes a design expression for nominal pull-out strength of a screw subjected to tension force [19], P_{not},

$$P_{not} = 0.85t_c dF_{u2} \quad (2)$$

where d: nominal screw diameter, F_{u2}: tensile strength of the member not in contact with screw head, and t_c : lesser of depth of penetration and thickness of the member not in contact with the screw head.

Using these provisions, Bolte and LaBoube 19] proposed the following equations to predict the capacity of stud-to-track connections with either deflection-track or screw-attached configurations:

$$Screw - attached: P_{nst} = P_n + R \times P_{not} \quad (3)$$

$$Deflection - track: P_{ndt} = b_{eff}t^2F_y/4e \quad (4)$$

where R: a reduction factor, e: the gap dimension, t: the track thickness, F_y: track material yield strength, and b_{eff}: effective flange length. The effective flange length was defined as a function of stud-flange width (w_{stud}) and the ratio of gap to track thickness:

$$b_{eff} = \Delta + w_{stud} \quad (5)$$

$$\Delta = \begin{cases} \dfrac{300(e/t^2)}{100} & for\ (e/t^2) < 100 \\ 300 & for\ (e/t^2) \geq 100 \end{cases} \quad (6)$$

In this study, Eq. (3) with an R=1 was employed to estimate the maximum capacity of specimens with screw-attached configuration. For other specimens, the lesser of the values calculated from Eqs. (1) and (4) were considered as the maximum capacity. In fact, both damage mechanisms *WC* and *ED* were checked to determine the mechanism that governed the capacity. Based on the manufacturer catalog, the following tensile strengths were used: for 75-mm-thick studs/tracks, a tensile strength of 228 MPa; for 19-mm-thick studs, a tensile strength of 448 MPa; and for 19-mm-thick tracks, a tensile strength of 345 MPa. Table 2 presents the comparison of the ultimate tested (P_{max}) and the estimated capacity as well as the ratio of these values. The equations predicted the tested capacity very well. Note that for design purposes, the AISI S100-12 [25] reduces the calculated capacity by factors of 1.7 and 2.8 (Ω factors) for web-crippling and deflection-track damage states, respectively.

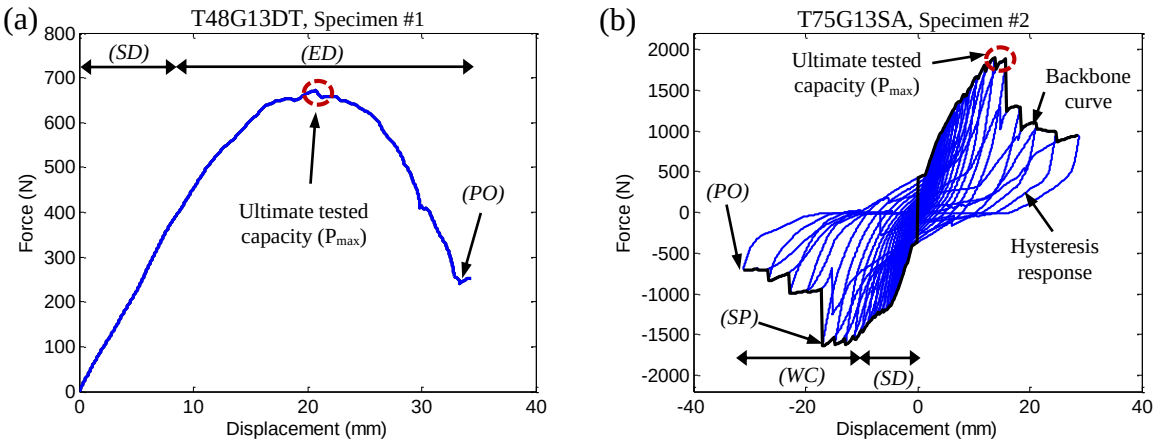

Fig. 5. Typical experimental responses for (a) monotonic and (b) cyclic tests

Table 2
Connection capacity

Series label	Loading protocol	Specimen #	Ultimate tested capacity (P_{max}), N	Estimated capacity, N	Tested/Estimated capacity ratio	Observed damage mechanisms
T48G13DT	Monotonic	1	671.2	589.4	1.14	SD, ED, PO
	Monotonic	1	689.4	589.4	1.17	SD, ED, WC, PO
	Monotonic	1	638.3	589.4	1.08	SD, ED, PO
	Cyclic	1	720.0	589.4	1.22	SD, ED, WC, PO
	Cyclic	2	669.5	589.4	1.14	SD, ED, PO
	Cyclic	3	692.8	589.4	1.18	SD, ED, PO
T48G03DT	Monotonic	1	1095.1	881.6	1.24	SD, WC, PO
	Cyclic	1	864.9	881.6	0.98	SD, WC, PO
	Cyclic	2	921.6	881.6	1.05	SD, WC, PO
	Cyclic	3	846.8	881.6	0.96	SD, WC, PO
T48G22DT	Monotonic	1	286.0	336.7	0.85	SD, TD, PO
	Cyclic	1	279.5	336.7	0.83	SD, TD, PO
	Cyclic	2	327.1	336.7	0.97	SD, TD, PO
	Cyclic	3	301.3	336.7	0.89	SD, TD, PO
T48G13SA	Monotonic	1	1765.1	1570.6	1.12	SD, WC, SP, PO
	Cyclic	1	1393.8	1570.6	0.89	SD, WC, SP, PO
	Cyclic	2	1559.1	1570.6	0.99	SD, WC, SP, PO
	Cyclic	3	1667.4	1570.6	1.06	SD, WC, SP, PO
T75G13DT	Monotonic	1	982.8	946.7	1.04	SD, TD, PO
	Cyclic	1	1089.8	946.7	1.15	SD, TD, PO
	Cyclic	2	1167.3	946.7	1.23	SD, TD, PO
	Cyclic	3	1144.1	946.7	1.21	SD, TD, PO
T75G13SA	Monotonic	1	1972.0	1593.3	1.24	SD, WC, SP, PO
	Cyclic	1	1835.5	1593.3	1.15	SD, WC, SP, PO
	Cyclic	2	1891.2	1593.3	1.19	SD, WC, SP, PO
	Cyclic	3	1945.2	1593.3	1.22	SD, WC, SP, PO
				Average =	1.08	
				COV =	0.12	

3.4. Effect of Loading Rate

In order to evaluate the effect of loading rate on the experimental results, the monotonic test of the first series of specimens was repeated with three different loading rates (0.04 mm/sec, 0.21 mm/sec, and 0.42 mm/sec). Fig. 6a and Fig. 6b compare the force-displacement responses and maximum force ratios in these monotonic tests. The maximum force ratio was defined as the ratio of the maximum force of each monotonic test to the maximum force of the monotonic test with a loading rate of 0.04 mm/sec. The comparison demonstrates a negligible variation in test results with an unclear trend. Moreover,

observed damage mechanisms were similar in these three tests. Accordingly, the performance of stud-to-track connections in the out-of-plane direction was assumed to be insensitive to the loading rate and a constant loading rate of 0.21 mm/sec was used for the rest of the experiments.

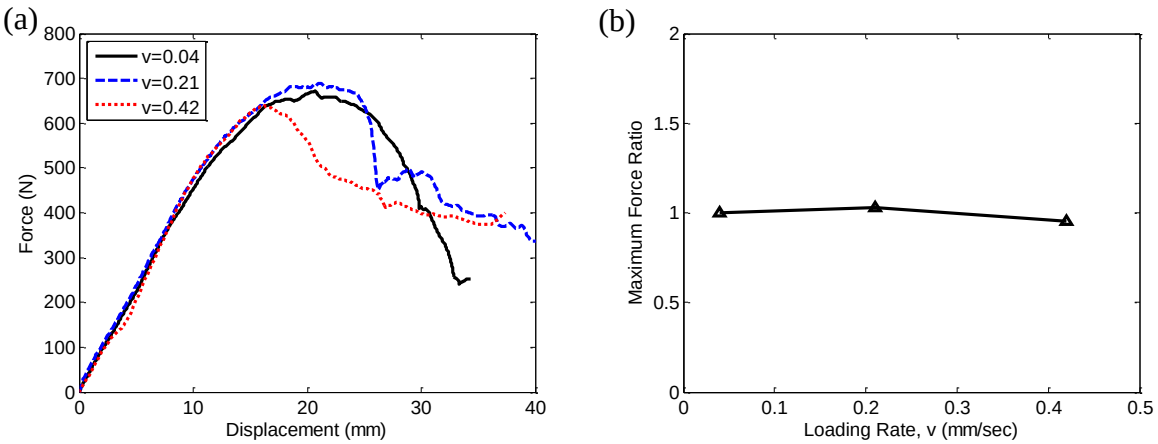

Fig. 6. Effect of loading rate (v, mm/sec) on: (a) monotonic force-displacement response, (b) maximum force ratio

3.5. Force-displacement response

The backbone curves of the cyclic tests, the median of the backbone curves, and the monotonic response of specimen series T48G03DT and T75G13DT, as two examples of tested series, are displayed in Fig. 7. The discrepancies between the responses of the three specimens in each series were marginal. The monotonic and cyclic responses were analogous in terms of initial stiffness, maximum force capacity, and observed damage mechanisms. Nonetheless, the complete failure of connections was usually initiated in lower displacements during the cyclic tests in comparison with the monotonic tests. This difference was mainly due to the effect of cumulative damage on the cyclic responses.

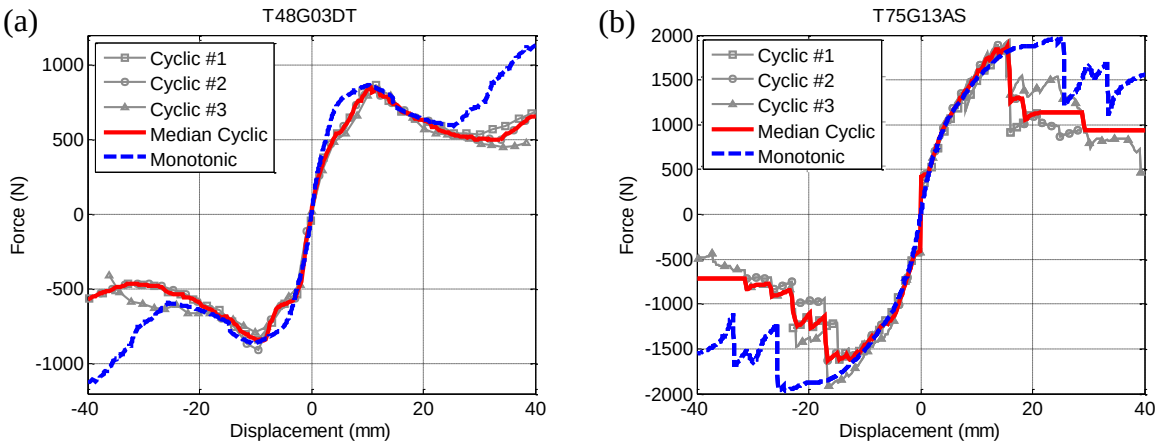

Fig. 7. Monotonic response and cyclic backbone curves for specimen series: (a) T48G03DT and (b) T75G13AS

Fig. 8a discloses the effect of stud-to-track gaps on the connection response. The figure indicates that a smaller gap leads to higher initial stiffness, larger force capacity, and larger failure displacement (the displacement associated with the complete failure of the connection). Furthermore, using a larger gap can change the dominant damage mechanism from track-flange deflection (*ED*) to stud-web crippling (*WC*) (see Table 2). The responses of connections with 48-mm- and 75-mm- thick studs/tracks, as well as connections with deflection-track and screw-attached configurations are compared in Fig. 8b. As expected, the initial stiffness and maximum force capacity were larger in connections with thicker studs/tracks and screw attachment. The reason is that the force characteristics of the specimen responses were controlled by the mechanisms (either *WC* or *ED*) that were enhanced by increasing stud/track thickness. However, utilizing thicker profiles limited the stud and track deformation. In fact, the thicker specimens were less ductile compared to the thinner specimens. Screwing the studs to the tracks also introduced additional stiffness and strength to the connection. The failure displacements of screw-attached connections were commonly larger than deflection-track connections.

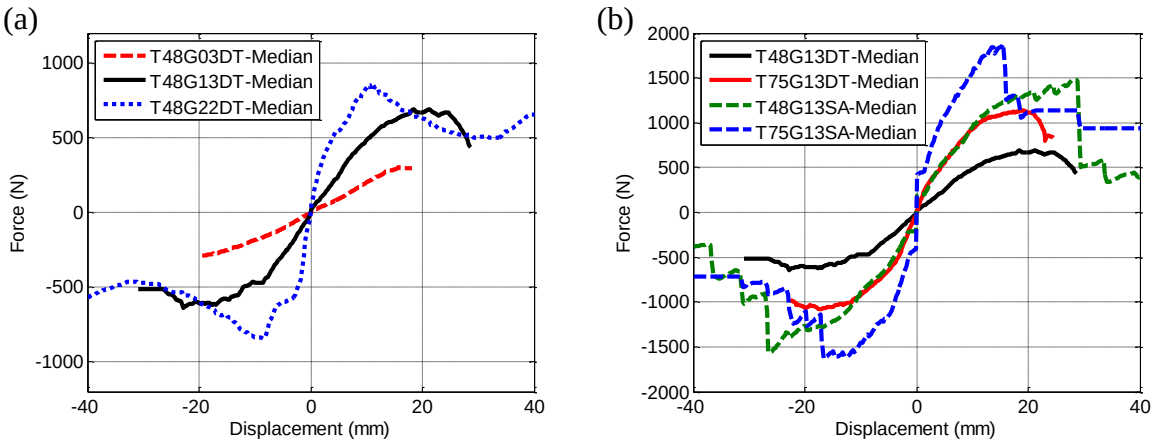

Fig. 8. Effect of (a) stud-to-track gap, (b) stud/track thickness and screw-attached configuration on the cyclic response

4. Capacity fragility analysis

Fragility curves state the probability of experiencing or exceeding a specific damage state (*DS*) conditioned on a particular value of an engineering demand parameter (*EDP*). The required steps to generate the fragility curves include: 1) choose a proper fragility formulation, 2) select appropriate engineering demand parameters, 3) determine capacity (damage state) estimates, and 4) develop fragility curves [26].

A number of methodologies for generating capacity fragility curves have been developed in the past. In this study, method *A* proposed by Porter et al. [27] was adopted to assess the vulnerability of stud-to-track connections in the out-of-plane direction. This method can be used in experimental studies in which all specimens reach all *DSs* at observed values of *EDPs*. This is most common where the damage can be associated with a point on the observed force-displacement of a component [27]. Porter et al. utilized a lognormal probability distribution, $F_{dm}(edp)$, to define the probability that the component

reaches or exceeds damage state *dm*, given a particular *EDP* value, $P[DM \geq dm|EDP = edp]$, as follows:

$$F_{dm}(edp) \equiv P[DM \geq dm|EDP = edp] = \Phi\left(\frac{ln(edp/x_m)}{\beta}\right) \quad (7)$$

where Φ denotes the standard normal (Gaussian) cumulative distribution function, x_m indicates the median value of the distribution, and β represents the logarithmic standard deviation [27]. The *EDPs* should be chosen to be most closely related to the failure probability of the specimen. The cyclic performance of the stud-to-track connections were mainly governed by the displacement of the stud. Therefore, this displacement was considered as the main *EDP*. However, the connection force was also used as an alternate demand parameter.

Three damage states were defined for stud-to-track connections based on the extent of the nonlinearity in connections and observed damage mechanisms. The first damage state (*DS1*), which represented the initiation of nonlinearity in the connection, was defined as the displacement associated with $0.40P_{max}$ [28]. This point correlated with the observation of a slight deformation in track flanges (*SD*) and can be considered as the serviceability limit. The second damage state (*DS2*) was set to the local maximum point on the backbone curve. Extensive track-flange deflection (*ED*) and/or stud-web crippling (*WC*) were observed at this damage state. Note that in addition to the more common issues related to excessive deformation such as cracking of finishes, large deformation at the stud-to-track location could prevent the proper operation of windows and doors. In this case, excessive deflection would be a limit state on safety rather than serviceability [22]. The third damage

state (*DS3*) was considered as the displacement corresponding to the pop-out of the stud from the track (*PO*). Fig. 9 depicts the *DSs* with their associated points on two representative backbone curves.

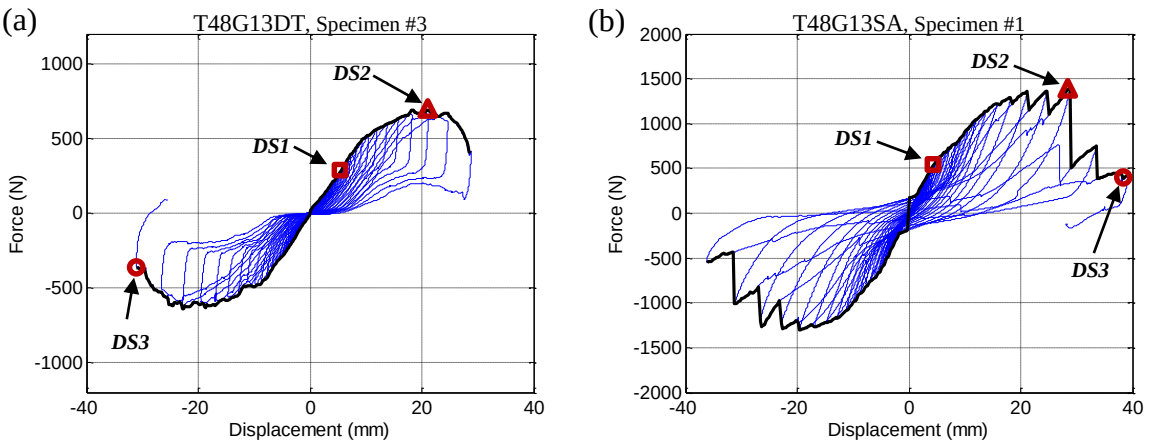

Fig. 9. Examples of damage state definitions for: (a) deflection-track configuration (b) screw-attached configuration

In method *A*, the individual damage states are characterized by representative values for the median, x_m, and dispersion, β, for the component damage state distributions as follows (Porter et al. 2007, Soroushian et al. 2014):

$$x_m = e^{\frac{1}{N}\sum_{i=1}^{N} ln(x_i)} \tag{8}$$

$$\beta = \sqrt{\frac{1}{N-1}\sum_{i=1}^{N}\left[\ln\left(\frac{x_i}{x_m}\right)\right]^2} \tag{9}$$

where x_i denotes the i-th measured displacement corresponding to specific damage observation (*EDPs*) and *N* is the number of cyclic tests conducted for each group of specimens. The fragility curves were generated for each series of specimens; therefore, *N*

was equal to 3 for all groups. Table 3 and Table 4 summarize the *EDPs* (x_i), x_m, and logarithmic standard deviation obtained for each series and damage level.

Table 3
Engineering demand parameters

Series label	Spec. No.	Disp., mm			Force, N
		DS1	*DS2*	*DS3*	*DS2*
T48G03DT	1	1.9	11.5	47.6	865
	2	1.5	10.0	42.0	922
	3	2.3	12.0	39.6	847
T48G13DT	1	5.8	21.7	31.5	720
	2	5.3	21.0	28.8	669
	3	5.4	21.1	31.0	693
T48G22DT	1	6.4	14.7	15.9	279
	2	5.1	16.9	18.2	327
	3	6.6	15.8	21.1	301
T48G13SA	1	4.6	28.8	39.1	1394
	2	5.4	26.3	44.9	1559
	3	6.7	26.1	39.1	1667
T75G13DT	1	4.0	15.2	24.6	1090
	2	4.4	18.3	24.6	1167
	3	3.1	19.0	22.8	1144
T75G13SA	1	3.0	15.1	24.6	1836
	2	2.8	13.7	33.6	1891
	3	2.9	15.8	44.9	1945

Table 4
Fragility curve parameters

Series label	*DS1*		*DS2*		*DS3*		*DS2*	
	x_m, mm	β	x_m, mm	β	x_m, mm	β	x_m, N	β
T48G03DT	1.9	0.21	11.1	0.09	42.9	0.09	877	0.04
T48G13DT	5.5	0.05	21.3	0.02	30.4	0.05	694	0.04
T48G22DT	6.0	0.14	15.8	0.07	18.3	0.14	302	0.08
T48G13SA	5.5	0.18	27.0	0.05	40.9	0.08	1536	0.09
T75G13DT	3.8	0.18	17.4	0.12	24.0	0.04	1133	0.04
T75G13SA	2.9	0.03	14.8	0.08	33.3	0.30	1890	0.03

Fig. 10a, Fig. 10b, and Fig. 10c depict the fragility curves for stud-to-track connections in the out-of-plane direction, considering displacement as *EDP*. A smaller stud-to-track gap improves the connection in the first and last damage states (*DS1* and *DS3*) but may deteriorate the connection performance in *DS2*. The curves also indicate that the connections with thicker studs/tracks are more vulnerable in all damage states. There was no clear difference between the deflection-track and screw-attached configurations in the first two damage states. However, the screw attachment could postpone the complete failure of the connection (*DS3*). A similar trend can be found by comparing the median values (x_m) in Table 4. It should be mentioned that the Lilliefors goodness-of-fit test at 5% significance level [29] was performed for each series of specimens in order to check the

validity of the lognormal distribution. The test was satisfied, therefore the lognormal distribution appropriately fitted the data.

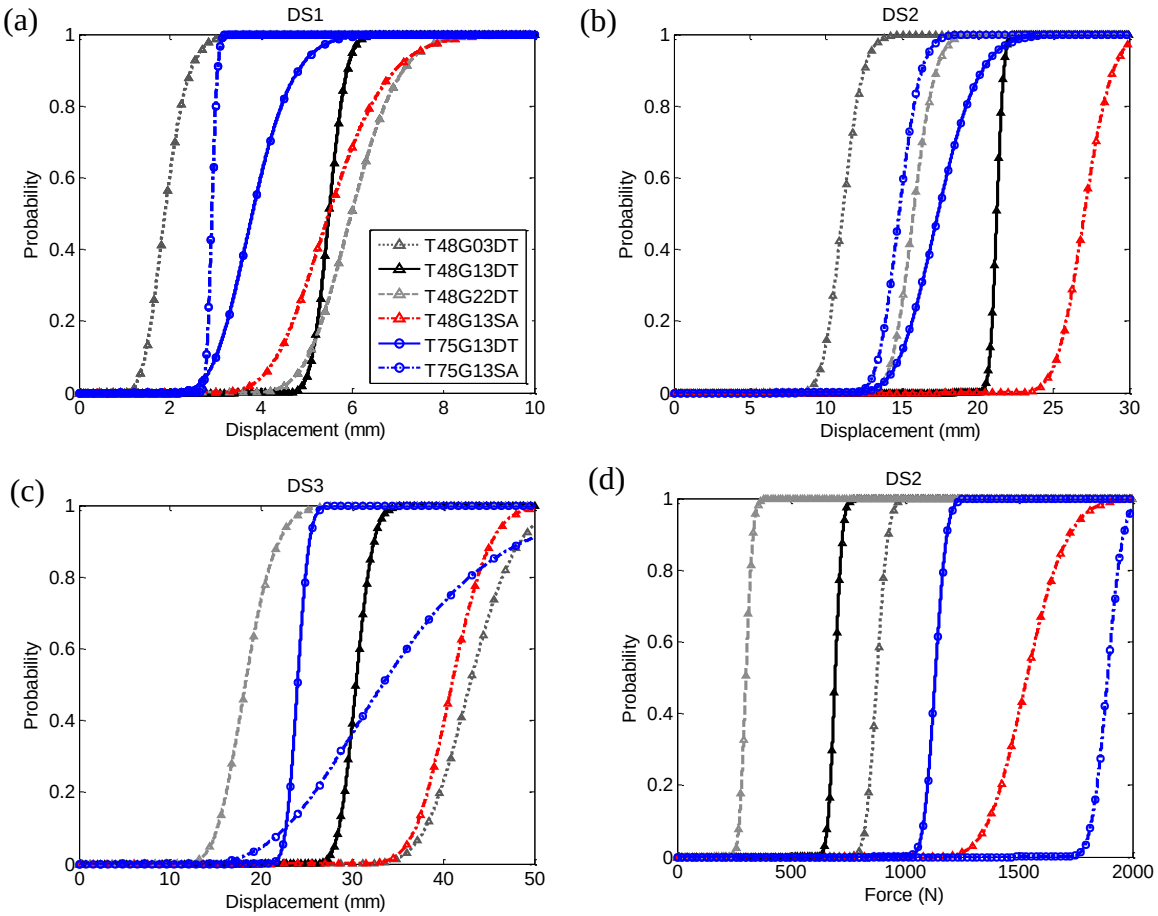

Fig. 10. Displacement-based fragility curves for (a) first damage state, (b) second damage state, (c) third damage state, and (d) force-based fragility curves for second damage state

An alternative set of fragility curves (for *DS2*) based on the connection force is presented in Fig. 10d. The figure reveals that although smaller gaps, thicker profiles, and screw attachment might increase the probability of occurrence of *DS2* in terms of connection displacement, they augment the connection in terms of force capacity. The fragility curves of Fig. 10d can be adopted, in lieu of the fragility curves of Fig. 10b, where the force-based design methodology is desired rather than the displacement-based.

Consider that Fig. 10d can be converted to the fragility curves of *DS1* by scaling the horizontal axis by a factor of 0.4.

5. Development of a numerical hysteresis model for stud-to-track connections in out-of-plane direction

The experimental data was employed to develop a numerical hinge material model for the behavior of stud-to-track connections in the out-of-plane direction. A one-dimensional hysteresis load-displacement relationship is defined using the “Pinching4” uniaxial material along with a “zeroLength” element in OpenSees [3026]. This material enables the simulation of complex, pinched force hysteresis responses accounting for degradations under cyclic loadings [26] similar to one shown in Fig. 5(b). The “Pinching4" material model requires the definition of 39 parameters as presented in Fig. 11. Sixteen parameters describe the backbone curve in positive (*ePdi* and *ePfi*) and negative directions (*eNdi* and *eNfi*), while an additional eight parameters characterize the “pinched” or unloading/reloading behavior of the model. The pinching parameters include the ratio of reloading/maximum historic deformation *rDisp(P-N),* the ratio of reloading/maximum historic force *rForce(P-N),* and the ratio of negative (positive) unloading/maximum (minimum) monotonic strength *uForceP(N)* [26]. Unloading and reloading stiffness degradation as well as strength degradation can be considered in the model using *gKi*, *gDi* , and *gFi*. A detailed description of these parameters can be found at the OpenSees website [3026].

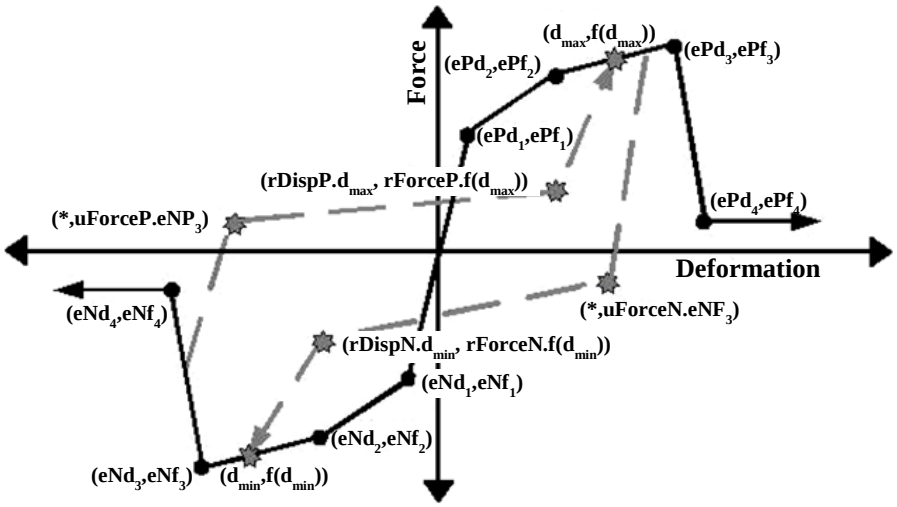

Fig. 11. Pinching 4 material properties (OpenSees 2015)

5.1. Calibration of proposed numerical model using experimental data

For each specimen, a "Pinching4" material was calibrated so that the hysteresis response, the value of cumulative hysteresis energy, and the force histories fit the experimental data on a visual basis [26]. In addition, the error in the maximum cumulative hysteresis energy was checked to be less than 10%. The recorded displacement histories were utilized as the inputs for numerical analysis. Fig. 12 describes the calibration process for one sample stud-to-track connection from the T48G03DT series.

Initially for each specimen, all 39 parameters of "Pinching4" material were calibrated to find the best correlation between numerical results and experimental data. However, after performing a sensitivity analysis on the parameters, it was noted that the force and stiffness degradation parameters (*gKi*, *gDi*, and *gFi*) as well as the pinching and unloading/reloading parameters (23 out of 39 parameters) could be fixed. Therefore, constant values were assigned to these parameters (Table 5). Subsequently, to generate a numerical model with a backbone curve consistent with the experimental results, backbone

points were determined for each particular specimen. Table 6 presents examples of the values used to define the backbone curves. Fig. 13a displays the comparisons of numerical and experimental results for a sample specimen.

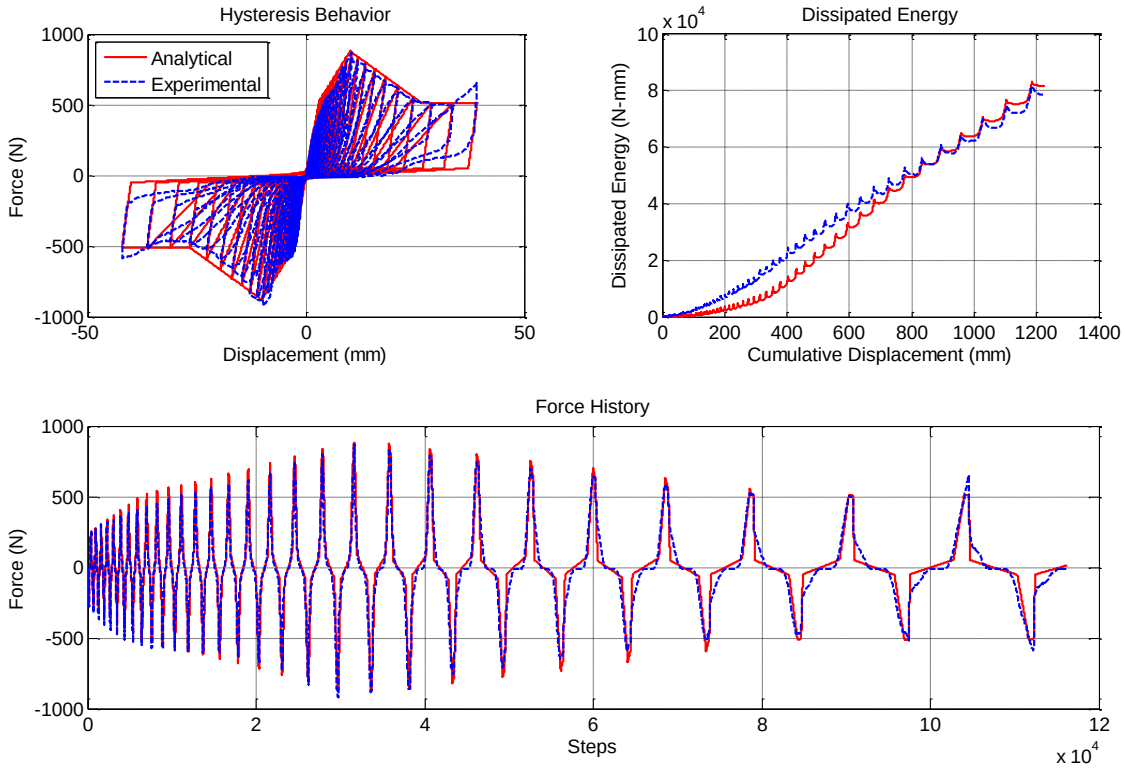

Fig. 12. Calibrated numerical model for a sample specimen (T48G03DT, specimen #2)

Table 5
Fixed "Pinching4" parameters

Parameters									
rDispP/N	*rForceP/N*	*uForceP/N*	*gK*	*gKLimit*	*gD*	*gDLimit*	*gF*	*gE*	*dam*
0.6	0.1	-0.1	0	0	0	0	0	1	cycle

Table 6
Sample calibrated "Pinching4" backbone parameters

Specimen No.	*ePfi* and *eNfi* in N, *ePdi* and *eNdi* in mm							
	ePf1 *ePd1*	*ePf2* *ePd2*	*ePf3* *ePd3*	*ePf4* *ePd4*	*eNf1* *eNd1*	*eNf2* *eNd2*	*eNf3* *eNd3*	*eNf4* *eNd4*
Specimen series T48G13AS								
Specimen #1	40.0 0.2	934.1 7.6	1378.9 21.6	489.3 35.6	-40.0 -0.2	-934.1 -7.6	-1378.9 -21.6	-489.3 -35.6
...	...	...	...	...	...	...	...	...
Specimen series T75G13DT								
Specimen #1	80.1 0.2	934.1 9.4	1112.1 20.3	734.0 24.6	-80.1 -0.2	-934.1 -9.4	-1112.1 -20.3	-734.0 -24.6
...	...	...	...	...	...	...	...	...

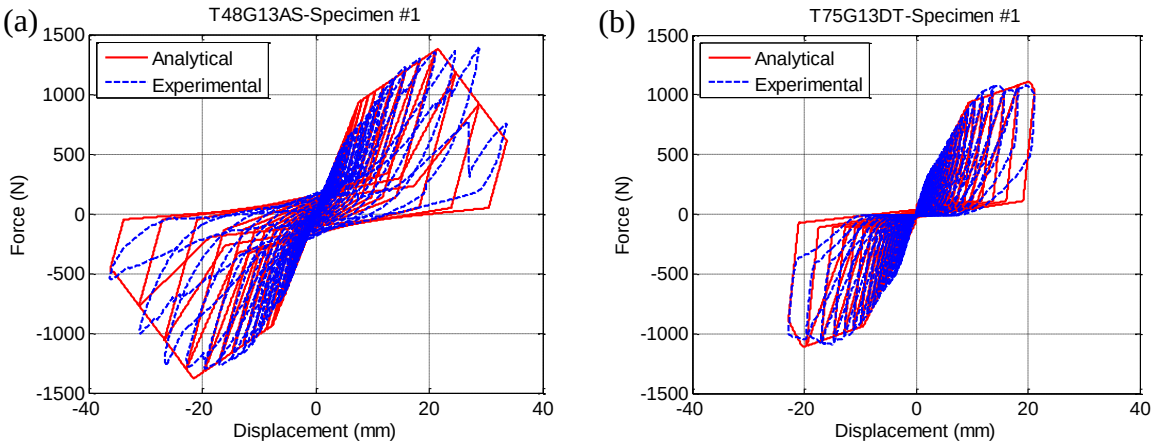

Fig. 13. Sample numerical-experimental hysteresis comparisons of specimen series (a) T48G13AS (b) T75G13DT

5.2. Development of generic models for tested connections

In the previous section, a total of 18 sets of the 16 backbone parameters of "Pinching4" material (*ePd*$_i$, *ePf*$_i$, *etc)* were optimized. A comparison of these sets indicated that there were major variations between the backbone parameters of specimens of different series, while the discrepancies between the backbone parameters of the three specimens within each series were minimal. In order to facilitate the future numerical modeling of stud-to-track connections, one suite of material parameters was defined as the generic parameters for every specimen series, called the generic model. These generic models represent the

stud-to-track connections with properties (stud/track thickness, gap size, and connection configuration) similar to what were tested in each series. Inspired by the work of Soroushian et al. [26], the generic models were developed following these assumptions: 1) the displacement points of the backbone curve (in each direction), ePd_1, ePd_2, ePd_3, ePd_4 (Fig. 11), are set to the median of the calibrated values corresponding to each of these points of the backbone curve; 2) a linear interpolation is used to find the force corresponding to the previously mentioned displacements where the force values at the calibrated backbone curves are unavailable. The median of these force values for each set denotes the backbone points in each direction (ePf_1 ePf_2, ePf_3, and ePf_4 in Fig. 11); 3) the remainder of the parameters (fixed parameters) are the same as those provided in Table 5.

The generic model parameters, obtained based on the aforementioned assumptions, are presented in Table 7. As an example, Fig. 14a shows the comparison between the generic backbone curves and all the calibrated backbone curves of series T75G50AS. Fig. 14b compares the hysteresis response of this generic model to the experimental data of specimen #2.

Table 7
"Pinching4" backbone parameters for generic models

Series label	*ePfi* and *eNfi* in N, *ePdi* and *eNdi* in mm							
	ePf1 *ePd1*	*ePf2* *ePd2*	*ePf3* *ePd3*	*ePf4* *ePd4*	*eNf1* *eNd1*	*eNf2* *eNd2*	*eNf3* *eNd3*	*eNf4* *eNd4*
T48G03DT	40.0 0.2	524.9 3.0	845.2 10.2	513.0 27.9	-40.0 -0.2	-524.9 -3.0	-845.2 -10.2	-513.0 -27.9
T48G13DT	48.9 0.2	498.2 8.9	682.4 21.1	462.3 29.2	-48.9 -0.2	-498.2 -8.9	-682.4 -21.1	-462.3 -29.2
T48G22DT	17.8 0.2	226.7 11.9	273.8 17.0	177.9 18.3	-17.8 -0.2	-226.7 -11.9	-273.8 -17.0	-177.9 -18.3
T48G13SA	40.0 0.2	943.0 8.1	1495.5 25.4	489.3 35.6	-40.0 -0.2	-943.0 -8.1	-1495.5 -25.4	-489.3 -35.6
T75G13DT	80.1 0.2	956.4 8.9	1112.1 19.1	800.7 24.6	-80.1 -0.2	-956.4 -8.9	-1112.1 -19.1	-800.7 -24.6
T75G13SA	111.2 0.2	1156.5 4.1	1714.8 14.7	1156.5 23.4	-111.2 -0.2	-1156.5 -4.1	-1714.8 -14.7	-1156.5 -23.4

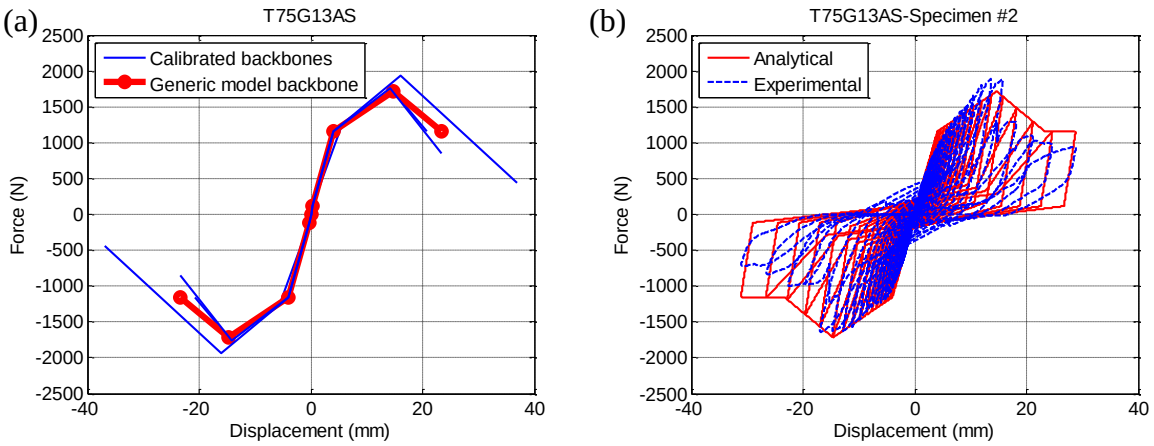

Fig. 14. (a) Generic backbone curves of specimen series T75G13AS, (b) Sample numerical-experimental hysteresis comparison

5.3. Proposed generic models for untested stud-to-track connections

The generic models for stud-to-track connections with three specific gaps and two stud/track thicknesses were provided in the preceding section. However, the connection gap and/or thickness in practical works might be different from the tested values. Therefore, an approximate procedure is proposed in this section to generate numerical models of stud-to-track connections for any stud/track thicknesses and/or gaps. The proposed method is based on the assumption that the maximum connection capacity is governed by either track-flange deflection or stud-web crippling. Supplemental experiments with a wider range of stud/track profiles and material properties, gaps, and screw types are essential in order to enhance the proposed model in the future.

A normalized generic backbone curve was developed for stud-to-track connections with deflection-track configuration using the following procedure: 1) the backbone curve is considered to be symmetric; 2) the first backbone-point displacement (ePd_1) was assumed to be constant (independent of the connection properties) and equal to 0.2 mm; 3)

the secant stiffness was found for the last three backbone points of each specimen (Fig. 15a); 4) the secant stiffness values were plotted against the corresponding values of $t \times b_{eff}/e$, where *e* is the gap dimension, *t* represents the stud/track thickness, and b_{eff} denotes the effective flange length, defined by Eqs. (5); 5) the least-square regression method is utilized to fit a line to the data (Fig. 16); 6) the equations of these lines can be used to determine the secant stiffness of backbone curves of stud-to-track connections with gap and/or profile thickness other than those that were tested in this study; 7) all the backbone curve force values (ePf_i and eNf_i) of each specimen model are normalized with respect to the maximum force value (ePf_3) (Fig. 15b); 8) the median of nine normalized force values corresponding to each backbone point are used to define the normalized generic backbone curve (Table 8). The normalized generic backbone curve (Fig. 17a) can be multiplied by the ultimate connection capacity (the lesser of the values calculated from Eqs. (1) and (4)) to find force values of the numerical backbone curve for connections with any stud/track thicknesses and/or gap size. Afterwards, the force values can be divide by the secant stiffness values (calculated based on the fitted line in Fig. 16) to find the displacement of the backbone points.

Screwing the stud to the tracks introduces additional strength to the connection that mainly affects the force values of the second and third backbone points (ePf_2, ePf_3, ePN_2, and eNf_3) (see Table 7). Thus, for screw-attached configurations (with gap dimensions and/or profile thicknesses other than those tested in this study), the numerical backbone curve can be generated following these steps: 1) an initial backbone curve is developed assuming a track-deflection configuration and based on Fig. 17a, 2) the force values of second and third backbone points are increased as much as $R \times P_{not}$ (see Eq. (3)). A

schematic development of a backbone curve for a screw-attached connection is illustrated in Fig. 17b.

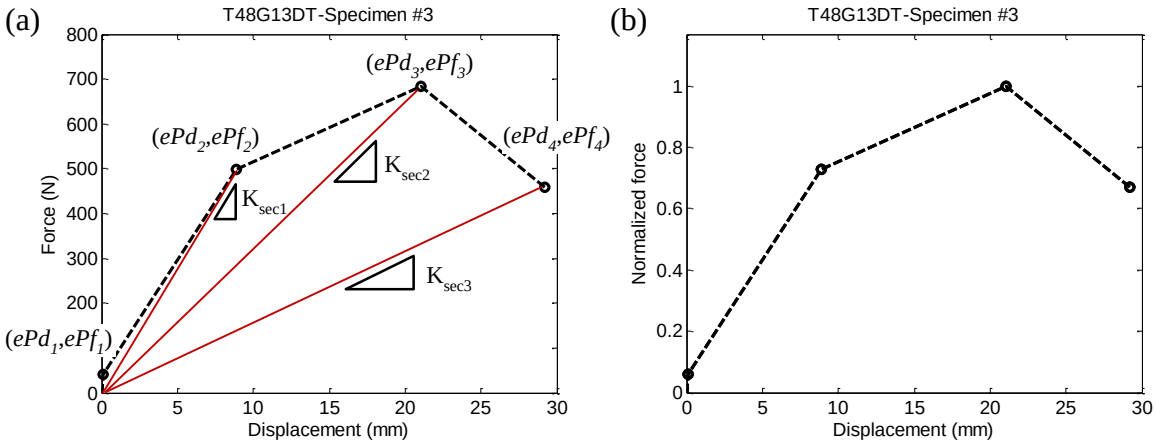

Fig. 15. (a) Secant stiffness calculation on a sample specimens, (b) force normalized backbone curve of a sample specimen

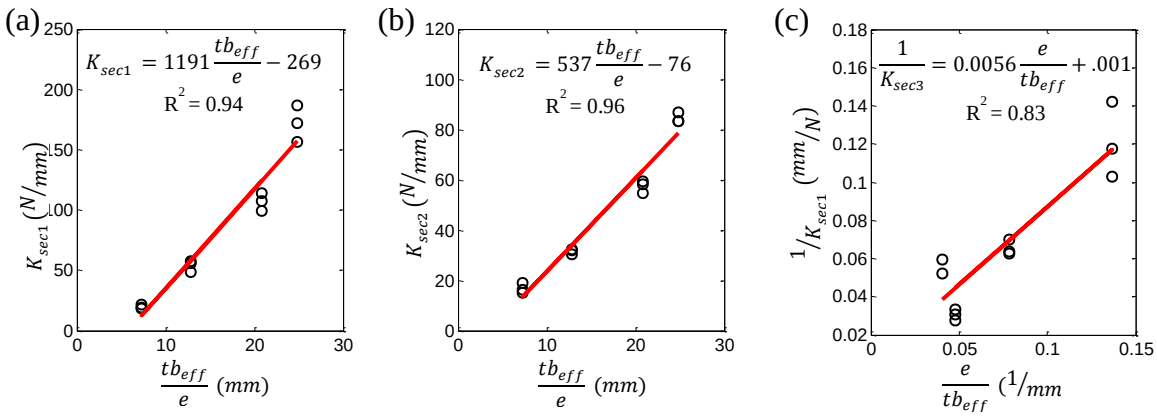

Fig. 16. Fitted lines to secant stiffness values (a) K_{sec1} , (b) K_{sec2}, and (c) K_{sec3}

Table 8
"Pinching4" backbone parameters for the generic model for untested connections

Normalized *ePfi* and *eNfi* (unitless)							
ePf1	*ePf2*	*ePf3*	*ePf4*	*eNf1*	*eNf2*	*eNf3*	*eNf4*
0.07	0.75	1.00	0.65	-0.07	-0.75	-1.00	-0.65

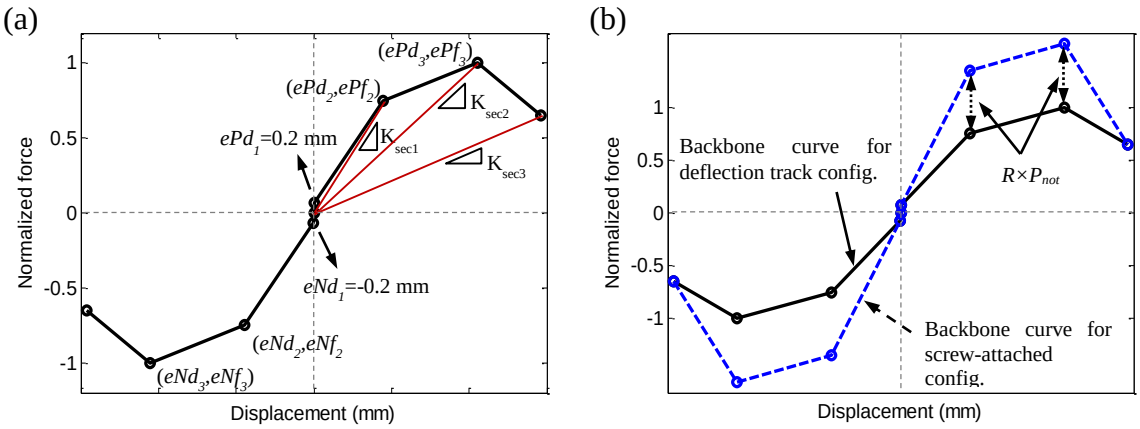

Fig. 17. (a) Normalized generic backbone curve for track-deflection configuration, (b) Schematic modified backbone curve for screw-attached configuration

6. Summary and Conclusions

Cold formed steel stud-to-track connections were tested under monotonic and reverse cyclic loading as part of a larger investigation of nonstructural partition wall behavior. Stud/track thickness, stud-to-track gap, and the connection configurations (either screw-attached or deflection-track) were varied between specimens. The test program was designed to assess the out-of-plane displacement and strength capacities and stiffness of stud-to-track connections in nonstructural partition walls.

The main observations and conclusions obtained from the experimental study are as follows:

- The dominant damage mechanism was excessive track-flange deformation for connections with large stud-to-track gap (larger than 3 mm in this study) and stud-web crippling for other connections. Where studs were screwed to tracks, the screws were pulled out from the studs after the web crippling.

- The equations proposed by Bolte and LaBoube [1925] and AISI S100-12 [25] could appropriately estimate the ultimate force capacity of the connection.
- Increasing the stud-to-track gap not only affects the dominant damage mechanism, but also leads to lower initial stiffness, smaller force capacity, and smaller failure displacement. Moreover, the initial stiffness and maximum force capacity were larger in connections with thicker studs/tracks and attached screws. The connections with thicker studs/tracks were less ductile compared to the thinner connections.
- The displacement-based fragility analysis revealed that: 1) a smaller stud-to-track gap improves the connection in the first and last damage states (*DS1* and *DS3*) but may deteriorate the connection performance in *DS2*, 2) connections with thicker studs/tracks are more vulnerable in all damage states, 3) adding screws can postpone the complete failure of the connection (*DS3*).
- The experimental data was employed to generate and calibrate a series of nonlinear hinge models for all specimens. Subsequently, for each series a generic model was defined that represented a stud-to-track connection with properties (stud/track material and thickness, stud-to-track gap, and screw type) similar to those that have been tested in that series. In addition, an approximate procedure is proposed to generate numerical models of stud-to-track connections with any stud/track thicknesses and/or gap dimensions.

The hinge model of stud-to-track connections could be utilized along with the numerical models of other wall components (such as gypsum-to-stud connections and steel studs) to numerically model the in-plane and out-of-plane behavior of a partition wall

assembly. The model could be subjected to realistic input motions (e.g. floor accelerations) to estimate the demand parameters on each component. These demand estimations could be used in conjunction with the capacity parameters (e.g. median and deviation) developed in this study (and similar studies for other partition wall components) to generate fragility curves for partition wall systems in terms of more global engineering demand parameters, such as floor accelerations and/or inter-story drifts

7. Acknowledgments

The current material is based upon work supported by the National Science Foundation under Grant No. 0721399. This Grand Challenge (GC) project to study the seismic response of nonstructural systems is under the direction of M. Maragakis from the University of Nevada, Reno and Co-PIs: T. Hutchinson (UCSD), A. Filiatrault (UB), S. French (G. Tech), and B. Reitherman (CUREE). Any opinions, findings, conclusions, or recommendations expressed in the current document are those of the investigators and do not necessarily reflect the views of the sponsors. The input provided by the Practice Committee of the NEES Nonstructural Project, composed of W. Holmes (Chair), D. Allen, D. Alvarez, and R. Fleming, and by the Advisory Board, composed of R. Bachman (Chair), S. Eder, R. Kirchner, E. Miranda, W. Petak, S. Rose and C. Tokas, has been crucial for the completion of this research. Assistance from M. Lattin of the University of Nevada, Reno material lab during the assembly and testing as well as support from Johnnie Stolz of Omboli Interior Inc. is appreciated.

8. References

1. Taghavi S, and Miranda E. Response Assessment of Nonstructural Building Elements, *PEER*

Report 2003/05, Pacific Earthquake Engineering Research Center (PEER), Berkeley, CA, 2003.

2. Restrepo JI, Lang AF. Study of Loading Protocol in Light-Gauge Stud Partition Wall. *Earthquake Spectra* 2011; 27:1169–1185. DOI: 10.1193/1.3651608.
3. Dhakal RP. Damage to non-structural components and contents in 2010 Darfield earthquake. *Bulletin of The New Zealand Society for Earthquake Engineering* 2010; 43:404-411.
4. Baird A, Tasligedik AS, Palermo S, Pampanin S. Seismic performance of vertical non-structural components in the 22nd February 2011 Christchurch earthquake. *Earthquake Spectra* 2014; 30(1), 401–425. DOI: 10.1193/031013EQS067M.
5. Mizutani K, Kim H, Kikuchihara M, Nakai T, Nishino M, Sunouchi S. The damage of the building equipment under the 2011 Tohoku pacific earthquake. *9th International Conference on Urban Earthquake Engineering & 4th Asia Conference on Earthquake Engineering*, Tokyo Institute of Technology, Tokyo, Japan, 2012.
6. EERI (Earthquake Engineering Research Institute). The El Mayor Cucapah, Baja California earthquake April 4, 2010. *An EERI Reconnaissance Rep* 2012; 2010-02, J. Meneses, ed., Oakland, CA.
7. Miranda E, Mosqueda G, Retamales R, Pekcan G. Performance of Nonstructural Components during the 27 February 2010 Chile Earthquake. *Earthquake Spectra* 2012; 28:S1:S453–S471. DOI: 10.1193/1.4000032.
8. Wood RL, Hutchinson TC. Design-Oriented Model for Capturing the In-Plane Seismic Response of Partition Walls. ASCE *Journal of Structural Engineering* 2014, 140. DOI: 10.1061/(ASCE)ST.1943-541X .0000899.
9. Wang X, Pantoli E, Hutchinson T, Restrepo J, Wood R, Hoehler M, Grzesik P, and Sesma F. Seismic Performance of Cold-Formed Steel Wall Systems in a Full-Scale Building, 2015, ASCE *Journal of Structural Engineering*. DOI: 10.1061/(ASCE)ST.1943-541X.0001245.
10. Fülöp LA, Dubina D. Performance of Wall-Stud Cold-Formed Shear Panels under Monotonic and Cyclic Loading, Part I: Experimental research. *Thin-Walled Structures* 2004; 42: 321–338. DOI: 0.1016/S0263-8231(03)00063-6.
11. Lee T, Kato M, Matsumiya T, Suita K, Nakashima M. Seismic Performance Evaluation of Non-structural Components: Drywall Partitions. *Earthquake Engineering and Structural Dynamics* 2007; 36: 367–382. DOI: 10.1002/eqe.638.
12. Retamales R, Mosqueda G, Filiatrault A, Reinhorn AM. New Experimental Capabilities and Loading Protocols for Seismic Qualification and Fragility Assessment of Nonstructural Components. *Technical Report MCEER-08-0026*, State University of New York at Buffalo, NY, 2008.
13. Restrepo JI, Bersofsky A. Performance Characteristics of Light Gage Steel Stud Partition Walls. *Thin-Walled Struct*ures 2010; 49:317–324. DOI: 10.1016/j.tws.2010.10.001.
14. Soroushian S, Ryan KL, Maragakis M, Wieser J, Sasaki T, Sato E, Okazaki T, Tedesco L, Zaghi AE, Mosqueda G, Alarez D. NEES/E-Defense tests: Seismic performance of ceiling/sprinkler piping nonstructural systems in base isolated and fixed base building. *15th World Conference on Earthquake Engineering (15WCEE)*, Lisbon, Portugal, 2012.
15. Retamales R, Davies R, Mosqueda G, Filiatrault A. Experimental Seismic Fragility of Cold-Formed Steel Framed Gypsum Partition Walls. ASCE *Journal of Structural Engineering* 2013;

139:1285-1293. DOI: 10.1061/(ASCE)ST.1943-541X.0000657.

16. Rahmanishamsi E, Soroushian S, Maragakis M. System-Level Experiments on Ceiling/Piping/Partition Systems at UNR-NEES Site. *Tenth U.S. National Conference on Earthquake Engineering*, Anchorage, AK, 2014. DOI: 10.4231/D3BR8MG8F.
17. Jenkins, C., Soroushian, S., Rahmanishamsi, E., and Maragakis, M. Experimental Fragility Analysis of Cold-Formed Steel-Framed Partition Wall Systems, *Structural Congress*, ASCE, Portland, OR, 2015. DOI: 10.1061/9780784479117.152.
18. Fox SR., Schuster RM. Lateral strength of wind load bearing wall stud-to-track connection. Proceedings of the 15th International Specialty Conference on Cold-Formed Steel Structures, Rolla (MO): University of Missouri –Rolla, 2000.
19. Bolte, W.G., LaBoube, R.A. Behavior of Curtain Wall Stud to Track Connections, *Thin-Walled Structures* 2004, 42, 1431–1443, DOI: 10.1016/j.tws.2004.01.005.
20. North American Specification for the Design of Cold- Formed Steel Structural Members. American Iron and Steel Institute, Washington, DC, 2001.
21. United States Army Corps of Engineers. Design of cold-formed load-bearing steel systems and masonry veneer/steel stud wall. Technical Instructions TI 809-07, Washington, DC; 1998.
22. Lewis, A.V., Fox, S.R., Schuster, R.M. Strength of Cold-Formed Steel Jamb Stud-to-Track Connections, Nineteenth International Specialty Conference on Cold-Formed Steel Structures, St. Louis, Missouri, 2008.
23. Rahmanishamsi E, Soroushian S, Maragakis EM. Cyclic Shear Behavior of Gypsum Board-to-Steel Stud Screw Connections in Nonstructural Walls. *Earthquake Spectra* 2015. In-Press. DOI: 10.1193/062714EQS091M
24. Retamales, R., Mosqueda, G., Filiatrault, A., and Reinhorn, A.M. Testing protocol for experimental seismic qualification of distributed nonstructural systems. *Earthquake Spectra* 2011, 27(3):835-856, DOI: 10.1193/1.3609868.
25. AISI S100-12, North American Specification for the Design of Cold- Formed Steel Structural Members. American Iron and Steel Institute, Washington, DC, 2012.
26. Soroushian S, Zaghi AE, Maragakis M, Tian T, Filiatrault A. Analytical Seismic Fragility Analyses of Fire Sprinkler Piping Systems with Threaded Joints. *Earthquake Spectra* 2015, 31, 1125–1155. DOI: 10.1193/083112EQS277M.
27. Porter, K., R. Kennedy and R. Bachman. Creating Fragility Functions for Performance-Based Earthquake Engineering. *Earthquake Spectra* 2007, 23, 471-489, DOI: 10.1193/1.2720892.
28. Peterman, K.D., Nakata, N., and Schafer, B.W. Hysteretic Characterization of Cold-formed Steel Stud-to-Sheathing Connections. *Journal of Construction Steel Research* 2014. 101, 254–264, DOI: 10.1016/j.jcsr.2014.05.019.
29. Lilliefors, H. On the Kolmogorov-Smirnov test for normality with mean and variance unknown. *Journal of the American Statistical Association* 1967, 62, 399-402, DOI: 10.2307/2283970.
30. Open System for Earthquake Engineering Simulation (OpenSees) website. http://www.opensees.berkeley.edu . PEER, Berkeley, CA, 2015.

Chapter 8

Analytical Model to Capture the In-Plane and Out-of-Plane Seismic Behavior of Nonstructural Partition Walls with Returns

Esmaeel Rahmanishamsi, S.M ASCE[1]; Siavash Soroushian, M. ASCE[2]; Emmanuel "Manos" Maragakis[3]; and Reihaneh Sarraf Shirazi[4]

Please note that this chapter is a self-contained paper submitted to the ASCE Journal of Structural Engineering where the word 'this paper/study' refers to the chapter itself.

Abstract

This paper presents an experimentally verified methodology to analytically model the in-plane and out-of-plane seismic behavior of steel-framed gypsum nonstructural partition walls with returns. In this methodology, the steel-framing members are simulated by nonlinear beam elements. The in-plane and out-of-plane nonlinear behaviors of the connections are represented by nonlinear load-deformation springs, which have been calibrated using the component-level experimental data. The representative models of corner connections are assembled accounting for stud configurations, stud-to-stud and gypsum-to-stud screw attachments, and gypsum-to-gypsum contacts. The gypsum boards are simulated using linear four-node shell elements. The proposed methodology is employed to generate analytical models of three configurations of experiments at the

1 PhD Candidate, Department of Civil and Environmental Engineering, University of Nevada, Reno, NV, 89557-0258, E-mail: erahmanishamsi@unr.edu

2 Structural Analyst, Advanced Technology & Research, Arup, 560 Mission Street, 7th Floor, San Francisco, CA, 94105.

3 Professor, Dean of College of Engineering, University of Nevada, Reno, 1664 N. Virginia Street, Reno, NV, 89557-0258.

4 PhD Candidate, Department of Civil and Environmental Engineering, University of Nevada, Reno, NV, 89557-0258.

University of Buffalo as well as the analytical model of a C-shaped wall system, tested at the University of Nevada, Reno. Comparison of analytical and experimental results shows that the analytical model accurately captures the force-displacement response, the out-of-plane dynamic characteristics, and the out-of-plane responses of nonstructural partition walls. In addition, the model can predict the possible damage mechanisms in partition walls.

Introduction

The structural systems of newly designed buildings commonly survive moderate-to-severe earthquakes with low-to-moderate damage that results in achieving an immediate occupancy performance level for structural systems (Tasligedik et al. 2014). Conversely, the nonstructural systems have repeatedly suffered widespread damage in recent earthquakes, even in low-intensity events (Dhakal 2010; Mizutani 2012; EERI 2012; Miranda et al. 2012; Baird 2014). This damage has led to the complete or partial closure of critical facilities, such as hospitals, the main function of which is to save lives and reduce the impact of disasters (Achour et al. 2011). Moreover, nonstructural systems account for the major portion (48% to 70%) of total initial investment in buildings (Taghavi and Miranda 2003). Consequently, it is not surprising that damage to nonstructural systems accounts for a severe economic burden required to recuperate buildings after an earthquake (Tasligedik et al. 2014).

Cold-formed steel-framed (CFS) gypsum partition walls represent a substantial portion of the nonstructural inventory in building constructions. They define the architectural layout of the building and support its functionality for occupants (Wood and Hutchinson

2014). As observed in past earthquakes, the partition walls are susceptible to various types of damage mechanisms, including bending of studs; failure of gypsum board-to-stud/track connections; cracking of gypsum boards around openings; damage in stud-to-track connections; failure of track-to-concrete connections; crushing of wall corners; failure of brace connections; damage in corner connections; and complete collapse (Dhakal 2010; Mizutani 2012; EERI 2012; Miranda et al. 2012; Baird 2014). The damage was often initiated at shake intensities much lower than those causing structural damage (Wang et al. 2015).

The seismic performance of nonstructural partition walls has been evaluated in previous experimental studies (Lee et al. 2007; Restrepo and Bersofsky 2010; Retamales et al. 2011; Restrepo and Lang 2011; Retamales et al. 2013, Rahmanishamsi et al. 2014; Soroushian et al. 2015a; Wang et al. 2015). The researchers studied the damage mechanisms and hysteresis behaviors of partition walls with different configurations. According to these studies, the majority of the damage mechanisms occurred at the connections between various elements of the partition walls (e.g. gypsum board-to-stud/track and track-to-concrete connections). It was also reported that the force and displacement characteristics and behavior of partition walls (i.e. stiffness, strength, degradation, and pinching) relied on the performance of these connections as well as the out-of-plane properties of return walls (Rahmanishamsi et al. 2015a). Therefore, in order to accurately capture the lateral behavior and damage mechanisms of partition walls through analytical modeling, it is essential to include the behavior of connections and return walls.

A number of studies were conducted on the analytical modeling of structural CFS walls. For example, Fülöp and Dubina (2004); Corte et al. (2006); and Nithyadharan and Kalyanaraman (2013) used experimental data to calibrate a single complex spring to simulate a shear wall. A simplified finite element model was suggested by Martínez-Martínez and Xu (2011) to obtain the global behavior of CFS buildings. Buonopane SG et al. (2015) developed a fastener-based model for CFS shear walls with wood sheathing. In this model, nonlinear springs represented screw fasteners. The remainder of the model employed rigid sheathing panels, elastic beam-column elements for framing, and elastic springs for stud-to-track connections.

Although limited, the analytical modeling of nonstructural CFS gypsum partition walls was also studied. Restrepo and Lang (2011) adopted the data from previous experiments performed by Restrepo and Bersofsky (2010) in addition to data from two new experiments to propose a four-line piecewise backbone response envelop for these walls. Using the experimental data from the NEESR-GC project (NEESR-GC: Simulation of the Seismic Performance of Nonstructural Systems) Davies et al. (2011) and Wood and Hutchinson (2014) calibrated equivalent analytical models (a single complex spring) for the in-plane behavior of CFS partition walls. The equivalent models are valuable for predicting the global behavior of a wall and evaluating its effect on the structural response. However, they only represent the partition walls with details and dimensions for which they were calibrated. Any change in partition dimensions (i.e., length and height) and/or construction details (e.g., stud or connection spacing) means that a new series of full-scale experiments should be performed in order to evaluate the performance and calibrate the equivalent

models. Also, the equivalent models do not provide any information on the local behavior of individual wall components.

Recently, the authors proposed and verified a detailed analytical model of the CFS gypsum partition walls, which included all wall components (Rahmanishamsi et al. 2015a). In this model, the nonlinear behavior of connections was represented by a series of hysteretic load-deformation springs while the framing was modeled using nonlinear beam-column elements. The model can be used to predict force-displacement response and damage mechanisms of partition wall configurations for which experimental results are not available. The model can also help to monitor components' local behaviors and identify the sequence of damage mechanisms in walls. Nonetheless, the model was limited to the in-plane behavior of partition walls. It also did not account for the effect of return walls.

This paper presents the results of an effort at the University of Nevada, Reno (UNR) to develop an analytical model of CFS gypsum partition walls that includes the effect of return walls and can capture the walls' out-of-plane response. The paper begins with a description of typical partition walls and a summary of an existing modeling technique. Afterwards, the effort to enhance the existing analytical model and include the out-of-plane behavior of partition walls is presented. The enhanced modeling methodology is then adopted to generate the analytical model of three configurations of full-scale partition wall assemblies that were tested at the University of Buffalo (UB). The analytical and experimental hysteresis force-displacement responses, dissipated energy, and damage mechanisms are compared. Finally, the modeling methodology is used to develop the analytical model of a C-shaped partition wall system, tested as part of a series of full-scale system-level

experiments at UNR. The analytical dynamic characteristics and partition acceleration responses in the out-of-plane direction are compared to experimental results.

The Proposed Modelling Methodology

The construction of CFS partition walls consists of steel studs and tracks, sheathed with gypsum boards. Tracks are usually attached to structural slabs with power-actuated fasteners (PAFs) (Fig. 1). The goal of the current study is to propose and validate an analytical model for the in-plane and out-of-plane behaviors of CFS partition walls that includes the effect of return walls. For this purpose, an existing technique for analytical modelling of the in-plane behavior of single partition walls is briefly described. The modeling methodology will then be expanded to include the effect of return walls and also capture the out-of-plane response of walls.

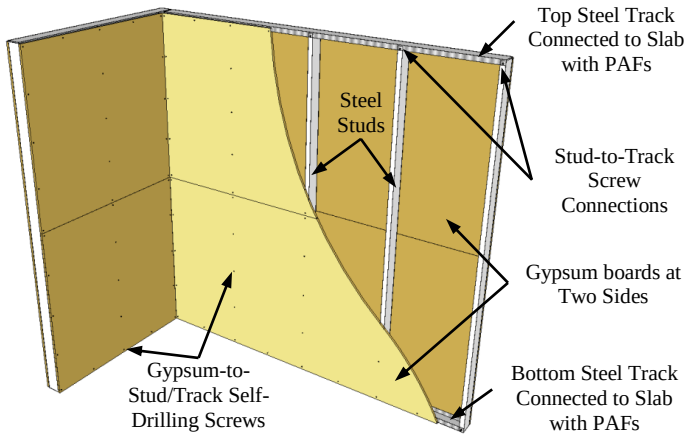

Fig. 1. Typical Steel-Framed Gypsum Partition Wall

Existing Modeling Technique

In a recent work by the authors, an elaborated technique was developed to analytically capture the in-plane behavior of a single CFS gypsum partition wall with no return

(Rahmanishamsi et al. 2015a). In this modeling technique, the studs and tracks were simulated using nonlinear "Force-Based Beam-Column" elements with a fiber-section (OpenSees 2015). The gypsum boards were modeled employing "ShellMITC4" four-node elements with the "ElasticMembranePlate-Section." The nonlinear in-plane behaviors of connections – namely the gypsum board-to-stud/track, stud-to-track, and track-to-concrete connections – were represented employing the "Pinching4" material along with "twoNodeLink" elements (OpenSees 2015).

The "Pinching4" material requires the definition of 39 parameters as presented in Fig. 2(a). Sixteen parameters describe the backbone curve in positive (*ePdi* and *ePfi*) and negative directions (*eNdi* and *eNfi*). An additional eight parameters characterizes the "pinched" (*rDispP*, *rForceP*, *uForceN*, etc.) and unloading/reloading (*gKi*, *gDi* , and *gFi*) behavior of the model. These parameters were calibrated using the component-level experimental data, conducted as a part of the current project. Tables 1 and 2 provide sample material parameters for the connections. More information on component-level experiments and calibrated materials can be found in Rahmanishamsi et al. (2015b-d).

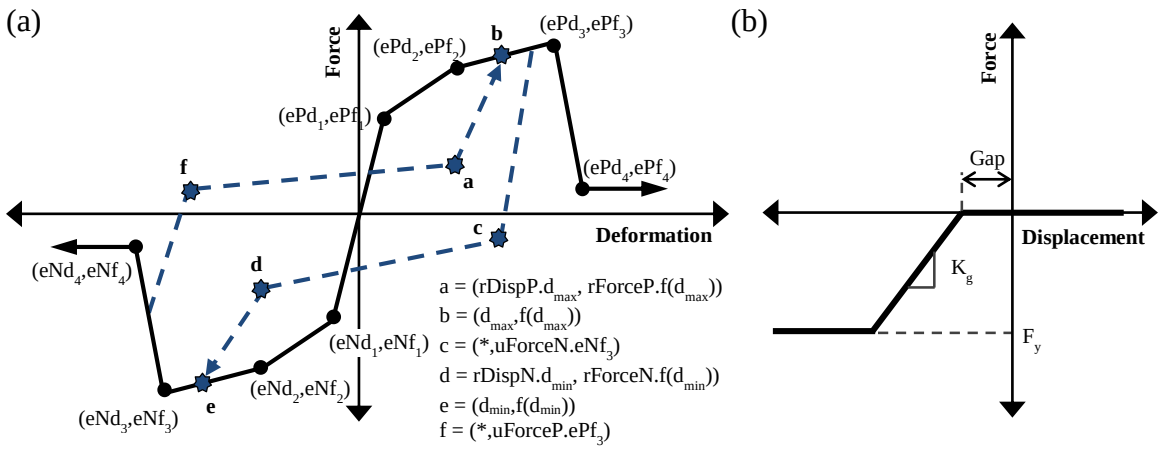

Fig. 2. (a) Pinching 4 Material Properties, (b) EPPG Material Properties (OpenSees 2015)

For all connections, the "Pinching4" material (Tables 1-2) was assigned to "twoNodeLink" elements in two perpendicular, in-plane directions (X and Y directions in Fig. 3). For stud-to-track connections, when the screw was not provided between studs and tracks, an "Elastic" material with minimal stiffness was used in lieu of the "Pinching4" material. Moreover, in the vertical direction (Y direction), an additional compression only "Elastic-Perfectly Plastic Gap" (EPPG) material was located in parallel with the primary material ("Pinching4" or "Elastic" material) to simulate the stud-track interactions (OpenSees 2015). The parameters of EPPG material include: 1) initial stiffness, k_g; 2) yield force, F_y; 3) initial gap, *gap*; 4) post-yield stiffness ratio, $b=k_h/k_g$; and 5) damage type (Fig. 2(b) and Table 3). To represent the compressive behavior of the concrete underneath the tracks, an "Elastic-No Tension (ENT)" material was added to track-to-concrete "twoNodeLink" elements in the vertical direction (OpenSees 2015). The initial stiffness of the ENT material was 16,000 kN/mm. All "twoNodeLink" elements were assumed to be rigid in the out-of-plane direction.

The contacts between the gypsum boards and the top and bottom concrete slabs were simulated using a combination of "zeroLengthContact3D" elements and "twoNodeLink" element with EPPG material while the contacts between the adjacent gypsum boards were represented by a single "zeroLengthContact3D" element (OpenSees 2015). The parameters of the contact element include: 1) penalty in the normal direction, *Kn*; 2) penalty in the tangential direction, *Kt*; 3) friction coefficient, μ; and 4) cohesion, *c*. The elements were always oriented perpendicular to the gypsum board edges. The contact elements captured the friction between two surfaces when the nodes move towards each other. The EPPG material accounted for the cumulative damage (crushing) in gypsum boards due to

interaction with concrete. The properties of contact elements and EPPG material are provide in Table 4. The initial gap of EPPG material should be determined based on the available gap in the construction.

Table 1. Sample Force and Displacement Values for Backbone Points in Various Connections

Description	*ePfi* and *eNfi* (N) and *ePdi* and *eNdi* (mm)							
	ePf1 *ePd1*	*ePf2* *ePd2*	*ePf3* *ePd3*	*ePf4* *ePd4*	*eNf1* *eNd1*	*eNf2* *eNd2*	*eNf3* *eNd3*	*eNf4* *eNd4*
Gypsum-to-Stud Connection, In-Plane Direction								
THK=0.48/0.76 mm, e1 ≥ 38 mm	376	565	310	0.01	-376	-565	-310	-0.01
	1.0	8.9	17.8	39.4	-1.0	-8.9	-17.8	-39.4
THK=0.48/0.76 mm, e1 ≥ 13 mm	245	289	23	0.01	-308	-374	-174	-0.01
	0.8	1.8	6.6	9.4	-0.9	-3.3	-7.4	-31.8
Stud-to-Track Connections, In-Plane Direction								
THK=0.48 mm, e2 < 13 mm	254	1909	1867	0.01	-200	-1554	-1517	-623
	0.1	2.5	5.1	10.2	-0.1	-2.0	-6.4	-8.4
THK=0.76 mm, e2 can vary	289	1802	1831	20	-334	-1728	-1672	-111
	0.1	1.5	4.6	10.0	-0.1	-1.5	-6.2	-10.2
Track-to-Concrete Connections Subjected to Tension Force								
THK=0.48 mm	47	356	2284	0.01	-200	-356	-2284	-0.01
	0.1	2.5	9.5	11.7	-0.1	-2.5	-9.5	-11.7
THK=0.76 mm	102	979	3506	0.01	-756	-979	-3506	-0.01
	0.1	2.5	12.4	13.3	-0.1	-2.5	-12.4	-13.3
Track-to-Concrete Connections Subjected to Shear Force								
THK=0.48 mm	2577	2111	1816	1151	-2577	-2111	-1816	-1151
	0.8	2.8	22.9	30.5	-0.8	-2.8	-22.9	-30.5
THK=0.76 mm	4115	3180	3051	204	-4115	-3180	-3051	-204
	0.8	2.8	19.7	30.1	-0.8	-2.8	-19.7	-30.1

THK: stud/track thickness
e1: edge distance, here the distance from the center of the screws to the edge of the gypsum board
e2: edge distance, here the distance from the center of the screws to the edge of the stud/track flanges

Table 2. Pinching Parameters in Various Connections

Description	*rForceP* *rForceN*	*rDispP* *rDispN*	*uForceP* *uForceN*	*gK1* *gK2*	*gK3* *gK4*	*gD1* *gD2*	*gD3* *gD4*	*gKLimit* *gDLimit*	*gF* *gE*	*dam*
Gypsum-to-Stud Connection, In-Plane Direction										
THK=0.48/0.76 mm, e1	0.12	0.77	-0.01	0	0	0	0	0	0	cycle
can vary	0.12	0.77	-0.01	0	0	0	0	0	1	
Stud-to-Track Connections, In-Plane Direction										
THK=0.48/0.76 mm, e2	0.10	0.50	-0.01	0	0.2	0	0	0.4	0	cycle
can vary	0.10	0.50	-0.01	0	0.2	0	0	0	1	
Track-to-Concrete Connections Subjected to Tension Force										
THK=0.48 mm	0.33	0.65	0.01	0	0	0	0	0	0	cycle
	0.33	0.65	-0.18	0	0	0	0	0	1	
THK=0.76 mm	0. 20	0.60	-0.05	0	0	0	0	0	0	cycle
	0.50	0.60	-0.07	0	0	0	0	0	1	
Track-to-Concrete Connections Subjected to Shear Force										
THK=0.48 mm	0.12	0.75	0.01	0	0	0	0	0	0	cycle
	0.12	0.75	0.01	0	0	0	0	0	1	
THK=0.76 mm	0.17	0.75	0.01	0	0	0	0	0	0	cycle
	0.17	0.75	0.01	0	0	0	0	0	1	

Table 3. EPPG Material Parameters*

Location	Stud/Track THK (mm)	k_g (N/mm)	F_y (N)	b	Gap	damage
Stud-to-Track Connection	0.48	650-1450	6000-9000	0.0	Can vary	"noDamage"
	0.76	1950-2500	6000-9000	0.0	Can vary	"noDamage"
Gypsum-to-Concrete Contact	n/a	3.0e3-3.0e4	900-1400	0.0	Can vary	"Damage"

* Please see Rahmanishamsi et al. (2015a) for more information.

Table 4. "ZeroLengthContact3D" Element Parameters*

Location	*Kn* (N/mm)	*Kt* (N/mm)	μ	c
Gypsum-to-Concrete Contact	3.0e3-3.0e4	3.0e2-3.0e3	0.5-0.8	0.0
Gypsum-to- Gypsum Contact	3.0e3-3.0e4	3.0e3-3.0e4	0.5-0.8	0.0

* Please see Rahmanishamsi et al. (2015a) for more information.

The Effort to Enhance the Existing Modeling Technique

The existing modeling technique (introduced in the previous section) is enhanced in the current study as described in the following subsections.

Stud Flexural Hysteretic Response

During past experimental studies on CFS partition walls, when studs were screwed to the top tracks, local buckling of the studs has been widely reported. The buckled region formed a plastic hinge commonly at the top horizontal line of gypsum-to-stud screws, approximately 300-mm below the top track (Retamales et al. 2013; Rahmanishamsi et al. 2014). In the existing modeling technique, the nonlinear behaviors of studs were factored in by assigning nonlinear Giuffre-Menegotto-Pinto steel material (CEB 1996) to "Force-Based Beam-Column" elements. This method accounts for the material nonlinearity; however, it does not include the nonlinearity due to the local deformation of stud-web/flange (geometric nonlinearity). The geometric nonlinearity results in a pinched hysteretic response, which cannot be captured by "Force-Based Beam-Column" elements [Fig. 4(a)].

To evaluate the flexural hysteretic responses of steel studs, including the effect of geometric nonlinearity, a new series of component-level experiments (12 experiments in

total) was performed at UNR. The experimental data was adopted to calibrate a "Pinching4" material along with a rotational "twoNodeLink" element [Fig. 4(a)]. In the partition model (Fig. 3), the "twoNodeLink" element will be located between two consecutive stud nodes, approximately 300-mm below the top track. Table 5 and Table 6 present the parameters of the calibrated "Pinching4" material for 0.48-mm- and 0.76-mm-thick studs. For 0.48-mm-thick studs, two subgroups were defined that mainly differ in the last backbone points (*eP/Nd4* and *eP/Nf4*).

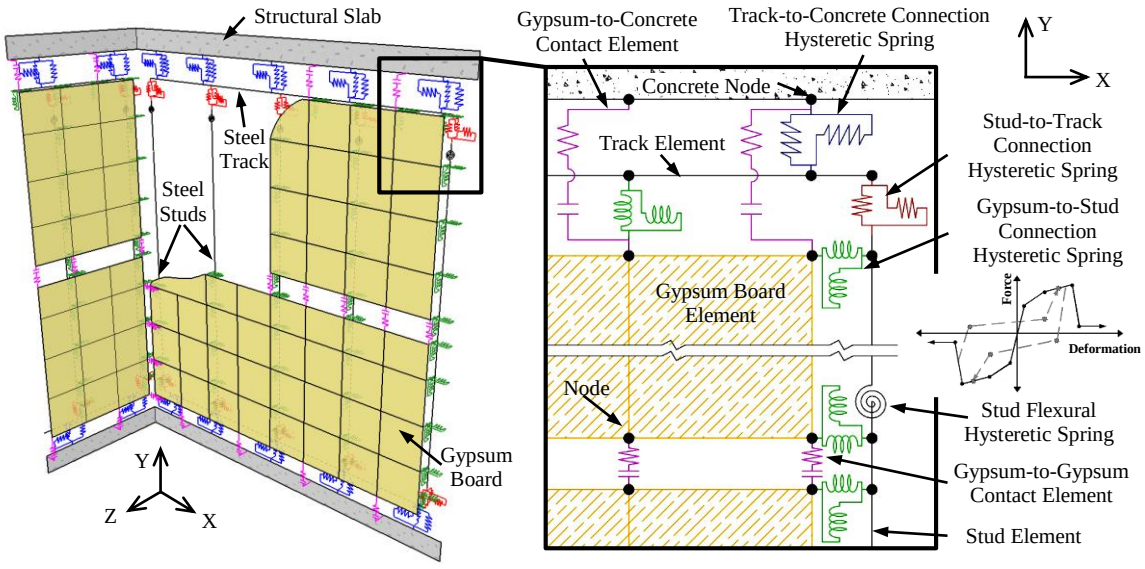

Fig. 3. Schematic Diagram of the Analytical Model of a CFS Gypsum Partition Wall with

Out-of-Plane Behavior of Connections

In the existing modeling technique, all "twoNodeLink" elements were assumed to be rigid in the out-of-plane direction. However, the out-of-plane behavior of connections needs be included in the model in order to capture the out-of-plane behavior of walls. For track-to-concrete connections, the material model used for the in-plane direction is employed in the out-of-plane direction as well. The out-of-plane behavior of stud-to-track

connections is represented by a “Pinching4” material (Table 5 and Table 6) that was calibrated based on the results of a new series of component-level experiments conducted at UNR [Fig. 4(b)] (Rahmanishamsi et al. 2015e). Note that all connections were represented by three independent perpendicular uniaxial material models, oriented towards the global X, Y, and Z axes. The hysteresis behaviors of these three materials were not coupled.

The out-of-plane behavior of gypsum-to-stud connections in tension (when the gypsum moves away from the stud) and compression (when the gypsum moves towards the stud) are characterized differently. The tensile properties are determined according to studies by Schafer et al. (2007) and Guan and Schafer (2008). These researchers evaluated the tensile stiffness and capacity of connections with 13-mm-thick gypsum boards; #6 screws; and 0.83-mm, 1.37-mm, or 1.73-mm-thick studs. It was indicated that the connection response was mainly affected by gypsum board and screw properties rather than stud properties. The tensile capacity varied from 155 N to 620 N, while the stiffness changed from 195 N/mm to 395 N/mm. Moreover, reaching the maximum capacity usually resulted in a brittle failure at the fastener location.

In the current study, the tensile behavior of gypsum-to-stud connections is captured by an EPPG material with a zero initial gap along with “twoNodeLink” elements. An initial stiffness of 288 N/mm and a yield force of 560 N are assigned to this material. These values are borrowed from one of the specimens (ID: 8-GYP-12-6-12-01) tested by Schafer et al. (2007), in which the stud thickness was the most similar to the typical gypsum-to-stud connections in nonstructural walls. In addition, the reported stiffness and capacity of this

specimen approximately represented the average of all experimental results. A post-yield stiffness ratio of -0.5 was used for the EPPG material to simulate the brittle failure of connections. An additional ENT material with a very large initial stiffness is paralleled with the EPPG material to simulate a rigid compressive behavior for gypsum-to-stud connections. Note that this is an approximate method to model gypsum-to-stud connections. Supplemental experimental studies are essential to determine the accurate response of these connections and improve their modeling in the out-of-plane direction.

Table 5. New Calibrated Backbone Curve Parameters for "Pinching4" Materials

Description	*ePfi* and *eNfi* (N) and *ePdi* and *eNdi* (mm)							
	ePf1 *ePd1*	*ePf2* *ePd2*	*ePf3* *ePd3*	*ePf4* *ePd4*	*eNf1* *eNd1*	*eNf2* *eNd2*	*eNf3* *eNd3*	*eNf4* *eNd4*
Stud Flexural Capacity								
THK=0.48 mm, Subgroup #1	2224	7830	2739	1223	-2224	-10438	-4340	-2535
	0.08	0.46	1.32	3.81	-0.08	-0.64	-1.70	-3.81
THK=0.48 mm, Subgroup #2	2146	8229	2002	890	-2094	-11334	-2882	-756
	0.08	0.43	1.27	2.54	-0.08	-0.69	-1.37	-2.03
THK=0.76 mm	2891	11121	4092	1581	-2891	-12455	-8980	-1677
	0.05	0.38	1.21	3.94	-0.05	-0.46	-2.44	-4.38
Stud-to-Track Connections, Out-of-Plane Direction								
THK=0.48 mm, $g \leq 3$ mm, W/O Screw Attachment	40	525	845	513	-40	-525	-845	-513
	0.2	3.0	10.2	27.9	-0.2	-3.0	-10.2	-27.9
THK=0.48 mm, 3 mm $< g \leq$ 13 mm, W/O Screw Attachment	49	498	682	462	-49	-498	-682	-462
	0.2	8.9	21.1	29.2	-0.2	-8.9	-21.1	-29.2
THK=0.48 mm, $g >$ 13 mm, W/O Screw Attachment	18	227	274	178	-18	-227	-274	-178
	0.2	11.9	17.0	18.3	-0.2	-11.9	-17.0	-18.3
THK=0.48 mm, 3 mm $< g \leq$ 13 mm, W/ Screw Attachment	40	943	1496	489	-40	-943	-1496	-489
	0.2	8.1	25.4	35.6	-0.2	-8.1	-25.4	-35.6
THK=0.76 mm, 3 mm $< g \leq$ 13 mm, W/O Screw Attachment	80	956	1112	801	-80	-956	-1112	-801
	0.2	8.9	19.1	24.6	-0.2	-8.9	-19.1	-24.6
THK=0.76 mm, 3 mm $< g \leq$ 13 mm, W/ Screw Attachment	111	1157	1715	1157	-111	-1157	-1715	-1157
	0.2	4.1	14.7	23.4	-0.2	-4.1	-14.7	-23.4

THK: stud/track thickness
g: gap, here the gap between the end of the stud and the track web
Screw Attachment: whether or not the studs were screwed to the tracks.

Table 6. Pinching Parameters for New Calibrated "Pinching4" Materials

Description	*rForceP* *rForceN*	*rDispP* *rDispN*	*uForceP* *uForceN*	*gK1* *gK2*	*gK3* *gK4*	*gD1* *gD2*	*gD3* *gD4*	*gKLimit* *gDLimit*	*gF* *gE*	*dam*
Stud Flexural Capacity										
THK=0.48/0.76 mm	0.70 0.30	0.60 0.25	0.10 -0.40	0 0	0 0.2	0 0	0 0	0.2 0	0 1	cycle
Stud-to-Track Connections, Out-of-Plane Direction										
THK=0.48/0.76 mm, g can vary, W/ or W/O Screw	0.10 0.10	0.60 0.60	-0.10 -0.10	0 0	0 0	0 0	0 0	0 0	0 1	cycle

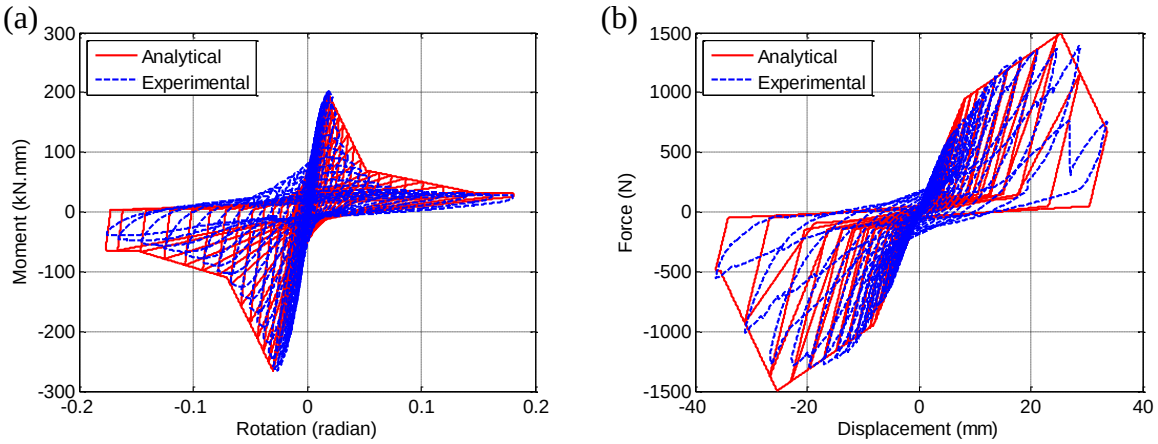

Fig. 4. Sample Calibrated "Pinching4" Material for (a) the Flexural Behavior of Studs and (b) the Out-of-Plane Behavior of Stud-to-Track Connections

Modeling the Corner Connections

Different details might be used to connect two perpendicular walls at corners such as commercial and institutional corner details, as defined by Retamales et al. (2013) and Rahmanishamsi et al. (2014) (Fig. 5). In the analytical simulation, the corner connection models need to be assembled so that they account for all the details, including the configuration of studs, the screw connections of gypsum boards to return-wall studs, the screw connections of two studs to each other, and the contact between two gypsum boards at the corner. One may use the "Pinching4" material calibrated for stud-to-track connections to represent the stud-to-stud connections. As an illustration, Fig. 5 depicts the

schematic diagram of the analytical modeling of commercial and institutional corner details.

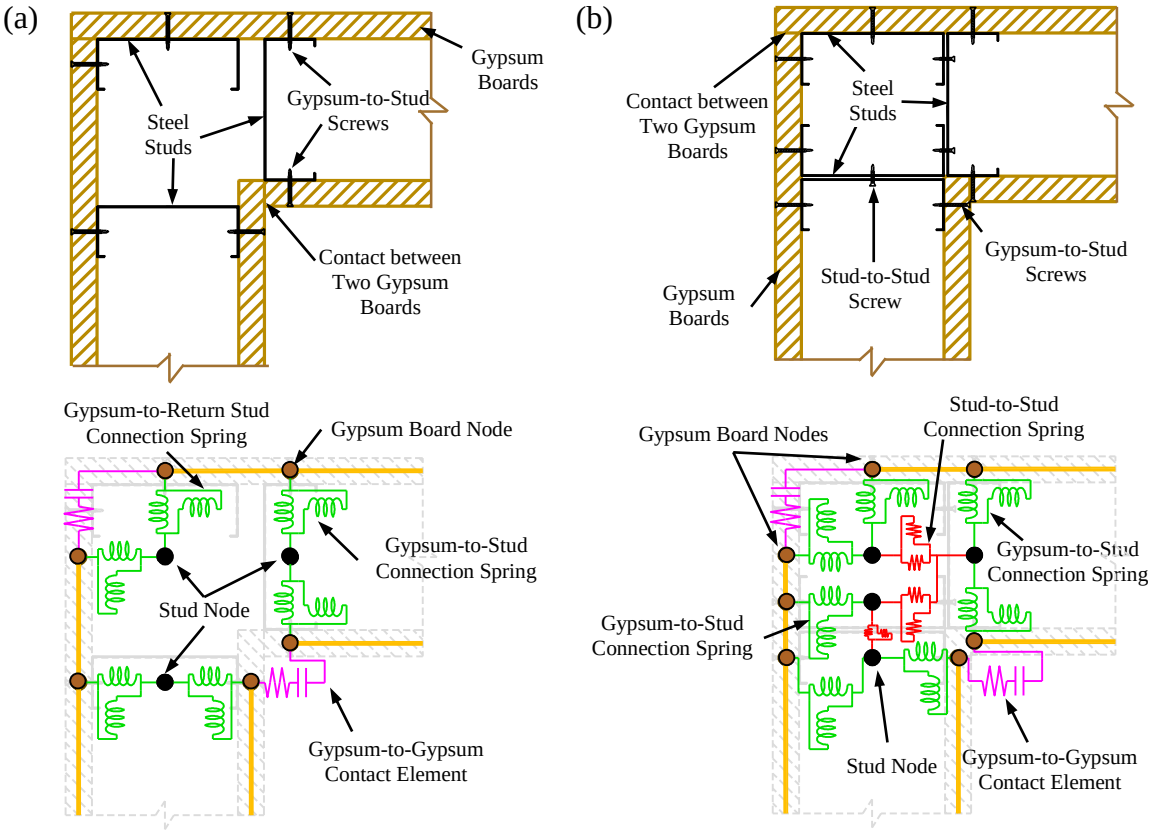

Fig. 5. Construction Details (top) and Schematic Diagram of the Analytical Model (bottom) of a (a) Commercial and (b) Institutional Corner Detail

Validation of the Proposed Modelling Methodology

Two different sets of experimental data were used in the validation process of the proposed modelling methodology. The data from the University of Buffalo (UB) experiments was utilized to mainly verify that the model is capable of predicating the force-displacement response and damage mechanisms of partition walls with returns. In addition, the data from the University of Nevada, Reno (UNR) experiments was employed to assess the proficiency of the model in estimating the out-of-plane response of partition walls.

Available Data from Full-scale Experiments at UB

As a part of the "NEESR-GC" project, 50 partition wall specimens corresponding to 22 different configurations of CFS gypsum partition walls were tested at the University of Buffalo (UB). The configurations varied in terms of 1) connectivity of the sheathing and studs to the top and bottom tracks, 2) spacing of the track-to-concrete fasteners, 3) wall intersection detailing, 4) stud/track thicknesses, and 5) spacing of the steel studs (Retamales et al. 2013). To validate the proposed analytical model, the configurations 1, 2, and 4 of the UB experiments were used in this study. Configurations 1 and 4 included three nominally identical specimens while configuration 2 only consisted of one specimen. All specimens were approximately 3500 mm tall and 3710 mm long with return walls (perpendicular to the loading direction) of 610 mm (Fig. 7). The specimens were constructed using 15.9-mm-thick gypsum boards attached to studs and bottom tracks by standard #6 Phillips self-drilling screws. The screws were spaced 305 mm on center at both the perimeter and field. The studs were 0.48 mm thick (350S125-18), located typically 610 mm apart, and nested into 0.48-mm-thick tracks (350T125-18). For corners, the commercial detailing was utilized (Fig. 7). The main difference between the three configurations (1, 2, and 4) was the construction detail employed for top and bottom connections. In configuration 4, all studs were screwed to top and bottom tracks; however, no screw connection was provided between field-studs and tracks in the other configurations. Moreover, the gypsum boards were connected to top tracks in configuration 2 and 4 while they were not in configuration 1. All specimens were subjected to a quasi-static loading protocol developed by Retamales et al. (2011).

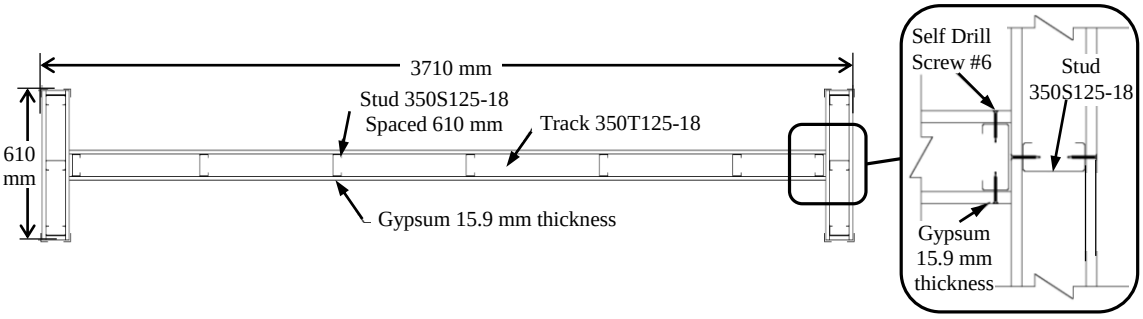

Fig. 6. Plane View and Corner Details of Configurations 1, 2, and 4, after Retamales et al. (2013)

The methodology described in the previous section was followed to generate the analytical models of the UB specimens. The material properties of studs and tracks (Table 7) were determined based on the coupon test results (Davies et al. 2011). The weight of the stud and track elements were assumed to be 5.7 N/m and 5.6 N/m, respectively (SSMA, 2011). A modulus of elasticity of 993 MPa, Poisson ratio of 0.3, and a weight density of 6931 N/m^3 were assigned to the gypsum board elements (GA-235-10). The wall connections were represented using the calibrated "Pinching4" materials (Tables 1-3 and 5-6). The edge distance for the perimeter gypsum-to-stud/track connections was considered to be 13 mm. For field connections, the material model with an edge distance larger than 38 mm was adopted. An initial gap of 6 mm and screw-to-stud/track edge distance of 13 mm were used for stud-to-track connections. The initial stiffness and yield force of the EPPG material was assumed to be 1000 N/mm and 7000 N, respectively. For specimens in which the screw connections were not provided between studs and tracks or between gypsum boards and tracks, an "Elastic" material with minimal stiffness was utilized in lieu of the "Pinching4" material. Representative contact elements were also included in the model with properties provided in Table 8. Note that these values were selected from common construction details since the actual values were not reported in the experiment.

Table 7. Steel Material Properties

Element	Modulus of Elasticity (GPa)	Yield Strength (MPa)	Hardening Slope Ratio (%)
UB Specimens			
Stud	219	330	0.1
Track	153	359	2.0
UNR Specimen			
Stud & Track	200	227	0.1

Table 8. Representative Contact Element Parameters

Location	*Kn* (N/mm)	*Kt* (N/mm)	*μ*	*c*	F_y (N)	*Gap (mm)*
Gypsum-to-Concrete Contact	7.0e3	3.5e2	0.6	0.0	1100	0-13
Gypsum-to- Gypsum Contact	3.0e4	3.0e4	0.6	0.0	-	0.0

Force-Displacement Response

Three analytical models were generated representing configurations 1, 2, and 4 from the UB experiments. The analytical models were subjected to the displacement histories recorded during the tests. Fig. 8 compares the analytical and experimental force-displacement hysteresis response and cumulative hysteresis energies for configuration 2. The experimental response has been accurately captured by the model. The comparison of the analytical and experimental force-displacement backbone curves and cumulative hysteresis energies for configurations 1 and 4 are presented in Fig. 9 and Fig. 10. The three specimens within each configuration were intended to be designed and constructed identically; however, their experimental responses were different in terms of maximum force, hysteresis energies, and observed damage mechanisms. Despite these discrepancies, the analytical model has successfully estimated the average experimental force-displacement response and cumulative hysteresis energies (Fig. 9 and Fig. 10).

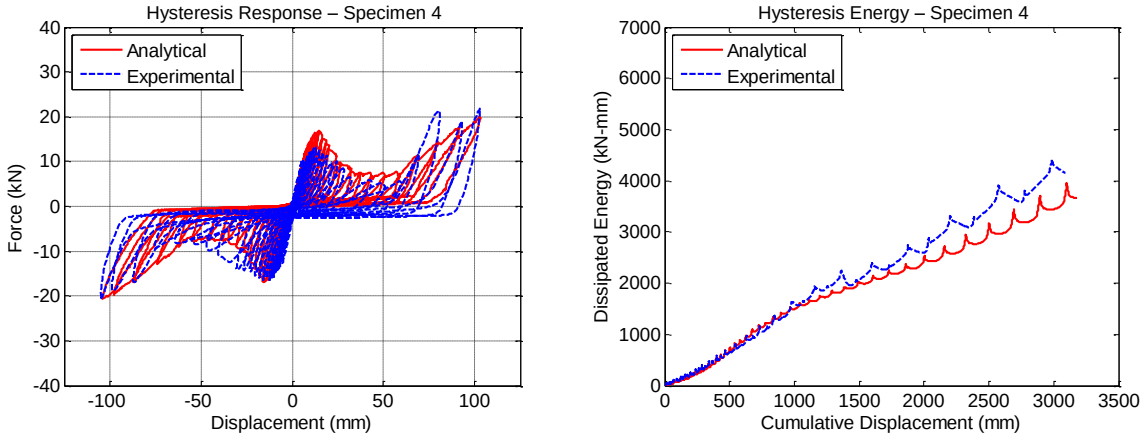

Fig. 7. Comparison of the Analytical Model and Experimental Results for Configuration 2

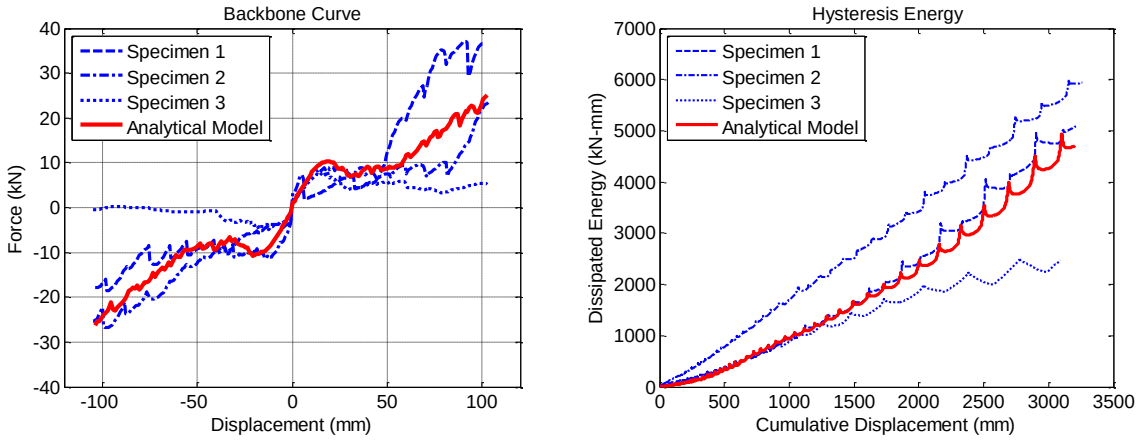

Fig. 8. Comparison of the Analytical Model and Experimental Results for Configuration 1

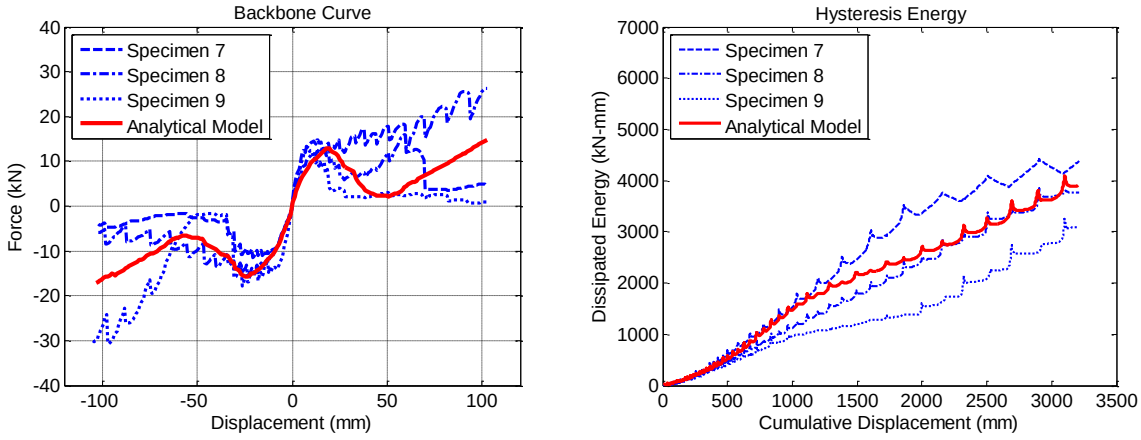

Fig. 9. Comparison of the Analytical Model and Experimental Results for Configuration 4

Damage to the Partition Walls

According to the analytical model, the possible damage mechanisms in configuration 1 include damage to screw connections of gypsum to bottom-track/boundary-studs [Fig. 11(a)], bending of boundary studs, damage to partition corners due to the separation of two perpendicular walls, damage to the top tracks of return walls, crushing of gypsum board corners, and damage to the top tracks-to-concrete connections in return walls. To determine whether a component sustained damage in the analytical model, the force-displacement response of components was monitored (Fig. 11). For configuration 2, the analytical model suggested a widespread failure of gypsum to top-track connections [Fig. 11(b)] in addition to the aforementioned damage mechanisms. Connecting the field studs to top tracks in configuration 4 resulted in damage to gypsum-to-field stud connections and the formation of plastic hinges in field studs [Fig. 11(d)]. It also increased the possibility of failure of PAF connections [Fig. 11(c)]. The predicted damage mechanisms by the analytical model were consistent with the observed damage mechanims in the experiments. Nontheless, the experimnetal observations also included breaking of gypsum boards in return walls, which cannot be captured by the anlytical model. This is due to the fact that the anlytical model assumes a linear behavior for gypsum boards.

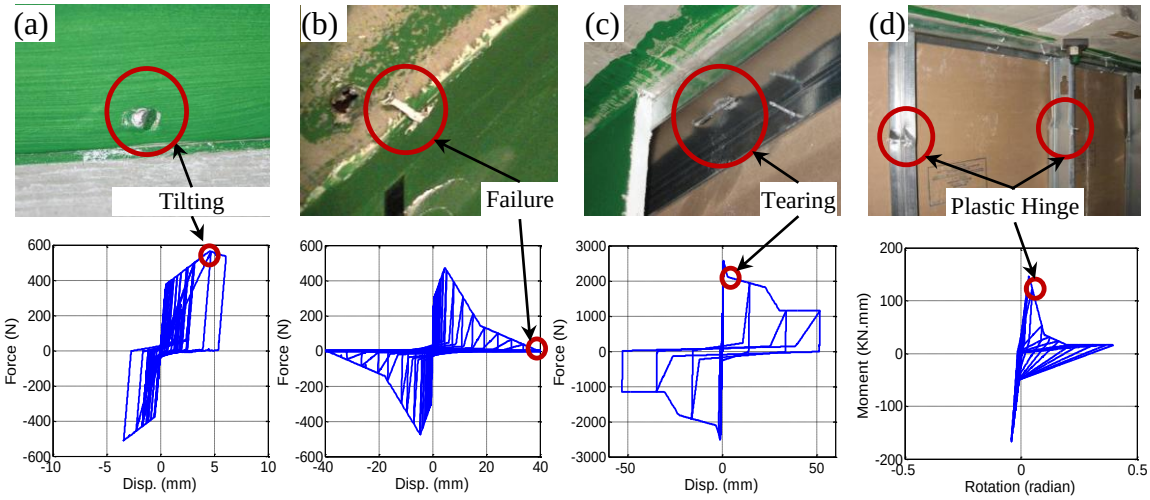

Fig. 10. Examples of Experimental and Analytical Damage Mechanisms: (a) and (b) Tilting and Failure of Screws Connecting Gypsum Boards to Bottom and Top Tracks, (c) Tearing of the Top Track at the PAF location, (d) Plastic Hinges Forming in Studs

Available Data from Full-Scale Experiments at UNR

A series of system-level, full-scale experiments was conducted at the UNR-NEES site. In these experiments, an integrated partition-ceiling-sprinkler piping system was installed on each floor of a two-story, steel-framed building. These experiments attempted to investigate the system-level response of nonstructural systems. The building was approximately 7.5 m tall, 18.3 m long, and 3.5 m wide (2 bays by 1 bay). The experimental program consisted of two phases. In the first phase (five linear tests), the structure remained linearly elastic during all runs in order to achieve high floor acceleration. Yielding braces were implemented in the second phase (three nonlinear tests) to impose large drifts to nonstructural systems. The fundamental period of the structure was 0.23 second and 0.36 second for linear and nonlinear buildings, respectively. A set of ramp-up table motions were artificially generated (using the spectrum-matching procedure) and applied to the building. The targeted acceleration spectra used in this experiment was developed

following the ICC-AC156 (ICC, 2010) parameters. In total, 59 motions were applied during linear and nonlinear test runs (in addition to white noise). The peak horizontal (unidirectional, direction X in Fig. 12) shaking table acceleration varied from 0.12g to 2.00g, which resulted in maximum 1.59g and 2.47g horizontal accelerations on the first and second floors, respectively. Further information about the experimental setup and motions is provided in Soroushian et al. (2015b).

Over 100 light-gauged steel-framed partition walls with various configurations were tested during the UNR study (Jenkins, et al. 2015). The variables in the wall configurations included the following: 1) connectivity of the gypsum boards and studs to the top tracks, 2) presence of return walls, 3) presence of window/door openings, 4) details of wall intersections, 5) height of the partition walls, and 6) stud and track thickness. In the current study, a combination of three walls (namely P3-S, P4-S, and P5-S) that formed a C-shaped wall system was utilized to validate the analytical model in the out-of-plane direction [Fig. 12(a)]. In particular, the experimental results from the first linear and second nonlinear tests (test L1 and test NL2) were used. The aforementioned partition walls were constructed between the first and the second floor of the building using 92-mm (3.5-in.) steel studs/tracks and 16-mm-thick gypsum boards. Studs were located 610 mm apart and screwed to the bottom tracks. The gypsum boards were attached to the studs and bottom tracks by #6 self-drilling screws spaced 305 mm in the field and 203 mm at the boundaries. Tracks were fastened to concrete slabs utilizing PAFs typically spaced 610 mm center-to-center. Fig. 12(b) and Fig. 12(c) show the elevation view of partition walls P3-S and P4-S. The geometry of wall P5-S was similar to the wall P3-S. The partition walls included one window and two door openings. Studs and tracks were 0.48 mm thick in P3-S, and 0.76

mm thick in P4-S and P5-S. Two different details, namely commercial and institutional details (Fig. 5), were employed for corner connections. In test L1, the gypsum boards of P4-S were screwed to the top tracks while in test NL2 they were not. No screw connection was ever provided between gypsum boards and top tracks in other walls. Other details were similar in the two tests. During the experiments, the floor accelerations and displacements were recorded. In addition, an accelerometer was located approximately 914 mm below the second floor to report the out-of-plane acceleration of partition P4-S.

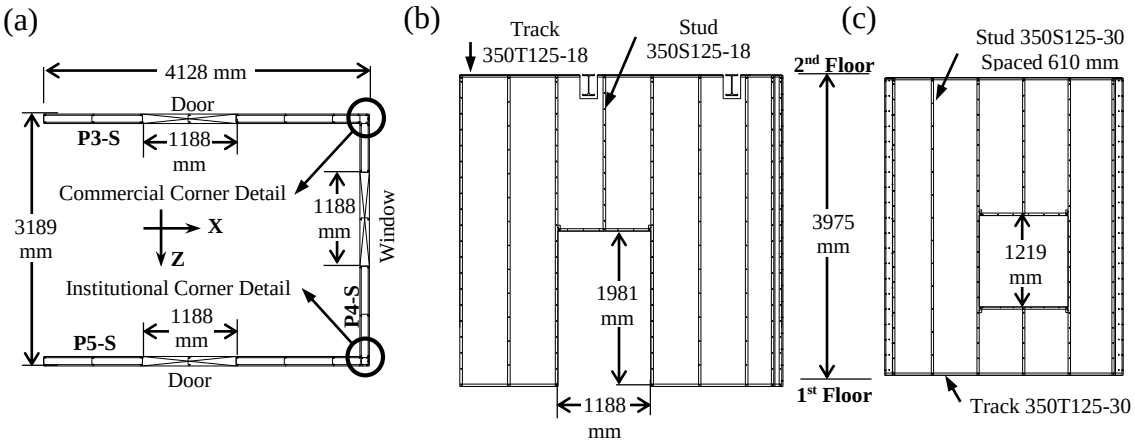

Fig. 11. UNR Partitions (a) Plan, (b) Elevation of Partitions P3-S and (c) P4-S (Rahmanishamsi et al. 2014)

The analytical model of the UNR partition system was generated in OpenSees. The stud/track material properties (Table 7), were selected based on the manufacturer catalog. All other properties, including gypsum properties, element weights, gypsum-to-stud/track edge distances, stud-to-track gap and edge distances, EPPG material properties, and contact element parameters (Table 8) were assumed to be similar to those presented for the UB partition walls. The weight of the 0.76-mm-thick stud and track elements were considered to be 9.6 N/m and 9.3 N/m, respectively (SSMA, 2011). Where the gypsum-to-track

connection was provided, a rigid-behavior was assigned to the out-of-plane rotation (e.g. about Z-axis in Fig. 12a for P4-S) of stud-to-track connections, assuming that the gypsum boards prevented the rotation of studs. Alternatively, the stud was considered to be free to rotate relative to the track in the out-of-plane direction. The corner connections were modeled following the procedure depicted in Fig. 5. The recorded floor displacement histories were applied to the top and bottom concrete nodes of the analytical model using the "Multi-Support Excitation Pattern" command in OpenSees (2015).

Dynamic Characteristics of the Partition Walls in the Out-of-Plane Direction

White noise motions were applied to the building before and after each test run. The normalized frequency responses of the recorded partition accelerations with respect to the floor (the floor that partitions were installed on) accelerations, also known as transfer functions, were generated. The transfer functions were smoothed using a periodic Hamming window with a 50% overlap ratio. The period and damping ratio corresponding to the fundamental mode of the partition in the out-of-plane direction were evaluated by fitting the theoretical transfer functions to the measured transfer functions using least squares analysis (Soroushian et al. 2015b). Fig. 13 presents the measured and fitted transfer functions for the partition wall system in the first white noise (W1) of tests L1 and NL2. The first peak in the transfer functions denotes the fundamental period (T_f) of the partitions in the out-of-plane direction that was calculated as 0.09 sec for tests L1 [Fig. 13(a)] and 0.184 sec for tests NL2 [Fig. 13(b)]. These values were compared to the fundamental periods obtained from the modal analysis of the analytical model. The analytical model predicted a fundamental period of 0.093 sec for tests L1 and 0.181 sec for tests NL2. The comparison of the analytical and experimental values shows that the model precisely

predicted the fundamental period of the partitions in the out-of-plane direction. Note that the partition wall in test L1 was stiffer than the wall in test NL1, due to the connection of the gypsum boards to the top tracks.

To estimate the damping ratio corresponding to the fundamental mode (h_f), the response of the partition wall in the fundamental mode was idealized by a single degree-of-freedom (SDOF) oscillator with a period equal to the period of this mode and damping ratio to be determined. The transfer function of the idealized SDOF system subjected to the floor acceleration was computed iteratively with a search damping ratio increment of 1%. The optimum damping ratio that resulted in the best correlation between the partition fitted transfer function and the idealized SDOF system transfer function was identified by calculating the coefficient of determination (R-square) for each iteration. The optimum damping ratio, that is the damping ratio corresponding to the fundamental mode of the partition wall (h_f), was 5% for tests L1 [Fig. 13(a)] and 16% for tests NL2 [Fig. 13(b)]. These damping ratios were used as the input values in the analytical model to perform response history analyses. In fact, a Rayleigh damping was used in the analytical model, and the damping ratios of the first and third modes of vibration were set to be 5% in test L1 and 16% in test NL2.

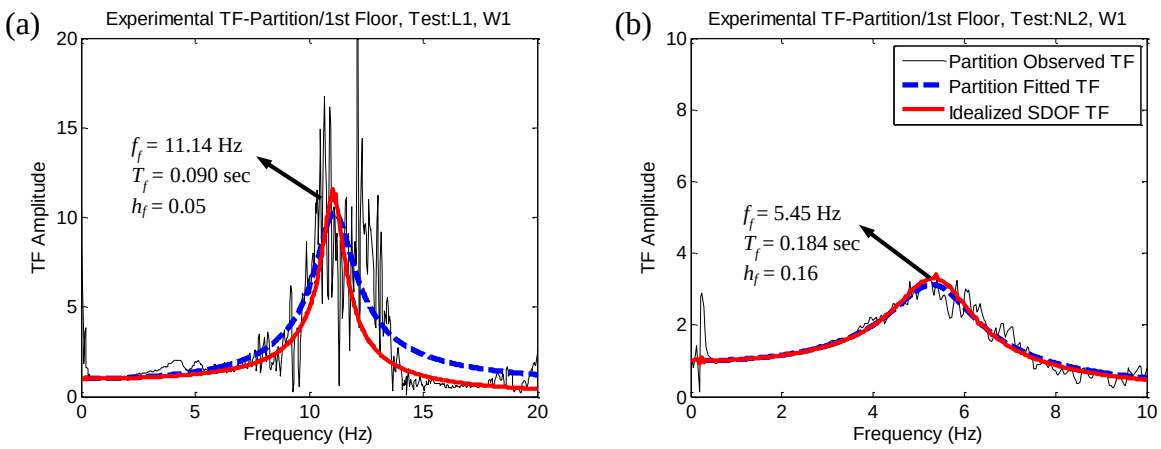

Fig. 12. Experimental Partition/First Floor Transfer Functions in the First White Noise of: (a) Test L1 and (b) Test NL2

The Out-of-Plane Response of the Partition Walls

The 5% damped spectrums of analytical and experimental partition acceleration responses were calculated and compared for several motions. Fig. 14 provides some examples of the spectrums while Fig. 15(a) displays a sample comparison of the analytical and experimental acceleration response histories. In these figures, White Noise-1 and Run-i refer to the first white noise and the i^{th} motion that were applied to the building in each test. The maximum partition acceleration (acceleration at period equal to zero) in the analytical model is comparable to the experimental results. Moreover, even though there are some differences between the analytical and experimental results, the analytical model has successfully estimated the trend of the out-of-plane response of the partition walls. The difference is more highlighted in Run-4 of test L1, which might be due to the interaction of ceiling systems and partition walls. The interaction occurred in motions that imposed high acceleration to the ceiling system (e.g. test L1, Run-4, Fig. 14c). The high acceleration led to damage to the ceiling perimeter and then pounding of the ceiling system on the

partition walls (Soroushian et al. 2015c). The pounding might affect the out-of-plane response of partition walls. Note that the analytical model does not account for the interaction since the ceiling system is not simulated.

To investigate the sensitivity of the responses to the damping ratio, the analyses of the model of the partition wall in test NL2 were repeated assuming a 5% (instead of 16%) damping ratio for the first and third modes. Fig. 15b and Fig. 16 provide the results of these analyses. Assuming a 5% damping ratio led to less correlation between the analytical and experimental results; however, the error in the estimation of partition response remained in an acceptable range. In other words, the model response is not very sensitive to the damping ratio.

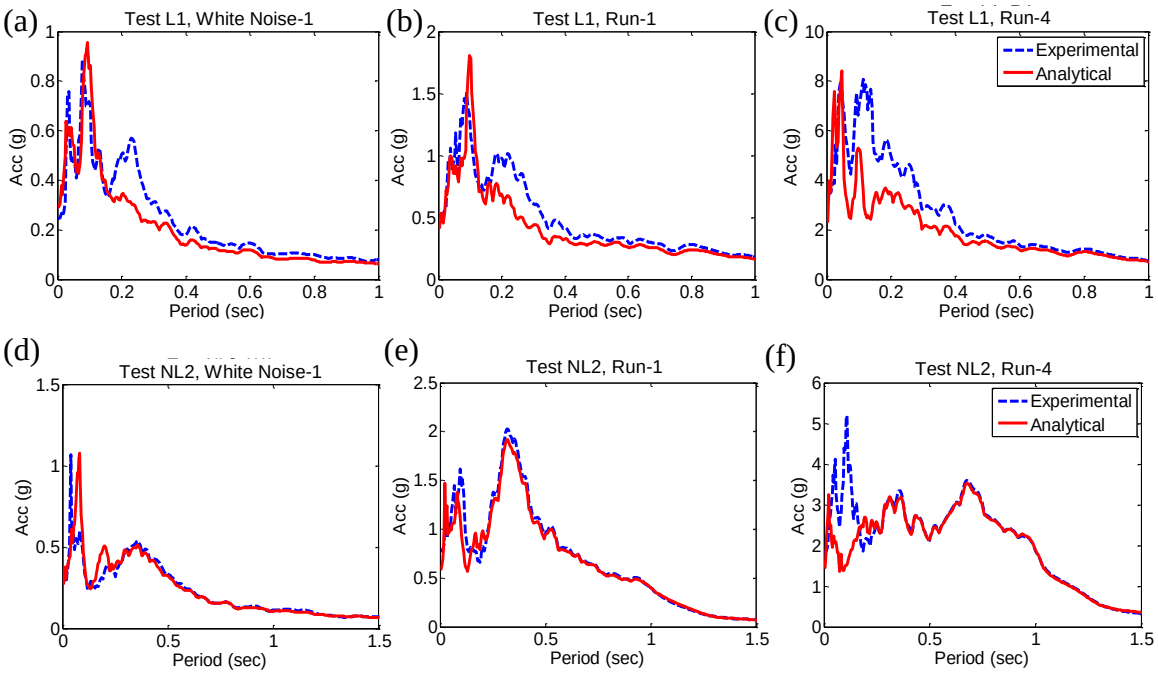

Fig. 13. Experimental and Analytical Partition Acceleration Response Spectrums for Sample Runs of Test L1 [(a), (b), and (c)] and Test NL2 [(d), (e), and (f)]

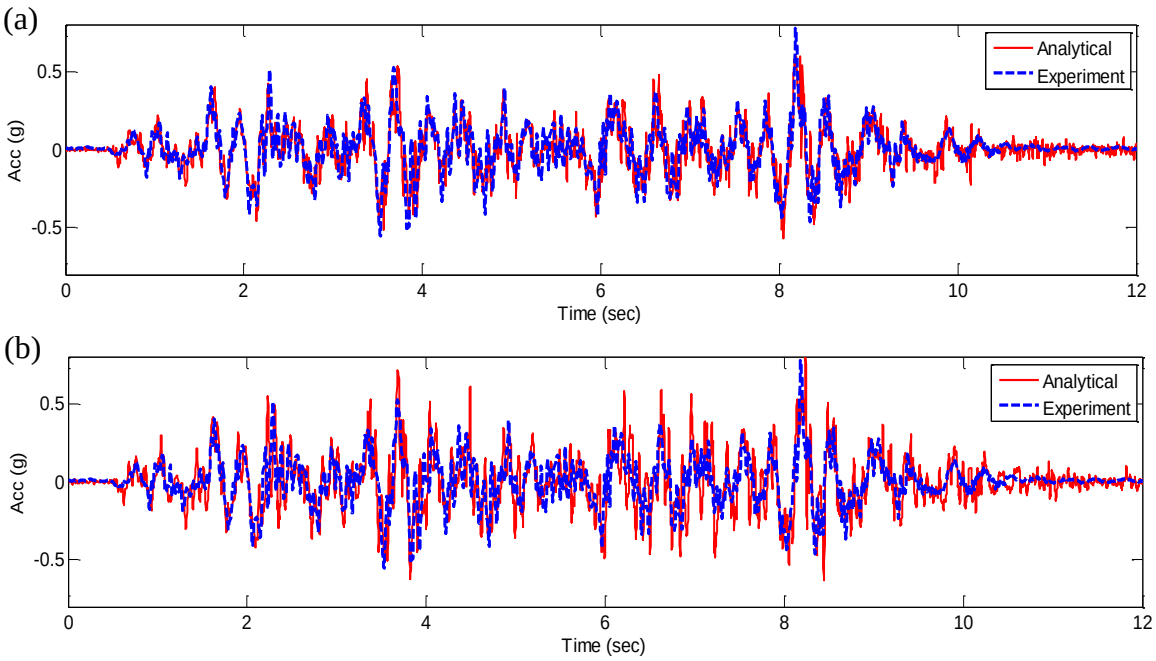

Fig. 14. Experimental and Analytical Partition Acceleration Response History in Test NL2-Run 1 assuming (a) %16 damping ratio or (b) %5 damping ratio in the model

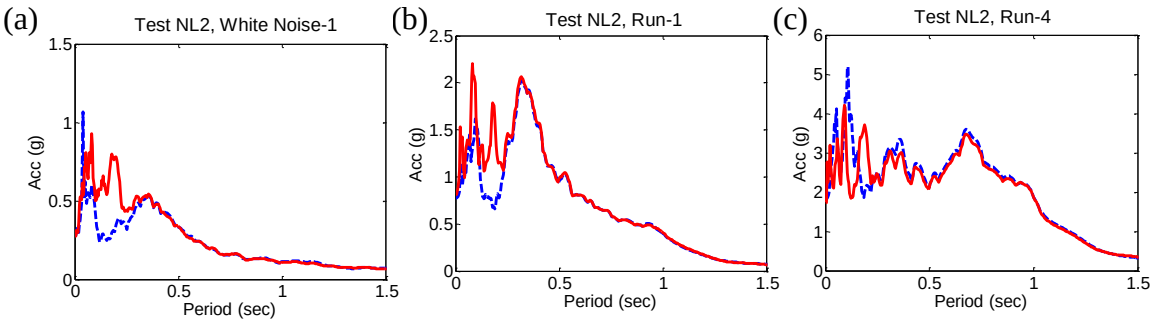

Fig. 15. Experimental and Analytical Partition Acceleration Response Spectrums for Sample Runs of Test L1 assuming %5 damping ratio in the model, (a) First White Noise, (b) Run-1, and (c) Run-4

Damage to the Partition Walls

The predicted damage mechanisms in the analytical model consisted of damage to partition corners due to the separation of two perpendicular walls, damage to the top tracks of return walls, damage to gypsum-to-tracks screw connections, crushing of gypsum

boards, and slight damage to track-to-concrete PAF connections. These damage mechanisms were consistent with the experimental damage mechanisms. However, similar to the UB specimens, breaking of gypsum boards in the out-of-plane direction was observed during the motions with large drift, which could not be captured by the model.

Summary and Conclusions

An elaborated and yet computationally efficient modeling methodology was proposed to capture the in-plane and out-of-plane behavior of cold-formed steel-framed gypsum partition walls accounting for the effect of return walls. In this modeling methodology, the steel framing members were simulated by nonlinear beam elements. Linear four-node shell elements were used to model the gypsum boards. The in-plane and out-of-plane nonlinear behaviors of the stud-to-track and track-to-slab connections, as well as the in-plane nonlinear behaviors of the gypsum-to-stud/track connections, were represented by hysteretic load-deformation springs. To consider the effect of geometric nonlinearity on the flexural response of studs, additional hysteretic springs were assigned to the studs approximately 300 mm below the top track. The behaviors of all springs were calibrated using the results of a series of the component-level experiments performed at the University of Nevada, Reno (UNR). An approximate method was utilized to model the out-of-plane behavior of gypsum-to-stud/track connections. The representative models of corner connections were assembled accounting for all details, including the configuration of studs, the screw connections of gypsum boards to return-wall studs, the screw connections of two studs to each other, and the contact between two gypsum boards at the corner. The model

also included the contacts between gypsum boards and concrete slabs as well as the contacts between the adjacent gypsum boards.

To validate the proposed modeling procedure, two different sets of experimental data were used. Initially, the analytical models of configurations 1, 2, and 4 of the University of Buffalo (UB) experiments were assembled. The analytical force-displacement responses, cumulative dissipated energy, and damage mechanisms were compared to the experimental results. The comparison showed that the analytical model accurately predicted the average response as well as the observed damage mechanisms. Subsequently, the proposed methodology was followed to generate the analytical model of a C-shaped wall system, tested at the University of Nevada, Reno (UNR). The out-of-plane dynamic characteristics, partition acceleration responses, and damage mechanisms from the analytical simulation were compared to the experimental results. Although there were some differences, the analytical model successfully captured the trend of the out-of-plane response of the partition wall and predicted the possible damage mechanisms.

The procedure proposed here can be implemented in future studies to investigate the in-plane and out-of-plane performance of existing partition walls with dimensions (i.e., length and height) and construction details (e.g., stud spacing, screw spacing, and corner detail) for which experimental results are not available. The investigation results may lead to improving/modifying the current design provisions of nonstructural walls. In addition, the proposed model can be utilized as a preliminary tool to examine and compare the performance of various innovative details for partition walls. The model can also estimate the out-of-plane acceleration response of partition walls, which can be used as the

perimeter input motion in the seismic analysis of ceiling systems. Nevertheless, the proposed analytical model does have limitations. For example, the model assumes a linear behavior for gypsum boards; therefore, it cannot capture cracking or breaking of gypsum boards. Moreover, an approximate method is used to model the out-of-plane behavior of gypsum-to-stud connections. Further experimental studies are essential to determine the accurate nonlinear response of gypsum boards and gypsum-to-stud connections in the out-of-plane direction.

Acknowledgments

The current material is based upon work supported by the National Science Foundation under Grant No. 0721399. This Grand Challenge (GC) project to study the seismic response of nonstructural systems is under the direction of M. Maragakis from the University of Nevada, Reno and Co-PIs: T. Hutchinson (UCSD), A. Filiatrault (UB), S. French (G. Tech), and B. Reitherman (CUREE). Any opinions, findings, conclusions, or recommendations expressed in the current document are those of the investigators and do not necessarily reflect the views of the sponsors. The input provided by the Practice Committee of the NEES Nonstructural Project, composed of W. Holmes (Chair), D. Allen, D. Alvarez, and R. Fleming, and by the Advisory Board, composed of R. Bachman (Chair), S. Eder, R. Kirchner, E. Miranda, W. Petak, S. Rose and C. Tokas, has been crucial for the completion of this research.

References

Achour, N., Miyajima, M., Kitaura, M., and Price, A. (2011). “Earthquake induced structural and nonstructural damage in hospitals.” *Earthq. Spectra*, 27(3), 617–634.

Baird A, Tasligedik AS, Palermo S, Pampanin S. (2014). "Seismic performance of vertical non-structural components in the 22nd February 2011 Christchurch earthquake." *Earthq. Spectra*, 30(1), 401–425.

Buonopane, S. G., Tun, T. H., Schafer, B. W. (2015). "Computationally efficient fastener-based models of cold-formed steel shear walls with wood sheathing." *J. of Constr. Steel Res.*, 110:137-148.

Comite Euro-interational du Beton (CEB). (1996). "RC elements under cyclic loading, state of the art report." Thomas Telford Publications, London, England.

Corte, D. G., Fiorino, L., Landolfo, R. (2006). "Seismic behavior of sheathed cold-formed structures: numerical study." *J. Struct. Eng*., 132:558-569.

Davies, D., Retamales, R., Mosqueda, G., Filiatrault, A. (2011) "Experimental Seismic Evaluation, Model Parameterization, and Effects of Cold-Formed Steel-Framed Gypsum Partition Walls on The Seismic Performance of an Essential Facility." *Technical Report MCEER-11-0005*, MCEER, State University of New York at Buffalo, NY.

Dhakal, R. P. (2010). "Damage to non-structural components and contents in 2010 Darfield earthquake." *Bulletin of The New Zealand Society for Earthquake Engineering*, 43, 404-411.

EERI (Earthquake Engineering Research Institute). (2012), "The El Mayor Cucapah, Baja California earthquake April 4, 2010." *An EERI Reconnaissance Rep,* 2010-02, J. Meneses, ed., Oakland, CA.

Fülöp, L. A., and Dubina, D. (2004). "Performance of wall-stud cold-formed shear panels under monotonic and cyclic loading." Part II: Numerical modelling and performance analysis." *Thin Wall. Struct.*, 42:339-349.

GA-235-10. (2010). "Gypsum Board Typical Mechanical and Physical Properties." Gypsum Association: Hyattsville, MD, USA.

Guan, Y., Schafer, B.W. (2008). "Analytical study on rotational restraint of sheathing." *AISI-COFS-RP08-2*, Washington, D.C.

ICC Evaluation Service: AC 156. (2010). "Acceptance criteria for seismic certification by shake table testing of nonstructural components, ICC Evaluation Service.

Jenkins, C., Soroushian, S., Rahmanishamsi, E., and Maragakis, M. (2015). "Experimental Fragility Analysis of Cold-Formed Steel-Framed Partition Wall Systems." *Thin Wall. Struct.*, under review.

Lee, T., Kato, M., Matsumiya, T., Suita, K., Nakashima, M. (2007) "Seismic Performance Evaluation of Non-structural Components: Drywall Partitions." *Earthquake Eng. Struct. D.*, 36, 367–382.

Martínez-Martínez, J., Xu, L. (2011). "Simplified nonlinear finite element analysis of buildings with CFS shear wall panels." J. of Constr. Steel Res., 67:565-575.

Miranda, E., Mosqueda. G., Retamales, R., and Pekcan, G. (2012). "Performance of Nonstructural Components during the February 27, 2010 Chile Earthquake." *Earthq. Spectra*, 28, 453-471.

Mizutani, K., Kim, H., Kikuchihara, M., Nakai, T., Nishino, M., Sunouchi, S. (2012). "The damage of the building equipment under the 2011 Tohoku pacific earthquake." *9th*

International Conference on Urban Earthquake Engineering & 4th Asia Conference on Earthquake Engineering, Tokyo Institute of Technology, Tokyo, Japan.

Nithyadharan, M., Kalyanaraman, V. (2013). "Modelling hysteretic behavior of cold-formed steel wall panels." *Eng. Struct.*, 46: 643–652.

Open System for Earthquake Engineering Simulation (OpenSees) website (2015). http://www.opensees.berkeley.edu . PEER, Berkeley, CA.

Rahmanishamsi, E., Soroushian, S., and Maragakis, M. (2014). "System-Level Experiments on Ceiling/Piping/Partition Systems at UNR-NEES Site." *Proc., Tenth U.S. National Conference on Earthquake Engineering*, Anchorage, AK.

Rahmanishamsi, E., Soroushian, S., and Maragakis, M. (2015a). "Analytical model for the in-plane seismic performance of cold-formed steel-framed gypsum partition walls." *Earthquake Eng. Struct. D.*, in press.

Rahmanishamsi, E., Soroushian, S., and Maragakis, M. (2015b). "Cyclic shear behavior of gypsum board-to-steel stud screw connections in nonstructural walls." *Earthq. Spectra*. , in press.

Rahmanishamsi, E., Soroushian, S., and Maragakis, M. (2015c). "Capacity evaluation of typical stud-track screw connections in nonstructural walls." *Earthq. Eng.*, in press.

Rahmanishamsi, E., Soroushian, S., and Maragakis, M. (2015d) "Capacity evaluation of typical track-to-concrete power-actuated fastener connections in nonstructural Partition Walls." *J. Struct. Eng*., in press.

Rahmanishamsi, E., Soroushian, S., and Maragakis, M. (2015e). "Evaluation of the out-of-plane behavior of stud-to-track connections in nonstructural partition walls." *Thin Wall. Struct.*, under review.

Restrepo, J. I., and Bersofsky, A. (2010). "Performance characteristics of light gage steel stud partition walls." *Thin Wall. Struct.*, 49, 317–324.

Restrepo, J. I., and Lang, A. F. (2011). "Study of loading protocol in light-gauge stud partition wall." *Earthq. Spectra*, 27, 1169–1185.

Retamales, R., Mosqueda, G., Filiatrault, A., and Reinhorn, A.M. (2011). "Testing protocol for experimental seismic qualification of distributed nonstructural systems." *Earthq. Spectra*, 27(3):835-856.

Retamales, R., Davies, R., Mosqueda, and G., Filiatrault, A. (2013). "Experimental Seismic Fragility of Cold-Formed Steel Framed Gypsum Partition Walls." *J. Struct. Eng.*, 139, 1285-1293.

Schafer, B.W., Sangree, R.H., Guan, Y. (2007). "Experiments on rotational restraint of sheathing: final report." *AISI-COFS-RP07-2*, Washington, D.C.

Soroushian, S., Maragakis, E., Ryan, K., Sato, E., Sasaki, T., Okazaki, T., and Mosqueda, G. (2015a). "Seismic Simulation of an Integrated Ceiling-Partition Wall-Piping System at E-Defense. II: Evaluation of Nonstructural Damage and Fragilities." *J. Struct. Eng*, in press.

Soroushian, S., Maragakis, E. M., Zaghi, A. E., Rahmanishamsi, E., Itani, M., and Pekcan, G.

(2015b). “Response of a 2-Story Test-Bed Structure for the Seismic Evaluation of Nonstructural Systems.” *Earthquake Engineering and Engineering Vibration*, in press.

Soroushian, S., Rahmanishamsi, E., Ryu, K. P., Maragakis, E. M., and Reinhorn, A. M. (2015c) Experimental Fragility Analysis of Suspension Ceiling Systems. *Earthq. Spectra*, in press.

Steel Stud Manufacturers Associations (SSMA). (2011). Product Technical Information, S.S.M. Association, Chicago, IL.

Taghavi, S. and Miranda, E. (2003) “Response Assessment of Nonstructural Building Elements.” *PEER Report 2003/05*, Pacific Earthquake Engineering Research Center (PEER), Berkeley, CA.

Tasligedik, A. S., Pampanin, S., Palermo, A. (2014) “Low Damage Non-structural Drywalls: Details and Their Performance.” *Proc. 2014 NZSEE Conference*, Auckland, New Zealand.

Wang, X., Pantoli, E., Hutchinson, T., Restrepo, J., Wood, R., Hoehler, M., Grzesik, P., and Sesma, F. (2015) “Seismic Performance of Cold-Formed Steel Wall Systems in a Full-Scale Building.” *J. Struct. Eng*.

Wood, R. L., Hutchinson, T. C. (2014) “Design-Oriented Model for Capturing the In-Plane Seismic Response of Partition Walls.” *J. Struct. Eng*., 140.

Chapter 9: Summary, Conclusion, and Future Research

9.1. Summary and Conclusions

It is well understood from past earthquakes and experimental studies that non-structural systems suffer more damage and sustain greater losses when compared to structural members. One of important nonstructural systems, regularly employed in construction of buildings around the world, is partition walls. Damage to partition walls can result in partial or complete closure of critical facilities (e.g. hospitals), extensive economic loss, and risk on life; therefore, it is essential to comprehend their seismic behavior. The purpose of this study was to develop a novel experimentally verified generic modelling methodology that can be adopted in future studies and applications by researchers and engineers to assess the seismic performance of partition walls with various geometries, boundary conditions, and construction details.

The initial task in this study was to perform a series of system-level, full-scale experiments at the UNR-NEES site from December 2012 to April 2013, as part of the project titled "NEESR-GC: Simulation of the Seismic Performance of Nonstructural Systems" (Chapter 1). These experiments attempted to investigate the system-level response and damage mechanisms of nonstructural systems, including cold-formed steel-framed (CSF) gypsum partition walls. The results of this study along with the results of previous experimental studies were investigated to identify the critical components that can affect the seismic performance of partition walls. The investigation implied that the connections between various elements of the walls (e.g. gypsum board-to-stud/track

connections and track-to-concrete connections) were the most vulnerable components. The experimental studies also revealed that the force and displacement characteristics and behavior of partition walls (i.e. stiffness, strength, degradation, and pinching) depended on the performance of the wall connections as well as the out-of-plane properties of return walls.

Accordingly, for the first time, a series of component-level experiments (more than 100 experiments) has been designed and conducted to characterize the in-plane cyclic response of partition wall connections, namely gypsum board-to-stud/track, stud-to-track and track-to-concrete connections (Chapters 3-5). The observed damage mechanisms and force-displacement responses of connections with various properties (e.g. stud/track thicknesses) were thoroughly studied and fragility curves were generated in terms of displacements. The main observations and conclusions obtained from the experiments were as follows:

- For all connections, the observed damage mechanisms were reported and the displacement value corresponding to each mechanism was determined.
- The damage states were defend based on the extent of the nonlinearity in connections and observed damage mechanisms.
- The shear capacity of the gypsum board-to-stud/track connections derived primarily from the bearing resistance of gypsum board at the fastener locations.
- The distance of fasteners to the gypsum board edges dramatically affected the behavior of the gypsum board-to-stud/track connections. Using edge distances

smaller than 1.0 in. led to significant drops in strength and displacement capacities.

- Gypsum board-to-stud connections with different stud thicknesses performed consistently in terms of initial stiffness, maximum capacity and failure mechanisms.
- The main portion of the shear capacity of the stud-to-track and track-to-concrete connections was provided by the bearing resistance of stud and track webs/flanges at the fastener locations.
- In specimens constructed from 25 gauge (0.48-mm-thick) studs and tracks, the distance of screws to the stud/track flange edges affected the behavior of stud-to-track connections. However, in 20 gauge (0.76-mm-thick) specimens, the force and displacement capacities of the stud-to-track connections were independent of the edge distance.
- Track-to-concrete connections with thicker tracks showed higher stiffness and larger force capacity in both tension and shear tests. However, using thicker tracks led to different failure mechanisms in shear tests, which resulted in failure of the connection in smaller displacements. The fragility analysis revealed these connections were more vulnerable in terms of achieving the last damage state (complete failure).

Moreover, the component-level experimental data was used to propose and calibrate analytical nonlinear material models for tested connections in OpenSees. Afterwards, for the simplicity of future analytical studies of partition walls, one suite of material parameters was defined as the generic (representative) parameters for connections with similar properties. Furthermore, as the test matrix did not include all the connections that are possible to find in a partition wall, approximate procedures were proposed to enable estimation of the parameters of the generic hysteresis model for the missing connections.

Subsequently, the results of component-level studies were employed to develop an innovative, detailed and yet computationally efficient analytical model for the in-plane behavior of CSF gypsum nonstructural partition walls (Chapter 6). In this model, the studs and tracks were simulated using beam elements with their section properties accounting for nonlinear behavior. The nonlinear behaviors of the connections (including gypsum-to-stud, stud-to-track, and track-to-slab connections) were represented by hysteretic load-deformation springs calibrated during the component-level studies. The gypsum boards were modeled by linear four-node shell elements. The contacts between gypsum boards and concrete slabs as well as the contacts between the adjacent gypsum boards were also incorporated in the model using contact elements in OpenSees. To validate the proposed modeling procedure, the analytical model of three full-scale partition wall assemblies, tested at the University of Buffalo (UB) was generated. Force-displacement responses, cumulative dissipated energy, and damage mechanisms from the analytical simulation were compared to the experimental results. The comparison showed that the generic analytical model accurately predicted the trend of the response as well as

the observed damage mechanisms. It was also indicated that the generic model could be slightly adjusted for each particular specimen in order to achieve even better correlation between the analytical and experimental results.

The analytical model proposed in Chapter 6 was limited to the in-plane behavior of partition walls. It also did not account for the effect of return walls. To address these limitations, a new series of component-level experiments (26 experiments in total) was performed to provide the missing information on the out-of-plane cyclic response of stud-to-track connections (Chapter 7). Similar to the previous component-level experiments, the experimental data was utilized to determine the damage mechanisms and generate capacity fragility curves. The experiments indicated that the dominant damage mechanism for stud-to-track connections in the out-of-plane direction was excessive track-flange deformation for connections with large stud-to-track gap (larger than 0.125 inch in this study) and stud-web crippling for other connections. Where studs were screwed to tracks, the screws were pulled out from the studs after the web crippling. Increasing the stud-to-track gap not only affected the dominant damage mechanism, but also led to lower initial stiffness, smaller force capacity, and smaller failure displacement. It was also noted that the connections with thicker studs/tracks were less ductile compared to the thinner connections. Finally, the experimental data was used to calibrate an analytical nonlinear material model for stud-to-track connections in the out-of-plane direction.

The new component model was employed in conjunction with an approximate model of the out-of-plane behavior of gypsum-to-stud/track connections to enhance the previous

analytical model of CFS gypsum partition walls (Chapter 8). The representative models of corner connections were also assembled accounting for stud configurations, stud-to-stud and gypsum-to-stud screw attachments, and gypsum-to-gypsum contacts. The new model included the effect of return walls and could capture the out-of-plane response of partition walls for the first time. The modeling procedure was then validated using two different sets of experimental data. Initially, the analytical models of configurations 1, 2, and 4 of the University of Buffalo (UB) experiments were assembled. The analytical force-displacement responses, cumulative dissipated energy, and damage mechanisms were compared to the experimental results. The comparison showed that the analytical model accurately predicted the average response as well as the observed damage mechanisms. Afterwards, the analytical model of a C-shaped wall system, tested at the University of Nevada, Reno (UNR) (Chapter 2), was generated in OpenSees. The out-of-plane dynamic characteristics, partition acceleration responses, and damage mechanisms from the analytical simulation were compared to the experimental results. Although there were some differences, the analytical model has successfully captured the trend of the out-of-plane response of the partition wall and predicted the possible damage mechanisms.

The procedure proposed in this research can be implemented in future studies to investigate the in-plane and out-of-plane performance of existing partition walls with dimensions (i.e. length and height) and construction details (e.g. stud spacing, screw spacing, and corner detail) for which experimental results are not available. The model helps to identify the sequence of damage mechanisms in the walls. This is particularly

important for damage mechanisms that cannot be detected during experiments, such as forming plastic hinges in field studs and tearing of track webs. These mechanisms occur at locations that are enclosed within the sheathing boards. The investigation results may lead to improving/modifying the current design provisions of nonstructural walls. In addition, there are some efforts underway by researchers to introduce new details to mitigate the damage in partition walls, such as details for stud to top-track connections. The proposed model can be used to investigate and compare various details and select the most persuasive ones to be tested in a subsequent experimental study. This reduces the required time and cost to design and evaluate the new details. The model can also estimate the out-of-plane acceleration response of partition walls, which can be used as the perimeter input motion in the seismic analysis of ceiling systems.

9.2. Future Research

In this section, a list of recommended future studies is presented as follows:

- The proposed model can be run parametrically to provide some insights into wall damage patterns and their relationship to various wall details, configurations and loading types. The parametric studies can be then extended to generate fragility curves for partition walls.

- Despite all the details, the proposed analytical model has limitations. For example, the model assumes a linear behavior for gypsum boards; therefore, it cannot capture crack/breaking of gypsum boards. Moreover, an approximate method is used to model the out-of-plane behavior of gypsum-to-stud

connections. Further experimental studies are essential to determine the accurate nonlinear response of gypsum boards and gypsum-to-stud connections in the out-of-plane direction. Then, the model can be improved by using a nonlinear material for the gypsum boards that can capture the horizontal, vertical, and diagonal crack patterns.

- The proposed modeling methodology can be expanded to partition walls with properties other than those presented in this dissertation. For this purpose, new series of component analytical models need to be calibrated through additional component-level experiments. The methodology can also be used to investigate the seismic performance of CFS shear (structural) walls.
- In common constructions, a partition wall generally interacts with two or more systems. These interactions can be with other non-structural systems (e.g. ceiling systems), between the partition wall and the supporting structure (e.g. structural beams), or between the partition wall and room contents. Therefore, while studying a partition wall as an isolated subsystem provides important information, it should be considered as an integrated system to represent the actual boundary conditions and to capture its effect on other nonstructural or structural systems.